A Mechanistic Understanding of Chromium-based Oligomerisation Catalysts; an EPR and ENDOR Investigation

Submitted for the degree of Doctor of Philosophy

By

Lucia E. McDyre

Department of Chemistry

Cardiff University

2011

ProQuest LLC
789 East Eisenhower Parkway
P.O. Box 1346
Ann Arbor, MI 48106-1346

Form: PGR_Submission_200701

NOTICE OF SUBMISSION OF THESIS FORM: POSTGRADUATE RESEARCH

DECLARATION

This work has not previously been accepted in substance for any degree and is not concurrently submitted in candidature for any degree.

Signed ..... (candidate) Date ....1/9/11.....

STATEMENT 1

This thesis is being submitted in partial fulfillment of the requirements for the degree of .....PhD.....(insert MCh, MD, MPhil, PhD etc, as appropriate)

Signed ..... (candidate) Date ....1/9/11.....

STATEMENT 2

This thesis is the result of my own independent work/investigation, except where otherwise stated. Other sources are acknowledged by explicit references.

Signed ..... (candidate) Date ....1/9/11.....

STATEMENT 3

I hereby give consent for my thesis, if accepted, to be available for photocopying and for inter-library loan, and for the title and summary to be made available to outside organisations.

Signed ..... (candidate) Date ....1/9/11.....

Acknowledgements

Many thanks must go to:

Dr. Damien Murphy, who has provided a great deal of support and guidance throughout the project.

Dr. Kingsley Cavell, for providing help and supervision with the synthetic parts of the project.

Sasol Technology for funding.

Dr. Emma Carter, for giving her invaluable time, assistance and friendship.

Dr. Tracy Hamilton, for training and guidance on synthetic aspects of the work.

Dr. Jason Green, for friendship and moral support during the tough times.

Finally, all my love goes to my parents and sister, who have supported me immensely throughout the course of the PhD, and who make every day a happy one.

Abstract

Electron Paramagnetic Resonance (EPR) and Electron Nuclear Double Resonance (ENDOR) spectroscopies have been used to study the fundamental nature of chromium-based selective oligomerisation catalysts.

A series of 'pre-catalyst' complexes were fully characterised; CW-EPR revealed each complex to possess an axial $\boldsymbol{g}$ matrix ($g\perp > g_e > g\parallel$) and superhyperfine coupling to two equivalent ^{31}P nuclei, consistent with a low-spin d^5 species of approximate C_{2v} symmetry, where the metal contribution to the SOMO is primarily d_{xy}. The isotropic component to the ^{31}P coupling was of a larger magnitude in those Cr(I) complexes bearing PNP ligands than those bearing PCP, indicating that the phosphorus $3s$ character in the SOMO was higher for the former. CW-ENDOR demonstrated that subtle structural differences in the complexes, namely in the phenyl ring conformations, occurred as a function of ligand type. Pulsed experiments proved that the technique is valid and viable for further work on the activated system.

Upon activation of the pre-catalyst with an alkylaluminium, four distinct paramagnetic centres were identified. A Cr(I) bis-arene complex was firstly detected; it was found to form either *via* intramolecular co-ordination of the ligand phenyl groups, or preferentially *via* solvent-based arene co-ordination, if such groups were available. Two further species (I and III) were subsequently observed at low temperatures; the spin Hamiltonian parameters extracted for both showed that a significant modification to the structure of the pre-catalyst had occurred. Half-field transitions indicated the possibility of a dimeric nature to Species III. ENDOR measurements detected an exceptionally large proton coupling in the activated system, possibly due to the co-ordination of alkyl fragments to the metal centre. A final, fourth paramagnetic centre (Species IV), was detected and classed as an intermediate species, due to the greater similarity between its $\boldsymbol{g}$ and $\boldsymbol{A}$ matrices with those of the parent complex, than the other activated species.

Finally, a preliminary investigation into analogous pre-catalyst complexes bearing N-heterocyclic carbene ligands was performed, due to their similar employment in oligomerisation catalysis; CW-EPR spectra revealed information on both their electronic and structural natures.

Abbreviations

acac	acetylacetonate
Ar	aryl group
br	broad
CW	continuous-wave
δ	chemical shift (ppm)
d	doublet
DCM	dichloromethane
dipp	2,6-diisopropylphenyl
dppe	bis(diphenylphosphino)ethane
dppm	bis(diphenylphosphino)methane
DMSO	dimethylsulfoxide
EPR	electron paramagnetic resonance
ENDOR	electron nuclear double resonance
ESEEM	electron spin-echo envelope modulation
ES-MS	electrospray mass spectrometry
Et	ethyl group
Et_2O	diethyl ether
FID	free induction decay
FSED	field-swept echo-detected
HRMS	high resolution mass spectrometry
IMes	1,3-dimesitylimidazol-2-ylidene
^{i}Pr	*iso*-propyl
IR	infra red
L	neutral, 2 electron donor ligand
LLDPE	linear low-density polyethylene
LAO	linear alpha olefin
m	multiplet
M	metal
MAO	methylaluminoxane
MMAO	modified methylaluminoxane
Me	methyl

MeCN	acetonitrile
Mes	mesityl, 2,4,6-trimethylphenyl
MO	molecular orbital
mw	microwave
NHC	N-heterocyclic carbene
NMR	nuclear magnetic resonance
Ph	phenyl
ppm	parts per million
q	quartet
R	alkyl group
RF	radiofrequency
s	singlet
sept	septet
sh	shoulder
SOMO	singly occupied molecular orbital
st	strong
t	triplet
^{t}Bu	*tertiary*-butyl
TEA	triethylaluminium
THF	tetrahydrofuran
TMA	trimethylaluminium
UV	ultraviolet
w	weak
X	halogen
ZFS	zero-field splitting

Contents

Chapter 3

Experimental Details

Chapter 4

An EPR and ENDOR Characterisation of Cr(I) 'pre-catalyst' complexes $[Cr(CO)_4PP]^+$ ($PP = Ph_2PN(R)PPh_2$, $Ph_2P(R)PPh_2$)

Chapter 5

Intramolecular formation of Cr^{I}(bis-arene) species *via* R_3Al activation of $[Cr(CO)_4PP]^+$ (PP = $Ph_2PN(R)PPh_2$, $Ph_2P(R)PPh_2$)

Chapter 6

A Low-Temperature EPR and ENDOR Investigation of the Interaction of TEA with the Cr(I) 'pre-catalyst' complexes $[Cr(CO)_4PP]^+$ (PP = $Ph_2PN(R)PPh_2$, $Ph_2P(R)PPh_2$)

Chapter 7

EPR spectroscopic analysis of N-heterocyclic carbene complexes of Cr(I), Cr(III) and Ti(III)

Chapter 1

The Chemistry of Selective Ethylene Oligomerisation

1.1 Introduction

Linear alpha-olefins ('LAO's or 1-alkenes) with chain lengths ranging from C_4 – C_{30} are in great demand in the chemical industry, due to the multitude of applications which exists for them. They are sought-after intermediates in the production of detergents (those with chain length C_{10} - C_{14}), synthetic lubricants (C_{16} - C_{18}), and in the manufacture of plasticiser alcohols (C_4 – C_8 alkenes).[1] Another major use of the C_4 – C_8 fraction, and in particular 1-hexene, is as a co-monomer, along with ethylene, in the production of linear low-density polyethylene (LLDPE).[2] This type of polyethylene has a large range of applications in many types of plastic products, including the manufacture of plastic bags, covering of cables and flexible tubing. For this reason, obtaining 1-hexene to act as a precursor for this polymer, is highly industrially significant and important.

Industrially, the most common method of manufacturing 1-hexene is *via* metal-catalysed oligomerisation of ethylene, either a 'full-range' process which results in a distribution of linear alpha olefins, or an 'on-purpose' route which selectively produces predominantly 1-hexene. The biggest full range producers are Shell, BP Amoco and Chevron Phillips.[1] However, the envelope of oligomers produced is inconvenient by industrial standards, as generally only one particular chain length is desired, and the fractions must be separated by distillation. It was therefore imperative to find a method of selectively producing only the chain length that was needed. On-purpose routes have been developed, but they are rare and currently the only commercial-scale trimerisation plant is run by Chevron Phillips.[3, 4] There is a need therefore for more fundamental research into the chemistry of selective oligomerisation, to enable selective systems to be developed.

Despite the relatively large volume of work conducted on the synthesis of catalyst systems, the details of the chemistry of the actual catalytic cycle are still not completely understood. The nature of the active catalyst itself is not fully known – for example, the oxidation state of the chromium centre during the process is still under debate. Although several papers have appeared on the correlation between ligand structure and reaction selectivity,[5, 6] a definitive relationship has yet to be discovered. The nature of the system renders it difficult to analyse – the active catalyst is usually

air-sensitive, and paramagnetic states are often involved, which makes analysis by conventional techniques such as NMR difficult. However, a highly effective tool for studying the paramagnetic chromium complexes under investigation is Electron Paramagnetic Resonance (EPR) spectroscopy. EPR provides much information on the nature of the species under consideration, and in particular, the co-ordination features of the catalytically active transition metal ions. For example, the spin Hamiltonian parameters can be related to the electronic structure of the complex, from simply the oxidation state of the chromium to detailed information on the molecular orbitals. Electron Nuclear Double Resonance (ENDOR) spectroscopy can also be utilised to provide information on the nuclei interacting with the electron, *via* the hyperfine matrix. Further details on these techniques will be provided in Chapter 2.

1.2 Development of Ethylene Oligomerisation

The conventional method for producing 1-hexene involves a Cossee-Arlman[7, 8] type oligomerisation mechanism, from which an envelope of olefins results, displaying a statistical distribution of chain lengths consistent with a Schulz-Flory distribution.[9, 10] Chain growth occurs *via* ethylene co-ordination to the active transition metal centre, followed by insertion into a metal-alkyl bond. Chain termination occurs *via* β-hydrogen transfer to the metal, forming a metal hydride and a linear alpha olefin. The range of olefin lengths arises due to the competition between chain termination and migratory insertion at each stage of the cycle (see Scheme 1.1).

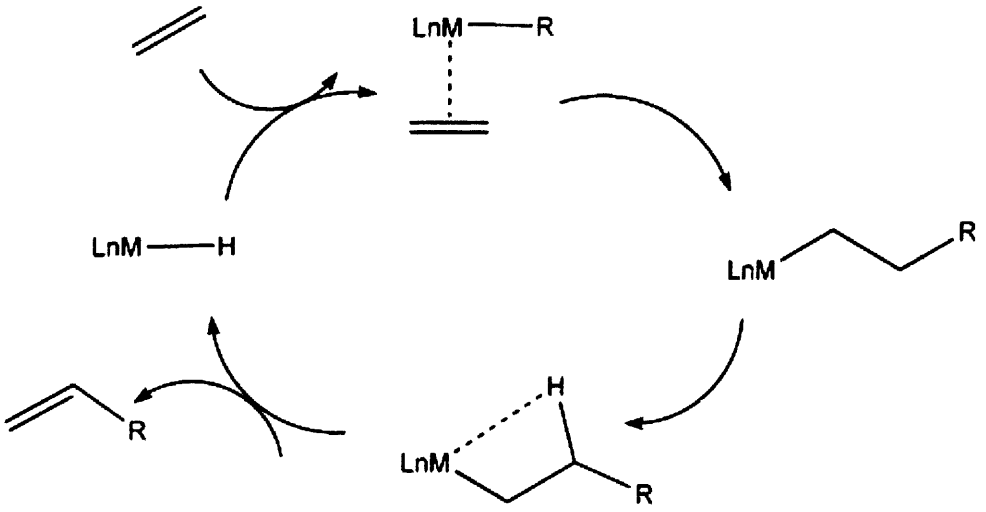

Scheme 1.1: Ethylene insertion/β-elimination mechanism proposed by Cossee and Arlman for the oligomerisation process.[7, 8]

active for polymerisation. However, the pyrrolide ligand being the closest heterocyclic analogue to cyclopentadienyl, both in electronic and steric terms, was also investigated. Various chromium pyrrolide complexes were tested for ethylene oligomerisation upon activation with triethylaluminium and found to be active and selective towards trimerisation. By 1999, Phillips had obtained a catalyst yielding 93% overall 1-hexene.[15] It incorporated 2,5-dimethylpyrrole as the ligand of choice due to its high light, air and temperature stability. Combined with Cr(III) 2-ethylhexanoate, diethylaluminium chloride (the halogen compound also increasing the activity and selectivity) and Et_3Al in toluene, it produced this unprecedented selectivity.

Concurrently, catalytic systems consisting of multidentate heteroatomic ligands complexed to chromium were also being investigated. Many different donor atoms have been considered, including oxygen (for example, 74% selectivity was obtained using the dimethoxyethane ligand),[13] nitrogen (e.g. the triazacyclohexane ligand),[16] and phosphorus (tridentate phosphines).[17]

Ligands containing more than one heteroatom have proved to produce extremely active and selective catalysts. Extremely high 1-C_6 selectivity (i.e., selectivity to 1-hexene within the hexene fraction (> 99%)) was achieved by BP using a chromium-based system incorporating a diphosphazane ligand containing an ortho-methoxy group.[18] Bis-phosphinoamine ligands, for example of the type $R_2PCH_2CH_2N(H)CH_2CH_2PR_2$ by Sasol Technology, produced a catalyst capable of 97% overall 1-hexene selectivity.[19]

All of the catalyst systems discussed so far have been based on chromium. Indeed, the vast majority of all selective oligomerisation systems are chromium-based. This is due to chromium producing systems with the best combination of activity, selectivity and thermal stability.[1] The catalytic performance of other transition metals has also been investigated however. The first non-chromium catalyst to combine high activity and selectivity was discovered by Deckers *et al.,* and based on a Ti(II) species.[20, 21] Systems based on zirconium and vanadium were also investigated,[22] but only 55 and 45% selectivity were obtained respectively. Andes *et al.*,[23] discovered a tantalum-based catalyst which was highly selective towards 1-C_6, but with a relatively low activity. Although certain other transition metals may catalyse ethylene trimerisation, the best results, in terms of optimum activity and selectivity, appear to lie with chromium-based catalysts.

1.3 Mechanistic Considerations

1.3.1 Activation of the pre-catalyst

All of the catalyst systems described herein consist of a metal centre with co-ordinating ligand(s) (which is generally known as the 'pre-catalyst') and co-catalyst which acts as an activator; experiments performed without such a co-catalyst showed no catalytic activity.[24] This co-catalyst usually takes the form of an alkylaluminium compound such as triethylaluminium (commonly referred to as TEA) or trimethylaluminium (TMA), or an aluminoxane such as methylaluminoxane (MAO), which is the most commonly used activator.

The purported role of the co-catalyst is to alkylate the metal centre.[1, 25, 26] It is believed that the metal alkyl species generated is then suitable to undergo ethylene insertion followed by chain growth.[1] The structure of MAO in solution is relatively poorly defined and used in large excess, and so the exact nature of the active species is generally not known. It is prepared by hydrolysis of Me_3Al and has the general formula $[\text{-Al(Me)-O-}]_n$, where n is typically around 5 – 20. However its exact composition is not well understood, and many structures have been proposed, some of which are shown in Scheme 1.3.[27]

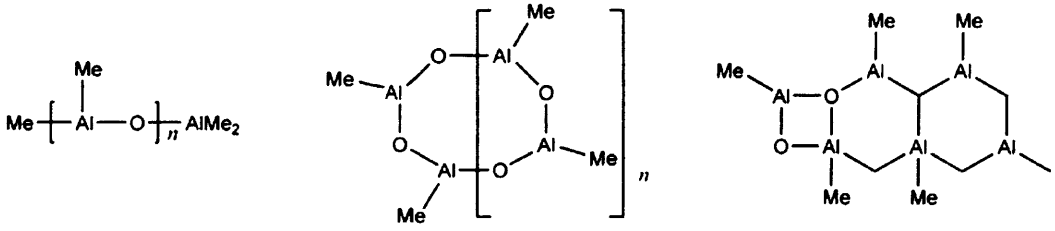

Scheme 1.3: Postulated structures of MAO.

Alkylaluminiums on the other hand have more well-defined structures. Triethylaluminium and trimethylaluminium are known to consist of dimers (Scheme 1.4).

Scheme 1.4: The structures of triethylaluminium and trimethylaluminium.

Some groups have obtained experimental evidence for a metal-alkyl intermediate, upon activation with an alkylaluminium compound. Hagen *et al.*,[26] added aluminium alkyls to cyclopentadienyl titanium chlorides, and monitored the results *via* NMR. Addition of 2 – 5 equivalents of Me_3Al produced the monomethyl complex $Cp'TiMeCl_2$, whereas 10 – 30 equivalents produced the dimethyl derivative.

In certain cases upon activation, dimerisation of the metal occurred. Jabri and co-workers[28] isolated a dinuclear chromium species, with two terminally bonded methyl groups, following activation of a $CrCl_3[CySCH_2CH_2N(H)CH_2CH_2SCy]$ precursor with excess Me_3Al. Each Cr atom retained its trivalent state upon dimerisation. Albahily *et al.*,[29] activated $[(^tBu)NPN(^tBu)]_2Cr$ with different stoichiometric ratios of $^iBu_3Al$. Two equivalents of the activator afforded a mononuclear, alkylated Cr species, whereas ten equivalents produced a dinuclear, hydride-bridged species. Both were catalytically active, with almost identical behaviour, indicating that each goes on to produce the same active species during the cycle, which still evades detection.

Most of the chromium oligomerisation systems originate with a Cr(III) precursor, which will be discussed in Section 1.3.2. However, the systems studied in this thesis are Cr(I) species. As is common for low-valent Cr complexes, carbonyls are present as stabilising ligands. It is assumed that in order for Cr(I) species to become active catalysts, the carbonyl ligands must be removed from the Cr co-ordination sphere, to free up co-ordination sites and thereby enable alkylation and ethylene co-ordination. Et_3Al is regarded as both an alkylating agent and a carbonyl-removing agent.[30] UV photolysis can potentially be used to remove the CO ligands; however, in a study by Rucklidge *et al.*,[30] it was not as effective as reaction with 100 equivalents Et_3Al, which resulted in a complete loss of IR signal in the metal-bound carbonyl region. Bowen *et al.*,[25] also attempted CO removal by both UV irradiation and reaction with Et_3Al; in this case, there was no evidence at all by IR spectroscopy of CO displacement *via* irradiation, but a loss of all CO peaks occurred upon addition of 300 equivalents Et_3Al.[25] It appears that the most efficacious way of CO removal and alkylation for the type of Cr(I) complexes studied here is addition of alkylaluminium.

1.3.2 Oxidation state of the active species

The question of the oxidation state of the catalyst after activation and throughout the catalytic cycle is one of the most debated of the mechanistic considerations. The activation of the pre-catalyst (usually a Cr(III) species) is, in some cases, thought to

result in reduction of the metal centre to a Cr(II) species.[28, 31-33] However, reoxidation to the trivalent state has also been observed in the same type of systems.[34] Reduction to form a Cr(I) species from a Cr(III) precursor has also been put forward as a possibility,[29] and indeed Brückner *et al.*,[35] detected a Cr(I) species upon activation of a $Cr(acac)_3$ precursor.

It is thought that a redox couple is in operation throughout the catalytic cycle.[1] After activation, oxidative addition of two ethylene molecules is thought to occur, increasing the metal oxidation state from M^n to M^{n+2}. The reductive elimination steps involve a decrease from M^{n+2} to M^n. However, the exact oxidation states are not known. In fact, all redox pairs have been proposed in the literature; Cr(I)/Cr(III), [12, 16, 36]Cr(II)/Cr(IV)[31, 32] and Cr(III)/Cr(V)[37] are all viable possibilites.

It is hoped that by starting from a Cr(I) precursor in this work, new insight may be gained into the oxidation state of the Cr centre throughout the catalytic process.

1.3.3 Metallacyclic mechanism

Manyik *et al.*,[12] proposed a different mechanism to the conventional linear chain growth mechanism described in Scheme 1.1. This new mechanism explained the unusual dependences of the rate of 1-hexene formation on the temperature and pressure of the reaction, which were inconsistent with a linear chain growth mechanism. The authors proposed a mechanism involving the co-ordination of two ethylene molecules to the chromium centre, followed by metallacyclopentane formation. The rate-determining step was assigned as this rearrangement of the co-ordinated alkenes to form a metallacyclopentane, to account for the second order dependence on ethylene pressure. A β-hydrogen transfer from the metallacycle to a third co-ordinated ethylene was then postulated to occur, and 1-hexene was formed *via* a reductive elimination of this intermediate.

Briggs[13] then developed this catalyst system but modified the postulated mechanism slightly; instead of a β-hydrogen transfer to ethylene, insertion of ethylene into the metallacyclopentane occurs to yield a metallacycloheptane. This must be faster than the decomposition of the metallacycle to 1-butene. Ring opening then occurs to form a chromium hexenyl hydride, which reductively eliminates to yield 1-hexene and the active species again. This ring opening process must be faster than further ethylene insertion into the metallacycloheptane, which would form a larger ring (Scheme 1.5).

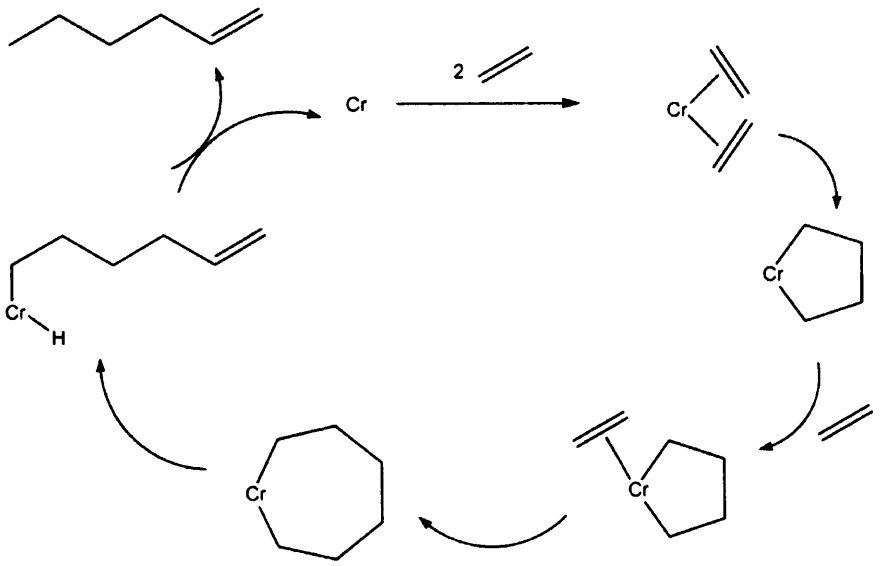

Scheme 1.5: Metallacyclic mechanism proposed by Manyik *et al.*,[12] and expanded by Briggs.[13]

The existence of transition metal metallacycles had been demonstrated previously by McDermott *et al.*,[38, 39] during their studies on the thermal decomposition of platinocycles, lending weight to the proposed formation of chromacycles during the oligomerisation process. These authors also determined that the metallacycles were particularly resistant to β-hydrogen elimination, in comparison to other modes of decomposition, indicating that Briggs' model of the metallacycle mechanism was correct. Crystal structures of five- and seven-membered chromacycles were subsequently published, and the seven-membered species decomposed more rapidly than the five-membered chromacycles, producing 1-hexene.[40] Recently, deuterium labelling studies have provided additional compelling evidence for a metallacyclic mechanism. Agapie *et al.*,[36] carried out the trimerisation reaction using a 1:1 mixture of C_2H_4 and C_2D_4. If a Cossee-Arlman type mechanism was at work, H/D scrambling would occur and isotopomers containing an odd number of deuterons would be formed. Conversely, the postulated metallacyclic route should produce no H/D scrambling and only C_6D_{12}, $C_6D_8H_4$, $C_6D_4H_8$ and C_6H_{12} should be observed. This indeed was observed, with the aforementioned isotopomers in a ratio of 1:3:3:1, which is entirely consistent with the metallacycle mechanism.

There has recently been some debate over the exact decomposition pathway of the metallacycloheptane. A single, concerted step was theorised by Yu and Houk[41] over the two-step route postulated by Briggs (and supported by evidence by McDermott *et al.*,).[38, 39] An agostic-assisted β-hydride shift leading directly to the alkene was

calculated as the lowest energy pathway for the metallacycloheptane decomposition. Interestingly, this led the authors to suggest an explanation for why dimerisation is disfavoured; the concerted process cannot occur in the metallacyclopentane due to geometric constraints of the small ring, and the two-step decomposition mechanism would have to occur instead, which is less favourable than ring expansion followed by the single-step decomposition mechanism. The study by Agapie *et al.*,[36] discussed previously, attempted to discern if this concerted mechanism was indeed happening, by looking for unusual kinetic isotope effects; however, their results did not prove or disprove the proposed metallacycle collapse process, and it is still a matter of debate.

1.3.4 Selective tetramerisation

Recently, the first catalyst systems capable of selectively tetramerising ethylene to produce 1-octene have been developed. It had been thought that tetramerisation *via* a similar mechanism to that described above for trimerisation was highly unlikely, as a nine-membered ring would have to form; this was thought to be disfavoured compared to the seven-membered metallacycle.[42] However, Sasol Technology have developed a system capable of selective tetramerisation, yielding 1-octene in selectivities up to 70%.[5] Deuterium labelling was performed on this system to seek evidence of a mechanism similar to that occurring during trimerisation. The observed isotopomer distribution correlated extremely well with that predicted for a metallacyclic mechanism. It was therefore postulated that both trimerisation and tetramerisation operate *via* a common metallacycloheptane intermediate, and the selectivity to 1-hexene or 1-octene controlled by subtle modifications to the steric and electronic effects of the co-ordinating ligand, discussed below.

1.3.5 Ligand effects

A vast majority of the oligomerisation systems are based on a chromium centre with co-ordinating bis- (diphenylphosphine), (dialkylphosphine) or (diphenylphosphinoamine) ligands, the general structure of which is shown in Scheme 1.6. The influence of the electronic and geometrical structure of these ligands on the activity and selectivity of catalysis has been studied in detail by many groups.

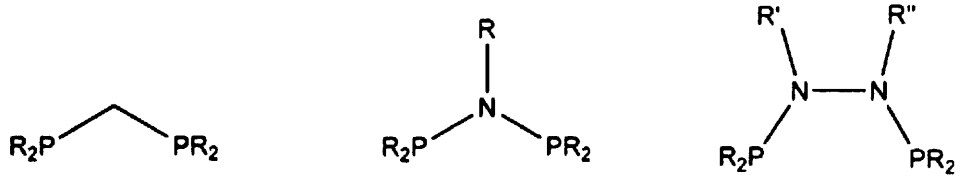

Scheme 1.6: Various ligands used in ethylene oligomerisation. R = alkyl or aryl group.

McGuinness *et al.*,[19, 43] investigated the effects of R group substitution in Cr(III) systems for trimerisation, with tridentate PNP ligands (PNP = $(R_2PCH_2CH_2)_2NR'$). It appeared that R groups with low steric demand led to the most active catalysts. Replacing the R = phenyl group with a cyclohexyl group, which was highly basic and sterically demanding, led to a decrease in activity and predominantly polymer production. When an ethyl group was used, which was highly basic but sterically compact, an increase in activity and excellent hexene selectivity was observed. The crystal structures of both the phenyl and cyclohexyl derivatives of the catalyst were obtained, and the similarity between them meant that the marked differences in activity each displayed made it likely that the ligand may be co-ordinated in different ways in the active species.

Bollmann *et al.*,[5] investigated ligand effects in a *tetramerisation* system, aluminoxane-activated chromium/$(R_2P)_2NR'$. Various substitutions on N and P, ranging from simple alkyl groups to branched and aromatic groups, all produced active catalysts for 1-octene production. However, certain derivatives produced 1-hexene in relatively large amounts as well. The substituent on N had little effect on the 1-octene selectivity, but the more α-branching there was, the higher the selectivity towards 1-hexene within the hexene fraction.

Blann *et al.*,[44] extended this study to Cr(III) complexes co-ordinated to bulky PNP ligands with an alkyl substituent at the *ortho*-position of each phenyl ring, and various substitutions on N (PNP = $Ar_2PN(R)PAr_2$). Increasing the steric bulk at the *ortho*- position, from a methyl to an ethyl or iso-propyl group, led to increased selectivity towards hexene over octene. Similarly, exchanging the methyl substituent on N for an isopropyl moiety led to a higher percentage of 1-hexene in the product mixture. This effect was reversed by the removal of one or more substituents from the phenyl rings, which led to a dramatic increase in the total fraction of 1-octene. It was thus postulated that steric bulk of the ligand plays a crucial role in switching the selectivity from tetramerisation to trimerisation.

Killian and co-workers studied similar complexes, but with aryl moieties on the nitrogen atom.[45] Increasing the size of an *ortho*-substituent on this aryl group led to increased selectivities for both hexene and octene, at the expense of cyclic by-products. However, the catalytic activity decreased. Including a carbon spacer between the nitrogen and phenyl group increased the α-selectivities further. PNP groups containing an electron-rich N-phenyl group also produced higher α-selectivity. It was concluded that both steric bulk and the electronic nature of the N-phenyl group both play a role in determining oligomerisation selectivities.

Kuhlmann *et al.*,[46] looked at differing cycloalkyl substituents on nitrogen. Ligands with small ring size substituents were comparatively unselective; a cyclodecyl substituent produced the highest fraction of hexene and octene. Of the complexes with a cyclohexyl substituent, those with a more bulky alkyl group on the 2-position of the cyclohexyl led to increased overall α-selectivity. As with the studies discussed above, in general, increased steric bulk favoured trimerisation over tetramerisation.

Overett and co-workers[47] determined that the smaller the bite angle of P-Cr-P in a similar system, the higher the 1-octene:1-hexene ratio. Poor activities were observed for diphosphine ligands with saturated linkers; possibly due to ligand rigidity and/ or electronic effects. Again, steric bulk on *ortho*-phenyl groups changed the selectivity from favouring octene to hexene production. However, this switch in selectivity also occurred on changing a diphenylphosphine with a bridging benzene ligand to one with a bridging isopropyl group, indicating that electronic factors may also play a prominent role in determining selectivity, and that more basic phosphines may favour trimerisation.

Jiang *et al.*,[48] studied the effect of the position of substitution of the N-aryl functionality. A *meta*-methyl group gave higher activity than the *ortho*- or *para*-versions. Similarly to other studies, increasing the bulk of the ortho substituent led to increased hexene selectivity at the expense of octene. However, increasing the bulk of the *meta* substituent produced the opposite effect.

Additional studies have been performed on PNP ligands containing an *ortho*-methoxy-substituted aryl group. Wass *et al.*,[18] demonstrated that this type of system was active and selective for trimerisation. It was initially postulated that the steric bulk provided by the methoxy group led to its exceptional performance. However, a complex containing a sterically equivalent *ortho*-ethyl group was inactive, as was one bearing *para*-methoxy groups. Variations on the *para*- and *meta*-substitution but retaining the

ortho-methoxy functionality were active. The authors postulated that the *ortho*-methoxy group acts as a pendant donor and increases the co-ordinative saturation of the chromium centre. The propensity for these groups to co-ordinate was confirmed by Bercaw and co-workers[36] in the crystal structures of Cr(III) complexes with a ligand such as $Ar_2PN(Me)PAr_2$ (Ar = 2-methoxyphenyl), where an octahedral geometry with one bound methoxy group was observed.

Blann *et al.*,[44] as discussed previously, showed that the selectivity of *ortho*-alkyl substituted diphosphinoamine systems shifted from trimerisation to tetramerisation by reducing the number of such substituents, and established that pendant co-ordination through aryl donor-substituents is not essential for catalytic activity. However, they also wished to establish whether the selectivity of *ortho*-methoxy substituted systems is determined by a steric effect or by pendant co-ordination as proposed by Wass *et al.*,[18] They determined that both effects are in operation.[49] They attributed the preference to trimerisation as steric bulk constraining the metallacycloheptane into a more favourable conformation for β-hydrogen transfer, leading to 1-hexene production; additionally, competitive co-ordination by a pendant methoxy donor may retard the co-ordination and insertion of another ethylene molecule.

Morgan *et al.*,[31] determined that the 2,6-diphenylphenol ligand, in conjunction with a chromium source, aromatic ether solvent and triethylaluminium, produced an active trimerisation catalyst. When 2-phenylphenol was used as a ligand, it rendered the system inactive, suggesting that both pendant phenyl groups are essential for catalytic activity. In contrast to the work by Blann[44] and Wass,[18] *ortho*-methoxy substitution on the phenyl groups failed to produce an active catalyst, attributed to steric crowding.

Various systems containing a hemi-labile donor ligand have been studied. Deckers *et al.*,[21] investigated the performance of $[\eta^5\text{-}C_5H_3R\text{-(bridge)-Ar}]TiCl_3$ catalysts activated with MAO, an example of which is shown in Scheme 1.7. The selectivity for trimerisation was dependent on the presence of the pendant arene group on the Cp ligand; without it, predominantly polyethylene was formed. It was proposed that the arene moiety co-ordinates to the metal during catalysis, stabilising intermediates by η^6 co-ordination, and then dissociating/slipping to make room for incoming substrates. The presence of small amounts of 1-hexene (along with the polyethylene) produced by the catalyst system without the pendant arene was ascribed to transient co-ordination of the toluene solvent to the metal centre. The nature of the bridging moiety was crucial in

obtaining good selectivity; only disubstituted C_1 bridges provided highly selective and active catalysts.

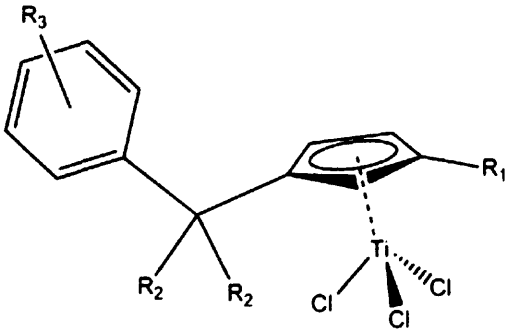

Scheme 1.7: Monocyclopentadienyl-arene titanium trichloride catalyst prepared by Deckers *et al.*,[21]

A computational study by Blok *et al.*,[42] examined this proposal and generally supported the mechanism. They also compared the catalyst described above, investigated by Deckers and co-workers,[21] to one that has co-ordinated to an external arene, i.e., from the solvent. They calculated that toluene or benzene molecules from the solvent would co-ordinate more strongly to the metal; however, intramolecular co-ordination was entropically favoured. If free benzene or toluene were to co-ordinate, they calculated that the reduction in space around the metal would hinder ethylene co-ordination and lower the reaction rate. de Bruin *et al.*,[50] also investigated this system and discovered that upon addition of two ethylene molecules to the system, the average Ti-C_{arene} distance increased by over 1 Å, which again supports the hypothesis of a hemi-labile nature of the arene ligand.

Similarly to the studies in titanium-based systems, the hemi-labile nature of the pyrrole ligand in the Phillips catalyst system was investigated by van Rensburg and co-workers;[51] this catalyst was discussed earlier in Section 1.2. Assuming a Cr(II)/Cr(IV) redox cycle, an η^5 bonding mode to the metal is preferred for Cr(II) intermediates, facilitating the metallacyclopentane formation. A σ-bonding mode is preferred however for Cr(IV) species, enabling metallacycle growth. Facile ring slippage was postulated to occur to facilitate the transformation of the Cr(IV) metallacycloheptane to the Cr(II)-1-hexene species.

The catalyst systems discussed above, all exhibit activities and selectivities dependent on the type of ligand present. Although these effects vary, some general trends are evident. For the Cr/PNP systems, increasing steric bulk on the ligand favours trimerisation over tetramerisation. This was attributed to the fact that during the

catalytic cycle, a metallacyclononane intermediate (yielding 1-octene) exhibits a larger steric demand compared to a metallacycloheptane; a preferential elimination of 1-hexene should occur if the metallacycloheptane is relatively more stable, due to a large steric interaction between the ligand and the metal.[46, 52] A recent DFT study on a $Cr(acac)_3/(PPh_2)_2N^iPr$ model system demonstrated that the two lowest energy conformations for a C_6-chromacycle intermediate, which went on to either produce 1-hexene or form a C_8-chromacycle respectively, were indeed geometrically different with respect to the orientations of the phenyl groups and the isopropyl group.[53] The presence of an *ortho*-methoxy substituted phenyl group, thought to be acting as a pendant donor, was determined to increase the selectivity to 1-hexene over 1-octene by both steric and donor effects.[49] The hemi-labile character of a pendant arene moiety in various Ti-based systems,[21, 42, 50] and the pyrrole ligand in the Phillips system,[51] was found to achieve high levels of selectivity to trimerisation by stabilisation of intermediates during the catalytic cycle, followed by dissociation/slippage to yield 1-hexene.

1.4 Model Catalytic Systems under Investigation

The model systems under investigation consist of Cr(I) tetracarbonyl species, with a chelating bis(diphenylphosphine)/(diphenylphosphinoamine) ligand. As mentioned previously, chromium-based catalysts are the most widely used and effective for oligomerisation, exhibiting high levels of activity and selectivity.[1, 12, 13] Cr(III) is the most widely used pre-catalyst, as it is relatively inexpensive, stable and easy to prepare. However, Cr(I) species have also been demonstrated to produce active catalysts;[25, 30] and there is the strong possibility that Cr(I) is implicated in the redox cycle when starting from a Cr(III) pre-catalyst.[29, 35] Hence the study of these Cr(I) pre-catalysts and their role in the catalytic process is highly desirable, but hitherto relatively unexplored.

Bis(phosphine) ligands are used frequently in catalysis, due to their ease of preparation and of modification of their properties to produce a diverse range of catalytic systems.[54] It has been demonstrated that subtle variations to this type of PNP ligand in the system can produce significant changes to the activity or selectivity of the catalysis, for example switching the process from trimerisation to tetramerisation. The presence of a group which can act as a donor, for example an aryl group with a methoxy donor, or a pendant aryl group itself, can affect the selectivity dramatically, producing 1-hexene in favour of polyethylene.

It has been determined that in this type of Cr(I) system, an extremely weakly co-ordinating anion is necessary.[25, 30] Wass *et al.*,[25] discovered that the use of the BF_4^- anion produced Cr(I) complexes with no catalytic activity, whereas $[B(C_6F_5)_4]^-$ gave complexes with catalytic activity, albeit relatively low. Rucklidge and co-workers[30] tried the tetrafluoroborate and hexafluorophosphate anions, and in both cases an inactive catalyst resulted. The anions were deemed to be too strongly co-ordinating to the chromium centre, as shown by the broadening of the ^{19}F NMR signal, consistent with a strong interaction to the paramagnetic cation.[55] However, the use of the perfluoro-*tert*-butoxy aluminate ion, $[Al(OC(CF_3)_3)_4]^-$, produced catalysts with good activities and selectivities. The delocalisation of the negative charge over the large area of non-nucleophilic and chemically robust moieties appears to be the reason for the extremely weakly co-ordinating nature of this anion.[56] For this reason in this work the silver aluminate $Ag[Al(OC(CF_3)_3)_4]$ has been utilised to oxidise the Cr(0) complexes and produce the model catalytic Cr(I) systems, displayed in Scheme 1.8.

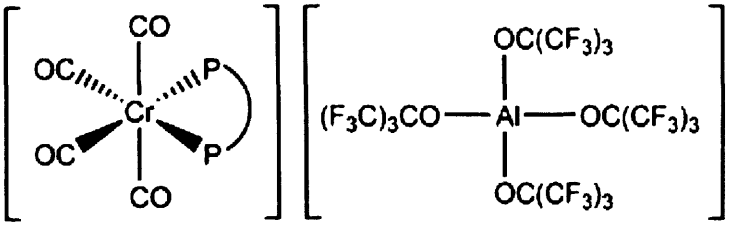

Scheme 1.8: Model Cr(I) catalytic system employed in this work.

The co-catalyst most often used to activate the pre-catalyst is MAO. A large excess of this is needed (approximately 300 equivalents MAO:Cr). This amount has been empirically determined as providing the best combination of activity and selectivity[16] during the catalytic process and many groups use this ratio of MAO:Cr.[5, 16, 44, 48, 52] Using a higher amount of MAO may increase the activity, but at the expense of the selectivity towards 1-hexene or 1-octene.[19, 43] The use of alkylaluminiums, for example Et_3Al, is becoming more prevalent, as they are much cheaper than alkylaluminoxanes. However, when a Cr(III) precursor is used, a separate alkyl abstracting agent is required as well, which can lead to short catalyst lifetimes. A Cr(I) pre-catalyst, on the other hand, can be activated solely by addition of an alkylaluminium.[30] Rucklidge *et al.*,[30] determined that the optimum catalytic activity of a Cr(I)/PNP system occurred at approximately 200 equivalents of Et_3Al to chromium. A very low activity was observed when 50 equivalents were used, and so the authors did

not investigate the use of lower amounts than this. Similarly, Wass *et al.*,[25] added 300 equivalents Et_3Al to Cr(I)/PNP systems and achieved catalytic activity. A further advantage, along with reduced cost, of using Et_3Al rather than MAO to activate a Cr(I) pre-catalyst is the more well-defined nature of the former. The exact composition and structure of MAO is still not entirely understood, and includes multiple equilibria in solution.[27] The analysis of species formed after activation may be complicated by the nature of MAO. It is for these reasons we have decided to activate our Cr(I) precursors with either Et_3Al or Me_3Al.

In this work, the oligomerisation of 1-hexene, as opposed to ethylene, will be investigated. It was not possible with the equipment available to perform an *in-situ* reaction at elevated temperatures and under an ethylene pressure, and simultaneously record EPR data. Instead, the addition of various equivalents of 1-hexene as a model alkene to the system was investigated. It has been demonstrated by Köhn *et al.*,[16, 57] that a chromium-based catalyst with a triazacyclohexane ligand, was capable of both ethylene trimerisation[16] and the selective trimerisation of 1-hexene.[57] The hexene trimerisation indeed appeared to operate *via* the same metallacyclic mechanism proposed by Briggs, and the trimer of 1-hexene was isolated in high selectivity. Importantly, the authors proved that the triazacyclohexane ligand was still co-ordinated to the chromium in the active complex. Study of the oligomerisation of 1-hexene as a model alkene thus seems valid. There is the additional advantage of being able to freeze the solution immediately upon addition of alkene and record the EPR spectrum, providing the possibility of identification of short-lived species.

1.5 Suitability of EPR for this Study

The complexes under investigation in this work, namely Cr(I) (d^5, $S = ½$) are particularly suitable for investigation *via* electron paramagnetic resonance spectroscopies. Conventional methods of analysis may be hindered due to the paramagnetic nature of the system; for example, NMR peaks are broadened with the presence of an unpaired electron. EPR also provides greater sensitivity than NMR, and has a detection limit of around 10^{-7} mol dm^{-3}, enabling very dilute samples to be studied. EPR techniques are ideal for studying the complexes under a variety of conditions, including variable temperatures, variable microwave powers, and in solution.

EPR potentially provides a wealth of information on transition metal complexes; the components of the ***g*** matrix vary as a function of *d* orbital splittings and so the molecular symmetry, energy separation between ground and excited states, and nature of the singly occupied molecular orbital can all be obtained. Utilising EPR in conjunction with ENDOR spectroscopy enables hyperfine interactions to be analysed in detail, both of the metal centre and ligands present; the type of bonding and mutual orientation can be determined.

1.6 Conclusions

The discovery and development of catalysts capable of selective ethylene oligomerisation is an extremely important area of research, due to the large industrial demand for linear alpha olefins, in particular 1-hexene and 1-octene. 1-hexene is used as a co-monomer in linear low-density polyethylene production, and as such its selective production, without the waste of concurrently producing a whole range of alkene chain lengths, is desired. Although the basic mechanistic details of the trimerisation reaction were proposed over 30 years ago, with the suggestion of a metallacyclic mechanism by Manyik *et al.*,[11, 12] there is still a raft of unknowns concerning the reaction. For example, the oxidation state of the metal (usually chromium) after activation and throughout the cycle is hotly debated. The role of the co-catalyst is assumed to be that of alkylation of the metal centre,[1] but few alkylated intermediates have been observed.[26, 28, 29] The nature of the ligand has a great effect on the activity and selectivity of catalysis, from switching the propensity of the reaction between tri- and tetramerisation,[44, 46, 47] to acting as a hemi-labile donor to stabilise reactive intermediates.[21, 49-51] However, these observations were generally empirical and no definitive explanation as to exactly how the ligand affects the catalysis in this way has been established. Hence further study into the fundamental chemistry of this reaction is crucial to understanding and improving catalytic performance.

1.7 References

1. J. T. Dixon, M. J. Green, F. M. Hess and D. H. Morgan, *J. Organomet. Chem.*, 2004, **689**, 3641.
2. A. H. Tullo, *Chem. Eng. News*, 2000, **78**, 35.
3. *US 5786431, Phillips Petroleum Company Pat.*, 1998.
4. *EP 0417477, Phillips Petroleum Company Pat.*, 1991.

5. A. Bollmann, K. Blann, J. T. Dixon, F. M. Hess, E. Killian, H. Maumela, D. S. McGuinness, D. H. Morgan, A. Neveling, S. Otto, M. Overett, A. M. Z. Slawin, P. Wasserscheid and S. Kuhlmann, *J. Am. Chem. Soc.*, 2004, **126**, 14712.
6. M. Overett, K. Blann, R. d. Villiers, J. T. Dixon, E. Killian, D. S. McGuinness, A. Rucklidge and A. M. Z. Slawin, *Adv. Synth. Catal.*, 2006, **348**, 1200.
7. P. Cossee, *J. Catal.*, 1964, **3**, 80.
8. P. J. Arlman and P. Cossee, *J. Catal.*, 1964, **3**, 99.
9. G. V. Schulz, *Z. Phys. Chem. B.*, 1935, **30**, 379.
10. P. J. Flory, *J. Am. Chem. Soc.*, 1940, **62**, 1561.
11. *US 3300458, Union Carbide Corporation Pat.*, 1967.
12. R. M. Manyik, W. E. Walker and T. P. Wilson, *J. Catal.*, 1977, **47**, 197.
13. J. R. Briggs, *J. Chem. Soc., Chem. Commun.*, 1989, **11**, 674.
14. H. Sinn, W. Kaminsky, H.-J. Vollmer and R. Woldt, *Angew. Chem. Int. Ed.*, 1980, **19**, 390.
15. *US 5856257, Phillips Petroleum Company Pat.*, 1999.
16. R. D. Köhn, M. Haufe, S. Mihan and D. Lilge, *Chem. Commun.*, 2000, 1927.
17. *US 5811618, Amoco Corporation Pat.*, 1995.
18. A. Carter, S. A. Cohen, N. A. Cooley, A. Murphy, J. Scutt and D. F. Wass, *Chem. Commun.*, 2002, 858.
19. D. S. McGuinness, P. Wasserscheid, W. Keim, C. H. Hu, U. Englert, J. T. Dixon and C. Grove, *Chem. Commun.*, 2003, 334.
20. P. J. W. Deckers, B. Hessen and J. H. Teuben, *Angew. Chem. Int. Ed.*, 2001, **40**, 2516.
21. P. J. W. Deckers, B. Hessen and J. H. Teuben, *Organometallics*, 2002, **21**, 5122.
22. *US 5451645, Phillips Petroleum Company Pat.*, 1995.
23. C. Andes, S. B. Harkins, S. Murtuza, K. Oyler and A. Sen, *J. Am. Chem. Soc.*, 2001, **123**, 7423.
24. T. Jiang, X. Liu, Y. Ning, H. Chen, M. Luo, L. Wang and Z. Huang, *Cat. Commun.*, 2007, **8**, 1145.
25. L. E. Bowen, M. F. Haddow, A. G. Orpen and D. F. Wass, *Dalton Trans.*, 2007, 1160.
26. H. Hagen, W. P. Kretschmer, F. R. van Buren, B. Hessen and D. A. van Oeffelen, *J. Mol. Catal. A: Chem.*, 2006, **248**, 237.
27. T. J. Marks and E. Y.-X. Chen, *Chem. Rev.*, 2000, **100**, 1391.
28. A. Jabri, C. Temple, P. Crewdson, S. Gambarotta, I. Korobkev and R. Duchateau, *J. Am. Chem. Soc.*, 2006, **128**, 9238.
29. K. Albahily, D. Al-Baldawi, S. Gambarotta, E. Koç and R. Duchateau, *Organometallics*, 2008, **27**, 5943.
30. A. J. Rucklidge, D. S. McGuinness, R. P. Tooze, A. M. Z. Slawin, J. D. A. Pelletier, M. J. Hanton and P. B. Webb, *Organometallics*, 2007, **26**, 2782.
31. D. H. Morgan, S. L. Schwikkard, J. T. Dixon, J. J. Nair and R. Hunter, *Adv. Synth. Catal.*, 2003, **345**, 939.
32. W. J. van Resnburg, C. Grove, J. P. Steynberg, K. B. Stark, J. J. Huyser and P. J. Steynberg, *Organometallics*, 2004, **23**, 1207.
33. D. S. McGuinness, D. B. Brown, R. P. Tooze, F. M. Hess, J. T. Dixon and A. M. Z. Slawin, *Organometallics*, 2006, **25**, 3605.
34. C. Temple, A. Jabri, P. Crewdson, S. Gambarotta, I. Korobkev and R. Duchateau, *Angew. Chem. Int. Ed.*, 2006, **118**, 7208.
35. A. Brückner, J. K. Jabor, A. E. C. McConnell and P. B. Webb, *Organometallics*, 2008, **27**, 3849.

36. T. Agapie, S. J. Schofer, J. A. Labinger and J. E. Bercaw, *J. Am. Chem. Soc.*, 2004, **126**, 1304.
37. N. Meijboom, C. J. Schaverien and A. G. Orpen, *Organometallics*, 1990, **9**, 774.
38. J. X. McDermott, J. F. White and G. M. Whitesides, *J. Am. Chem. Soc.*, 1973, **95**, 4451.
39. J. X. McDermott, J. F. White and G. M. Whitesides, *J. Am. Chem. Soc.*, 1976, **98**, 6521.
40. R. Emrich, O. Heinemann, P. W. Jolly, C. Krüger and G. P. J. Verhovnik, *Organometallics*, 1997, **16**, 1511.
41. Z. Yu and K. N. Houk, *Angew. Chem. Int. Ed.*, 2003, **42**, 808.
42. A. N. J. Blok, P. H. M. Budzelaar and A. W. Gal, *Organometallics*, 2003, **22**, 2564.
43. D. S. McGuinness, P. Wasserscheid, D. H. Morgan and J. T. Dixon, *Organometallics*, 2005, **24**, 552.
44. K. Blann, A. Bollmann, J. T. Dixon, F. M. Hess, E. Killian, H. Maumela, D. H. Morgan, A. Neveling, S. Otto and M. J. Overett, *Chem. Commun.*, 2005, 620.
45. E. Killian, K. Blann, A. Bollmann, J. T. Dixon, S. Kuhlmann, M. C. Maumela, H. Maumela, D. H. Morgan, P. Nongodlwana, M. J. Overett, M. Pretorius, K. Höfener and P. Wasserscheid, *J. Mol. Catal. A: Chem.*, 2007, **270**, 214.
46. S. Kuhlmann, K. Blann, A. Bollmann, J. T. Dixon, E. Killian, M. C. Maumela, H. Maumela, D. H. Morgan, M. Pretorius, N. Taccardi and P. Wasserscheid, *J. Catal.*, 2007, **245**, 279.
47. M. J. Overett, K. Blann, A. Bollmann, R. de Villiers, J. T. Dixon, E. Killian, M. C. Maumela, H. Maumela, D. S. McGuinness, D. H. Morgan, A. Rucklidge and A. M. Z. Slawin, *J. Mol. Catal. A: Chem.*, 2008, **283**, 114.
48. T. Jiang, S. Zhang, X. Jiang, C. Yang, B. Niu and Y. Ning, *J. Mol. Catal. A: Chem.*, 2008, **279**, 90.
49. M. J. Overett, K. Blann, A. Bollmann, J. T. Dixon, F. Hess, E. Killian, H. Maumela, D. H. Morgan, A. Neveling and S. Otto, *Chem. Commun.*, 2005, 622.
50. T. J. M. de Bruin, L. Magna, P. Raybaud and H. Toulhoat, *Organometallics*, 2003, **22**, 3404.
51. W. J. van Rensburg, C. Grove, J. P. Steynberg, K. B. Stark, J. J. Huyser and P. J. Steynberg, *Organometallics*, 2004, **23**, 1207.
52. K. Blann, A. Bollmann, H. de Bod, J. T. Dixon, E. Killian, P. Nongodlwana, M. C. Maumela, H. Maumela, A. E. C. McConnell, D. H. Morgan, M. J. Overett, M. Pretorius, S. Kuhlmann and P. J. Wasserscheid, *J. Catal.*, 2007, **249**, 244.
53. J.-A. van den Berg, P. J. Steynberg and W. J. van Rensburg, *Organometallics*, 2007, **26**, 1000.
54. S. Ittel and G. Parshall, *Homogeneous Catalysis: The Applications and Chemistry of Catalysis by Soluble Transition Metal Complexes*, Wiley, New York, 1992.
55. R. D. Köhn, D. Smith, M. F. Mahon, M. Prinz, S. Mihan and G. Kociok-Köhn, *J. Organmet. Chem.*, 2003, **683**, 200.
56. I. Krossing and I. Raabe, *Angew. Chem. Int. Ed.*, 2004, **43**, 2066.
57. R. D. Köhn, M. Haufe, G. Kociok-Köhn, S. Grimm, P. Wasserscheid and W. Keim, *Angew. Chem. Int. Ed.*, 2000, **39**, 4337.

Chapter 2

The Theory of Electron Paramagnetic Resonance and Electron Nuclear Double Resonance Spectroscopy

2.1 Fundamentals of Continuous-Wave (CW) EPR Spectroscopy

2.1.1 Introduction to EPR

Electron Paramagnetic Resonance (EPR) is a spectroscopic magnetic resonance technique used to study species containing one or more unpaired electrons. The quantum mechanical property of the electron that is utilised in EPR, its spin angular momentum, was first demonstrated by Stern and Gerlach in 1922.[1] In their experiment, they directed a beam of silver atoms through a magnetic field, which resulted in the beam being split into two. This result was incompatible with the classical view which predicted a continuous beam throughout, and led to the realisation by Goudsmit and Uhlenbeck[2] that the unpaired electron of each Ag atom must have an intrinsic property quantised into two discrete states, which become separated in energy when an external magnetic field is applied. This property became known as spin angular momentum, or simply spin, '*S*', and the two states are characterised by the spin magnetic quantum number M_S.

The first EPR experiment was carried out by Zavoisky in 1945,[3] who investigated samples of $CuCl_2.2H_2O$ using a radiation source of 133 MHz and magnetic field of 500 G. Today, EPR experiments are carried out using a wide range of frequencies and magnetic field strengths, the most common being the X-band frequency (~ 9.5 GHz, microwave region) and corresponding magnetic field strength of around 3500 Gauss (350 mT).

The continuous-wave EPR spectrum is a plot of the microwave radiation absorbed by the paramagnetic sample as a function of external magnetic field magnitude. Resonant absorption occurs when the energy difference between electron spin states induced by the magnetic field is exactly matched by the frequency of applied radiation. The electron undergoes a transition from the lower to higher energy state *via* absorption of a photon, and this net absorption across the sample results in a peak in the spectrum. In this method, radiation is continually being applied to the sample.

Although X-band is the frequency is the most commonly used, 'high-field high-frequency' spectrometers, of up to 95 GHz (W-band), are becoming more widespread. The advantages of increasing the frequency include increased resolution of $\boldsymbol{g}$ and ν_N

values, which increase linearly with field, and as a consequence may be too closely spaced to other components at lower frequencies to enable accurate analysis. Additionally, there is an increase in sensitivity at higher frequencies, due to the increased population difference in the spin levels, which could be very important in obtaining information on species with a low concentration of paramagnetic entities. However, the high cost of this equipment makes it less readily available and indeed, X-band is perfectly suitable for most EPR work.

Additionally to continuous-wave spectroscopy, the spectrum can be recorded using a different approach, namely 'pulsed EPR'. In this experiment short, intense pulses of radiation are applied to the sample, and the spectrum is then recorded in the absence of this radiation. Pulsed methods are ideal for providing information on molecular dynamics, rates of reaction and spin relaxation times. This method is covered separately in the Appendix.

2.1.2 Theoretical background

The magnitude of the spin angular momentum $\boldsymbol{S}$ is given by:

$$|\boldsymbol{S}| = \sqrt{S(S+1)}\hbar \tag{2.1}$$

Where S is the electron spin quantum number and $\hbar = h/2\pi$.

For a single electron $S = 1/2$, therefore:

$$|\boldsymbol{S}| = \sqrt{\tfrac{3}{4}}\hbar \tag{2.2}$$

According to quantum mechanics, only one component of this vector can assume a definite value. Conventionally the component along the z direction is chosen (S_z), and it can only assume the values $M_S\hbar$, where $M_S = S, S - 1, \ldots, -S$. For a single unpaired electron, $S = 1/2$, therefore M_S (the spin magnetic quantum number) = $\pm 1/2$. The absolute magnitude of these states is therefore $\pm 1/2\hbar$. These allowed orientations, or spin states, are known as the α and β states respectively. When a 'space isotropy' condition holds, i.e., there is no preferential alignment of the z direction in space, these states are energetically degenerate.

The spin angular momentum $\boldsymbol{S}$ has an associated magnetic moment μ_s which is co-linear and antiparallel to it:

$$\mu_S = -g\mu_B\boldsymbol{S} \tag{2.3}$$

where μ_B is the Bohr magneton constant, equal to 9.274 x 10^{-24} J T^{-1}. g is the spectroscopic splitting factor, known as the g factor, and for a free electron is equal to 2.0023.

In the presence of a magnetic field, an interaction occurs between this magnetic moment and the field, which causes the states to separate in energy. This is known as the Zeeman interaction. The interaction energy is given by:

$$E = -\mu_S B_0 = g\mu_B \boldsymbol{S} B_0 \tag{2.4}$$

where B_0 is the external magnetic field magnitude.

In quantum mechanics this is expressed *via* the operator leading to a simplified form of the spin Hamiltonian:

$$\hat{H} = g\mu_B \boldsymbol{S} B_0 \tag{2.5}$$

The reference frame is chosen so that the z axis coincides with the direction of B_0, so only the values of the component S_Z of the spin angular momentum vector are included. The equation becomes:

$$\hat{H} = g\mu_B M_S B_0 \tag{2.6}$$

Because the allowed values of the component M_S are only ½ or -½, the spin state energy assumes only one of two possible values:

$$E = \pm\tfrac{1}{2} g\mu_B B_0 \tag{2.7}$$

Thus the energy difference between the states is:

$$\Delta E = g\mu_B B_0 = h\nu \tag{2.8}$$

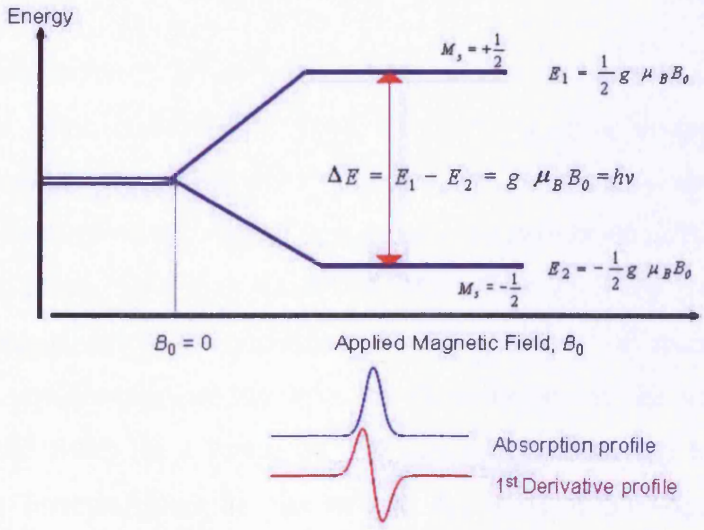

Figure 2.1. The electronic Zeeman effect.

When the photon energy of applied electromagnetic radiation matches the energy difference between the states, transitions are induced and an EPR signal is observed (see Figure 2.1). It is the oscillating magnetic field component of the microwave radiation (B_1) which interacts with the magnetic dipoles in the sample and induces a transition between the Zeeman levels. The transition involves a change in orientation of the magnetic moment. For this to occur, B_1 must be polarized perpendicularly to the static Zeeman field B_0.

In thermal equilibrium with the lattice (the chemical surroundings), the distribution of spins between the states is given by the Boltzmann law:

$$\frac{N_\alpha}{N_\beta} = \exp\frac{-g\mu_B B_0}{k_B T} \tag{2.9}$$

Where k_B is the Boltzmann constant and T is the absolute temperature. The excess of β spins over α is about 1/1000 at room temperature and with an external magnetic field strength of around 3500 G (a typical X-band spectrometer operating field). Even this small excess is enough for a net absorption signal to be observable.

The general principle of EPR spectroscopy, transitions between spin states induced by magnetic resonance conditions, is identical to that of NMR. However, the mass of the electron is approximately 2000 times smaller than that of the proton. This makes EPR a much more sensitive technique than NMR, as the magnetic moment of the electron is much larger than that of the proton, hence the energy difference between the spin states is therefore bigger. The greater resulting population difference between spin states thus results in larger net absorption values.

2.1.3 Relaxation

If electrons were continually being promoted to the spin-up (α) state then the small excess of spins in the lower level (β) would quickly disappear and no net absorption would take place. However there are two relaxation mechanisms by which the spins return to the lower level, thus maintaining the population difference.

The spin-lattice (or longitudinal) relaxation time T_1 is the time taken for the macroscopic magnetization z component of the ensemble of spins to reduce the deviation from equilibrium (arising from its perturbation *via* the application of the external magnetic field) by a factor of 1/*e*. Energy is transferred between the spin system and the surroundings (the 'lattice') in the form of phonons, i.e., quantised translational, vibrational and rotational energy. The actual interaction is between the

orbitals and the lattice, and the spin becomes involved *via* spin-orbit coupling.[4] The magnitude of T_1 depends on factors relating to the motion of the molecule, e.g. temperature and viscosity of solution.

The spin-spin (or transverse) relaxation time T_2 refers to the decay of the component of the macroscopic magnetization perpendicular to B_0. This mechanism involves energy exchange between spins within the lattice, through dipolar or exchange coupling. It is dependent on factors such as the concentration of the sample.

In some instances the relaxation times of the molecule will be too short to permit EPR detection. This can be the case for transition metal ions, due to strong spin-orbit coupling and hence strong coupling to the lattice. Short spin-lattice relaxation times also broaden the EPR linewidth, as a manifestation of the Heisenberg Uncertainty Principle, which can make interpretation of spectra more difficult. In these cases the temperature of the system can be lowered to lengthen the relaxation time sufficiently for an absorption signal to be observed and well-resolved.

Relaxation times can be most easily measured *via* pulsed EPR methods; this will be discussed in greater detail in the Appendix.

2.2 Anisotropy of the *g* tensor

The above theory is relevant for an isolated electron with no interaction with other magnetic moments, and where the only contribution to its angular momentum is from its spin. This gives rise to the isotropic g factor expected for a free electron in space (g_e = 2.0023). In most real systems however, there is an additional contribution arising from orbital angular momentum, i.e., the orbital motion of the electron around the nucleus. This gives rise to an anisotropic $\boldsymbol{g}$ tensor. Orbital angular momentum L is non-zero for orbitals with p, d or f character and has an associated magnetic moment:

$$\mu_L = \mu_B L \tag{2.10}$$

Even if the electron is in an s orbital, the spin and orbital angular momenta can interact by 'spin-orbit coupling', i.e., admixing of a small amount of orbital angular momentum from an excited state with the spin angular momentum of the ground state. This adds a perturbation to the spin Hamiltonian described earlier:

$$\hat{H} = g\mu_B B_0 \hat{S} + \mu_B B_0 L + \lambda L\hat{S} \tag{2.11}$$

where λ is the spin-orbit coupling constant, which admixes the ground state wavefunction with excited states.

This perturbation causes a small local magnetic field which adds to the external field, producing a deviation of the g factor from the free electron value $\Delta g = g - g_e$ and hence a shift in the resonance field magnitude from the free-spin value. The degree of admixing depends on which type of orbital it is arising from and the energy difference between the ground and excited states. The extent of g value shift is therefore dependent on all these factors and can be summarised thus:

$$g_{ij} = g_e\delta_{ij} + 2\lambda \sum \langle m|l_i|n\rangle\langle n|l_j|m\rangle / E_n - E_m \qquad (2.12)$$

where ij are the molecular co-ordinate axes, λ is the spin-orbit coupling constant, E_n is the energy of the SOMO, m is the filled and empty orbitals with energy E_m and l_i is the component of the orbital angular momentum operator.

Unpaired electrons associated with heavier nuclei exhibit higher orbital angular momentum and so have a larger g factor deviation than do electrons associated with light nuclei. This is common with transition-metal ions. The shift in spectral line resonance position from free-spin value therefore provides important information on the unpaired electron environment.

The spin-orbit interaction is an anisotropic one, i.e., direction-dependent. Therefore the g value also depends on the direction of the magnetic field with respect to the molecular axes. If the molecule is perfectly spherical or tumbling fast enough that asymmetries average out, an average g value (g_{iso}) is observed. However in all other cases the g value differs depending on the field direction with respect to the molecular axis directions and hence is no longer a scalar quantity.

Any anisotropic system has three mutually perpendicular directions, known as the principal axes, and the values of the properties of the system measured along these axes are called the principal values. The whole system can be defined using these parameters. The Zeeman interaction is now expressed *via* a 3 x 3 matrix called the $\boldsymbol{g}$ matrix (with principal values of g_1, g_2 and g_3), and the resonant field value is dependent on the field orientation relative to the $\boldsymbol{g}$ matrix axes. This orientation of the field vector with respect to g is displayed in Scheme 2.1:

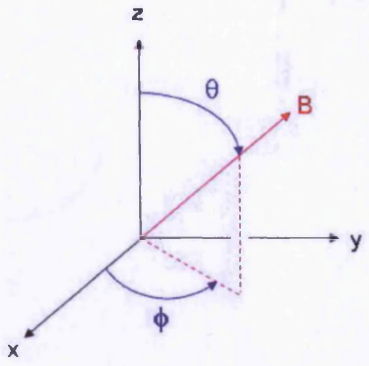

Scheme 2.1: Orientation of the magnetic field vector (B) with respect to the ***g*** matrix principal axis system.

where θ refers to the angle between B_0 and the g_z axis, and ϕ to the angle between the g_x axis and the projection of B_0 in the xy plane.

The expected g value for a system characterised by principal values of the ***g*** tensor g_1, g_2 and g_3 and with an orientation (θ,ϕ) with respect to the field is:[5]

$$g(\theta,\phi) = \sqrt{\sin^2\theta\cdot\cos^2\phi\cdot g_1^2 + \sin^2\theta\cdot\sin^2\phi\cdot g_2^2 + \cos^2\theta\cdot g_3^2} \qquad (2.13)$$

There are three symmetries of EPR spectral profiles most commonly encountered, and these are detailed below.

2.2.1 Isotropic systems

Isotropic spectra are most frequently observed when studying liquid solutions, where the rate of molecular tumbling is fast enough to average to zero any anisotropic contributions. However they can more rarely be observed in the solid state / frozen solution, arising from systems exhibiting pure cubic symmetry, for example O_h or T_d. Due to the spatial equivalence of the molecular axes, the g factor is independent of molecular orientation with respect to the field and so a single absorption is observed in the spectrum (Figure 2.2).

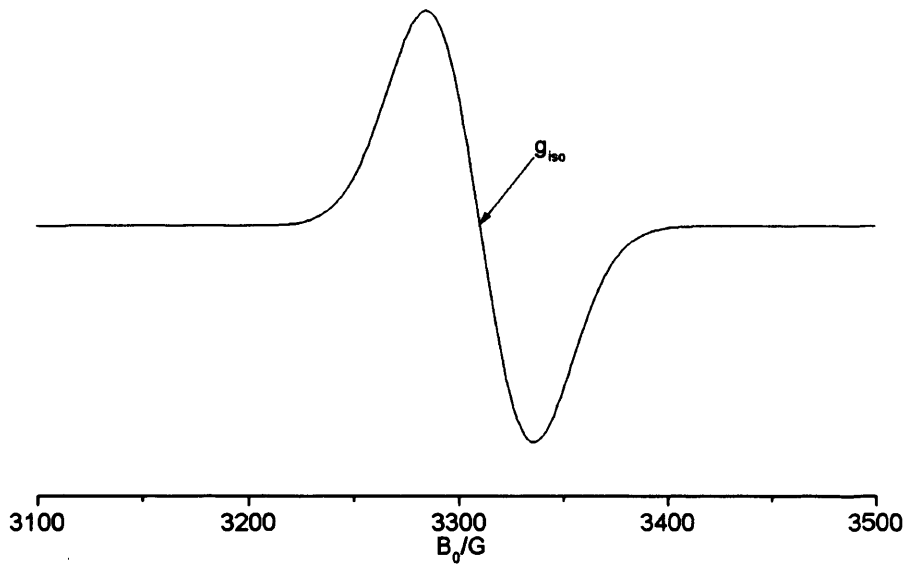

Figure 2.2.Simulated isotropic EPR spectrum (g = 2.05, ν = 9.5 GHz) for the case where I = 0.

2.2.2 Axial systems

These consist of one unique (z) axis and two equivalent x and y axes. The system will have a different g factor (and accordingly different resonance energy) depending on the orientation of these axes with respect to the external field. The unique g value is designated $g_{\|}$, and is observed when the z axis of the ***g*** tensor is parallel to the field vector. $g_{\perp}$ is observed when the z axis is perpendicular to the field. The resonant field magnitude can be calculated for any angle θ between the z axis and the field vector:

$$B_{res} = \frac{h\nu}{\mu_B (g_{\perp}^{\,2} \sin^2\theta + g_{\|}^{\,2} \cos^2\theta)^{\frac{1}{2}}} \qquad (2.14)$$

In an axial system the x and y directions are equivalent and so ϕ (the angle between the x axis and the projection of the field vector in the xy plane) becomes meaningless. The powder spectrum is the superimposition of individual resonances from randomly orientated molecules, which adopt all possible orientations with respect to the field. The distribution of orientations follows a statistical pattern where the absorption intensity (proportional to the number of molecules at that orientation) has a maximum when θ = π/2 (i.e., at $g_{\perp}$) and a minimum at θ = 0 ($g_{\|}$). The absorption EPR spectrum for an axial system therefore shows a complete band of absorption with $g_{\|}$ and $g_{\perp}$ marking the extremes of this absorption range. However in the first derivative mode which most spectra are recorded in, only these extremes are observable as peaks due to the fact these are 'turning-points' in the angular variation of the resonant field.

The easiest way to visualise this is *via* an angular dependency plot. The orientation selection of the ***g*** tensor was calculated for an axial system and shown in Figure 2.3:

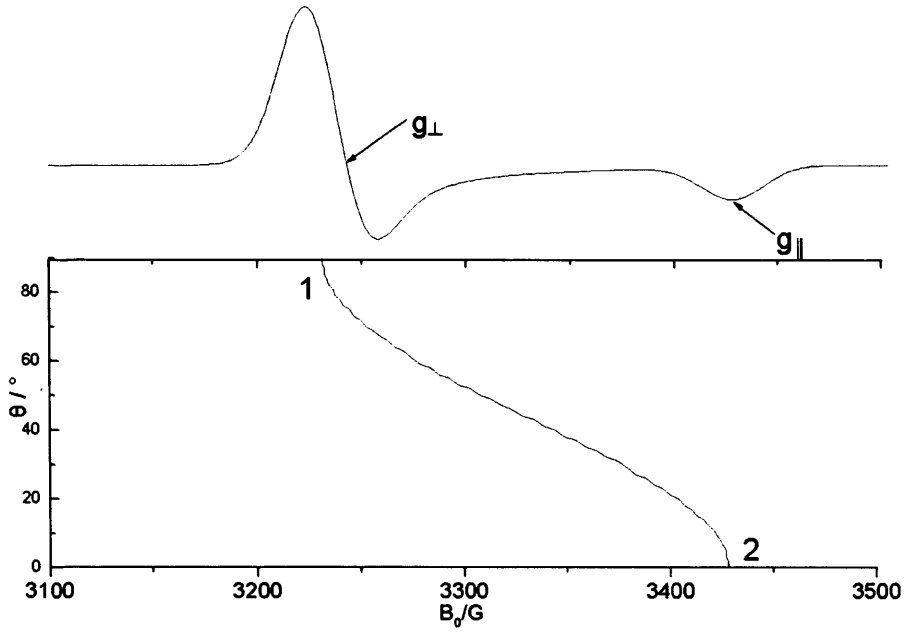

Figure 2.3.Simulated axial EPR spectrum ($g_\perp = 2.1$, $g_\parallel = 1.98$, $\nu = 9.5$ GHz) for the case where $I = 0$ and angular dependence of the EPR transition as a function of the angle between the unique axis and the field.

The graph shows this variation in resonance field position as a function of the angle θ between B_0 and the unique axis of the ***g*** tensor. At position 1 the magnetic field magnitude corresponds to resonance for molecules whose g_z axis is aligned perpendicular to the field vector. The g value at this field position is known as $g_\perp$. At position 2, the magnetic field magnitude corresponds to resonance for molecules whose g_z axis is aligned parallel to the field vector. The g value for the system at this field position is known as $g_\parallel$. Knowledge of the turning points in the powder EPR pattern becomes extremely important in orientation selective ENDOR measurements.

.

2.2.3 Orthorhombic systems

Systems where each principal axis is unique (i.e., $x \neq y \neq z$) display orthorhombic symmetry, and hence 3 distinct g values (denoted g_1, g_2 and g_3) are observed as peaks in the derivative spectrum (Figure 2.4). (The notation of g_x etc. may only be used when the absolute orientation of the ***g*** tensor with respect to the field has been established *via* single-crystal measurements). The variation in the g value now depends on both θ and the angle ϕ (the angle between g_x and the projection of the magnetic field vector in the xy plane).

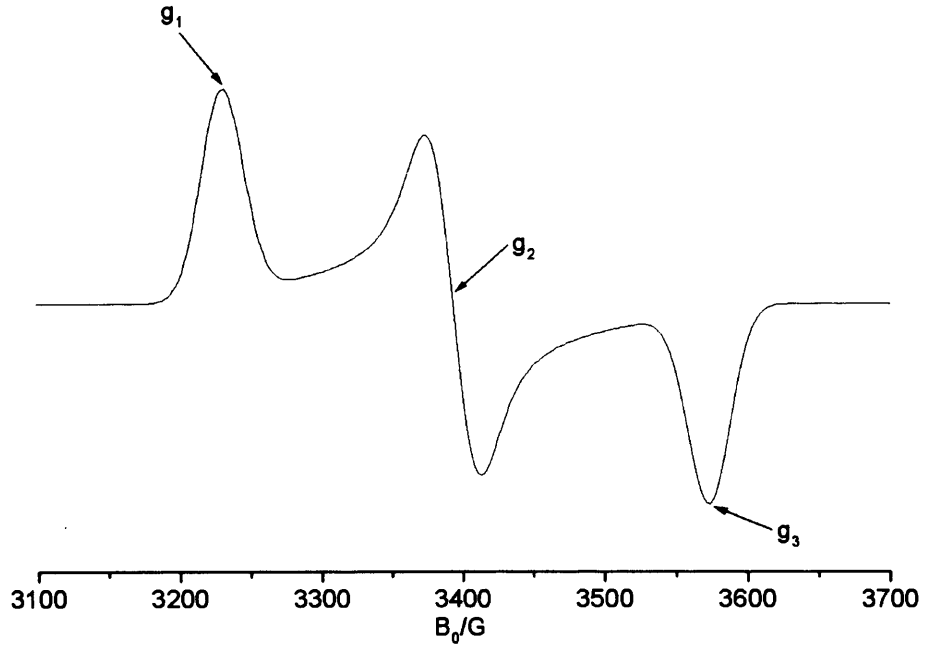

Figure 2.4.Simulated orthorhombic EPR spectrum ($g_1 = 2.1$, $g_2 = 2.0$, $g_3 = 1.9$, $\nu = 9.5$ GHz) for the case where $I = 0$.

2.3 Nuclear Hyperfine Interaction

In addition to the interaction described previously, of the electron magnetic moment interacting with the external magnetic field, interactions also occur between any spin-active nuclei present in the sample and their associated magnetic moments, both with the field and the electron itself. These Nuclear Zeeman and hyperfine interactions split and modify the electron Zeeman levels respectively. The origin and consequence of these interactions will be discussed in this section.

The magnetic moment of the nucleus is related to its spin angular momentum, analogously to that of the electron:

$$\mu_I = -g_N \mu_N I \tag{2.15}$$

where μ_N is a constant (the nuclear magneton), g_N the nuclear g factor (which depends on the nucleus under consideration) and I is the nuclear spin angular momentum.

As with electrons, the magnitude of the angular momentum and its component along the conventionally chosen direction z ($M_I\hbar$) are quantised. Unlike a single electron however, the nuclear spin angular momentum may take a value other than ½. The allowed values of M_I are $-I, -I+1, \ldots, I$.

The energy of spin angular momentum component along z is proportional to the magnetic field strength and is known as the nuclear Zeeman interaction:

$$E = g_N \mu_N B_0 M_I \tag{2.16}$$

There also exists an interaction between the magnetic dipoles of the electron and the nucleus, known as the 'hyperfine interaction'. The spin Hamiltonian consisting of all three contributions to the energy is:

$$\hat{H} = g\mu_B B_0 \hat{S} - g_N \mu_N B_0 \hat{I} + \hat{I} A_0 \hat{S} \tag{2.17}$$

where A_0 is the hyperfine term.

The total energy of the electron spin levels in frequency units is thus given by:

$$E(M_S, M_I) = g\mu_B B_0 M_S - g_N \mu_N B_0 M_I + hA_0 M_S M_I \tag{2.18}$$

For a simple case of an S = ½, I = ½ spin system, there are therefore four possible values of the total spin energy, depending on which electron and nuclear spin components are under consideration. These are displayed in Figure 2.5:

$$E_1 = \tfrac{1}{2} g\mu_B B_0 M_S - \tfrac{1}{2} g_N \mu_N B_0 M_I + \tfrac{1}{4} hA_0 \tag{2.19}$$

$$E_2 = \tfrac{1}{2} g\mu_B B_0 M_S + \tfrac{1}{2} g_N \mu_N B_0 M_I - \tfrac{1}{4} hA_0 \tag{2.20}$$

$$E_3 = -\tfrac{1}{2} g\mu_B B_0 M_S + \tfrac{1}{2} g_N \mu_N B_0 M_I + \tfrac{1}{4} hA_0 \tag{2.21}$$

$$E_4 = -\tfrac{1}{2} g\mu_B B_0 M_S - \tfrac{1}{2} g_N \mu_N B_0 M_I - \tfrac{1}{4} hA_0 \tag{2.22}$$

EPR transitions are only allowed however if the change in electron spin magnetic quantum number is ±1 and that of the nuclear spin magnetic quantum number is 0. In other words, the following selection rules apply: $\Delta M_S = \pm 1$, $\Delta M_I = 0$.

Hence for an $S = ½$, $I = ½$ spin system, there are two allowed transitions:

$$\Delta E_A = E_1 - E_4 = g\mu_B B_0 + \tfrac{1}{2} hA_0 \tag{2.23}$$

$$\Delta E_B = E_2 - E_3 = g\mu_B B_0 - \tfrac{1}{2} hA_0 \tag{2.24}$$

These give rise to two absorption peaks in the spectrum, which at constant applied microwave frequency, occur at magnetic fields of values:

$$B_1 = \frac{h\nu}{g\mu_B} + \frac{hA_0}{2g\mu_B} = \frac{h\nu}{g\mu_B} + \frac{a}{2} \tag{2.25}$$

$$B_2 = \frac{h\nu}{g\mu_B} - \frac{hA_0}{2g\mu_B} = \frac{h\nu}{g\mu_B} - \frac{a}{2} \tag{2.26}$$

i.e., separated by $(hA_0 / g_e\mu_B) = a$, the hyperfine coupling constant.

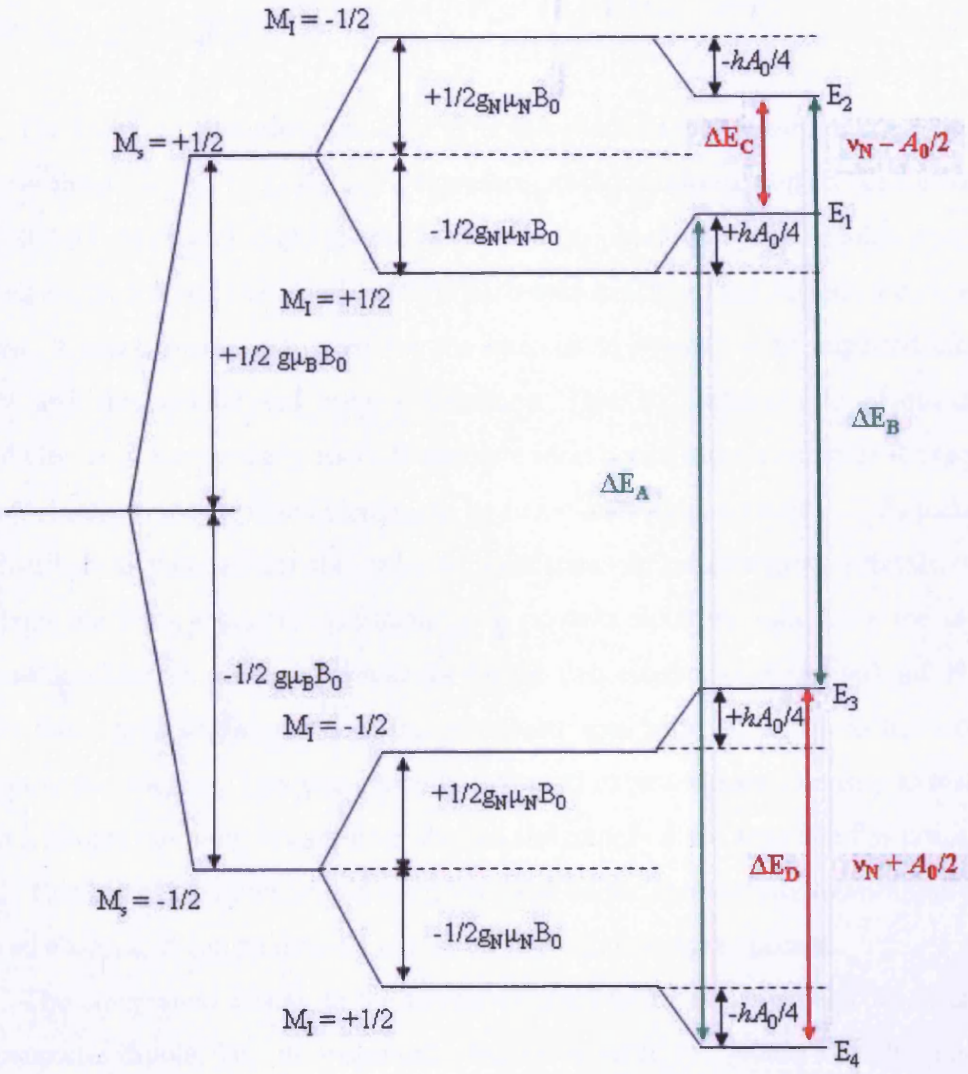

Figure 2.5. Energy level diagram for the interaction of a proton (I =1/2) with an electron (S = ½) in an applied magnetic field. The allowed EPR transitions ($\Delta M_S = \pm 1$, $\Delta M_I = 0$) are shown in green.

2.3.1 Origin of the Hyperfine Interaction

There are two components to the hyperfine interaction; one arising from the interaction of the electron magnetic moment with the hyperfine field external to the nucleus, and one interaction inside the nucleus itself. This finite interaction inside the nucleus is independent of direction and is called the contact or Fermi interaction. The energy of this interaction is given by:

$$E_{hf} = aS.I \tag{2.27}$$

a is known as the isotropic hyperfine coupling constant, which depends on the square of the wavefunction at the nucleus:

$$a = (8\pi/3)g\mu_B g_N \mu_N |\Psi(0)|^2 \quad (2.28)$$

The contact interaction can only exist in orbitals which have non-zero electron density at the nucleus, i.e., *s* orbitals. *a* therefore provides information on the *s*-character of the SOMO. Isotropic couplings are however also observed for molecules where the unpaired electron resides in an orbital with zero spin density at the nucleus, i.e., a *p*, *d* or *f* orbital. A mechanism must exist for the nucleus to interact with unpaired electron density and this occurs *via* spin polarization. Due to Hund's rule of maximum multiplicity, it is energetically more favourable (and hence more probable) for the next electron closest to the unpaired electron to be in the same spin state as it. This particular spin distribution then affects the order of spin states in neighbouring orbitals, which obey both the Pauli exclusion principle (i.e., no two electrons may have the same 4 quantum numbers, so different spin states for the two electrons per orbital) and Hund's rule. In this way a slight excess of one particular spin state builds up in the *s* orbital adjacent to the nucleus. This energetically favoured excess electron density is isotropic and so isotropic coupling occurs even though the unpaired electron itself is not in an *s* orbital. This interaction thus provides information on the spin density distribution of the unpaired electron. It can be directly extracted from liquid-phase spectra.

The component arising in the region external to the nucleus behaves classically as a magnetic dipole, i.e., its magnitude decreases with $1/r^3$ where r is the electron-nucleus distance, and is dependent on the orientation of the vector connecting the electron and nucleus with respect to the directions of the dipoles. This dipolar interaction is important in single crystals and powders, i.e., any case where it is not time-averaged to zero by tumbling. This interaction enables the distance and mutual orientation between interacting spins to be calculated. The interaction energy is given by:

$$E_{dip} = (\mu_0/4\pi)g\mu_B g\mu_N [S.I/r^3 - 3(S.r)(I.r)/r^5] \quad (2.29)$$

μ_0 is the magnetic permeability of the vacuum and is equal to $4\pi \times 10^{-7}$ J C^{-2} s^2 m^{-1}.

Both the isotropic (a_{iso}) and anisotropic (A_{dip}) interactions contribute to the overall electron-nuclear hyperfine interaction, and can be calculated from the principal values extracted from the spectra:

$$a_{iso} = \frac{A_\perp + A_\perp + A_\parallel}{3} \quad (2.30)$$

$$A_{dip} = A_\parallel - a_{iso} \quad (2.31)$$

The hyperfine term adds to the Zeeman terms to give the total energy of the electron-nuclear spin system in the magnetic field.

Similarly to the ***g*** tensor, the hyperfine interaction tensor is composed of three principal axes A_x, A_y and A_z. Whether the ***g*** and ***A*** tensor principal axes are required to be coincident is dependent on the point symmetry of the molecule.[6] The particular geometry of the EPR spectrum observed is only associated with a certain class of point symmetries. For the geometries described above (isotropic, axial and orthorhombic) the principal axes are coincident; however this is not the case for lower classes of symmetry. The relationships between the types of EPR spectrum, coincidence of tensor axes and point symmetries are listed in the table below.

Table 2.1. Relationship between ***g*** and ***A*** tensors, EPR symmetry and point symmetry of the paramagnetic complex.

EPR geometry	***g* and *A* tensor**	**Coincidence of principal axes**	**Point symmetry**
Isotropic	$g_{xx} = g_{yy} = g_{zz}$ $A_{xx} = A_{yy} = A_{zz}$	All coincident	O_h, T_d, O, T_h, T
Axial	$g_{xx} = g_{yy} \neq g_{zz}$ $A_{xx} = A_{yy} \neq A_{zz}$	All coincident	D_{4h}, C_{4v}, D_4, D_{2d}, D_{6h}, C_{6v}, D_6, D_{3h}, D_{3d}, C_{3v}, D_3
Orthorhombic	$g_{xx} \neq g_{yy} \neq g_{zz}$ $A_{xx} \neq A_{yy} \neq A_{zz}$	All coincident	D_{2h}, C_{2v}, D_2
Monoclinic	$g_{xx} \neq g_{yy} \neq g_{zz}$ $A_{xx} \neq A_{yy} \neq A_{zz}$	One axis of g and A coincident	C_{2h}, C_S, C_2
Triclinic	$g_{xx} \neq g_{yy} \neq g_{zz}$ $A_{xx} \neq A_{yy} \neq A_{zz}$	Complete non-coincidence	C_1
Axial non-colinear	$g_{xx} = g_{yy} \neq g_{zz}$ $A_{xx} = A_{yy} \neq A_{zz}$	Only g_{zz} and A_{zz} coincident	C_3, S_6, C_4, S_4, C_{4h}, C_6, C_{3h}, C_{6h}

2.4 Fundamentals of Continuous-Wave ENDOR Spectroscopy

2.4.1 Introduction to ENDOR

Electron Nuclear DOuble Resonance spectroscopy was first introduced by Feher[8] in 1956 for solids and later by Hyde and Maki[9] for liquids. In ENDOR, both electron and nuclear spin transitions are excited simultaneously, *via* application of microwave and radiofrequency irradiating fields.

ENDOR is particularly useful for obtaining information on spin-active nuclei present in the sample. Because of the EPR selection rule $\Delta M_I = 0$, information about μ_N cannot be obtained directly from the EPR spectrum. This can make it difficult to determine which couplings are due to which nuclei if different nuclei happen to have the same nuclear spin quantum number; for example, ^1H and ^{31}P both have $I = ½$. However in ENDOR the nuclear Larmor frequency can be directly extracted from the spectrum and as this is particular to each nucleus, identification of spin-active nuclei present and their associated couplings can be easily obtained.

The second advantage concerns the enhancement in resolution of hyperfine couplings. Each set of equivalent nuclei contributes only 2 lines to the (isotropic) ENDOR spectrum, as each transition within the same M_I manifold is degenerate. Under EPR conditions however, each set of nuclei have a multiplicative rather than additive effect on the spectrum. Additionally, hyperfine couplings can be measured with greater precision due to the much smaller line widths in ENDOR compared to EPR. Thirdly, ENDOR enables structural information on the system to be obtained *via* the electron nuclear hyperfine parameter matrix. In the 'orientation selective' ENDOR experiment (see later), each measurement is made at a selected field position which contains only a subset of molecules contributing to the EPR transition. If a 'turning point' is selected, a single-crystal like ENDOR spectrum is obtained, i.e., one corresponding to only a single molecular orientation. Simulation of the data enables the principal components of the nuclear magnetic tensors to be extracted, and from these both the distance and mutual orientation of nucleus and electron with respect to the field to be calculated.

There are two main reasons for performing an ENDOR experiment to look at nuclei present rather than an NMR experiment. The first is the difficulty in extracting meaningful data from NMR spectra of paramagnetic species, as the lines are broadened due to relatively fast electron spin-lattice relaxation times compared to nuclear ones. Another advantage is the increase in sensitivity of ENDOR versus NMR. Information is gained about nuclear energy levels indirectly *via* their influence on the EPR transition, which is inherently more sensitive due to the larger spin-state population difference.

This is known as a 'quantum transformation'[10] and the intensity enhancement is of the order of 10^3.

2.4.2 Theoretical background

The more complete spin Hamiltonian for an $S = ½$ system interacting with an external applied field B and one or more nuclei i of spin I is:

$$\hat{H} = \mu_B B^T.g.S/h + \sum(S^T.A_i.I_i - g^i{}_N \mu^i{}_N B^T.I/h + I^T{}_i.Q.I_i) \quad (2.32)$$

The first term describes the electron Zeeman interaction, whereby information on the electronic nature of the system is obtained *via* the $\boldsymbol{g}$ tensor. The remaining terms are a summation of contributing nuclear spin interactions, i.e., the hyperfine tensor $\boldsymbol{A}$, the nuclear Zeeman term and the quadrupole term Q. It is these interactions which are probed in the ENDOR experiment.

A simplified form of the spin Hamiltonian equation for an $S = ½$, $I = ½$ spin system was given earlier (Equation 2.17). In that equation, g and A were treated as isotropic scalar quantities.

If we consider again the 4 possible energy levels for this two-spin system (Equations 2.19 – 2.22), two allowed transitions are possible according to the NMR selection rules $\Delta M_I = \pm 1$, $\Delta M_S = 0$:

$$\Delta E_C = E_2 - E_1 = g_N \mu_N B_0 - \tfrac{1}{2} h A_0 \quad (2.33)$$

$$\Delta E_D = E_3 - E_4 = g_N \mu_N B_0 + \tfrac{1}{2} h A_0 \quad (2.34)$$

The energies expressed in terms of $E_{MS,MI}$ are:

$$E_{MS,MI} = \nu_e M_S - \nu_N M_I + A_0 M_S M_I \quad (2.35)$$

where $\nu_e = g\mu_B B_0 / h$ and $\nu_N = g_N \mu_N B_0 / h$

Hence these allowed transitions are separated by A_0, the isotropic hyperfine coupling constant and centred on ν_N, the nuclear Larmor frequency (see Figure 2.5).

The above equation (2.35) is valid for any system where $\nu_N > |A_0|/2$, typical for protons. In some cases $\nu_N < |A_0|/2$, which occurs for ^2H, ^{13}C and ^{14}N. Here two ENDOR lines are again observed, but separated by $2\nu_N$ and centred upon $|A_0|/2$. However, both A_0 and ν_N can still be directly determined. The ENDOR experiment is therefore invaluable in the study of nuclear interactions in paramagnetic species, as both the hyperfine coupling constant and the nuclear Larmor frequency are directly determined.

The ENDOR spectrum itself is a plot of the change in the EPR absorption intensity as a function of radiofrequency. The EPR transition is firstly saturated by applying a high-power microwave field. As there is now no net absorption, the EPR signal disappears. An RF field is then applied and swept until at two certain frequencies (which correspond to each NMR resonance) the EPR signal is desaturated by inducing an NMR transition. There is now net absorption of microwave radiation and a peak appears in the spectrum at each of these frequencies.

2.5 The Steady-State ENDOR Effect

The population difference between the electronic spin levels is described by the Boltzmann distribution (Equation 2.9). Because the energy difference between the nuclear spin levels is approximately 10^{-3} of that of the electronic levels, it can be ignored. A vital part of the ENDOR experiment is the saturation of the electronic spin levels. This is achieved by relatively high-power microwaves and low temperatures ($\leq$ 10K) so that the electron spin-lattice relaxation rate cannot compete with the absorption and the populations of $M_S = +½$ and $M_S = -½$ equalise. When a nuclear radiofrequency is applied corresponding to the energy difference between two of the nuclear spin levels within the same M_S manifold (e.g., E_1 and E_2 in Figure 2.5), the population difference between the electron levels is restored and the EPR line becomes desaturated *via* induced absorption. The increase in intensity of the EPR transition constitutes an ENDOR peak in the spectrum at the frequency corresponding to $E_2 - E_1$. A second peak appears at the frequency $E_3 - E_4$ when the corresponding radiofrequency is applied, by desaturation of the EPR transition *via* induced emission.

After a short while however the NMR transitions will also become saturated and the induced EPR signal will disappear, i.e., a transient ENDOR response. A mechanism is needed to preserve the population difference in the nuclear spin levels. The primary way the spins relax to the lower level is *via* the electron spin-lattice relaxation route. A different pathway to parallel this is needed due to the saturating microwave field, and this is known as the 'bypass' route. This route is usually inefficient in the EPR experiment, as the nuclear relaxation rate is much less than the electronic rate. However, since a saturating RF field is being applied to the nuclear spin levels, the 'bottleneck' is overcome and the transition becomes feasible. The electrons relax back to the electron spin ground state *via* this route and the ENDOR response persists.

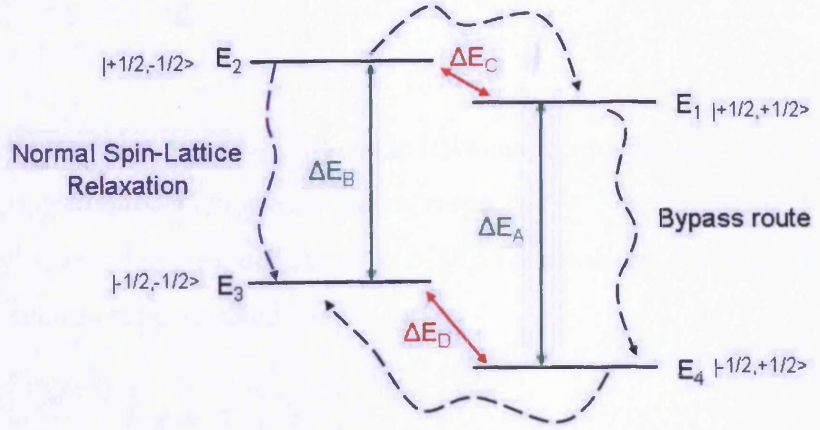

Figure 2.7: Energy level diagram for the interaction of a proton ($I = ½$) with an electron ($S = ½$) in an applied magnetic field. E_1, E_2, E_3 and E_4 correspond to the same energy levels as shown in Figure 2.5. Solid lines correspond to induced transitions; dashed lines to radiationless relaxations.

However these rates depend on the rotational correlation for Brownian diffusion (τ_R); $W_e \alpha 1/\tau_R$ and $W_N \alpha \tau_R$. τ_R is related to the molar volume (V_{eff}), the viscosity of the solvent (η) and the temperature:

$$\tau_R = V_{eff}(\eta / k_B T) \tag{2.36}$$

Hence by fine-tuning the temperature and viscosity of the solvent, the optimum ratio of $W_N/W_e \approx 1$ can be obtained, leading to the most effective CW-ENDOR response.

2.6 Orientation-Selective ENDOR

The above theory is relevant for isotropic systems or spectra recorded in liquid solution. As mentioned earlier however, valuable structural information on anisotropic systems can be obtained by performing the orientation-selective experiment. It is the anisotropy in the EPR spectrum itself that is utilised in orientation-selective ENDOR. The powder/ frozen solution EPR spectrum is composed of a superimposition of resonances from randomly oriented molecules, which adopt a statistical distribution of all possible orientations with respect to the field. By recording the ENDOR measurement at selected field positions, unique resonance transitions, i.e., single molecular orientations, can be observed, and the principal components of the magnetic tensors for each nucleus can be obtained *via* simulation. The first step therefore in performing an orientation-selective ENDOR experiment is determination of the ***g*** tensor contribution to the EPR spectrum as a function of magnetic field magnitude. The EPR resonance positions B_0 for given (θ,ϕ) orientations are, to first order:

$$B_0 = \left[\frac{h\nu - M_I A_0(\theta,\phi)}{\mu_B g(\theta,\phi)} \right] \tag{2.37}$$

The angles θ and ϕ are the angle between g_z and B_0, and the angle between g_x and the projection of B_0 in the x-y plane, respectively. The resonance field for each M_I state may be calculated for different sets of (θ,ϕ) orientations. The transition frequencies for each nucleus are calculated thus:

$$\nu_{\pm} = \left[\sum_{i=1}^{3} \left[\frac{M_S}{g(_{\theta,\phi})} \left(\sum_{j=1}^{3} g_j h_j A_{ji} \right) - h_i \nu_N \right]^2 \right]^{1/2} \tag{2.38}$$

Where h_i are the direction cosines of B_0, A_{ji} is the orientation-dependent value of the hyperfine coupling, M_S is the electron spin quantum number and ν_N the nuclear Larmor frequency. The hyperfine tensor is analysed *via* simulation at different field positions to extract the a_{iso} and A_{dip} contributions, the latter of which enables calculation of both the distance and mutual orientation between interacting spins, *via* a point dipole calculation:

$$A_{dip} = \left(\frac{\mu_0}{4\pi h} \right) \frac{g\mu_B g_N \mu_N}{R^3} \left(3\cos^2 \xi - 1 \right) \tag{2.39}$$

$$R = \sqrt[3]{\left(\frac{\mu_0}{4\pi h} \right) \frac{g\mu_B g_N \mu_N}{A_{dip}} \left(3\cos^2 \xi - 1 \right)} \tag{2.40}$$

R is the distance between the particles and ξ the angle between the magnetic field vector and the line joining the two spins. (μ_0 is the vacuum permittivity and the rest of the symbols have their usual meaning). Generally the parallel dipolar component (A_{dip}) is used for convenience; that at the perpendicular field position is – ½ times that at θ = 0°. The point dipole approximation is extremely good for distances of around ≥ 2.5 Å.

To illustrate the orientational selectivity of the technique, we will consider some model spectra for an axially symmetric two-spin (S = ½, I = ½) system. Firstly the variation in resonance field position as a function of the angle θ between B and the unique axis of the $\boldsymbol{g}$ tensor is determined as described previously.

The first case involves a hypothetical coupling of $A_1 = A_2 = A\perp$ = 5 MHz and $A_3 = A_\parallel$ = 10 MHz. The position of the external magnetic field is altered (θ_B) which is

equivalent to sweeping the field. The position of the proton is constant ($\theta_H = 0°$, i.e. A_3 aligned along the z axis of the ***g*** tensor and the field vector; see Figure 2.8).

When $\theta_B = 0°$, only the largest ($A_3 = A_\parallel$) coupling is observed. At $\theta_B = 90°$, all orientations perpendicular to the z axis are selected, and as $A_1 = A_2 = A\perp = 5$ MHz, two peaks separated by 5 MHz are observed. At all other field positions, statistical contributions from all principal axes of the nuclear tensor are observed; note though that only one resonance is observed at all field positions in this example.

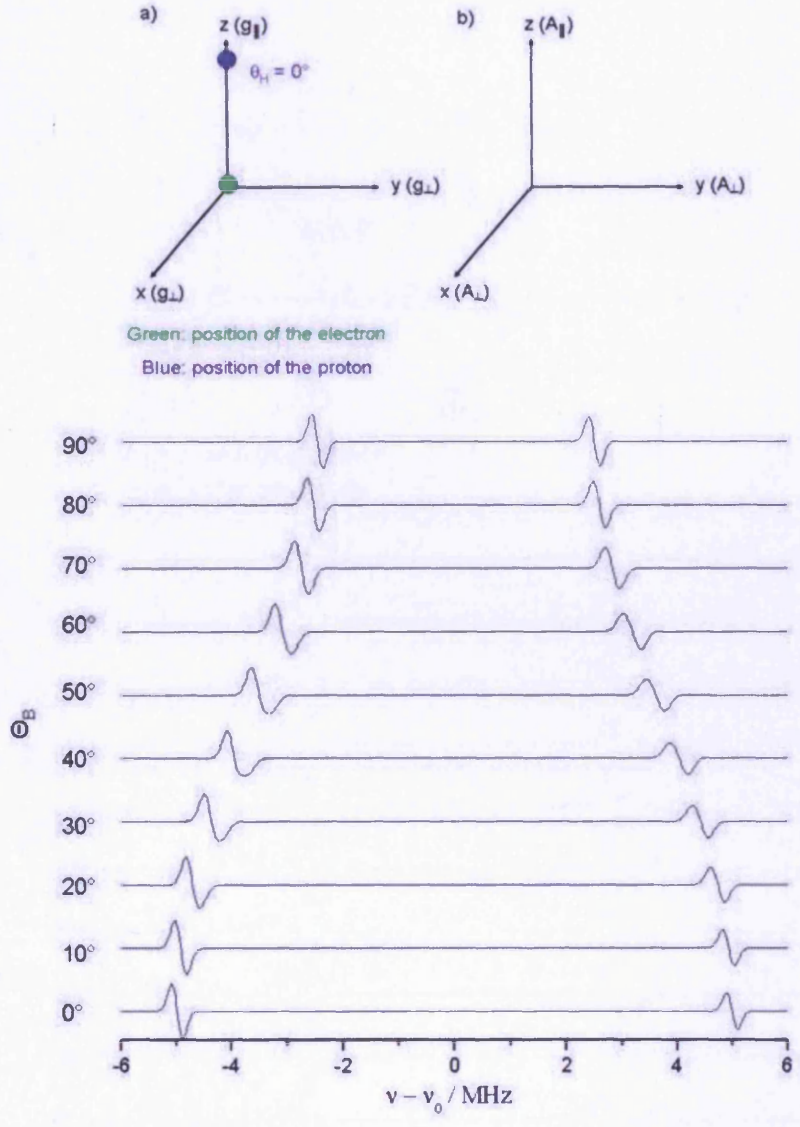

Figure 2.8: Magnetic field orientation (θ_B) dependence of the ENDOR spectrum, simulated for an axially symmetric $S = ½$, $I = ½$ system; a) co-ordinate system of the ***g*** tensor, showing the relative proton position ($\theta_H = 0°$); b) co-ordinate system of the hyperfine tensor; $A_1 = A_2 = A\perp = 5$ MHz, $A_3 = A_\parallel = 10$ MHz.

In an alternative geometrical arrangement, the position of the proton tensor is perpendicular to that of the ***g*** tensor, i.e. $\theta_H = 90°$ (Figure 2.0). In this example, when $\theta_B = 0°$, only the smallest coupling A_2 ($A\perp$) is observed, as this is now aligned along z (in the *g* frame). At angles between 0 and 90°, a linear combination of $A_{\|}$ and $A_\perp$ leads to resonances of intermediate coupling values. At all field positions a coupling of 5 MHz is observed, due to the occurrence of the $A_\perp$ component in both the z direction and the x-y plane of the *g* frame. The maximum coupling $A_{\|}$ is now observed at a field position corresponding to $\theta_B = 90°$.

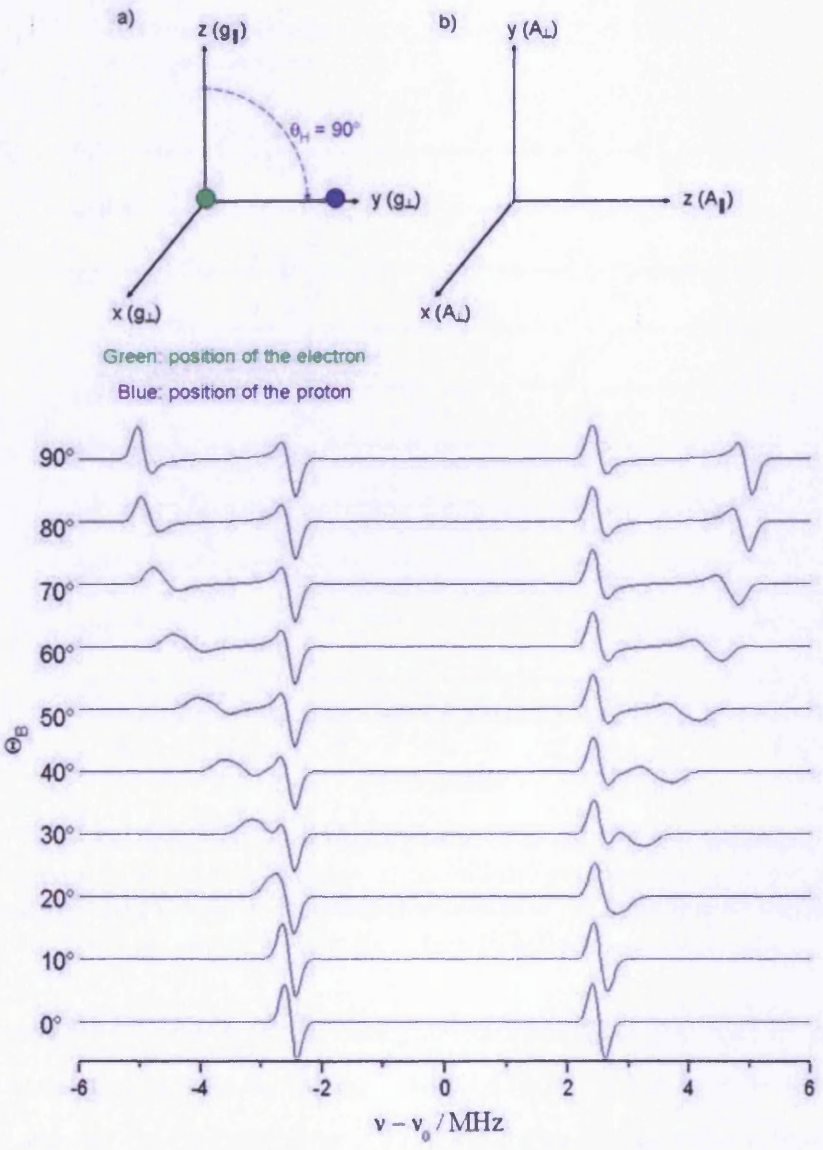

Figure 2.9: Magnetic field orientation (θ_B) dependence of the ENDOR spectrum, simulated for an axially symmetric $S = ½$, $I = ½$ system; a) co-ordinate system of the ***g*** tensor, showing the relative proton position ($\theta_H = 90°$); b) co-ordinate system of the hyperfine tensor; $A_1 = A_2 = A\perp = 5$ MHz, $A_3 = A_{\|} = 10$ MHz.

If an arbitrary angle for the position of the proton is chosen, for example Θ_H = 50° (Figure 2.10), more complicated spectra arise. However it is still fairly straightforward to analyse them.

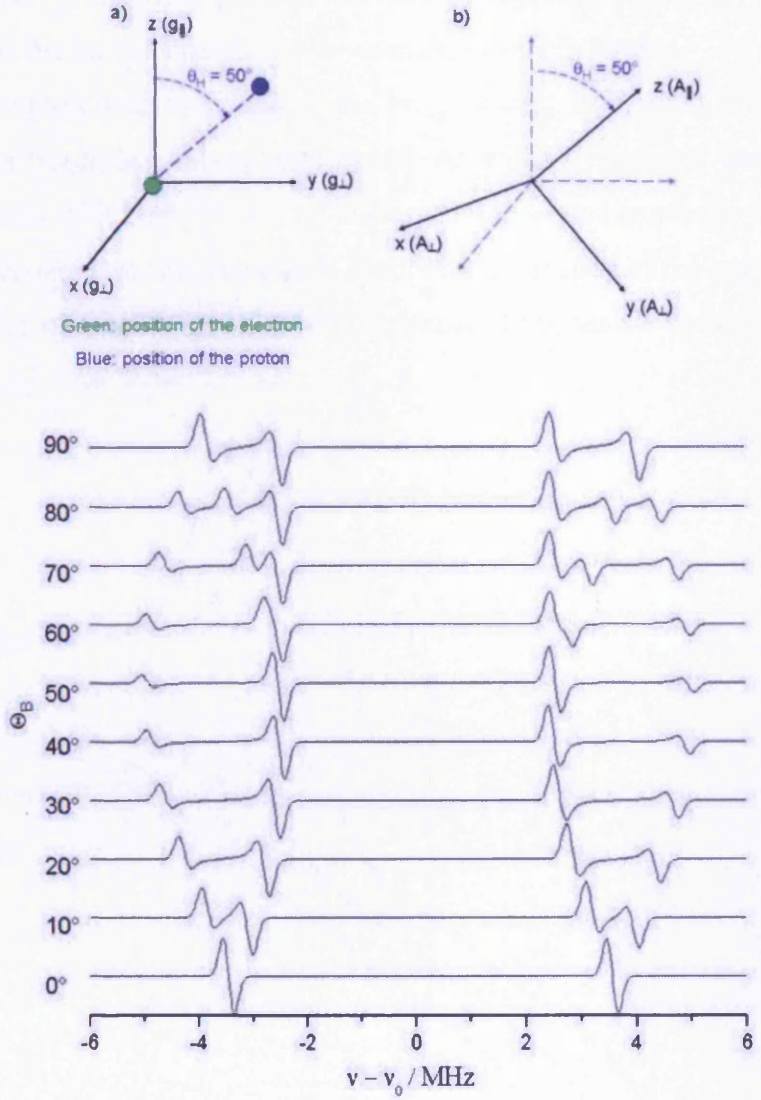

Figure 2.10: Magnetic field orientation (θ_B) dependence of the ENDOR spectrum, simulated for an axially symmetric $S = ½$, $I = ½$ system; a) co-ordinate system of the ***g*** tensor, showing the relative proton position ($\theta_H = 50°$); b) co-ordinate system of the hyperfine tensor; $A_1 = A_2 = A\perp$ = 5 MHz, $A_3 = A_\parallel$ = 10 MHz.

When $\theta_B = 0°$, only a partial contribution from A_3 is observed in the spectrum, the size of which depends on θ_H. At $\theta_B = 40°$ (i.e. 90° - θ_H) $A_1 = A_2 = 5$ MHz is seen, and is then present in the spectra at all remaining angles as the xy plane is always contributing. Only at $\theta_B = 50°$ is $A_3 = 10$ MHz seen, as this is the only angle at which the z axis of the hyperfine tensor is aligned with that of the field vector.

The important point to note is that the largest coupling for an axial hyperfine tensor is only observed at the field position corresponding to the angle at which that tensor is in relation to the ***g*** tensor (assuming g_z is aligned with the z axis of the field vector). Hence for a real axial system, performing the orientation-selection experiment to determine at which field position the largest coupling occurs provides valuable information on the mutual orientation between the interacting spins.

The systems studied in this thesis are primarily axial $[Cr(CO)_4PP]^+$ systems, where PP is a bis(diphenylphosphine) ligand. As will be discussed in Chapter 4, the electron interacts with both ^{31}P (I = ½) nuclei, adding some complexity to the ENDOR spectra. The variation in resonance field position as a function of the angle θ between B and the unique axis of the ***g*** tensor was determined for such a system and shown in Figure 2.11.

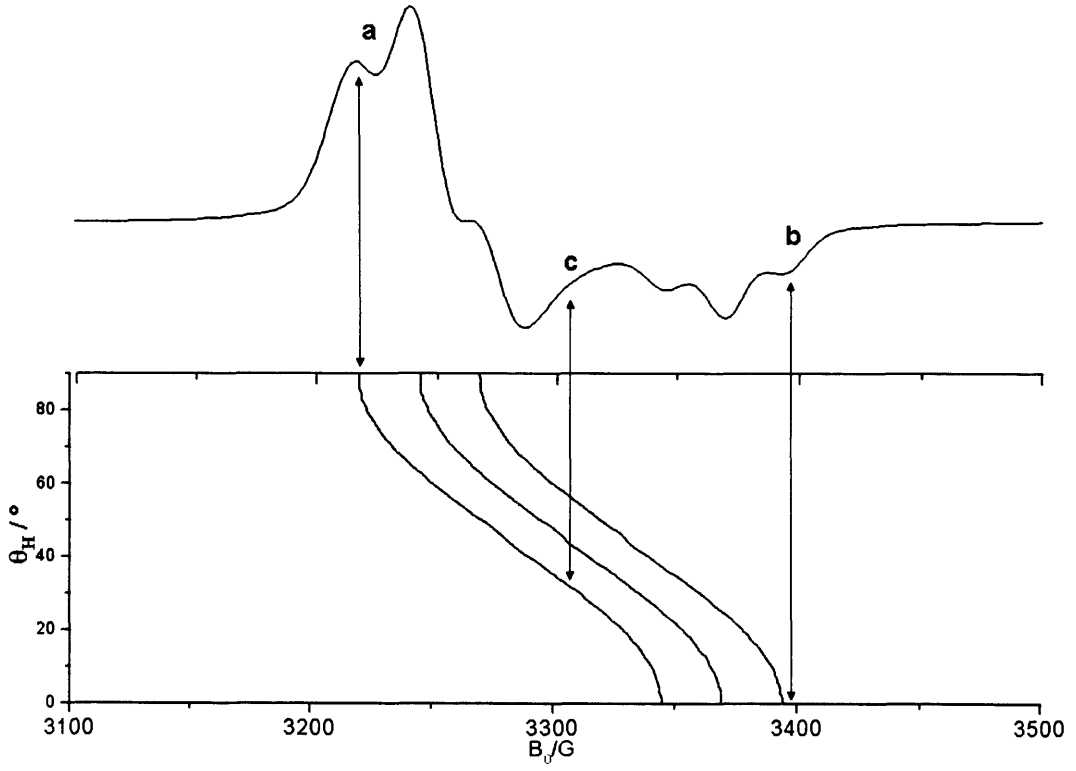

Figure 2.11: Simulated CW-EPR spectrum (top) of an electron interacting with two equivalent I = ½ nuclei. The angular dependency curves calculated for the ***g*** tensor and the A tensor are shown in the lower trace.

As can be observed in the above Figure, some intermediate field positions now correspond to more than one orientation of the molecule because of the multiple nuclear spin transitions (see position **c** in Figure 2.11). However, field positions corresponding to a unique orientation of the molecule do still exist at positions **a** and **b**. Analysis of these spectra in particular enables single-crystal like information to be obtained.

2.7 References

1. W. Gerlach and O. Stern, *Z. Phys.*, 1921, **8**, 110.
2. G. E. Uhlenbeck and S. Goudsmit, *Nature*, 1926, **117**, 264.
3. E. Zavoisky, *J. Phys. U.S.S.R.*, 1945, **9**, 211.
4. J. R. Pilbrow, *Transition Ion Electron Paramagnetic Resonance*, OUP, Oxford, 1990.
5. M. Brustolon and E. Giamello, eds., *Electron Paramagnetic Resonance: A Practitioner's Toolkit*, Wiley, 2009.
6. F. E. Mabbs, *Chem. Soc. Rev.*, 1993, **22**, 313.
7. J. Krzystek, A. Ozarowski and J. Telser, *Coord. Chem. Rev.*, 2006, **250**, 2308.
8. G. Feher, *Phys. Rev.*, 1956, **103**, 834.
9. J. S. Hyde and A. H. Maki, *J. Chem. Phys.*, 1964, **40**, 3117.
10. D. M. Murphy and R. D. Farley, *Chem. Soc. Rev.*, 2006, **35**, 249.
11. E. L. Hahn, *Phys. Rev.*, 1950, **80**, 580.
12. L. G. Rowan, E. L. Hahn and W. B. Mims, *Phys. Rev. A*, 1965, **137**, 61.
13. A. Schweiger and G. Jeschke, *Principles of Pulse Electron Paramagnetic Resonance*, OUP, Oxford, 2001.
14. W. B. Mims, *Proc. R. Soc. Lond. Ser. A. Math. Phys. Sci.*, 1965, **283**, 452.
15. E. R. Davies, *Phys. Lett. A*, 1974, **47**, 1.

Chapter 3

Experimental Details

3.1 Introduction

In this chapter an overview of the synthetic procedures used to make the complexes, the sample preparation techniques and spectrometer methodology will all be discussed.

3.2 Synthetic Procedures

3.2.1 General Procedures

All manipulations were performed using standard Schlenk techniques under an argon atmosphere, or under a nitrogen atmosphere in a MBraun UNILAB glovebox with less than 0.1ppm H_2O and O_2. Solvents were dried using a Braun Solvent Purification System, and degassed prior to use. NMR spectra were recorded at 298 K on Bruker Avance AMX 400 or Bruker-ACS 60 spectrometers. Chemical shift values are given relative to residual solvent peak. ESI-MS were performed on a Waters LCT Premier XE instrument. Electronic spectra were recorded in dichloromethane on a Perkin Elmer Lambda 900 UV/VIS/NIR spectrometer.

*3.2.2 Preparation of Cr(0) bis(diphenylphosphine) complexes **1a-g***

The ligands used in the preparation of Cr bis(phosphine) complexes are shown in Scheme 1. Ligands **a**, **b**, **c** and **h** were purchased from *Aldrich* and used as received; **d, e** and **f** were prepared and supplied by Sasol Technology; **g** was prepared according to a literature procedure.[1] The chromium(0) **1a-1g** and chromium(I) compounds **2a-2g** were prepared according to literature procedures.[2-5] $Ag[Al(OC(CF_3)_3)_4]$ was prepared according to a literature procedure.[6]

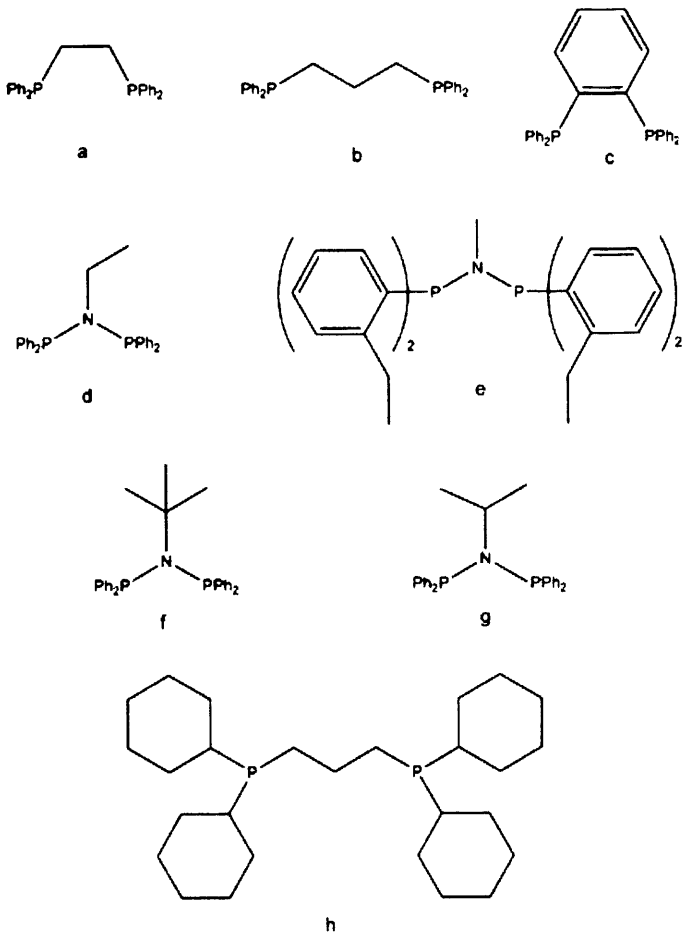

Scheme 3.1: Ligands used in the preparation of Cr bis(phosphine) complexes.

[$Cr(CO)_4(Ph_2PCH_2CH_2PPh_2)$] (1a)

Toluene (40 ml) was added to a mixture of chromium hexacarbonyl (372 mg, 1.69 mmol) and **a** (505 mg, 1.27 mmol) and the mixture was heated to reflux for 48 h, ensuring that the sublimed hexacarbonyl was periodically washed back into the stirred mixture. The solution was then cooled to 0°C and filtered to remove excess chromium hexacarbonyl. Solvent was removed *in vacuo* and the product extracted into dichloromethane (10 ml). Methanol (20 ml) was added to precipitate the product which was isolated by filtration and dried *in vacuo* yielding a yellow microcrystalline solid (300 mg, 42%). ^1H NMR (CD_2Cl_2, 400 MHz, 298 K): δ (ppm) 2.00 (t, 4H, CH_2CH_2 $^3J_{HH}$ = 4.1 Hz), 7.20-7.35 (m, 16H, *ortho-* and *meta*-C_6H_5), 7.50 (m, 4H, *para*-C_6H_5). ^{31}P {^1H} NMR (CD_2Cl_2, 121 MHz, 298 K): δ (ppm) 80.35 (s). ^{13}C {^1H} NMR (CD_2Cl_2, 125 MHz, 298 K): δ (ppm) 27.3 (CH_2CH_2), 127.7 (*meta*-C_6H_5), 130.4 (*para*-C_6H_5),

131.9 (*ortho*-C_6H_5), 137.6 (*ipso*-C_6H_5), 219.6 (*cis*-CO), 228.3 (*trans*-CO). High Resolution ESI_{pos}-MS (MeCN): found 562.0542 ($C_{30}H_{24}O_4P_2Cr^+$ requires 562.0555 dev: -2.3 ppm). IR (CH_2Cl_2): ν= 1870 (s) (CO), 1902 (s) (CO), 2005 (s) (CO) cm^{-1}.

[$Cr(CO)_4(Ph_2P(CH_2)_3PPh_2)$] (1b)

An analogous method to that of **1a** (described above) was followed, using chromium hexacarbonyl (355 mg, 1.61 mmol) and **b** (502 mg, 1.22 mmol). The product was obtained as a yellow solid (400 mg, 57%). ^1H NMR ($CDCl_3$, 400 MHz, 298 K): δ (ppm) 1.88 (m, 2H, CH_2), 2.34 (m, 4H, CH_2), 7.32 (m, 20H, C_6H_5). ^{31}P {^1H} NMR ($CDCl_3$, 121 MHz, 298 K): δ (ppm) 42.38 (s). ^{13}C {^1H} NMR ($CDCl_3$, 125 MHz, 298 K): δ (ppm) 18.6 (CH_2), 29.6 (CH_2), 127.3 (*meta*-C_6H_5), 128.4 (*para*-C_6H_5), 130.8 (*ortho*-C_6H_5), 136.7 (*ipso*-C_6H_5), 220.7 (*cis*-CO), 225.1 (*trans*-CO). High Resolution ESI_{pos}-MS (MeCN): found 576.0717 ($C_{31}H_{26}O_4P_2Cr^+$ requires 576.0711 dev: 1.0 ppm). IR (CH_2Cl_2): ν= 1885 (s) (CO), 1913 (s) (CO), 2005 (s) (CO) cm^{-1}.

[$Cr(CO)_4(Ph_2PBzPPh_2)$] (1c)

An analogous method to that of **1a** (described earlier) was followed, using chromium hexacarbonyl (325 mg, 1.48 mmol) and **c** (498 mg, 1.11 mmol). The product was obtained as a yellow solid (320 mg, 47%). ^1H NMR (CD_2Cl_2, 400 MHz, 298 K): δ (ppm) 7.30 (m, 20H, *ortho*-, *meta*-C_6H_5, C_6H_4), 7.45 (m, 4H, *para*-C_6H_5). ^{31}P {^1H} NMR (CD_2Cl_2, 121 MHz, 298 K): δ (ppm) 83.33 (s). ^{13}C {^1H} NMR (CD_2Cl_2, 125 MHz, 298 K): δ (ppm) 127.4 (*meta*-C_6H_5), 127.6 (*para*-C_6H_5), 128.9, 129.7, 131.3 (C_6H_4), 131.4 (*ortho*-C_6H_5), 135.6 (*ipso*-C_6H_5). High Resolution ESI_{pos}-MS (MeCN): found 610.0564 ($C_{34}H_{24}O_4P_2Cr^+$ requires 610.0555 dev: 1.4 ppm). IR (CH_2Cl_2): ν = 1893 (s) (CO), 1916 (s) (CO), 2012 (s) (CO) cm^{-1}.

[$Cr(CO)_4(Ph_2PN(Et)PPh_2)$] (1d)

An analogous method to that of **1a** (described earlier) was followed, using chromium hexacarbonyl (355 mg, 1.61 mmol) and **d** (500 mg, 1.21 mmol). The product was obtained as a yellow solid (350 mg, 50%). ^1H NMR ($CDCl_3$, 400 MHz, 298 K): δ (ppm) 0.75 (t, 3H, CH_3, $^3J_{HH}$ = 7.3 Hz), 3.00 (m, 2H, CH_2), 7.41 (m, 20H, C_6H_5). ^{31}P {^1H} NMR ($CDCl_3$, 121 MHz, 298 K): δ (ppm) 114.36 (s). ^{13}C {^1H} NMR ($CDCl_3$, 125 MHz, 298 K): δ (ppm) 15.1 (CH_3), 44.0 (CH_2), 127.5 (*meta*-C_6H_5), 129.6 (*para*-C_6H_5),

130.9 (*ortho*-C_6H_5), 135.6 (*ipso*-C_6H_5), 221.2 (*cis*-CO), 227.2 (*trans*-CO). High Resolution ESI_{pos}-MS (MeCN): found 577.0656 ($C_{30}H_{25}O_4P_2CrN^+$ requires 577.0664 dev: -1.4 ppm). IR (CH_2Cl_2): ν= 1891 (s) (CO), 1915 (s) (CO), 2007 (s) (CO) cm^{-1}.

[Cr(CO)$_4$(Ar$_2$PN(Me)PAr$_2$)] (Ar = 2-C$_6$H$_4$(Et)) (1e)

An analogous method to that of **1a** (described earlier) was followed, using chromium hexacarbonyl (293 mg, 1.33 mmol) and **e** (511 mg, 1.0 mmol). The product was obtained as a yellow solid (350 mg, 53%). ^1H NMR (CD_2Cl_2, 400 MHz, 298 K): δ (ppm) 0.85 (br s, 12H, CH_3), 2.46 (s, 3H, CH_3), 2.61 (br s, 8H, CH_2), 7.32 (m, 16H, *Ar*-H). ^{31}P {^1H} NMR (CD_2Cl_2, 121 MHz, 298 K): δ (ppm) 103.4 (br s). ^{13}C {^1H} NMR (CD_2Cl_2, 125 MHz, 298 K): δ (ppm) 13.3 (CH_3), 26.0 (CH_2), 33.5 (N-CH_3), 124.9 (*meta*-C_6H_5), 129.1 (*para*-C_6H_5), 134.5 (*ortho*-C_6H_5), 144.6 (*ipso*-C_6H_5), 219.8 (*cis*-CO), 227.7 (*trans*-CO). High Resolution ESI_{pos}-MS (MeCN): found 675.1746 ($C_{37}H_{43}O_4P_2CrN^+$ requires 675.1759 dev: -1.9 ppm). IR (CH_2Cl_2): ν = 1864 (s) (CO), 1895 (s) (CO), 2006 (s) (CO) cm^{-1}.

[Cr(CO)$_4$(Ph$_2$PN(^{t}Bu)PPh$_2$)] (1f)

An analogous method to that of **1a** (described earlier) was followed, using chromium hexacarbonyl (340 mg, 1.55 mmol) and **f** (510 mg, 1.16 mmol). The product was obtained as a yellow solid (350 mg, 50%). ^1H NMR ($CDCl_3$, 400 MHz, 298 K): δ (ppm) 0.49 (s, 9H, $C(CH_3)_3$), 7.48 (m, 20H, C_6H_5). ^{31}P {^1H} NMR ($CDCl_3$, 121 MHz, 298 K): δ (ppm) 115.86 (s). ^{13}C {^1H} NMR ($CDCl_3$, 125 MHz, 298 K): δ (ppm) 30.6 (CH_3), 61.6 ($C(CH_3)_3$), 127.3 (*meta*-C_6H_5), 129.5 (*para*-C_6H_5), 130.8 (*ortho*-C_6H_5), 135.9 (*ipso*-C_6H_5), 222.5 (*cis*-CO), 227.7 (*trans*-CO). High Resolution ESI_{pos}-MS (MeCN): found 605.0962 ($C_{32}H_{29}O_4P_2CrN^+$ requires 605.0976 dev: -2.3 ppm). IR (CH_2Cl_2): ν= 1890 (s) (CO), 1919 (s) (CO), 2006 (s) (CO) cm^{-1}.

[Cr(CO)$_4$(Ph$_2$PN(^{i}Pr)PPh$_2$)] (1g)

An analogous method to that of **1a** (described earlier) was followed, using chromium hexacarbonyl (340 mg, 1.55 mmol) and **g** (494 mg, 1.16 mmol). The product was obtained as a yellow solid (260 mg, 38%). ^1H NMR ($CDCl_3$, 400 MHz, 298 K): δ (ppm) 0.62 (d, 6H, CH_3, $^3J_{HH}$ = 6.8 Hz), 3.52 (sept, 1H, CH, $^3J_{HH}$ = 7.0 Hz), 7.41 (m, 12H, *meta*-, *para*-C_6H_5), 7.69 (m, 8H, *ortho*-C_6H_5). ^{31}P {^1H} NMR ($CDCl_3$, 121 MHz, 298 K): δ (ppm) 112.70 (s). ^{13}C {^1H} NMR ($CDCl_3$, 125 MHz, 298 K): δ (ppm) 22.5

(CH_3), 54.8 (CH), 127.4 (*meta*-C_6H_5), 129.5 (*para*-C_6H_5), 130.9 (*ortho*-C_6H_5), 136.1 (*ipso*-C_6H_5), 221.9 (*cis*-CO), 227.4 (*trans*-CO). High Resolution ESI_{pos}-MS (MeCN): found 591.0796 ($C_{31}H_{27}O_4P_2CrN^+$ requires 591.0820 dev: -4.1 ppm). IR (CH_2Cl_2): ν = 1887 (s) (CO), 1923 (s) (CO), 2006 (s) (CO) cm^{-1}.

3.2.3 Synthesis of the counterion[32] *Ag[Al(OC(CF$_3$)$_3$)$_4$]*

$LiAlH_4$ (1.0g, 0.026mol) was suspended in hexane (60ml), cooled to 253K and $HOC(CF_3)_3$ (15ml, 0.11mol) added slowly. The mixture was stirred for 45 minutes then heated under reflux overnight using a condenser set at 253K. The solution was filtered, the product washed with hexane and solvent removed *in vacuo* to yield the white solid $Li[Al(OC(CF_3)_3)_4]$ (20.0g, 80 %); ^{19}F NMR ($(CD_3)_2SO$, 250 MHz, 298K); δ (ppm) -75.06.

$Li[Al(OC(CF_3)_3)_4]$ (10.0g, 0.01mol) and AgF (1.7g, 0.013mol) were suspended in CH_2Cl_2 (50ml) in the dark and mixed in an ultrasonic bath overnight. The solution was filtered and the solvent removed in vacuo to yield the white solid $Ag[Al(OC(CF_3)_3)_4]$ (8.3g, 77%).

*3.2.4 Preparation of Cr(I) bis(diphenylphosphine) complexes **2a-g***

$[Cr(CO)_4(Ph_2PCH_2CH_2PPh_2)][Al(OC(CF_3)_3)_4]$ (2a)

Complex **1a** (50 mg, 0.089 mmol) and the silver aluminate (143 mg, 0.13 mmol) were combined in a Schlenk tube and dichloromethane (5 ml) added. The mixture, which immediately changed colour from yellow to dark purple, was left to stir for 16 h at room temperature under the exclusion of light. After filtration, the solvent was removed *in vacuo* leaving a dark purple residue which was washed with hexane (2 × 5 ml) and dried *in vacuo* to yield the product as a deep purple powder (90 mg, 66%). High Resolution ESI_{pos}-MS (MeCN): found 562.0562 ($C_{30}H_{24}O_4P_2Cr^+$ requires 562.0555 dev: 1.2 ppm). High Resolution ESI_{neg}-MS (MeCN): found 966.9030 ($C_{16}H_{36}O_4Al^+$ requires 966.9037 dev: -0.7 ppm). IR (CH_2Cl_2): ν = 1971 (s) (CO), 2034 (s) (CO), 2085 (s) (CO) cm^{-1}.

$[Cr(CO)_4(Ph_2P(CH_2)_3PPh_2)][Al(OC(CF_3)_3)_4]$ (2b)

An analogous method to that of **2a** (described above) was followed, using chromium compound **1b** (100 mg, 0.17 mmol) and silver aluminate (275 mg, 0.255 mmol). The product was obtained as a dark blue powder (145 mg, 54%). High

Resolution ESI_{pos}-MS (MeCN): found 576.0706 ($C_{31}H_{26}O_4P_2Cr^+$ requires 576.0711 dev: -0.8 ppm). High Resolution ESI_{neg}-MS (MeCN): found 966.9084 ($C_{16}H_{36}O_4Al^+$ requires 966.9037 dev: 4.8 ppm). IR (CH_2Cl_2): ν= 1954 (s) (CO), 2046 (s) (CO), 2086 (s) (CO) cm^{-1}.

$[Cr(CO)_4(Ph_2PBzPPh_2)][Al(OC(CF_3)_3)_4]$ (2c)

An analogous method to that of **2a** (described earlier) was followed, using chromium compound **1c** (50 mg, 0.081 mmol) and silver aluminate (130 mg, 0.121 mmol). The product was obtained as a dark blue powder (65 mg, 50%). High Resolution ESI_{pos}-MS (MeCN): found 610.0540 ($C_{34}H_{24}O_4P_2Cr^+$ requires 610.0555 dev: -2.4 ppm). IR (CH_2Cl_2): ν= 1969 (s) (CO), 2032 (s) (CO), 2086 (s) (CO) cm^{-1}.

$[Cr(CO)_4(Ph_2PN(Et)PPh_2)][Al(OC(CF_3)_3)_4]$ (2d)

An analogous method to that of **2a** (described earlier) was followed, using chromium compound **1d** (100 mg, 0.17 mmol) and silver aluminate (278 mg, 0.26 mmol). The product was obtained as a dark blue powder (120 mg, 45%). High Resolution ESI_{pos}-MS (MeCN): found 577.0648 ($C_{30}H_{25}O_4P_2CrN^+$ requires 577.0664 dev: -2.7 ppm). IR (CH_2Cl_2): ν= 1968 (s) (CO), 2036 (s) (CO), 2089 (s) (CO) cm^{-1}.

$[Cr(CO)_4(Ar_2PN(Me)PAr_2)][Al(OC(CF_3)_3)_4]$ (Ar = 2-C_6H_4(Et)) (2e)

An analogous method to that of **2a** (described earlier) was followed, using chromium compound **1e** (100 mg, 0.15 mmol) and silver aluminate (238 mg, 0.22 mmol). The product was obtained as a dark blue powder (150 mg, 62%). High Resolution ESI_{pos}-MS (MeCN): found 675.1773 ($C_{37}H_{43}O_4P_2CrN^+$ requires 675.1759 dev: 2.0 ppm). IR (CH_2Cl_2): ν= 1975 (s) (CO), 2022 (s) (CO), 2082 (s) (CO) cm^{-1}.

$[Cr(CO)_4(Ph_2PN(^tBu)PPh_2)][Al(OC(CF_3)_3)_4]$ (2f)

An analogous method to that of **2a** (described earlier) was followed, using chromium compound **1f** (50 mg, 0.083 mmol) and silver aluminate (133 mg, 0.124 mmol). The product was obtained as a dark blue powder (62 mg, 48%). High Resolution ESI_{pos}-MS (MeCN): found 605.0993 ($C_{32}H_{29}O_4P_2CrN^+$ requires 605.0976 dev: 2.8 ppm). IR (CH_2Cl_2): ν= 1965 (s) (CO), 2031 (s) (CO), 2084 (s) (CO) cm^{-1}.

$[Cr(CO)_4(Ph_2PN(iPr)PPh_2)][Al(OC(CF_3)_3)_4]$ (2g)

An analogous method to that of **2a** (described earlier) was followed, using chromium compound **1g** (100 mg, 0.17 mmol) and silver aluminate (271 mg, 0.25 mmol). The product was obtained as a dark blue powder (105 mg, 40%). High Resolution ESI_{pos}-MS (MeCN): found 591.0824 ($C_{31}H_{27}O_4P_2CrN^+$ requires 591.0820 dev: 0.6 ppm). IR (CH_2Cl_2): ν= 1964 (s) (CO), 2032 (s) (CO), 2086 (s) (CO) cm^{-1}.

3.2.5 Preparation of the Cr(0) bis(dicyclohexylphosphine) complex ***1h***

$[Cr(CO)_4(C_6H_{11})_2PCH_2CH_2CH_2P(C_6H_{11})_2]$ (1h)

An analogous method to that of **1a** (described earlier) was followed, using chromium hexacarbonyl (350 mg, 1.6 mmol) and **h** (500 mg, 1.22 mmol). The product was obtained as a yellow solid (438 mg, 64%); ^1H NMR ($CDCl_3$, 400.8 MHz, 298K): δ (ppm) 1.18 (m, 16H, CH_2), 1.25 (m, 8H, CH_2), 1.55 (m, 2H, CH_2), 1.65 (m, 4H, CH_2), 1.75 (m, 16H, CH_2), 1.9 (s, 4H, CH); ^{31}P $\{^1H\}$ NMR ($CDCl_3$, 121.7 MHz, 298K): δ (ppm) 40.0 (s); ^{13}C NMR ($CDCl_3$, 125.8 MHz, 298K): δ (ppm) 19.00 (CH_2), 20.58 (CH_2), 25.29 (1-C_6H_{11}), 26.62 (4-C_6H_{11}), 27.70 (3-C_6H_{11}), 38.90 (2-C_6H_{11}), 222.50 (*cis*-CO), 227.0 (*trans*-CO).

3.2.6 Preparation of the Cr(I) bis(dicyclohexylphosphine) complex ***2h***

$[Cr(CO)_4(C_6H_{11})_2PCH_2CH_2CH_2P(C_6H_{11})_2)][Al(OC(CF_3)_3)_4]$ (2h)

An analogous method to that of **2a** (described earlier) was followed, using chromium compound **1h** (50 mg, 0.083 mmol) and silver aluminate (110 mg, 0.12 mmol). The product was obtained as an orange-red powder (101 mg, 78%).

3.3 Preparation of Cr(I), Cr(III) and Ti(III) N-heterocyclic carbene complexes

The synthesis of all N-heterocyclic carbene complexes was kindly performed by Dr. Tracy Hamilton.[7]

The ligands and imidazolium salts used in the preparation of these complexes are shown in Schemes 3.2 and 3.3 respectively. Free carbenes **d, e, f, g, h, i, j, k, l, m** and **n** were prepared according to a literature procedure.[8] **a - c** were prepared from the imidazolium salt precursors **50 – 52**.

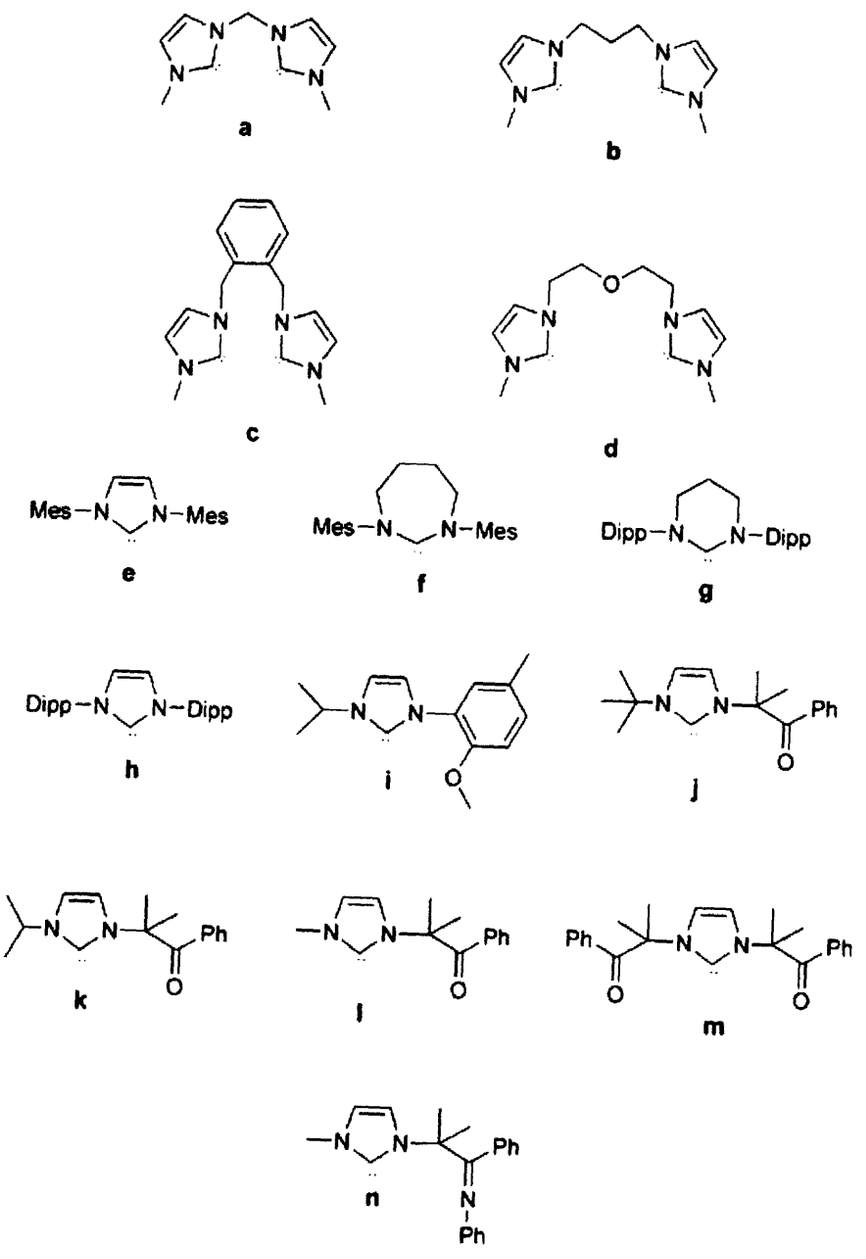

Scheme 3.2: Ligands used in the preparation of Cr and Ti N-heterocyclic carbene complexes.

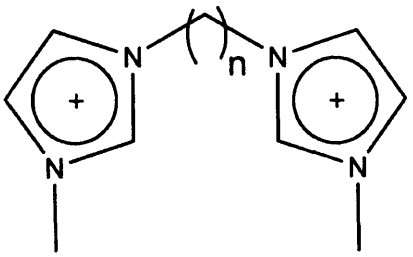

n = CH_2 **50**
$(CH_2)_3$ **51**
$CH_2(C_6H_4)CH_2$ **52**

Scheme 3.3: Imidazolium salts used in the preparation of Cr and Ti N-heterocyclic carbene complexes.

*3.3.1 Preparation of Cr(0) NHC complexes **3a – c, 3e, 3h** and **3g***

cis-Tetracarbonyl-[1,1'-methylene-3,3'-dimethylimidazole-2,2'-diylidene]chromium (3a)

Di-imidazolium salt **50** (1.5 g, 4.44 mmol) and chromium hexacarbonyl (980 mg, 4.44 mmol) were suspended in THF (30 ml). NaH (213 mg, 8.88 mmol) and KO^{t}Bu (50 mg, 0.44 mmol) were added, and the yellow mixture heated to reflux for 6 h. After cooling to room temperature, the solvent was removed *in vacuo* and the residue washed with methanol (2 × 20 ml). Extraction with THF (3 × 20 ml) and filtration through silica, followed by removal of the solvent *in vacuo* resulted in isolation of a yellow microcrystalline solid (150 mg, 9.9 %). ^{1}H NMR (acetone-d_6, 400 MHz, 298 K): δ (ppm) 7.29 (d, 2H, NC*H*CHN, $^3J_{HH}$ = 1.6 Hz), 7.07 (d, 2H, NCHC*H*N, $^3J_{HH}$ = 2.0 Hz), 5.98 (s, 2H, NCH_2N), 3.80 (s, 6H, NCH_3). ^{13}C {^{1}H} NMR (acetone-d_6, 125 MHz, 298 K): δ (ppm) 221.5 (*C*O), 211.3 (*C*O), 201.5 (N*C*N), 121.9 (N*C*HCHN), 120.2 (NCH*C*HN), 61.8 (N*C*H$_2$), 36.7 (N*C*H$_3$). High Resolution ESI$_{pos}$-MS (MeCN): found 340.0430 ($C_{13}H_{12}N_4O_4Cr^+$ requires 340.0421 dev: 2.6 ppm). IR (CH_2Cl_2): ν = 1951 (s) (CO), 1920 (s), 1870 (s) (CO) cm^{-1}.

cis-Tetracarbonyl-[1,1'-propylene-3,3'-dimethylimidazole-2,2'-diylidene]chromium (3b)

An analogous method to that of **3a** was followed, using salt **51** (2.0 g, 5.47 mmol), chromium hexacarbonyl (1.2 g, 5.47 mmol), NaH (262 mg, 10.9 mmol) and KO^{t}Bu (60 mg, 0.54 mmol). The product was obtained as a yellow microcrystalline solid (200 mg,

9.95 %). ^{1}H NMR (acetone-d_6, 400 MHz, 298 K): δ (ppm) 7.19 (d, 2H, NC*H*CHN, $^{3}J_{HH}$ = 1.7 Hz), 7.05 (d, 2H, NCHC*H*N, $^{3}J_{HH}$ = 1.8 Hz), 3.97 (s, 6H, NCH_3), 3.78 (m, 2H, NCH_2), 3.66 (m, 2H, NCH_2), 1.62 (m, 2H, NCH$_2$CH_2). ^{13}C {^{1}H} NMR (acetone-d_6, 125 MHz, 298 K): δ (ppm) 225.9 (CO), 211.5 (CO), 202.5 (N*C*N), 124.6 (N*C*H*C*HN), 120.2 (N*C*H*C*HN), 45.6 (N*C*H$_2$), 40.1 (N*C*H$_3$), 34.5 (*C*H$_2$). High Resolution ESI$_{pos}$-MS (MeCN): found 368.0593 ($C_{15}H_{16}N_4O_4Cr^+$ requires 368.0577 dev: 4.3 ppm). IR (CH_2Cl_2): ν= 1861 (s) (CO), 1874 (s) (CO), 1980 (s) (CO) cm^{-1}.

cis-Tetracarbonyl-[1,1'-xylylene-3,3'-dimethylimidazole-2,2'-diylidene]chromium (3c)

An analogous method to that of **3a** was followed, using salt **52** (1.5 g, 3.5 mmol), chromium hexacarbonyl (771 mg, 3.5 mmol), NaH (168 mg, 7.0 mmol) and KO^{t}Bu (40 mg, 0.35 mmol). The product was obtained as a yellow microcrystalline solid (130 mg, 8.6 %). ^{1}H NMR (acetone-d_6, 400 MHz, 298 K): δ (ppm) 7.37 (m, 2H, NC*H*CHN), 7.24 (m, 2H, NCHC*H*N), 7.10 (d, 2H, C$_6H_4$ $^{3}J_{HH}$ = 1.6 Hz), 6.75 (m, 2H, C$_6H_4$), 5.31 (d, 2H, NCH_2, $^{2}J_{HH}$ = 14 Hz), 4.58 (d, 2H, NCH_2, $^{2}J_{HH}$ = 14 Hz), 3.99 (s, 6H, NCH_3). ^{13}C {^{1}H} NMR (acetone-d_6, 125 MHz, 298 K): δ (ppm) 226.9 (CO), 217.5 (CO), 201.3 (N*C*N), 129.0 (C$_6H_4$), 134.1 (C$_6H_4$), 126.7 (C$_6H_4$), 121.7 (N*C*H*C*HN), 53.1 (N-*C*H$_2$), 41.2 (N-*C*H$_3$). High Resolution ESI$_{pos}$-MS (MeCN): found 431.0816 ($C_{20}H_{18}N_4O_4Cr^+$ requires 431.0811 dev: 1.2 ppm); IR (CH_2Cl_2): ν= 1823 (s) (CO), 1922 (s) (CO), 1976 (s) (CO) cm^{-1}.

Pentacarbonyl-[1,3-bis-(2,4,6-trimethylphenyl)imidazole-2-ylidene]chromium (3e)

A solution of free carbene **e** (500 mg, 1.65 mmol) in toluene (40 ml) was added to a Schlenk containing chromium hexacarbonyl (480 mg, 2.18 mmol), and the mixture heated to reflux for 48 h. The sublimed hexacarbonyl was periodically washed back into the stirred mixture. The solution was cooled to 0°C and filtered to remove excess chromium hexacarbonyl. Solvent was removed *in vacuo* and the product extracted into dichloromethane (10 ml). Methanol (20 ml) was added to precipitate the product which was isolated by filtration and dried *in vacuo* yielding a yellow microcrystalline solid (350 mg, 43 %). ^{1}H NMR (acetone-d_6, 400 MHz, 298 K): δ (ppm) 6.99 (s, 2H, NC*H*C*H*N), 6.95 (s, 4H, C$_6H_2$), 2.29 (s, 6H, *para*-CH_3), 2.02 (s, 12H, *ortho*-CH_3). ^{13}C {^{1}H} NMR (acetone-d_6, 125 MHz, 298 K): δ (ppm) 220.9 (CO), 215.4 (CO), 197.3 (N*C*N), 138.7, 136.6, 134.8, 128.4 (*C*$_6H_2$), 123.3 (N*C*H*C*HN), 20.1 (*para*-*C*H$_3$), 16.6

(*ortho*-CH_3). High Resolution ESI_{pos}-MS (MeCN): found 496.1073 ($C_{26}H_{24}N_2O_5Cr^+$ requires 496.1078 dev: -1.0 ppm). IR (CH_2Cl_2): ν= 1922 (s) (CO), 2059 (s) (CO) cm^{-1}.

Pentacarbonyl-[1,3-bis-(2,6-diisopropylphenyl)imidazole-2-ylidene]chromium (3h)

An analogous method to that of **3e** was followed, using free carbene **h** (500 mg, 1.28 mmol) and chromium hexacarbonyl (370 mg, 1.68 mmol). The product was obtained as a yellow microcrystalline solid (300 mg, 40 %). ^1H NMR (acetone-d_6, 400 MHz, 298 K): δ (ppm) 7.44 (m, 2H, C_6H_3), 7.25 (m, 4H, C_6H_3), 7.00 (s, 2H, NC*H*C*H*N), 2.62 (*sept*, 4H, C*H*(CH_3)$_2$, $^3J_{HH}$ = 6.80 Hz), 1.30 (d, 12H, CH(C*H*$_3$)$_2$, $^3J_{HH}$ = 6.81 Hz), 1.05 (d, 12H, CH(C*H*$_3$)$_2$, $^3J_{HH}$ = 6.82 Hz). ^{13}C {^1H} NMR (acetone-d_6, 125 MHz, 298 K): δ (ppm) 219.9 (*C*O), 214.9 (*C*O), 198.6 (N*C*N), 145.3, 136.5, 129.6, 124.4 (*C*$_6$H$_3$), 123.2 (N*C*H*C*HN), 28.0 (*C*H(CH_3)$_2$), 24.9 (CH(*C*H$_3$)$_2$), 22.8 (CH(*C*H$_3$)$_2$). High Resolution ESI_{pos}-MS (MeCN): found 580.1125 ($C_{32}H_{36}N_2O_5Cr^+$ requires 580.1114 dev: 1.9 ppm). IR (CH_2Cl_2): ν= 1923 (s) (CO), 2053 (s) (CO) cm^{-1}.

Pentacarbonyl-[1,3-bis(2,6-diisopropylphenyl)-4,5,6-trihydropyrimidin-2-ylid]chromium (3g)

An analogous method to that of **g** was followed, using free carbene **62** (500 mg, 1.23 mmol) and chromium hexacarbonyl (363 mg, 1.61 mmol). The product was obtained as a yellow microcrystalline solid (280 mg, 46%). ^1H NMR (acetone-d_6, 400 MHz, 298 K): δ (ppm) 7.28 (m, 2H, C_6H_3), 7.17 (m, 4H, C_6H_3), 3.45 (m, 4H, NC*H*(CH_3)$_2$), 3.07 (m, 4H, NC*H*$_2$), 1.48 (m, 2H, NCH$_2$C*H*$_2$), 1.19 (d, 12H, CH(C*H*$_3$)$_2$, $^3J_{HH}$ = 6.7 Hz), 1.07 (d, 12H, CH(C*H*$_3$)$_2$, $^3J_{HH}$ = 6.7 Hz). ^{13}C {^1H} NMR (acetone-d_6, 125 MHz, 298 K): δ (ppm) 219.8 (CO), 214.5 (CO), 201.2 (NCN), 144.6 (*C*$_6$H$_3$), 128.3 (*C*$_6$H$_3$), 124.5 (*C*$_6$H$_3$), 123.3 (*C*$_6$H$_3$), 27.7 (N*C*H$_2$), 26.8, 25.3 (NCH(*C*H$_3$)$_2$), 22.9 (NCH$_2$*C*H$_2$). High Resolution ESI_{pos}-MS (MeCN): found 596.1435 ($C_{28}H_{40}N_2O_5Cr^+$ requires 596.1425 dev: 1.7 ppm). IR (CH_2Cl_2): ν= 1927 (s) (CO), 2044 (s) (CO) cm^{-1}.

*3.3.2 Preparation of Cr(I) NHC complexes **4a – c**, **4e**, **4h** and **4g***

Synthesis of cationic chromium(I)-NHC complexes was carried out by one-electron oxidation using Ag[Al(OC(CF_3)$_3$)$_4$] as described for the Cr(I) bis-phosphine complexes in Section 3.2.4.

[*cis*-Tetracarbonyl-[1,1'-methylene-3,3'-dimethylimidazole-2,2'-diylidene]chromium][aluminate] (4a)

Complex **3a** (50 mg, 0.14 mmol) and the silver aluminate (317 mg, 0.29 mmol) were combined in a Schlenk tube and dichloromethane (10 ml) added. The mixture, which immediately changed colour, was left to stir for 30 min at room temperature with the exclusion of light. After filtration, the solvent was removed *in vacuo* leaving a red-purple residue which was washed with hexane (2 × 5 ml) and dried *in vacuo* to yield the product as a red-purple solid (80 mg, 41 %). IR (CH_2Cl_2): ν = 1986 (s) (CO), 2015 (s) (CO), 2047 (s) (CO) cm^{-1}.

[*cis*-Tetracarbonyl-[1,1'-propylene-3,3'-dimethylimidazole-2,2'-diylidene]chromium][aluminate] (4b)

An analogous method to that of **4a** was followed, using chromium compound **3b** (50 mg, 0.14 mmol) and silver aluminate (290 mg, 0.27 mmol). The product was obtained as a dark red solid (75 mg, 40 %). IR (CH_2Cl_2): ν = 1982 (s) (CO), 2019 (s) (CO), 2043 (s) (CO) cm^{-1}.

[*cis*-Tetracarbonyl-[1,1'-xylylene-3,3'-dimethylimidazole-2,2'-diylidene]chromium][aluminate] (4c)

An analogous method to that of **4a** was followed, using chromium compound **3c** (50 mg, 0.12 mmol) and silver aluminate (250 mg, 0.23 mmol). The product was obtained as a dark purple solid (70 mg, 43 %). IR (CH_2Cl_2): ν = 1980 (s) (CO), 2021 (s), 2054 (CO) cm^{-1}.

[Pentacarbonyl-[1,3-bis-(2,4,6-trimethylphenyl)imidazole-2-ylidene]chromium][aluminate] (4e)

An analogous method to that of **4a** was followed, using chromium compound **3e** (50 mg, 0.10 mmol) and silver aluminate (210 mg, 0.20 mmol). The product was obtained as a dark red solid (60 mg, 40 %). IR (CH_2Cl_2): ν = 2011 (s) (CO), 2129 (s) (CO) cm^{-1}.

[Pentacarbonyl-[1,3-bis-(2,6-diisopropylphenyl)imidazole-2-ylidene]chromium][aluminate] (4h)

An analogous method to that of **4a** was followed, using chromium compound **3h** (50 mg, 0.08 mmol) and silver aluminate (184 mg, 0.17 mmol). The product was obtained as a dark red solid (60 mg, 45 %). IR (CH_2Cl_2): ν= 2012 (s) (CO), 2119 (s) (CO) cm^{-1}.

[Pentacarbonyl-[1,3-bis(2,6-diisopropylphenyl)-4,5,6-trihydropyridin-2-ylid]chromium][aluminate] (4g)

An analogous method to that of **4a** was followed, using chromium compound **3g** (50 mg, 0.08 mmol) and silver aluminate (181 mg, 0.17 mmol). The product was obtained as a red solid (65 mg, 49 %). IR (CH_2Cl_2): ν= 2056 (s) (CO), 2143 (s) (CO) cm^{-1}.

*3.3.3 Preparation of Cr(III) NHC complexes **5a, 5c - g, 5i - n***

$CrCl_3$(NHC)(THF) *(NHC = 1-methyl-3-isobutyrophenoneimidazole-2-ylidene)* (5l)

To a slurry of $CrCl_3(THF)_3$ (535 mg, 1.43 mmol) in THF (10 ml) at -10 °C a solution of free carbene **l** (340 mg, 1.49 mmol) in THF (10 ml) was added dropwise over 30 min. The resulting mixture was allowed to slowly warm to room temperature, and left to stir for 16 h. The solution was concentrated and diethyl ether (10 ml) added to precipitate the complex. The product was isolated by filtration, washed with diethyl ether (3 × 10 ml) and dried *in vacuo* to give the product as a green solid (350 mg, 53%). IR (CH_2Cl_2): ν= 1551 (s) (CO) cm^{-1}. $\lambda_{max}(CH_2Cl_2)$/nm 620, 450. Magnetic moment μ_{eff} = 3.87 μ_B.

$CrCl_3$(NHC)(THF) *(NHC = 1-isopropyl-3-isobutyrophenoneimidazole-2-ylidene)* (5k)

An analogous method to that of **5l** was followed, using $CrCl_3(THF)_3$ (530 mg, 1.41 mmol) and free carbene **k** (376 mg, 1.47 mmol). The product was obtained as a green powder (360 mg, 52%). IR (CH_2Cl_2): ν = 1551 (s) (CO) cm^{-1}. $\lambda_{max}(CH_2Cl_2)$/nm 620, 440. Magnetic moment μ_{eff} = 3.85 μ_B.

$CrCl_3$(NHC)(THF) *(NHC = 1-^{t}Butyl-3-isobutyrophenoneimidazole-2-ylidene)* (5j)

An analogous method to that of **5l** was followed, using $CrCl_3(THF)_3$ (515 mg, 1.37 mmol) and free carbene **j** (386 mg, 1.43 mmol). The product was obtained as a purple

powder (340 mg, 49%). IR (CH_2Cl_2): ν = 1550 (s) (CO) cm^{-1}. $\lambda_{max}(CH_2Cl_2)$/nm 570, 470. Magnetic moment μ_{eff} = 3.88 μ_B.

$CrCl_3$(NHC) ***(NHC = 1,3-diisobutyrophenoneimidazole-2-ylidene)*** **(5m)**

An analogous method to that of **5l** was followed, using $CrCl_3(THF)_3$ (530 mg, 1.42 mmol) and free carbene **m** (533 mg, 1.48 mmol). The product was obtained as a pale blue powder (370 mg, 51%). IR (CH_2Cl_2): ν = 1549 (s) (CO) cm^{-1}. $\lambda_{max}(CH_2Cl_2)$/nm 590, 460. Magnetic moment μ_{eff} = 3.79 μ_B.

$CrCl_3$(NHC)(THF)

(NHC = 1-methyl-3-phenylpropylidenebenzenamineimidazole-2-ylidene) **(5n)**

An analogous method to that of **5l** was followed, using $CrCl_3(THF)_3$ (535 mg, 1.43 mmol) and free carbene **n** (451 mg, 1.49 mmol). The product was obtained as a red powder (370 mg, 48%). IR (CH_2Cl_2): ν = 1484 (s) (CO) cm^{-1}. $\lambda_{max}(CH_2Cl_2)$/nm 560, 420. Magnetic moment μ_{eff} = 3.81 μ_B.

$CrCl_3$(NHC)(THF)

(NHC = 1-Isopropyl-3-(2-methoxy-5-methylphenyl)imidazole-2-ylidene) **(5i)**

An analogous method to that of **5l** was followed, using $CrCl_3(THF)_3$ (540 mg, 1.44 mmol) and free carbene **i** (345 mg, 1.50 mmol). The product was obtained as a green powder (300 mg, 45%). IR (CH_2Cl_2): ν = 1156 (s) (COC) cm^{-1}; $\lambda_{max}(CH_2Cl_2)$/nm 640, 410. Magnetic moment μ_{eff} = 3.80 μ_B.

$CrCl_3$(NHC)(THF) ***(NHC=1,1'-methylene-3,3'-dimethylimidazole-2,2'-diylidene)*** **(5a)**

An analogous method to that of **5l** was followed, using $CrCl_3(THF)_3$ (530 mg, 1.42 mmol) and free carbene **a** (260 mg, 1.48 mmol). The product was obtained as a yellow powder (300 mg, 52%). $\lambda_{max}(CH_2Cl_2)$/nm 610, 430; Magnetic moment μ_{eff} = 3.67 μ_B.

$CrCl_3$(NHC)(THF) ***(NHC = 1,1'-xylylene-3,3'-dimethylimidazole-2,2'-diylidene)*** **(5c)**

An analogous method to that of **5l** was followed, using $CrCl_3(THF)_3$ (520 mg, 1.40 mmol) and free carbene **c** (386 mg, 1.45 mmol). The product was obtained as a green powder (350 mg, 50%). $\lambda_{max}(CH_2Cl_2)$/nm 630, 450. Magnetic moment μ_{eff} = 3.74 μ_B.

$CrCl_3$(NHC)(THF) ***(NHC = 1,1'-bis(2-(3-methylimidazolin-2-yliden-1-yl)ethyl)ether)*** **(5d)**

An analogous method to that of **5l** was followed, using $CrCl_3(THF)_3$ (525 mg, 1.40 mmol) and free carbene **d** (339 mg, 1.45 mmol). The product was obtained as a lilac powder (260 mg, 47%). IR (CH_2Cl_2): ν = 1259 (s) (COC) cm^{-1}. $\lambda_{max}(CH_2Cl_2)$/nm 570, 450. Magnetic moment μ_{eff} = 3.72 μ_B.

$CrCl_3$(NHC)$(THF)_2$ ***(NHC = 1,3-bis-(2,4,6-trimethylphenyl)imidazole-2-ylidene)*** **(5e)**

An analogous method to that of **5l** was followed, using $CrCl_3(THF)_3$ (530 mg, 1.42 mmol) and free carbene **e** (450 mg, 1.48 mmol). The product was obtained as a green powder (470 mg, 55%). $\lambda_{max}(CH_2Cl_2)$/nm 640, 470. Magnetic moment μ_{eff} = 3.92 μ_B.

$CrCl_3$(NHC)$(THF)_2$

(NHC = 1,3-bis(2,6-diisopropylphenyl)-4,5,6-trihydropyridin-2-ylid) **(5g)**

An analogous method to that of **5l** was followed, using $CrCl_3(THF)_3$ (520 mg, 1.40 mmol) and free carbene **g** (563 mg, 1.45 mmol). The product was obtained as a lilac powder (500 mg, 51%). $\lambda_{max}(CH_2Cl_2)$/nm 590, 440. Magnetic moment μ_{eff} = 3.63 μ_B.

$CrCl_3$(NHC)$(THF)_2$

(NHC = 1,3-bis-(2,4,6-trimethylphenyl)-4,5,6,7-tetrahydro-[1,3]-diazepin-2-ylid) **(5f)**

An analogous method to that of **5l** was followed, using $CrCl_3(THF)_3$ (500 mg, 1.34 mmol) and free carbene **f** (468 mg, 1.40 mmol). The product was obtained as a lilac powder (450 mg, 53%). $\lambda_{max}(CH_2Cl_2)$/nm 580, 450. Magnetic moment μ_{eff} = 3.70 μ_B.

3.3.4 Preparation of Ti(III) NHC complexes ***6a – d, 6i – k and 6m - n***

$TiCl_3$(NHC)(THF) ***(NHC = 1-isopropyl-3-isobutyrophenoneimidazole-2-ylidene)*** **(6k)**

An analogous method to that of 5l was followed, using $TiCl_3(THF)_3$ (525 mg, 1.42 mmol) and free carbene **k** (379 mg, 1.48 mmol). The product was obtained as a green powder (350 mg, 51%). IR (CH_2Cl_2): ν = 1551 (s) (CO) cm^{-1}. $\lambda_{max}(CH_2Cl_2)$/nm 630. Magnetic moment μ_{eff} = 1.65 μ_B.

$TiCl_3$(NHC)(THF) ***(NHC = 1-^{t}Butyl-3-isobutyrophenoneimidazole-2-ylidene)*** **(6j)**

An analogous method to that of **5l** was followed, using $TiCl_3(THF)_3$ (545 mg, 1.46 mmol) and free carbene **j** (413, 1.53 mmol). The product was obtained as a green powder (360 mg, 50%). IR (CH_2Cl_2): ν = 1548 (s) (CO) cm^{-1}. $\lambda_{max}(CH_2Cl_2)$/nm 630. Magnetic moment μ_{eff} = 1.86 μ_B.

$TiCl_3$(NHC) ***(NHC = 1,3-diisobutyrophenoneimidazole-2-ylidene)*** **(6m)**

An analogous method to that of **5l** was followed, using $TiCl_3(THF)_3$ (515 mg, 1.39 mmol) and free carbene **m** (522 mg, 1.45 mmol). The product was obtained as a brown powder (380 mg, 53%). IR (CH_2Cl_2): ν = 1546 (s) (CO) cm^{-1}. $\lambda_{max}(CH_2Cl_2)$/nm 580. Magnetic moment μ_{eff} = 1.98 μ_B.

$TiCl_3$(NHC)(THF)

(NHC = 1-methyl-3-phenylpropylidenebenzenamineimidazole-2-ylidene) **(6n)**

An analogous method to that of **5l** was followed, using $TiCl_3(THF)_3$ (500 mg, 1.36 mmol) and free carbene **n** (430 mg, 1.42 mmol). The product was obtained as a green powder (380 mg, 52%). IR (CH_2Cl_2): ν = 1463 (s) (CO) cm^{-1}. $\lambda_{max}(CH_2Cl_2)$/nm 600. Magnetic moment μ_{eff} = 1.77 μ_B.

$TiCl_3$(NHC)(THF)

(NHC = 1-Isopropyl-3-(2-methoxy-5-methylphenyl)imidazole-2-ylidene) **(6i)**

An analogous method to that of **5l** was followed, using $TiCl_3(THF)_3$ (530 mg, 1.43 mmol) and free carbene **i** (343 mg, 1.49 mmol). The product was obtained as a green powder (350 mg, 54%). IR (CH_2Cl_2): ν = 1159 (s) (COC) cm^{-1}. $\lambda_{max}(CH_2Cl_2)$/nm 610. Magnetic moment μ_{eff} = 1.80 μ_B.

$TiCl_3$(NHC)(THF) ***(NHC=1,1'-methylene-3,3'-dimethylimidazole-2,2'-diylidene)*** **(6a)**

An analogous method to that of **5l** was followed, using $TiCl_3(THF)_3$ (530 mg, 1.44 mmol) and free carbene **a** (264 mg, 1.50 mmol). The product was obtained as a purple powder (290 mg, 50%). $\lambda_{max}(CH_2Cl_2)$/nm 590. Magnetic moment μ_{eff} = 1.83 μ_B.

$TiCl_3$(NHC)(THF) ***(NHC = 1,1'-propylene-3,3'-dimethylimidazole-2,2'-diylidene)*** **(6b)**

An analogous method to that of **5l** was followed, using $TiCl_3(THF)_3$ (508 mg, 1.37 mmol) and free carbene **b** (292 mg, 1.43 mmol). The product was obtained as a brown powder (300 mg, 51%). $\lambda_{max}(CH_2Cl_2)$/nm 560. Magnetic moment $\mu_{eff} = 1.92\ \mu_B$.

$TiCl_3$(NHC)(THF) ***(NHC = 1,1'-xylylene-3,3'-dimethylimidazole-2,2'-diylidene)*** **(6c)**

An analogous method to that of **5l** was followed, using $TiCl_3(THF)_3$ (500 mg, 1.34 mmol) and free carbene **c** (372 mg, 1.40 mmol). The product was obtained as a green powder (350 mg, 53%). $\lambda_{max}(CH_2Cl_2)$/nm 610. Magnetic moment $\mu_{eff} = 1.84\ \mu_B$.

$TiCl_3$(NHC)(THF) ***(NHC = 1,1'-bis(2-(3-methylimidazolin-2-yliden-1-yl)ethyl)ether)*** **(6d)**

An analogous method to that of **5l** was followed, using $TiCl_3(THF)_3$ (520 mg, 1.40 mmol) and free carbene **d** (342 mg, 1.46 mmol). The product was obtained as a lilac powder (250 mg, 46%). IR (CH_2Cl_2): ν = 1258 (s) (COC) cm^{-1}. $\lambda_{max}(CH_2Cl_2)$/nm 590. Magnetic moment $\mu_{eff} = 1.90\ \mu_B$.

$TiCl_3$(NHC)$(THF)_2$ ***(NHC = 1,3-bis-(2,4,6-trimethylphenyl)imidazole-2-ylidene)*** **(6e)**

An analogous method to that of **5l** was followed, using $TiCl_3(THF)_3$ (500 mg, 1.34 mmol) and free carbene **e** (426 mg, 1.40 mmol). The product was obtained as a brown powder (450 mg, 56%). $\lambda_{max}(CH_2Cl_2)$/nm 510. Magnetic moment $\mu_{eff} = 1.83\ \mu_B$.

3.4 Sample Preparation

For X-band CW-EPR and ENDOR sample preparation, each complex was placed in the Schlenk-adapted EPR tube and dissolved in 200 µl dry dichloromethane/toluene or dichloromethane only. For pulsed EPR and ENDOR measurements a similar method was followed except a rubber septum was used to seal the tube, to enable insertion into the sample holder. For Q-band CW-EPR and ENDOR, the complex was dissolved in solvent in a vial and then transferred to the sample tube. This was sealed with wax/grease in the glove box.

The complexes were activated by the *in situ* addition of various equivalents of either Et_3Al or Me_3Al in either toluene or hexane. All alkylaluminium activation agents were supplied from *Aldrich* and degassed prior to use. Upon addition of the

alkylaluminium, the pre-catalyst solutions turned from a deep blue or purple solution to a pale brown solution. Activation was conducted at room temperature, but once the sample had been prepared, the solution was immediately frozen by placing the tube in liquid nitrogen. 1-hexene was purchased from *Aldrich* and degassed prior to use. Various equivalents of the alkene were added *in situ*. Again, following addition the solution was immediately frozen by placing the tube in liquid nitrogen. The resulting solutions were deep blue or purple in colour for all $[Cr(CO)_4\mathbf{a\text{-}g}]^+$ complexes and orange-red for $[Cr(CO)_4\mathbf{h}]^+$. The activated solutions were pale brown in colour. Upon addition of the alkene there was no colour change to the solution. Spectra were recorded at 140 K – 298 K (EPR) or 10 K (ENDOR).

3.5 Instruments

All continuous-wave (CW)-EPR spectra were recorded on an X-band Bruker EMX spectrometer operating at 100 kHz field modulation, 10mW microwave power unless stated otherwise, and equipped with a high sensitivity cavity (ER 4119HS). EPR computer simulations were performed using the SimEPR32,[9] EasySpin[10] and WINEPR Simfonia[11] programs. *g* values were determined using a DPPH standard. All CW-ENDOR meaurements were performed on a Bruker ESP300E series spectrometer operating at 12.5kHz field modulation and equipped with an ESP360 DICE ENDOR unit in an EN-801 ENDOR cavity. The spectra were recorded at 10K, using 8 dB RF power from an ENI A-300 RF amplifier, 251kHz modulation depth and 4mW microwave power. The ENDOR spectra were simulated using EasySpin[10] and an in-house programme based on the resonance expressions given in references 12 and 13.[12, 13] Pulsed EPR and ENDOR measurements were recorded on a Bruker E580 spectrometer equipped with a liquid helium cryostat from Oxford Inc. The spectra were taken at 7K, with a repetition rate of 1kHz.

3.6 References

1. M. S. Balakrishna, T. K. Prakasha and S. S. Krishnamurthy, *J. Organmet. Chem.*, 1990, **390**, 203.
2. S. O. Grim, W. L. Briggs, R. C. Barth, C. A. Tolman and J. P. Jesson, *Inorg. Chem.*, 1974, **13**, 1095.
3. L. E. Bowen, M. F. Haddow, A. G. Orpen and D. F. Wass, *Dalton Trans.*, 2007, 1160.
4. A. J. Rucklidge, D. S. McGuinness, R. P. Tooze, A. M. Z. Slawin, J. D. A. Pelletier, M. J. Hanton and P. B. Webb, *Organometallics*, 2007, **26**, 2782.

5. N. G. Connelly, P. K. Ashford, P. K. Baker, R. L. Kelly and V. A. Woodley, *J. Chem. Soc., Dalton Trans.*, 1982, 477.
6. I. Krossing and A. Reisinger, *Coord. Chem. Rev.*, 2006, **250**, 2721.
7. T. Hamilton, PhD Thesis, Cardiff University, 2010.
8. M. Iglesias, D. J. Beetstra, J. C. Knight, L. Ooi, A. Stasch, S. Coles, L. Male, M. B. Hursthouse, K. J. Cavell, A. Dervisi and I. Fallis, *Organometallics*, 2008, **27**, 3279.
9. T. P. P. Spalek and Z. Sojka, *J. Chem. Inf. Model.*, 2005, **45**, 18.
10. S. Stoll and A. Schweiger, *J. Mag. Reson.*, 2006, **178**, 42.
11. WINEPRSimFonia, *Bruker Analytische Messtechnik GmbH*, 1996.
12. G. C. Hurst, T. A. Henderson and R. W. Kreilick, *J. Am. Chem. Soc.*, 1985, **107**, 7294.
13. T. A. Henderson, G. C. Hurst and R. W. Kreilick, *J. Am. Chem. Soc.*, 1985, **107**, 7299.

Chapter 4

An EPR and ENDOR Characterisation of the Cr(I) 'pre-catalyst' complexes $[Cr(CO)_4PP]^+$ (PP = $Ph_2PN(R)PPh_2$, $Ph_2P(R)PPh_2$)

4.1 Introduction

Investigation into the electronic and structural characteristics of catalytic systems of relevance to the selective oligomerisation of ethylene is extremely valuable. As discussed in Chapter 1, vital details of the process are still unknown. Obtaining fundamental knowledge in the hitherto unexplored science of these systems throughout the catalytic cycle, and thereby gaining a deep understanding of their makeup, may assist in the design of more effective and cheaper catalysts. In general, ethylene oligomerisation has long been an important way of producing linear α-olefins which have many important uses, for example as co-monomers in the production of LLDPE, and the manufacture of surfactant precursors and synthetic lubricants.[1]

The first step in conducting a thorough investigation into a catalytic system is the full characterisation of the starting complex, known as the 'pre-catalyst'. The complexes most commonly used in selective oligomerisation are based on chromium, because these catalyst systems have high activity, thermal stability and selectivity; Cr(III) is the most common.[1] However, Cr(I) pre-catalysts have also recently been shown to be active and selective for catalysis.[2] The bis(diphenylphosphine / phosphinoamine) family of ancillary ligands are frequently employed in these complexes, and have been shown to impart high selectivity.[3-5] There is very little research in the literature concerning the role of Cr(I) species in the catalytic cycle.[6] The difficulties in characterizing the active catalytic species involved are the main reason for this. The use of transition-metal catalysts means that paramagnetic species are often involved and these can be difficult to characterize by conventional methods, such as NMR for example.

Due to the fact however that a Cr(I) oxidation state is highly possible during the catalytic cycle, a complete characterisation of these complexes is necessary. Their paramagnetic nature makes Electron Paramagnetic Resonance (EPR) spectroscopy an ideal tool for this investigation.

There is relatively little research in the literature concerning the study of Cr(I) carbonyl complexes *via* EPR (and none utilising ENDOR). The most numerous studies of Cr(I) compounds were investigations of bis-arene 'sandwich' complexes,

which will be discussed further in Chapter 5. Work on Cr(I) carbonyls with phosphine ligands is relatively scarce, particularly in frozen solution. Cummings *et al.*,[7] conducted a spectroscopic and theoretical study of several Cr(I) carbonyls including $[Cr(CO)_4(dppe)]^+$ (dppe = bis(diphenylphosphinoethane). They recorded the frozen solution spectrum of this complex, and a nearly axial spectrum was observed (g_1 = 2.09, g_2 = 2.08, g_3 = 1.988). The $g\perp$ region was poorly resolved but superhyperfine couplings were extracted as $A\perp$ = 70.0 MHz and $A\parallel$ = 68.4 MHz. No ^{53}Cr hyperfine peaks were visible.[7] Rieger and Rieger conducted a detailed investigation into the photochemical reactions of Cr(I) tricarbonyls,[8] while Bond and co-workers reported isotropic spectra for a variety of phosphine and phosphite derivatives of $[Cr(CO)_6]^+$ [9, 10] and Castellani *et al.*,[11] characterised a series of Cr(I) dicarbonyls $[Cr(CO)_2L(\eta\text{-}C_6Me_6]^+$. However, based on a detailed review of the literature, the work described in this thesis involves the first in-depth characterisation *via* EPR and ENDOR of a series of Cr(I) tetracarbonyl complexes bearing bidentate phosphine ligands.

The first step in this investigation involves the characterisation of the 'pre-catalyst' species. Detailed analysis of their electronic properties, including the formal electron configuration of the metal, degree of delocalisation of electron density on to the ligands, and extent of back-bonding, can be obtained *via* EPR spectroscopy. ENDOR provides additional information on the nuclei interacting with the unpaired electron. Of particular interest is the orientation of the phenyl rings in the complex. The catalytic selectivity is believed to be influenced by their relative orientation to the chromium centre.[12-15] The most sensitive probe for structure determination is the electron nuclear hyperfine tensor.[16] Its anisotropic component provides information on the distance and orientation of interacting spins with respect to the magnetic field. By careful study of the proton tensors originating from these rings, this information may be extracted so that correlations with catalytic trends may be investigated.

4.2 Experimental Details.

Full details of the synthetic procedures used to prepare the Cr(I) complexes were given in Chapter 3. The general conformation of the $[Cr(CO)_4PP]^+$ complexes studied is shown in Scheme 4.1.

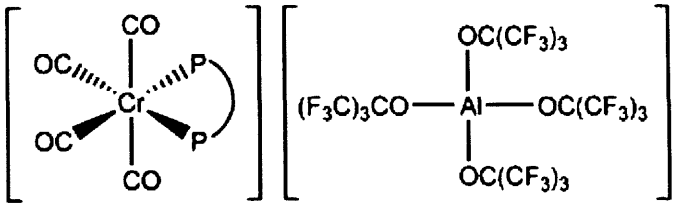

Scheme 4.1: General structure and conformation of the $[Cr(CO)_4PP]^+$ complexes investigated.

The 1,3-bis(diphenylphosphine) (hereafter abbreviated to 'PCP') and 1,3-bis(diphenylphosphino-amine) (hereafter abbreviated to 'PNP') ligands used in the synthesis of these $[Cr(CO)_4PP]^+$ complexes were shown earlier in Chapter 3, Scheme 3.1.

Syntheses of chromium(0)[6] and chromium(I)[2] complexes of these ligands (**1a-g** and **2a-g** for Cr(0) and Cr(I) respectively) followed published procedures and are described in Chapter 3. All EPR / ENDOR sample preparations were carried out under an inert atmosphere, either in a glove box or on the Schlenk line.

For X-band CW-EPR and ENDOR sample preparation, each complex **2a-g** (6 mg) was placed in the Schlenk-adapted EPR tube and dissolved in 200 µl dry dichloromethane / toluene. For pulsed EPR and ENDOR measurements, a similar method was followed except a rubber septum was used to seal the tube, to enable insertion into the spectrometer sample holder. For Q-band CW-EPR and ENDOR, and general room temperature measurements, the complex was dissolved in the solvent in a vial and then transferred to the sample tube. This was sealed with wax/ grease in the glove box.

The resulting solutions were deep blue or purple in colour for all $[Cr(CO)_4$**a-g**$]^+$ complexes. A frozen solution was produced by immediately placing the tube in liquid nitrogen once the sample was prepared. Spectra were recorded at 140, 185 and 298 K for X-band CW-EPR measurements, or 10 K for Q-band CW-EPR/ ENDOR, pulsed EPR/ ENDOR measurements.

4.3 Results and Discussion

4.3.1 Continuous-wave EPR

The CW-EPR spectra (experimental and simulated) for $[Cr(CO)_4\mathbf{b}]^+$ (as a representative example), along with the angular selectivity of the EPR transitions, is shown below in Figure 4.1.

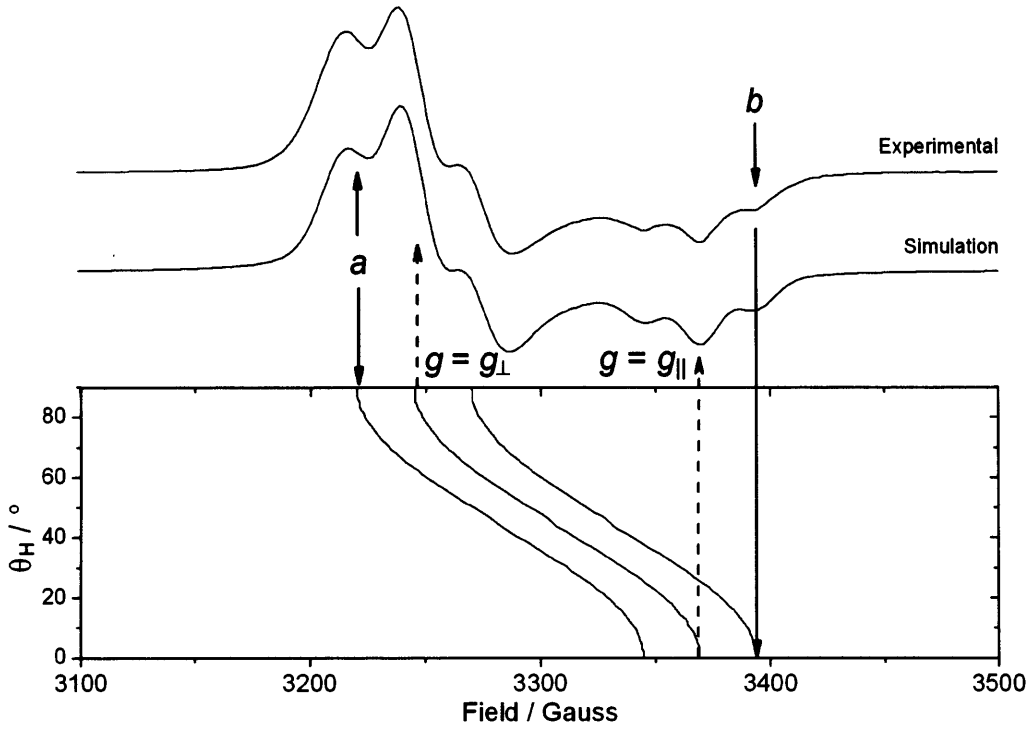

Figure 4.1; Experimental and simulated CW-EPR spectra (140K) of $[Cr(CO)_4\mathbf{b}]^+$ recorded in dichloromethane/toluene at a microwave frequency of 9.371 GHz (X-band). The angular dependency curves calculated for the Cr(I) ***g*** tensor and the ^{31}P ***A*** tensor are shown in the lower trace.

The experimental spectrum shown in Figure 4.1 can be approximately described as possessing an axial ***g*** matrix ($g_{xx} = g_{yy} \neq g_{zz}$) with well resolved superhyperfine structure in both the perpendicular ($g_{xx} = g_{yy}$) and parallel (g_{zz}) components. The corresponding EPR simulation is also displayed in Figure 4.1 and the resulting spin Hamiltonian parameters are listed in Table 1. Each component of the ***g*** matrix is split into an unmistakable 1:2:1 triplet pattern arising from the superhyperfine interaction with two equivalent ^{31}P nuclei ($I = ½$) in the PCP based ligand **b**. Since the natural abundance of ^{53}Cr ($I = 3/2$) is only 9.5%, coupled with the large linewidths associated with the ^{31}P hyperfine pattern (see Appendix for linewidths associated with CW-EPR simulations), no anisotropic hyperfine interaction associated with ^{53}Cr was detected in the frozen solution spectrum.

The EPR spin Hamiltonian parameters (***g*** and ***A***) for any paramagnetic complex will depend on the co-ordination state and symmetry of the metal centre. For the six co-ordinate $[Cr(CO)_4\mathbf{b}]^+$ complex, the strong ligand fields are expected to cause a large splitting between the t_{2g} orbitals and the e_g orbitals resulting in a low spin (LS) d^5 state (S = ½) (see Scheme 4.2). High spin (HS) or intermediate spin d^5 states (S = $^5/_2$ or $^3/_2$) could only occur in the presence of a weak ligand field, which is not expected in the $[Cr(CO)_4\mathbf{b}]^+$ case.

Additionally, the LS Cr(I) complex could exist in two possible electronic ground states: a $(d_{xz},d_{yz})^4(d_{xy})^1$ or $(d_{xy})^2(d_{xz},d_{yz})^3$ configuration. Simple crystal field arguments would suggest that the expected ground state for the $[Cr(CO)_4\mathbf{b}]^+$ complex is $(d_{xz},d_{yz})^4(d_{xy})^1$.[7, 8, 17] It is proposed that π-back donation to CO helps to stabilize the d_{xz} and d_{yz} orbitals relative to the d_{xy} based HOMO. The stabilisations of d_{xz} and d_{yz} should be identical (each interacts with 3 CO ligands) leading to $g_{xx} = g_{yy} > g_e$,[7] and this is borne out by the observed ***g*** matrix.

For a SOMO where the metal contribution is primarily d_{xy}, the components of the ***g*** matrix are given by the following equations[7, 8, 17, 18]:

$$g_{xx} - g_e = 2\lambda \sum_{m\neq 0} \frac{(c_{xy})^2 (c^m_{xz})^2}{E_0 - E_m} \tag{4.1a}$$

$$g_{yy} - g_e = 2\lambda \sum_{m\neq 0} \frac{(c_{xy})^2 (c^m_{yz})^2}{E_0 - E_m} \tag{4.1b}$$

$$g_{zz} - g_e = 8\lambda \sum_{m\neq 0} \frac{(c_{xy})^2 (c^m_{x^2-y^2})^2}{E_0 - E_m} \tag{4.1c}$$

In these equations g_e is the free electron g value, λ is the Cr^+ spin-orbit coupling constant for the free ion (-185 cm^{-1}),[19] c^m_{xy} is the LCAO coefficient, E_0 is the energy of the SOMO and m sums over the other MOs with energies E_m. Spin-orbit coupling mixes in d_{xz}, d_{yz} and $d_{x^2-y^2}$ character, but for a low spin d^5 system, d_{xz} and d_{yz} will lie just below the SOMO, while $d_{x^2-y^2}$ will be empty and much higher in energy. As a result the above equations predict that the g_{xx} and g_{yy} values should be significantly higher than g_e while g_{zz} should be slightly less than g_e. These trends are indeed observed experimentally, with $g_\perp$ ($g_{xx} = g_{yy}$) = 2.063 and $g_e > g_\parallel$ (g_{zz}) = 1.987 (Table 4.1), agreeing with a d_{xy} ground state of $[Cr(CO)_4\mathbf{b}]^+$.

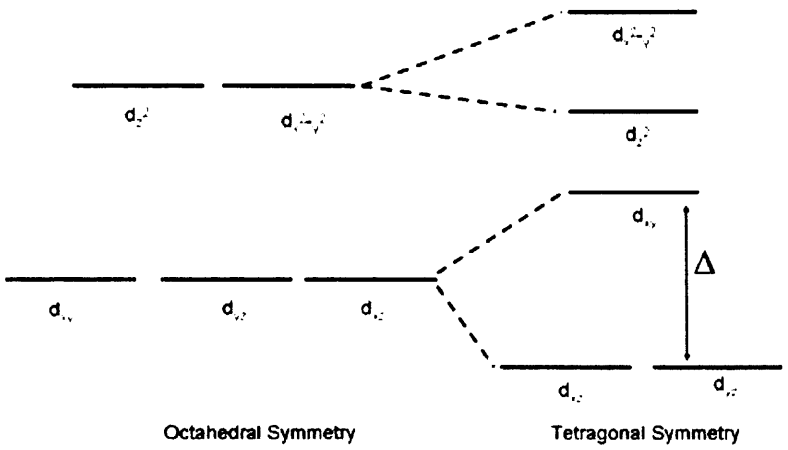

Scheme 4.2: Orbital arrangement in LS d^5 systems.

The CW-EPR experimental and simulated spectra of $[Cr(CO)_4\mathbf{f}]^+$ are shown in Figure 4.2. For brevity, the simulated spectra of all remaining complexes are displayed in the Appendix; however, the complete series of experimental spectra are shown in Figure 4.3. In all cases axial ***g*** matrices ($g_\perp > g_e > g_\parallel$) are observed and the corresponding spin Hamiltonian parameters for each complex, extracted from the simulations, are listed in Table 4.1.

Similar to the above discussion on $[Cr(CO)_4\mathbf{b}]^+$, it appears that the ground state in all of these complexes can be described as d_{xy}, as all spectra display $g_\perp > g_e > g_\parallel$. These spin Hamiltonian parameters agree with those extracted by Cummings *et al.*,[7] on $[Cr(CO)_4(dppe)]^+$ (i.e., **2a**). They observed a nearly axial frozen-solution spectrum, with the $g\perp$ region poorly resolved ($g_1 = 2.09$, $g_2 = 2.08$, $g_3 = 1.988$ and ${}^{P}A\perp = 70$ MHz and ${}^{P}A_\parallel = 68.4$ MHz). These are very similar to the parameters listed in Table 1 from **2a**, namely $g\perp = 2.083$, $g_\parallel = 1.989$, and ${}^{P}A\perp = 72$ MHz, ${}^{P}A_\parallel = 68.1$ MHz.

From this initial analysis of the spectra, similarities between them have shown that all the complexes possess the same electronic ground state. The resolution of the spectra however, and indeed the spin Hamiltonian values, are found to be highly dependent on the ligand type (Table 4.1).

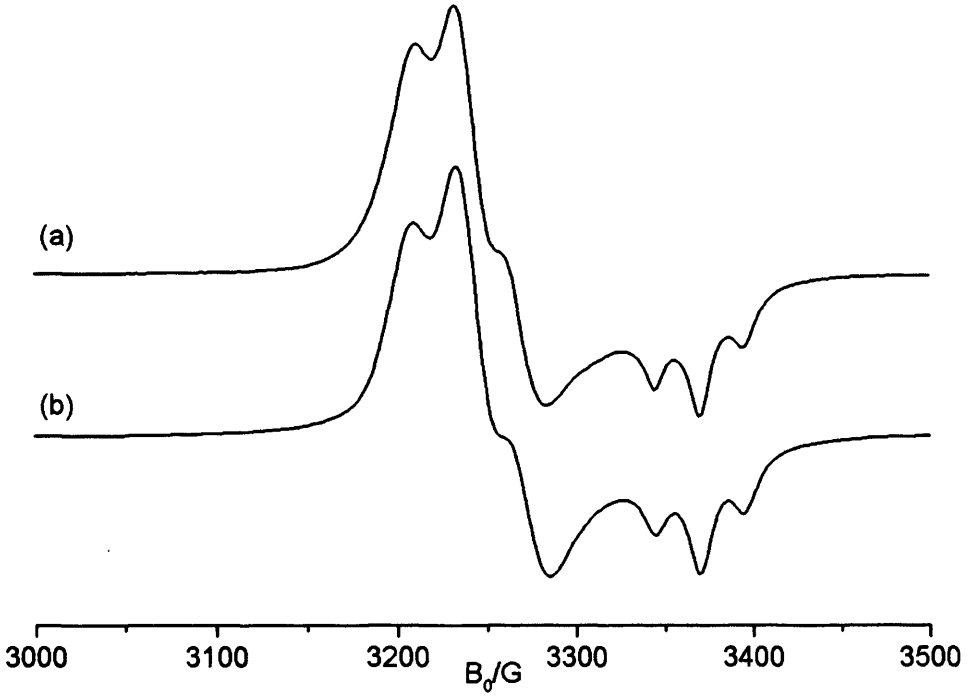

Figure 4.2: Experimental (a) and simulated (b) CW-EPR spectra (140K) of $[Cr(CO)_4(Ph_2PN(iBu)PPh_2)]^+$ (**2f**) recorded in dichloromethane/toluene at a microwave frequency of 9.379 GHz. For simulation parameters refer to Table 1.

The difference in g values (defined as $\Delta g = g_\perp - g_\parallel$), for example, is greatest for $[Cr(CO)_4\mathbf{e}]^+$ and smallest for $[Cr(CO)_4\mathbf{b}]^+$ (see Figure 4.3 and Table 1).

Table 4.1: Spin Hamiltonian parameters obtained by simulation for the compounds $[Cr(CO)_4\mathbf{a\text{-}g}]^+$.

Complex	Ligand	$g_\perp$	$g_\parallel$	$^PA_\perp$ /		$^PA_\parallel$ /		a_{iso} /		% *s**
				G	MHz	G	MHz	G	MHz	
2e	PNP	2.089	1.983	29.0	84.8	24.0	66.6	27.3	78.7	0.573
2c	PCCP	2.084	1.989	25.5	74.4	25.0	69.6	25.3	72.8	0.532
2a	PCCP	2.083	1.989	24.8	72.3	24.5	68.2	24.8	70.9	0.518
2d	PNP	2.077	1.985	27.7	80.5	25.5	70.8	27.0	77.3	0.534
2g	PNP	2.072	1.988	27.0	78.3	25.5	71.0	26.5	75.9	0.556
2f	PNP	2.068	1.988	27.0	78.1	25.5	71.0	26.5	75.8	0.556
2b	PCCCP	2.063	1.987	24.9	72.0	24.5	68.1	24.7	70.7	0.520

* % s = percentage s orbital contribution to the hyperfine coupling (Fermi contact term).

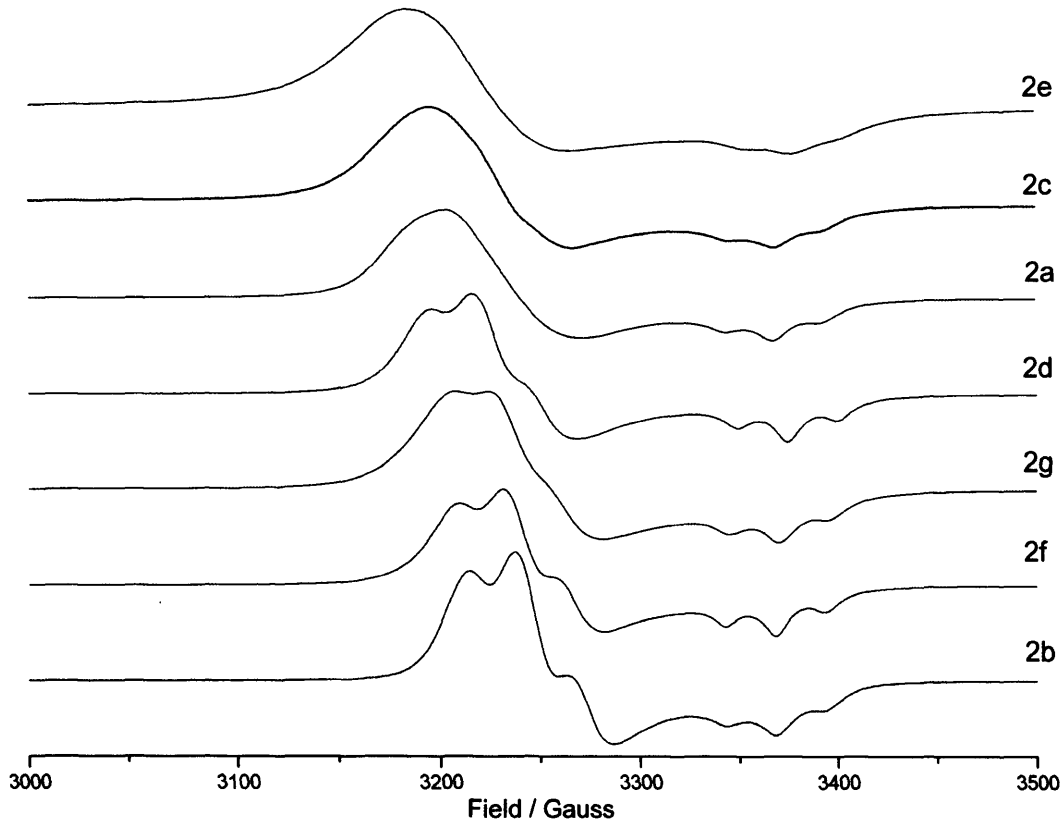

Figure 4.3;:CW-EPR spectra (140K) of $[Cr(CO)_4$**a-g**$]^+$ recorded in dichloromethane/toluene. The spin Hamiltonian parameters obtained by simulation are shown in Table 4.1.

As discussed in Chapter 2 (and above), the magnitude of Δg (i.e. the deviation from the free-spin value) relates to the molecular orbital coefficients of the metal centre. Anisotropy in g arises due to the interaction, *via* the spin-orbit coupling mechanism, between spin- and orbital-angular momenta. The admixing of the ground state with certain excited states enables residual orbital angular momentum (l) to appear in the ground state. The extent of admixing is dependent on, among other factors, which excited-state orbital contributes to the ground state and also the energy difference between them. Clearly, knowledge of both of these enables the orbital and electronic configurations respectively of the complex to be estimated.

In the complexes described above, $[Cr(CO)_4PP]^+$, each displays a different value of Δg, but the same trend in the anisotropy of g values ($g_\perp > g_e > g_\parallel$). Therefore the differences in g must relate to the energy difference between the xy- and z-based orbitals, i.e. the extent of tetragonal distortion from octahedral symmetry, rather than a different molecular orbital arrangement. The only change from complex to complex is the identity of the bis(diphenylphosphine) ligand. Hence each of these ligands imparts a

slightly different degree of tetragonal distortion, *via* the MO coefficients, to the Cr(I) complex.

Despite these clear differences in the Δg shift, no obvious correlation emerges between the observed spectral shifts and the ligand type (i.e., PNP or PCP based ligands). Some correlations were however identified with respect to the ^{P}A hyperfine values. The superhyperfine ^{31}P couplings are clearly visible as a 1:2:1 triplet in each component ($g\perp$ and $g\parallel$) of the spectrum. Simulation of the data enabled extraction of the nuclear hyperfine matrix ($^{P}\boldsymbol{A}$) and calculation of the isotropic contribution to this coupling (a_{iso}) (see Table 1). As discussed in Chapter 2, hyperfine interactions are composed of two parts. One is the anisotropic component, which is a through-space interaction that is a function of both the electron-nuclear distance and the spins' mutual orientation with respect to the external field. Therefore the magnitude of the interaction differs depending on the orientation of the nucleus and the values along the x,y,z axes (the 'principal values') are observed at turning points in the powder pattern. The second component is isotropic, i.e., the same magnitude in all directions. It occurs *via* a direct contact interaction or alternatively a spin polarisation mechanism, where an excess of one particular spin orientation is found at the nucleus, i.e. spin density which is isotropic in nature due to the spherical symmetry of the *s* orbital.

In all $[Cr(CO)_4PP]^+$ cases here, the dominant contribution to the ^{31}P hyperfine interaction is the isotropic component, i.e., the coupling is predominantly a direct / through-bond interaction rather than through-space. Furthermore, the a_{iso} values are larger for the PNP type ligands compared to the PCP ligands. These isotropic ^{31}P hyperfine couplings arise from an interaction between the magnetic moments of the electron and nucleus. Spin density is transferred from the SOMO *via* spin polarisation of inner shell ^{31}P orbitals to the nucleus. The magnitude of the coupling therefore provides information on the *s*-character of the SOMO, as only *s* orbitals have a non-zero probability of the electron being present at the position of the nucleus. These results indicate that the electronic ^{31}P 3*s* character in the SOMO (d_{xy}) is higher for the PNP type ligands (**2e** > **2d** > **2g** ~ **2f**) compared to the PCP type ligands (**2c** > **2a** ~ **2b**). It is possible that the σ-bonding character (and hence the 3*s* character in the SOMO) of the phosphine increases due to increased electron density transferral from the more electron-rich N atom, with its lone pair, than the alkyl bridges.

The percentage *s* character in Table 1 refers to the extent of spin population in an *s* orbital. The theoretical isotropic hyperfine coupling for a ^{31}P nucleus is 3640 G.[19]

Hence the coupling values obtained for the $[Cr(CO)_4PP]^+$ complexes show that there is a much higher probability for the spin density to be found on the metal, i.e., there is a much higher contribution to the SOMO from metal-based orbitals (primarily d_{xy}) than ^{31}P-based.

Q-band (34.1 GHz) CW-EPR was also performed on $[Cr(CO)_4(Ph_2PN(iPr)PPh_2)]^+$ (**2g**). At higher frequencies there is an increase in orientation selectivity of the spectrum, i.e., the components of the ***g*** tensor of an anisotropic system occur at more widely separated field magnitudes (see Appendix). This increase in spectral resolution can be extremely informative if, for instance, the *g* anisotropy is small at X-band. The hyperfine coupling is not field-dependent, but because it is superimposed on the Zeeman interactions, it may suffer the same ambiguity at X-band. The experimental and simulated spectra of **2g** recorded at Q-band are shown in Figure 4.4.

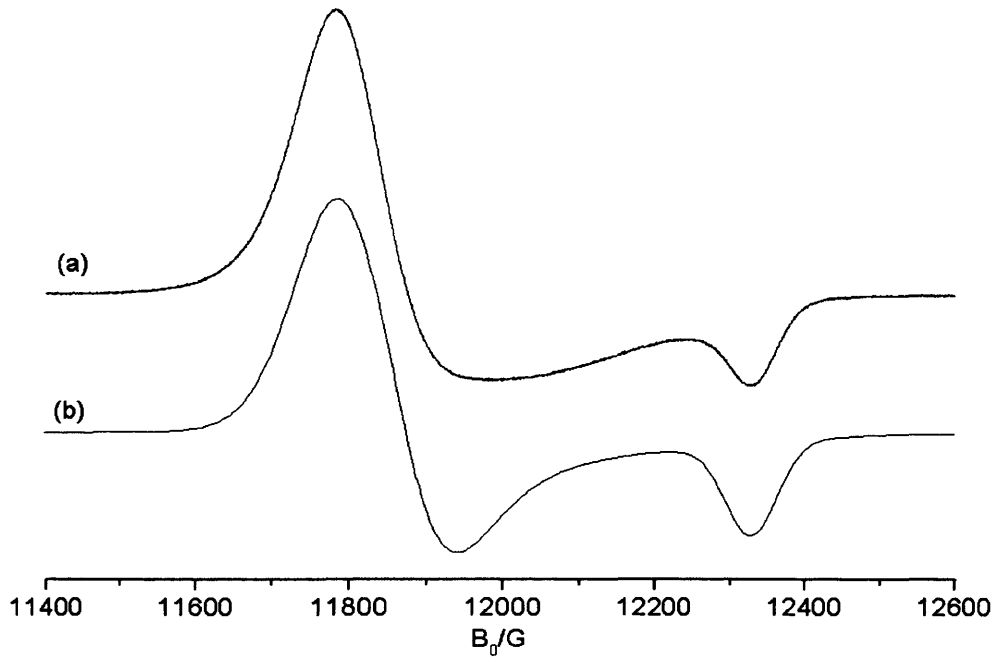

Figure 4.4: Experimental (a) and simulated (b) CW-EPR spectra (10K) of $[Cr(CO)_4(Ph_2PN(iPr)PPh_2)]^+$ (**2g**) recorded in dichloromethane/toluene at a microwave frequency of 34.113 GHz.

The components of the ***g*** tensor are indeed more well-resolved than those observed at X-band. The spin Hamiltonian parameters obtained by simulation of the data were: $g_\perp = 2.072$, $g_\parallel = 1.988$. These *g* values are analogous to those observed at X-band frequency. No ^{31}P superhyperfine coupling is visible in the spectrum. This is probably due to the considerable line-broadening effects. At higher fields, linearly field-dependent *g*-strain effects can determine the linewidth; the spread in principal

g values and corresponding inhomogenous line broadening effectively increases.[20] The hyperfine coupling will be the same as at X-band, so it is probably hidden by the broad line widths (of approximately 55 G in the parallel component and 130 G in the perpendicular component). Therefore although recording spectra at higher frequencies may be beneficial in some cases, there are many instances, such as this one, when the increase in inhomogeneous line broadening actually makes the resulting spectrum less informative. A variable temperature study was then performed on each complex. The resulting spectra for $[Cr(CO)_4\mathbf{b}]^+$, as a representative example, are shown in Figure 4.5.

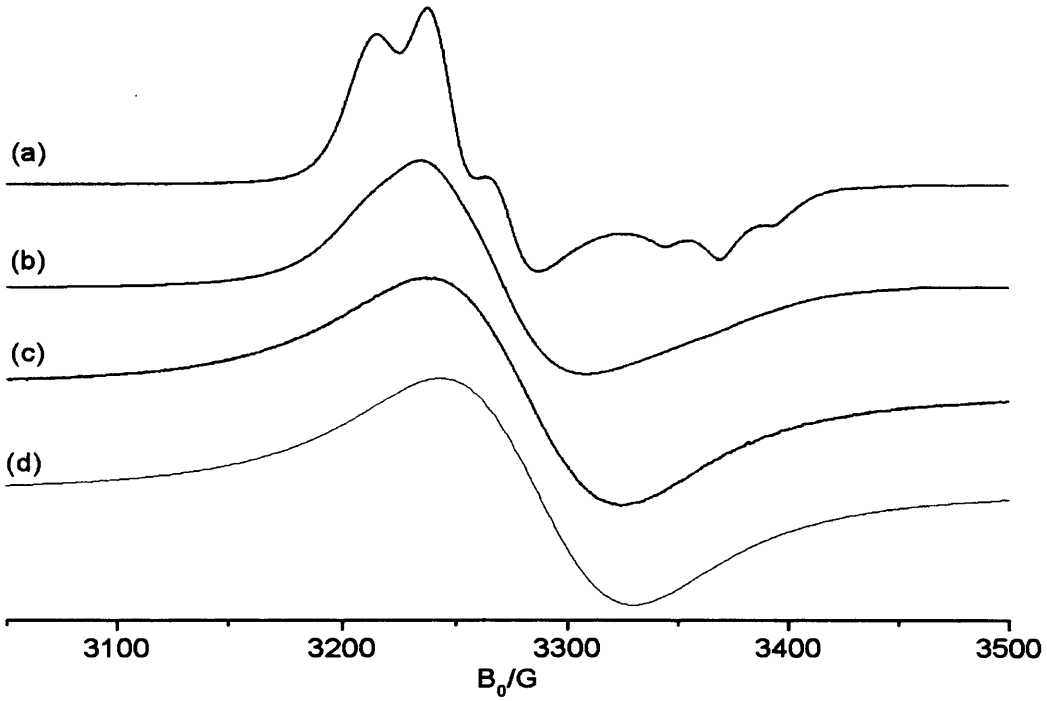

Figure 4.5: Experimental CW-EPR spectra of $[Cr(CO)_4(dppp)]^+$ (**2b**) recorded at (a) 140 K, (b) 185 K and (c) 298 K and simulated spectrum (d) of 298 K spectrum. Recorded in dichloromethane/toluene.

At 185 K and higher, the distinct anisotropy of the signal disappears and a broad featureless peak is observed. This is common for a transition-metal based complex; the short spin-lattice relaxation time broadens the signal. The room temperature spectrum was simulated and the isotropic g-value was extracted as g_{iso} = 2.04. This is, as expected, the average of the parameters extracted from the frozen solution ($g_\perp$ = 2.063 and $g_\parallel$ = 1.987). No hyperfine coupling could be detected due to the broad linewidth of the peak (70 G). All other systems displayed similar 185 K and room temperature spectra, i.e. a broad peak centred on the average g value of that complex.

4.3.2 Pulsed EPR

In order to confirm the data obtained by continuous-wave methods, and to provide a basis for later comparison with the activated species (see Chapter 6), pulsed EPR (field-swept echo detected (FSED)) spectra, in addition to 2- and 3-pulse electron spin echo envelope modulation (ESEEM) spectra, were recorded for $[Cr(CO)_4(Ph_2P(CH_2)_3PPh_2)]^+$ **(2b)** and $[Cr(CO)_4(Ph_2PN(iPr)PPh_2)]^+$ **(2g)**. A more detailed explanation of the theoretical background to the experiments, including the vector model of spins, is given in Section A.4 of the Appendix.

The FSED EPR spectrum of $[Cr(CO)_4\mathbf{b}]^+$ is shown in Figure 4.6. In the FSED experiment the echo amplitude is recorded (in absorption mode) as a function of magnetic field magnitude. Anisotropy of g, and hence the net magnetisation and corresponding spin echo intensity, is reflected in the spectral profile. The spin Hamiltonian parameters extracted from the simulation are similar to those obtained in the CW spectra, i.e., an axial $\boldsymbol{g}$ matrix with well-defined superhyperfine coupling to two equivalent ^{31}P nuclei. The values extracted for the principal components of the $\boldsymbol{g}$ and hyperfine tensors ($g_\perp$ = 2.062, $g_\parallel$ = 1.987, $^{P}A_\perp$ = 72.0 MHz, $^{P}A_\parallel$ = 68.1 MHz) agree extremely well with those extracted from CW-methods (see Table 4.1).

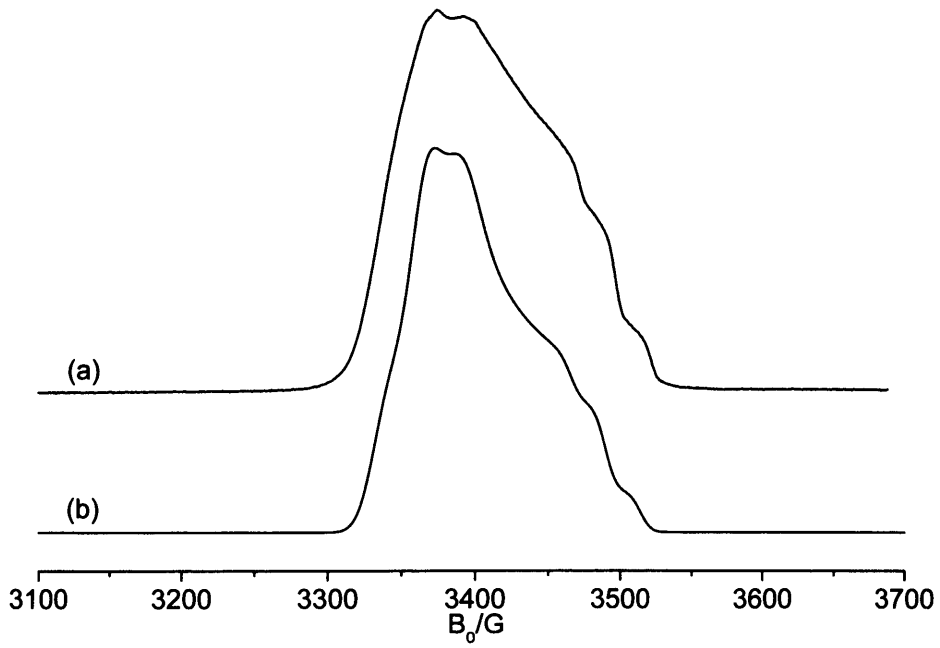

Figure 4.6: Experimental (a) and simulated (b) FSED spectra (10 K) of $[Cr(CO)_4\mathbf{b}]^+$ recorded in dichloromethane/toluene. Spin Hamiltonian parameters extracted from simulation: $g_\perp$ = 2.062, $g_\parallel$ = 1.987, $^{P}A_\perp$ = 72.0 MHz (24.9 G), $^{P}A_\parallel$ = 68.1 MHz (24.5 G).

ESEEM measurements were then conducted to obtain information about relaxation times and interacting nuclei present. The ESEEM experiment also utilises the spin echo phenomenon, but here the echo intensity is measured as a function of the time separating the pulses that give rise to the echo. ESEEM provides information on spin-spin relaxation time T_2, but also on nuclear frequencies of interacting nuclei. The echo height oscillates periodically, displaying nuclear modulations due to the interference between pairs of excited EPR transitions. It is therefore an ideal technique for probing the identity and position of nuclear spins in the electron spin environment.

The raw ESEEM data is shown in Figure 4.7. This was then processed by subtraction of the spin echo decay and Fourier transformation of the oscillations to yield the nuclear frequencies (Figure 4.8). The spin-spin relaxation times T_2 (the time taken for the transverse component of the macroscopic magnetization to decay) were extracted from the raw data *via* a stretched exponential decay fitting, and calculated as 1781 ns (3373 G) and 5570 ns (3491 G). This field-dependency of T_2 is commonly observed for transition metal complexes.

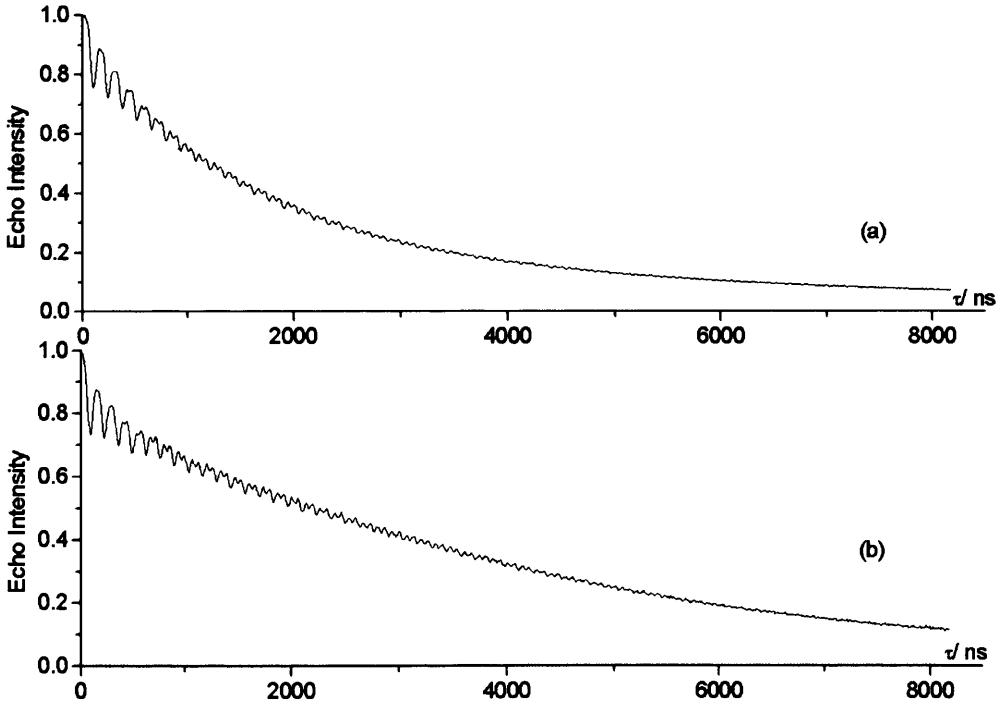

Figure 4.7: T_2 measurements (10 K) of $[Cr(CO)_4(dppp)]^+$ **(2b)** recorded at (a) 3373 G (perpendicular field position, $B_\perp$) and (b) 3491 G (parallel field position, $B_\parallel$). Recorded in dichloromethane/toluene.

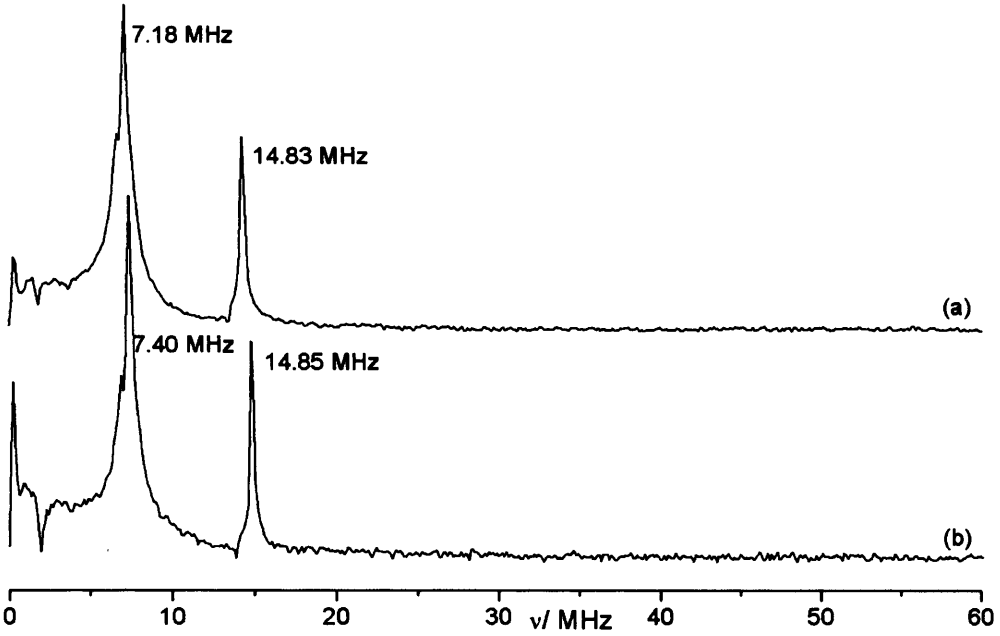

Figure 4.8: 3-pulse (3P) ESEEM (10K) recorded at (a) 3373 G ($B\perp$) and (b) 3491 G ($B\parallel$) of $[Cr(CO)_4(dppp)]^+$ **(2b)**. Recorded in dichloromethane/toluene.

Fourier-transformed three-pulse (3P) ESEEM data (Figure 4.8) display a peak at the nuclear Larmor frequency of each particular nucleus visible in the system. The Larmor frequency (ν_N) is field-dependent and hence will be slightly different when recorded at the parallel and perpendicular field positions. It is calculated as:

$$\nu_N = \frac{|g_N|\mu_N B_0}{h} \tag{4.3}$$

where μ_N is nuclear magneton (a constant) and g_N the nuclear g factor, which is particular to each nucleus (and each isotope), and B_0 is the magnetic field in Tesla. The data above confirm the presence of ^1H (14.83 and 14.85 MHz at $B\perp$ and $B\parallel$ respectively). There are also peaks at 7.18 ($B\perp$) and 7.40 MHz ($B\parallel$) which likely indicate the presence of ^{31}P as expected.

A saturation inversion recovery experiment was performed to determine the spin-lattice relaxation time T_1 and the corresponding data are shown in Figure 4.9. T_1 is a measure of the time taken for the longitudinal component of the macroscopic magnetisation M_Z to return to its equilibrium state after a perturbation (i.e., a pulse of radiation), *via* dissipation of the energy acquired through phonons to the lattice.

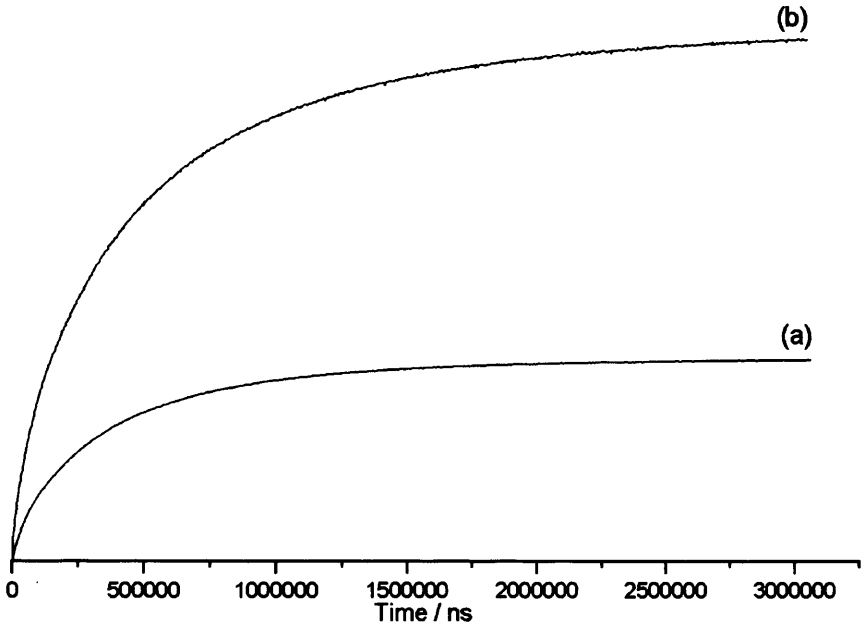

Figure 4.9: T_1 measurements (10 K) of $[Cr(CO)_4(dppp)]^+$ **(2b)** recorded at (a) 3373 G ($B\perp$) and (b) 3491 G ($B_\parallel$). Recorded in dichloromethane/toluene.

The relaxation times were calculated *via* a bi-exponential decay function for each field position. They were determined as (at 3373 G) τ_1 = 550640 ns, τ_2 = 137667 ns, and (at 3491 G) τ_1 = 714141 ns, τ_2 = 146435 ns. The total spin-lattice relaxation is composed of more than one contribution, due to spin diffusion and other effects, as observed by the two distinct times determined in both experiments. These relatively short relaxation times are typical for transition-metal ions, which at room temperature can range from 10^{-6} to 10^{-12} s.[21]

If anisotropy is resolved in the EPR spectrum, as is the case here, relaxation times measured at different field positions can be different. The orientation-dependence of the longitudinal relaxation occurs because of a number of factors. The predominant mechanism of spin-lattice relaxation occurs *via* vibrational modes of the molecule, which have preferential directions with respect to the molecular axes. Along certain directions the vibrations modulate the spin-orbit coupling, and hence the *g* anisotropy, to a larger extent.[22] Therefore the spin-lattice relaxation time will differ depending on which of the vibrational modes is providing the mechanism for relaxation. Additionally, rotational diffusion also contributes to spin-lattice relaxation, and is anisotropic for non-spherical moelcules.[22]

Pulsed measurements were also performed on $[Cr(CO)_4(Ph_2PN(iPr)PPh_2)]^+$ **(2g)**. The FSED EPR spectrum is shown in Figure 4.10.

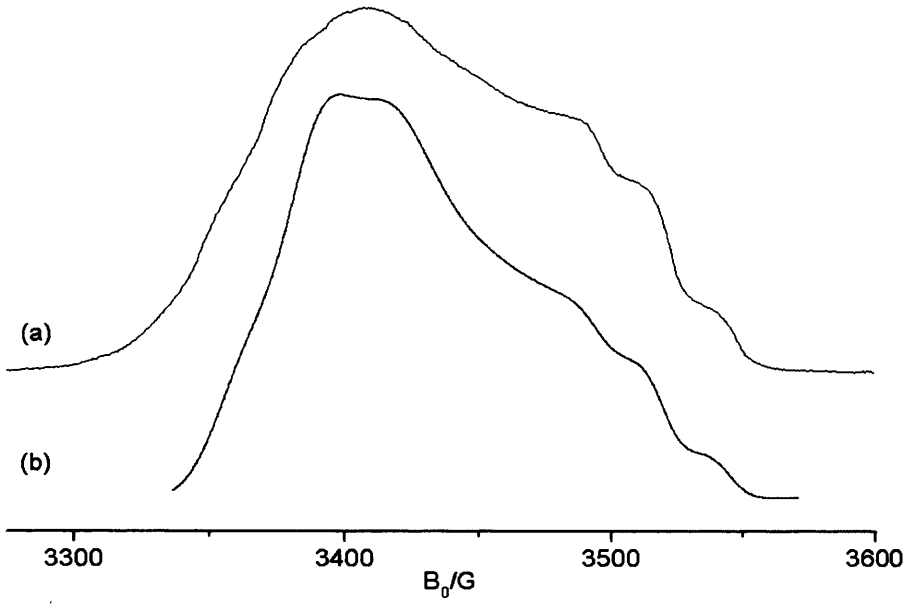

Figure 4.10: Experimental (a) and simulated (b) FSED spectra (10K) of $[Cr(CO)_4(Ph_2PN(iPr)PPh_2)]^+$ (**2g**), recorded in dichloromethane/toluene. Spin Hamiltonian parameters extracted from simulation: $g_\perp = 2.068$, $g_\parallel = 1.99$, $^{P}A_\perp = 78.3$ MHz (27.1 G), $^{P}A_\parallel =$ 71 MHz (25.5 G).

Two- and three-pulse ESEEM measurements were also performed. The Fourier-transformed frequency plot of the 3P ESEEM data is shown in Figure 4.11, displaying the nuclear frequencies.

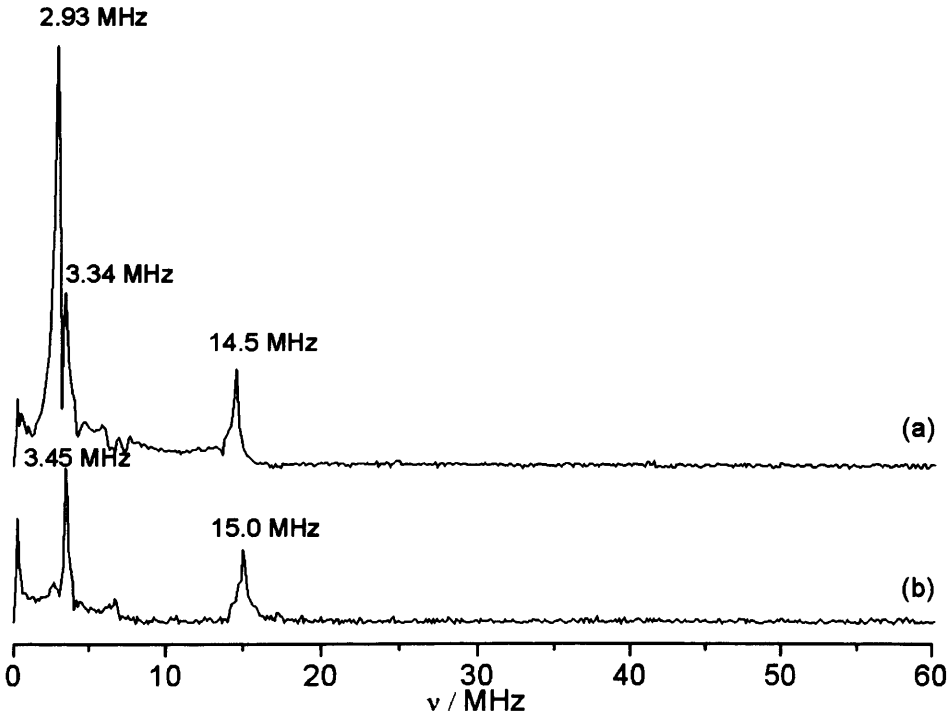

Figure 4.11: 3P ESEEM (10K) recorded at (a) 3410 G (perpendicular field position) and (b) 3530 G (parallel field position) of $[Cr(CO)_4(Ph_2PN(iPr)PPh_2)]^+$ (**2g**). Recorded in dichloromethane/toluene.

The data above confirm the presence of ^{1}H nuclei (14.5 and 15.0 MHz at $B\perp$ and $B\parallel$ respectively). There are also peaks at 2.93 MHz (and 3.34 MHz) at $B\perp$ and 3.45 MHz at $B\parallel$. These may correspond to ^{27}Al, present from the counterion (the calculated frequencies for ^{27}Al however are 3.79 and 3.92 MHz). ^{27}Al has been detected in ESEEM spectra before;[23-25] sharp, intense peaks such as these are a feature of dipolar matrix interactions,[23] suggesting the nucleus reaponsible for these peaks is situated relatively far from the electron, as nuclei in the counterion would be. However, in all these studies the peaks occured at exactly the nuclear Larmor frequency for ^{27}Al,[23-25] whereas the peaks detected in this study are approximately 0.45 MHz below the calculated Larmor frequency. Surprisingly, there were no peaks at 7.18 ($B\perp$) and 7.40 MHz ($B\parallel$) in Figure 4.11, unlike the situation for $[Cr(CO)_4\mathbf{b}]^+$ (Figure 4.8).

Two-pulse ESEEM data displays both the fundamental nuclear Larmor frequency of the nucleus present (ν_N) and also its first harmonic ($2\nu_N$). Direct comparison of both 2P and 3P data at the same field position can be extremely informative, as it can enable unequivocal identification of which peaks correspond to which nuclei. For example, if two peaks are very close in frequency in the 3P spectrum, and it is difficult to distinguish between them, then recording the 2P may help as their respective harmonic peaks will be spaced further apart. Therefore it is informative to record both types of measurement and compare them.

The data shown in Figure 4.12 confirm the presence of ^{1}H without doubt, as both the fundamental and first harmonic of ^{1}H are present. There are also peaks at 2.8 MHz ($B\perp$) and 3.5 MHz ($B\parallel$). However, the first harmonic of these appears as a trough in the spectrum.

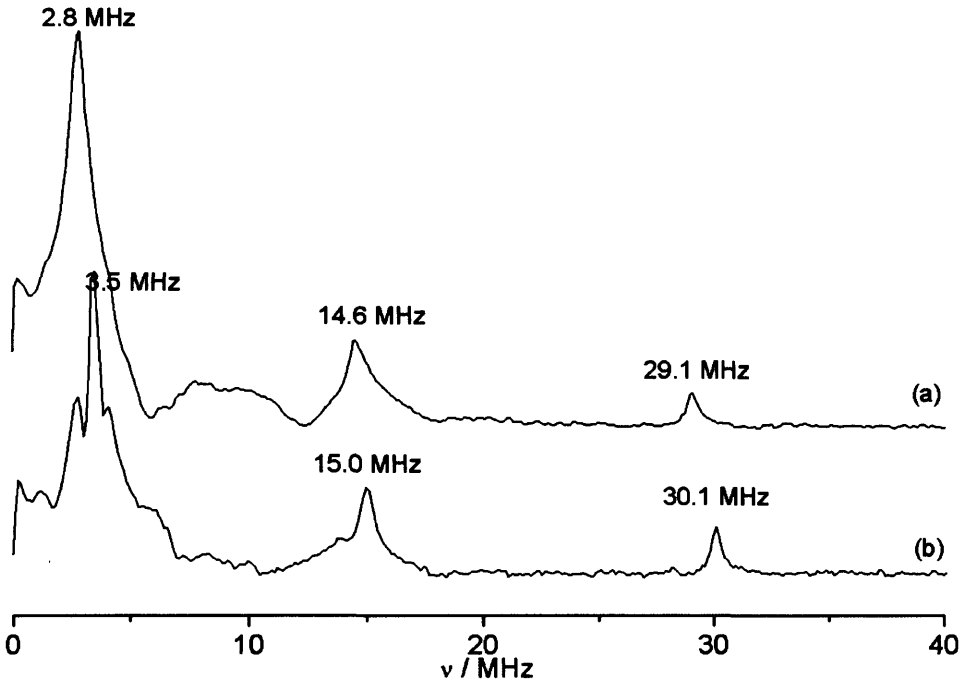

Figure 4.12: 2P ESEEM (10K) recorded at (a) 3410 G (perpendicular field position) and (b) 3530 G (parallel field position) of $[Cr(CO)_4(Ph_2PN(iPr)PPh_2)]^+$ (**2g**). Recorded in dichloromethane/toluene.

4.3.3 Continuous-wave ENDOR

To probe the structure of the model 'pre-catalyst' systems further, Electron Nuclear Double Resonance (ENDOR) measurements were performed. ^1H couplings were not visible in the CW-EPR spectra, due to the large linewidths associated with the system and the small expected hyperfine couplings.

^1H, ^{14}N and ^{31}P CW-ENDOR spectra were recorded for all complexes in frozen (deuterated) dichloromethane/toluene at 10 K. Analysis of these ENDOR spectra was based on the observed orientational selection in the EPR spectra. It should be recalled that the powder EPR spectra (shown in Figure 4.1) reflect a statistical average of all molecular orientations of the complex with respect to the external field (B_0). If the $\boldsymbol{g}$ and $\boldsymbol{A}$ matrices are known, one can then easily associate distinct sets of molecular orientations with a given resonant field value. For example when the applied field (B_0) = $B_\perp$ the specific orientations corresponding to the xy molecular direction ($g = g_\perp$) are chosen. Similarily when $B_0 = B_{||}$, specific orientations corresponding to the z molecular direction ($g = g_{||}$) are selected. These two resonant field positions (sometimes referred to as 'single-crystal like' positions in the powder pattern[16, 26-28]) are indicated in Figure 4.1. This set of molecular orientations can then be selected at fixed magnetic field settings for nuclear

resonance in the ENDOR experiment. The result is a hyperfine spectrum that contains only one part of the powder pattern, or at least very few molecular orientations.

Whilst the current $[Cr(CO)_4$**a-g**$]^+$ complexes are dominated by the g anisotropy at X-band, the ^{P}A coupling is also appreciable at this frequency (Table 4.1) and this complicates the choice of field position for the ENDOR measurements. In this case, when the applied field (B_0) = $B_\perp$ at least two sets of specific orientations are selected (as seen in the angular dependency plot for the Cr $\boldsymbol{g}$ tensor combined with the ^{P}A superhyperfine lines in the lower trace of Figure 4.1). However, when the ENDOR spectra are recorded at the field position labeled ***a*** in Figure 4.1, only a single orientation (corresponding to $\theta = 90°$) is selected: effectively a field position analogous to $g = g_\perp$. Similarly when the ENDOR spectra are recorded at the field position labeled ***b*** in Figure 4.1, only a single orientation (corresponding to $\theta = 0°$) is selected: effectively a field position analogous to $g = g_\parallel$. Although the ENDOR spectra were measured at several (mixed) field positions, these latter two unique field positions greatly simplify the analysis of the subsequent ENDOR data.

^{1}H ENDOR spectra

The ^{1}H ENDOR spectra of each complex recorded at the field position ***a*** (effective $g = g_\perp$ position) are shown in Figure 4.13 for comparison. The spectra contain a matrix ^{19}F peak (labeled * in Figure 4.13; ν_N = 14.0272 MHz for ^{19}F at 3500 G) which arises from the $[Al(OC(CF_3)_3)_4]^-$ counter ion used in the preparation of the Cr(I) complex (see Chapter 3). All of the spectra appear to be qualitatively similar, containing couplings from weakly interacting protons. The outer ENDOR peaks are quite broad, and this is usually indicative of a distribution of proton environments, producing a minor strain on the ^{H}A values.

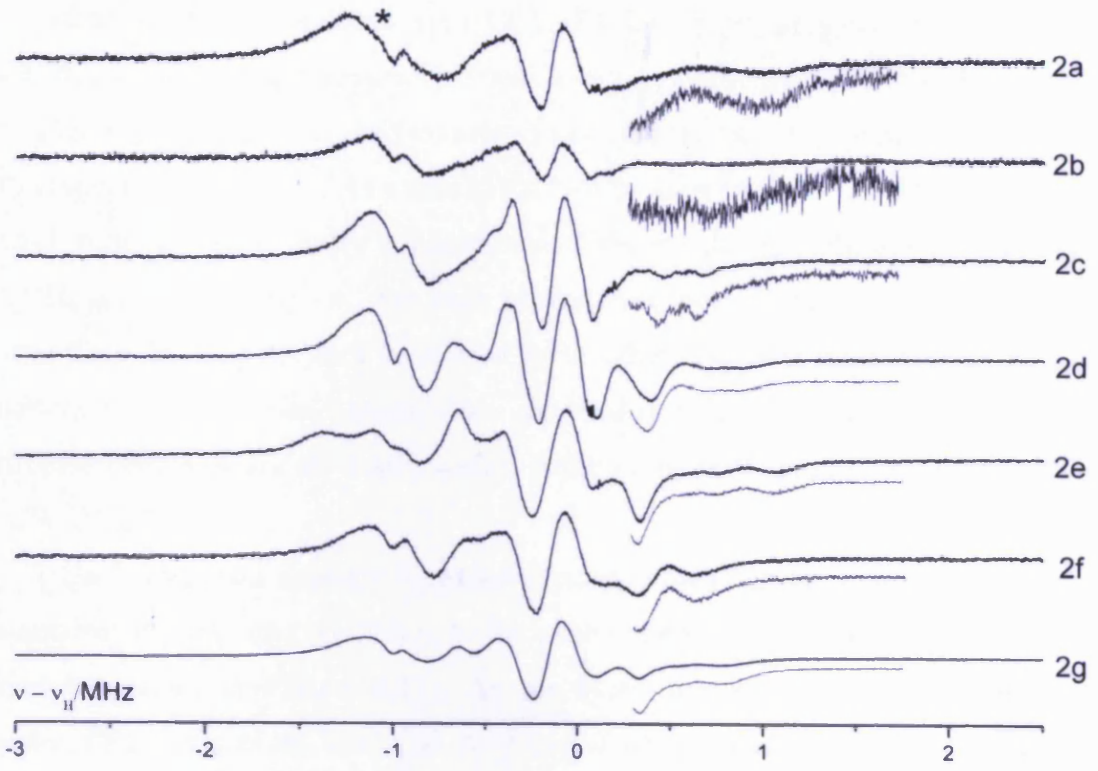

Figure 4.13: CW-^{1}H ENDOR spectra (10K) of $[Cr(CO)_4$**a-g**$]^+$ recorded in deuterated dichloromethane/toluene. The spectra were obtained at the effective field position corresponding to $g = g_{\perp}$ for each system. * = ^{19}F matrix peak from $[Al(OC(CF_3)_3)_4]^-$ ion.

The weakly coupled protons, responsible for the outer lines in the ENDOR spectra (expanded on the right hand side of the Figure), most likely originate from the phenyl substituents on ligand **a-g**, since they are common to all complexes and closest to the Cr centre (see Scheme 4.3).

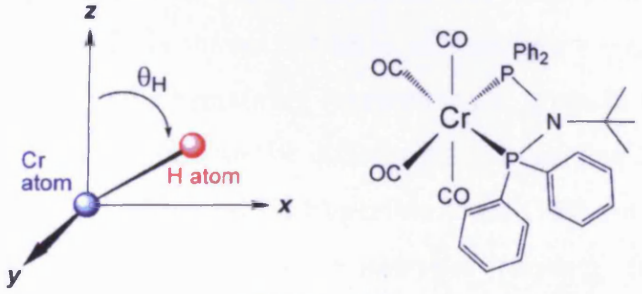

Scheme 4.3

The methyl and methine protons in the PNP ligand backbone (**d-g**) are, for example, more than 5 Å away from the Cr centre (too remote to account for the observed hyperfine couplings). Although the methine protons in the PCP ligand backbone (**a** and **b**) are closer to Cr (*ca.* 4.5 Å), their interaction would still be expected to be too small to account for the observed couplings.

One of the complexes ($[Cr(CO)_4\mathbf{g}]^+$) has been prepared previously by Rucklidge *et al.*,[2] and characterised *via* X-ray crystallography. According to the published crystal structure, the two sets of phenyl groups in the complex are twisted with respect to each other. As a result, the two protons in the *ortho*-position of each phenyl ring are structurally inequivalent. This results in substantially different Cr....$^1H_{o\text{-phenyl}}$ distances; i.e., for each phenyl ring one of the *ortho*-protons has a shorter Cr....$^1H_{o\text{-phenyl}}$ distance compared to the other. The four shortest Cr....$^1H_{o\text{-phenyl}}$ distances from the crystal structure are reported to be 3.30, 3.54, 3.71 and 4.18 Å, and these distances are all easily within range of weakly coupled nuclei detectable by CW-ENDOR.

Each spectrum appears slightly different, which can be seen most clearly in the outermost peaks corresponding to the phenylene protons closest to the Cr centre (expanded peaks in Figure 4.13). As discussed previously, an insight into the position of these protons could be very useful when analysing catalytic data. Any differences observed in the mutual angle between the proton and the electron, or their distance, as a function of bis(diphenylphosphine) ligand under consideration, could shed light on whether the ligand backbone does in fact affect the spatial orientation of the phenyl ring. Variation in catalytic selectivity and activity have definitely been established as a result of change of ligand,[12-15] but no definitive explanation for these observations has yet been put forward.

To obtain structural information on the nuclear environment of each complex, orientation-selective ENDOR was performed for each complex $[Cr(CO)_4\mathbf{a}$-$\mathbf{g}]^+$. The set of spectra for **2c** is shown in Figure 4.14 and for brevity, the orientation-selective ENDOR data for the remaining complexes are given in the Appendix. The orientation-selective spectra confirm the differences in hyperfine coupling values for these nuclei. Since the experimental ^1H hyperfine tensor will contain both isotropic (arising from spin polarisation) and anisotropic (arising from dipole-dipole interactions) terms, the observed differences in the spectra must therefore arise either from changes to the relative conformation of the phenyl groups or due to changes in the electronic spin delocalisation in the complexes.

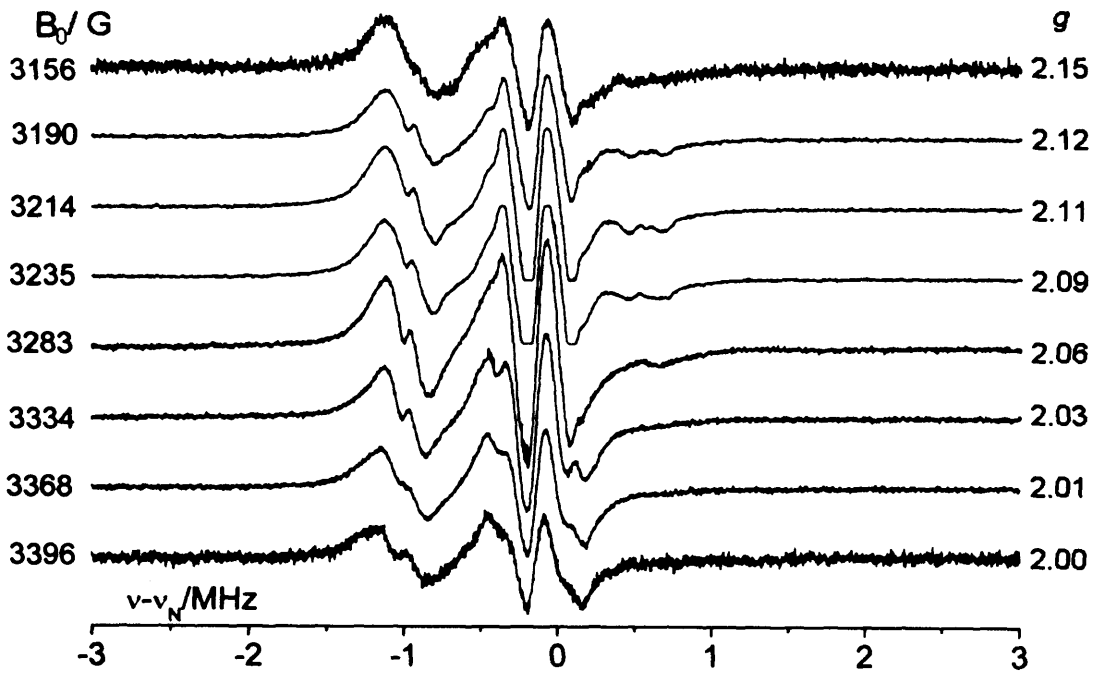

Figure 4.14: Experimental CW-^{1}H ENDOR spectra (10K) of $[Cr(CO)_4(Ph_2PBzPPh_2)]^+$ (**2c**) recorded in deuterated dichloromethane/toluene at a microwave frequency of 9.485 GHz and a modulation depth of 79 kHz. The angular selective spectra were obtained at the magnetic field positions (B_0 in Gauss) and corresponding g values shown in the Figure.

In order to examine these changes in more depth, detailed simulations of the ENDOR data were performed. The ^{1}H ENDOR spectra recorded at several field positions for $[Cr(CO)_4\mathbf{g}]^+$, as a representative example, are shown in Figure 4.15 along with the associated simulations. The simulated data for the remaining complexes are given in the Appendix. Two distinct proton environments account for the peaks in the spectra. However, owing to the broad linewidths observed, only the nuclei with the largest coupling can be simulated with any accuracy (i.e., the error associated with the simulated hyperfine couplings for the second proton, responsible for the inner peaks, is too large and suggests a Cr...^{1}H distance of >4 Å). The nucleus responsible for the largest couplings contains a small a_{iso} contribution (-0.05 MHz), and the resulting A_{dip} term (3.4 MHz) gives an estimated Cr...^{1}H distance of 3.58 Å (calculated using a simple point-dipole approximation based on the principal hyperfine components of A_1 = -1.5, A_2 = -2.0, A_3 = 3.35 MHz) and an angle θ (mutual orientation between the electron and nuclear z axes with respect to the field vector) of 15° (see Table 4.2).

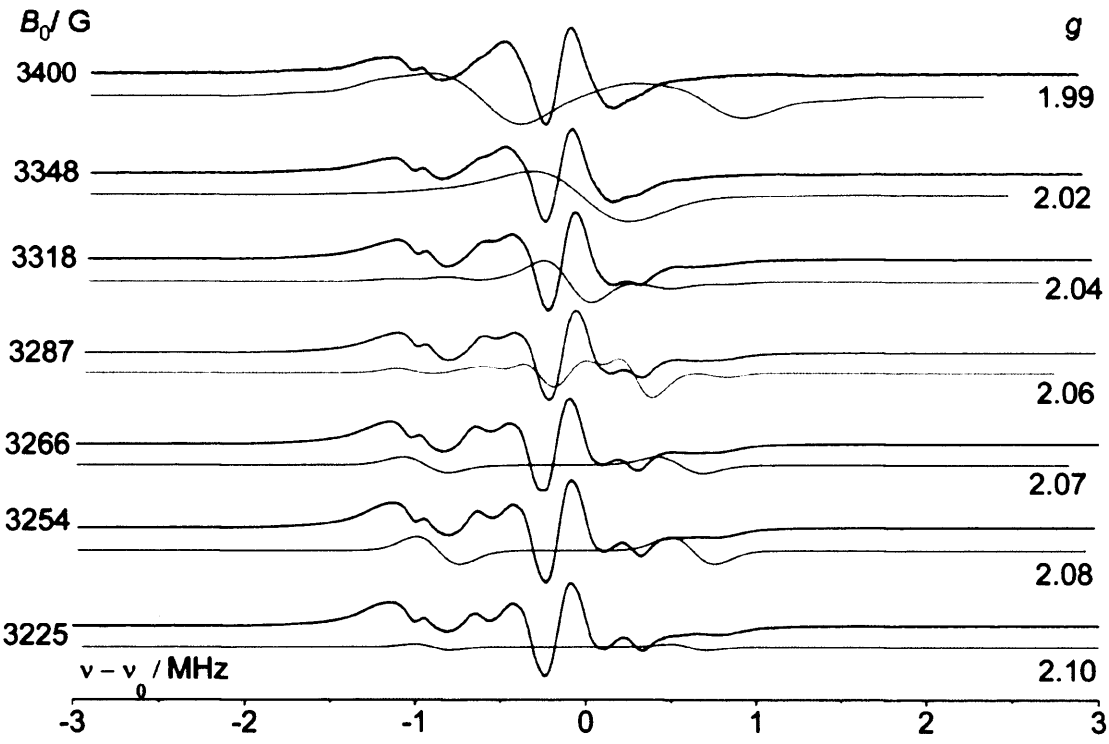

Figure 4.15: Experimental and simulated CW-^{1}H ENDOR spectra (10K) of $[Cr(CO)_4\mathbf{g}]^+$ recorded in deuterated dichloromethane/toluene. The angular selective spectra were obtained at the magnetic field positions (B_0 in Gauss) and corresponding g values shown the Figure.

Table 4.2: Spin Hamiltonian parameters obtained by simulation of the CW-ENDOR data for compounds $[Cr(CO)_4\mathbf{a\text{-}g}]^+$. A linewidth of 0.25 MHz was used for all ^{1}H CW-ENDOR simulations.

Complex	Ligand	A_1 / MHz	A_2 / MHz	A_3 / MHz	a_{iso} / MHz	A_{dip} / MHz	R / Å	θ / °
2a	PCCP	-1.5	-1.5	2.6	-0.13	2.73	3.88	50
2b	PCCCP	-3.0	-3.0	5.4	-0.20	5.60	3.05	45
2c	PCCP	-1.5	-1.5	4.0	0.33	3.67	3.52	50
2d	PNP	-1.8	-1.8	3.0	-0.20	3.20	3.67	40
2e	PNP	-3.0	-3.0	4.0	-0.67	4.67	3.22	40
2f	PNP	-2.7	-2.7	3.3	-0.70	4.00	3.41	50
2g	PNP	-1.5	-2.0	3.35	-0.05	3.40	3.58	15

Analysis of these spectra reveals small a_{iso} values in all cases, which suggests that the variations observed in Figure 4.13 for the different complexes must originate from slight differences in the phenyl group conformations as the coupling is mainly dipolar, i.e. through space. As mentioned earlier, distinctive Cr...^{1}H distances of 3.30, 3.54, 3.71 and 4.18 Å, were identified in the single crystal of $[Cr(CO)_4\mathbf{g}]^+$. It is highly likely that the main proton observed in the frozen solution ENDOR spectra, with the Cr...^{1}H distance of 3.58 Å, represents an averaged

distribution of the single crystal distances. This would certainly account for the unusually broad linewidths of the ENDOR spectra.

The values obtained by simulation of the orientation-selective ENDOR spectra reveal axial hyperfine matrices with small a_{iso} values in all cases, consistent with a predominantly dipolar coupling of the proton and electron. The distance R between the two spins is similar to published data obtained from crystallographic measurements on similar complexes.[2, 6] Orientation-selective ^{1}H ENDOR measurements were also performed at Q-band on $[Cr(CO)_4\mathbf{g}]^+$, and the results shown in the Appendix (Figure A.8). The spectra were not as well-resolved as those recorded at X-band; only one broad pair of ^{1}H couplings were observed at each field position, and no ^{31}P couplings were observed.

^{31}P ENDOR spectra

The ^{31}P couplings are sufficiently large that they are clearly visible in the EPR spectra (Figure 4.1). However, they are also visible in the ENDOR spectra, as shown in Figure 4.16 for $[Cr(CO)_4\mathbf{f}]^+$. Owing to the higher resolving powers of ENDOR, in principle their couplings, and possibly orientations, can be determined with more accuracy. The isotropic ^{31}P hyperfine couplings should arise from ^{31}P 3*s* character in the SOMO, from polarisation of inner shell ^{31}P *s* orbitals by spin density on the metal or in ^{31}P 3*p* orbitals. These summed contributions can then be analysed by EPR to account for the observed spin densities. However, as discussed by Rieger *et al.*,[7, 8, 17] reliable interpretation of the ^{31}P hyperfine matrix should be treated carefully as the anisotropies are often small and the ***g*** matrix anisotropy is much greater than the $^{P}\boldsymbol{A}$ matrix (hence observed spectral features correspond to orientations of the magnetic field along one of the ***g*** matrix principal axes). This will depend on the symmetry of the complex. Assuming an approximate C_{2v} symmetry for the $[Cr(CO)_4\mathbf{L}]^+$ complexes (since the C_2 axis runs from Cr through the N atom bridging the two P atoms, with one vertical mirror plane containing the two P atoms and another containing the two CO molecules) the ***g*** matrix axes are necessarily along the x, y and z molecular axes, with the Cr-P vectors lying approximately midway between the x and y axes. However, at the low X-band frequency used in this work, the symmetry of the complex can be treated as axial for analysis purposes.

The CW-^{31}P ENDOR spectra were simulated at a number of field positions for $[Cr(CO)_4\mathbf{f}]^+$ (Figure 4.16). It is frequently the case that ^{31}P hyperfine interactions

fall into the category where $\nu_N > a/2$, i.e., the Larmor frequency is larger than half the value of the hyperfine coupling, at a particular field position. In this case (unlike with the proton spectra above), the ENDOR peaks are centred on $a/2$ and separated by $2\nu_N$. The ^{31}P (and ^{14}N) ENDOR spectra all follow this rule.

Although the observed linewidths were broad (approximately 10 MHz), the matrix is largely axially symmetric with $A_1 = 70\pm1$, $A_2 = 72\pm1$ and $A_3 = 83\pm1$ MHz ($a_{iso} = 75$ MHz $\cong$ 26.75 G). This isotropic value is similar to that observed by EPR (see Table 1, $a_{iso} = 26.5$ G, allowing for the larger error in the EPR spectra). Interestingly the $^{P}A_{||}$ value is calculated as 8 MHz, giving an estimated Cr...P bond length of 2.02 Å. Clearly this is an under estimation of the distance compared to the known crystal structures of $[Cr(CO)_4\mathbf{g}]^+$ (Cr...P bond lengths of 2.26 and 2.66 Å)[2] and $[Cr(CO)_4(diphos)]$ (Cr...P distance of 2.36 Å).[29] This discrepancy arises primarily from the dominant a_{iso} contribution to the hyperfine tensor, resulting in a higher degree of error associated with the dipolar term, and due to the limitations in the point-dipole approximation at such short electron-nuclear distances. For example, with a hyperfine tensor of $A_1 = 70$, $A_2 = 72$ and $A_3 = 81$ MHz, then $A_{||} = 6.0$ MHz giving a Cr...P distance of 2.2 Å. For these reasons, it is qualitatively more meaningful to compare in detail the a_{iso} values rather than the anisotropic ^{P}A terms.

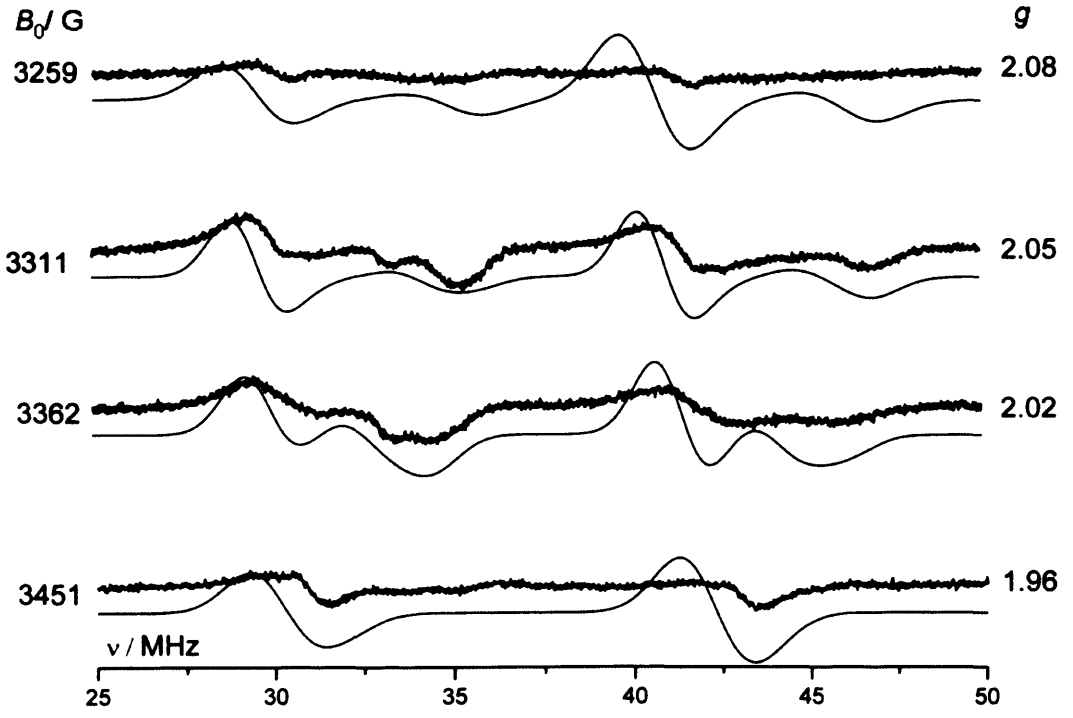

Figure 4.16: Experimental and simulated CW-^{31}P ENDOR spectra (10K) of $[Cr(CO)_4\mathbf{f}]^+$ recorded in deuterated dichloromethane/toluene. The angular selective spectra were obtained at the magnetic field positions (B_0 in Gauss) and corresponding g values shown in the Figure. A linewidth of 10 MHz was used in all ^{31}P CW-ENDOR simulations.

CW-^{31}P ENDOR measurements were also performed on $[Cr(CO)_4\mathbf{d}]^+$ and $[Cr(CO)_4\mathbf{e}]^+$ (see Figures A.9a and A.9b in the Appendix). It should be noted that the small degree of anisotropy observed in the $^P\boldsymbol{A}$ matrix is analogous to the experimental and calculated values for a series of Cr(I) carbonyl phosphine and phosphonite complexes as reported by Cummings *et al.*,[7] The $[Cr(CO)_4(dppe)]^+$ complex had reported g values of 2.09, 2.08 and 1.988 and ^PA values of 66, 66 and 68 MHz. In all cases, the calculated anisotropies were small while the predicted a_{iso} values were analogous to those experimentally observed in this work.

^{14}N ENDOR spectra

The ^{14}N ENDOR spectra were also recorded for three of the the PNP containing complexes ($[Cr(CO)_4\mathbf{e\text{-}g}]^+$). As the ^{14}N nuclei are not directly co-ordinated to Cr, their couplings are expected to be weak. In such weak coupling cases, pulsed hyperfine techniques such as ESEEM and HYSCORE are ideally suited to extract the full hyperfine ($\boldsymbol{A}$) and quadrupolar ($\boldsymbol{Q}$) matrices. Nevertheless, a good estimate can also be extracted from the more poorly resolved CW-ENDOR spectra. The ^{14}N ENDOR spectra for $[Cr(CO)_4\mathbf{f}]^+$, recorded at four different field positions, are shown in Figure 4.17.

As deuterated solvents were used, a deuterium matrix peak is clearly visible in the spectra (labeled * in Figure 4.17; ν_N = 2.2876 MHz for ^{2}H at 3500 G). The remaining features in the spectra are attributed to the superimposed A and Q terms. To a first approximation, the values obtained were A_1 = ±4.38 MHz, A_2 = ±4.41 MHz, A_3 = ±6.65 MHz and Q_1 = ±0.13 MHz, Q_2 = ±0.19 MHz, Q_3 = ±0.32 MHz and these parameters are typical for weakly coupled ^{14}N nuclei. ^{14}N experimental ENDOR spectra were also recorded for $[Cr(CO)_4\mathbf{e}]^+$ and $[Cr(CO)_4\mathbf{g}]^+$, displayed in Figures A.10a and A.10b in the Appendix. All of the ^{14}N ENDOR spectra display very small hyperfine couplings, which is why they were not visible in the EPR spectra, due to the relatively broad linewidths. They also display very similar hyperfine and quadrupolar matrices to each other, showing that the interaction between the electron and the nitrogen nucleus is not highly ligand dependent.

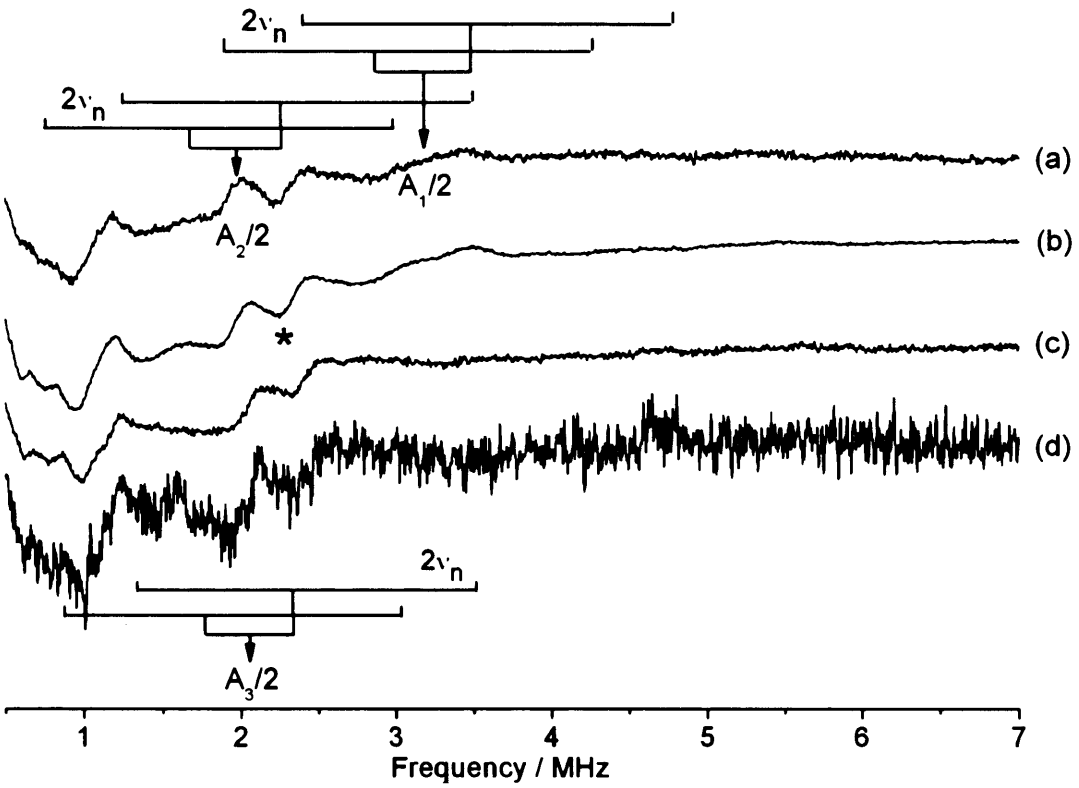

Figure 4.17: Experimental CW-^{14}N ENDOR spectra (10K) of $[Cr(CO)_4f]^+$ recorded in deuterated dichloromethane/toluene. The angular selective spectra were obtained at the magnetic field positions and corresponding *g* values of (a) 3220 G, g = 2.10 (b) 3260 G, g = 2.08 (c) 3370 G, g = 2.01 and (d) 3394 G, g = 1.99. * = ^{2}H matrix peak.

4.3.4 Pulsed ENDOR

Similarly to CW-ENDOR, pulsed ENDOR also excites both electron and nuclear spins using microwave and RF fields. One of the most frequent problems encountered during CW-ENDOR is that of being unable to saturate the electron Zeeman transition due to a short spin-lattice relaxation time of the species; this is particularly common for transition-metal based systems. However, relatively long relaxation times are not so crucial in pulsed ENDOR and so more types of system can be studied.

There are two main types of pulsed ENDOR measurements; Mims (discovered by Bill Mims in 1965)[30] and Davies (1974).[31] Both use high-intensity microwave pulse(s) to disturb the equilibrium state of the spins, after which an RF pulse is applied which flips the spin of the nucleus in question. The resonant frequency of the coupled electron spin is changed by the hyperfine splitting *A*. This is detected by another microwave pulse(s) and resultant echo.

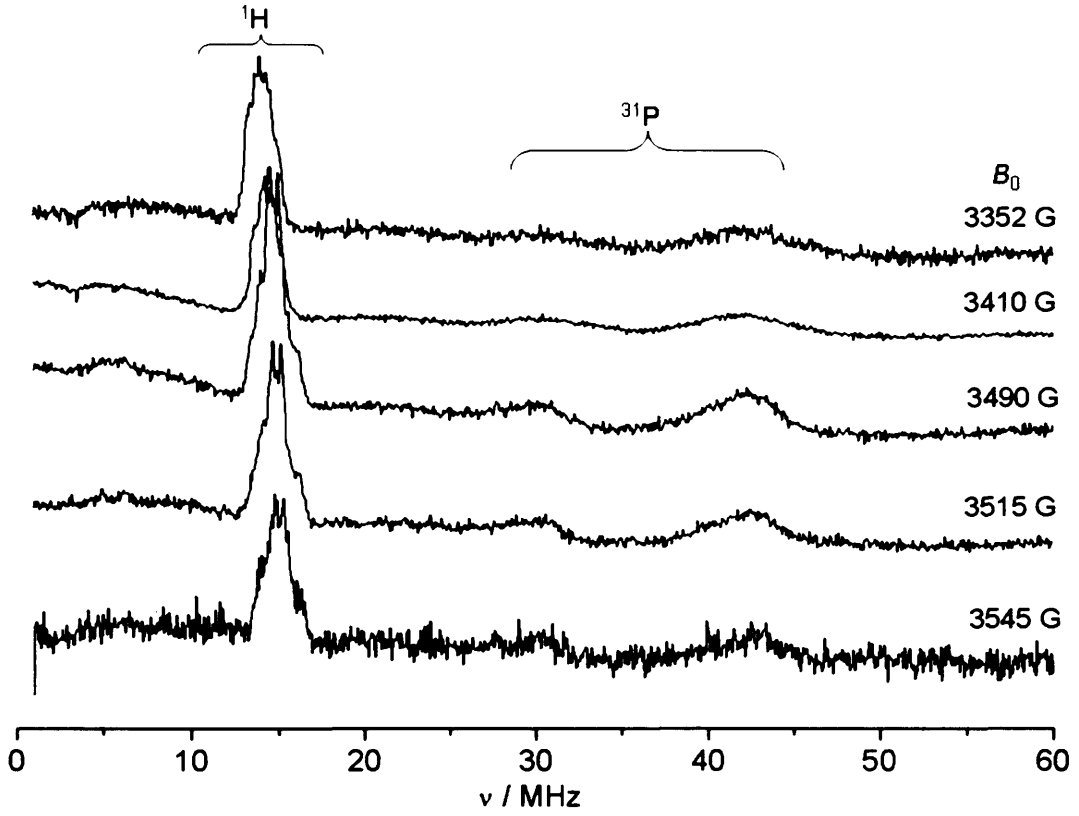

Figure 4.18: Experimental pulsed Davies ENDOR spectra (10K) of $[Cr(CO)_4\mathbf{g}]^+$ recorded in deuterated dichloromethane/toluene. The angular selective spectra were obtained at the field positions shown in the Figure.

Davies ENDOR measurements were performed on $[Cr(CO)_4\mathbf{g}]^+$ and the results shown in Figure 4.18 above. The ^{31}P coupling is clearly visible in the spectra as two peaks centred upon $A/2$ (around 37 MHz) and separated by twice the phosphorus nuclear Larmor frequency at each field position, $2\nu_N$. These phosphorus couplings were simulated (Figure 4.19) to extract the $^P\boldsymbol{A}$ hyperfine matrix. The parameters extracted from the simulation are A_1 = 70 MHz, A_2 = 70 MHz, A_3 = 80 MHz, a_{iso} = 73.3 MHz. Again, these are similar to the isotropic value obtained *via* simulation of the CW and pulsed EPR spectra.

The ^{1}H couplings, centred around the nuclear Larmor frequency of the proton (around 15 MHz), are not sufficiently resolved to enable accurate simulation. However, qualitatively they are consistent with those observed *via* CW-ENDOR, meaning that pulsed ENDOR will be a viable technique to study the activated systems, and comparison with the data obtained by continuous-wave methods will be valid.

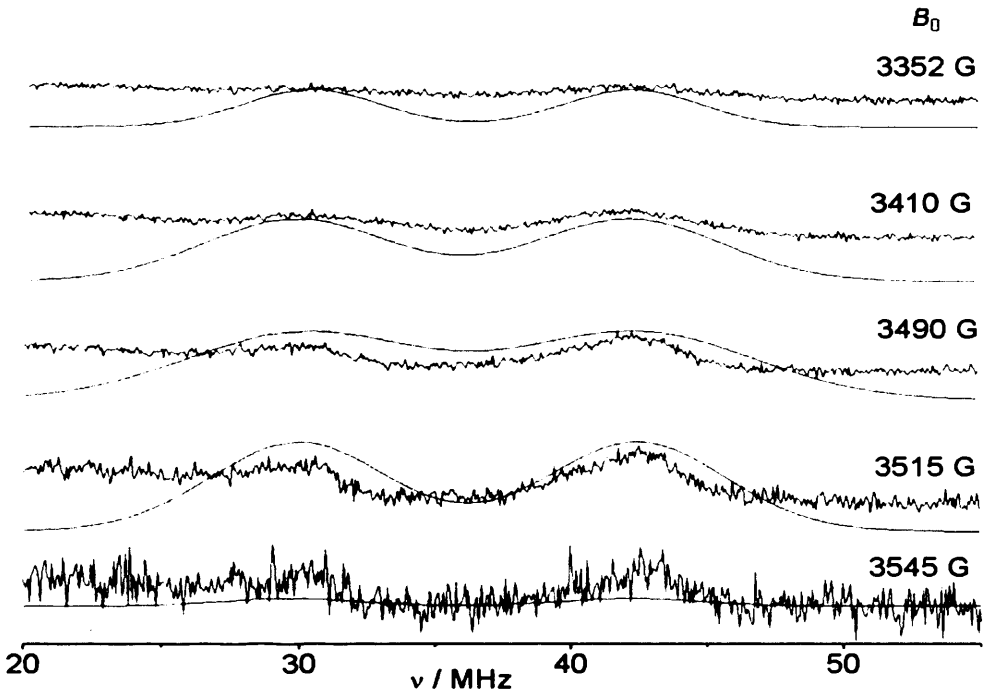

Figure 4.19: Experimental and simulated pulsed Davies ENDOR spectra (10K) of $[Cr(CO)_4g]^+$ recorded in deuterated dichloromethane/toluene. A linewidth of 10 MHz was used in all ^{31}P pulsed ENDOR simulations. The angular selective spectra were obtained at: the field positions shown in the Figure.

4.3.5 Structure function relations

The ligands chosen for this study were done so on the basis that catalytic ethylene tetramerisation data have been previously reported,[2, 32,12] and furthermore that they represent significantly different variations of the diphosphine scaffold capable of enabling this reaction. Pertinent catalytic data was tabulated[12] and a correlation searched for between the measured EPR-derived parameters (specifically the *g* values, phosphorus spin densities and % *s* character, see Table 4.1) and various parameters of significance to the tetramerisation reactions (activity, % C_6, % C_8, % 1-C_6, % 1-C_8, % C_6-cyclics, 1-C_8:1-C_6 ratio and PE formation). However, no meaningful correlation in trends could be identified between any combination of parameters. Given the significant perturbation to the chromium environment when $[Cr(CO)_4PP][Al(OC(CF_3)_3)_4]$ is activated for catalysis using excess trialkylaluminium and then placed under elevated pressure of ethylene, this lack of correlation is perhaps not surprising, and suggests that more meaningful analysis can only be achieved by studying species that have been activated in the first instance, and subsequently under pressure of ethylene. For this reason it was necessary to monitor the changes to both electronic and structural properties after activation of the catalysts (as discussed in Chapters 5 and 6).

4.4 Conclusions

A series of Cr(I) complexes, $[Cr(CO)_4\mathbf{a\text{-}g}]^+$, where **a-g** represent bis(diphenylphosphine) ('PCP') and bis(diphenylphosphinoamine) ('PNP') ligands, has been extensively characterised for the first time *via* CW- and pulsed EPR, ENDOR and ESEEM spectroscopy. This type of complex has been established as an effective pre-cursor for the catalysts which selectively oligomerise ethylene.[2] Although traditionally it is Cr(III) pre-cursors which have been most commonly used, Cr(I) species have been implicated in the catalytic cycle even starting from this Cr(III) state.[33] Despite this, very little EPR spectroscopic data has been collected on this type of complex, even though the technique can provide unprecedented information on both the electronic and geometric structure of the species under consideration. This study is the first of its kind into such a series of Cr(I) tetracarbonyls with co-ordinating phosphine ligands.

The CW-EPR data revealed an axial $\boldsymbol{g}$ matrix for each complex ($g_\perp > g_e > g_\parallel$), with superhyperfine coupling to two equivalent ^{31}P nuclei, visible in each component of the spectrum. The spectra were simulated and the spin Hamiltonian parameters extracted. The $\boldsymbol{g}$ matrix is consistent with a low-spin d^5 species of approximate C_{2v} symmetry, whose metal contribution to the SOMO is primarily d_{xy}. The extent of tetragonal distortion to the system, reflected in the magnitude of Δg ($g_\perp - g_\parallel$), differed from complex to complex. No correlation between this trend and ligand type was found. The isotropic component to the ^{31}P coupling also varied from complex to complex; it was found to be higher in those Cr(I) complexes bearing PNP ligands than those bearing PCP. This indicated that the phosphorus 3*s* character in the SOMO was higher for the nitrogen-containing complexes; perhaps due to increased σ-bonding character of the phosphorus atom as a result of increased electron density delocalisation from the nitrogen to the phosphorus.

CW-ENDOR provided information on the ^1H, ^{31}P and ^{14}N nuclear hyperfine tensors. ^1H couplings from the protons on the phenyl rings were discovered to be mainly dipolar in nature, showing their superhyperfine interaction with the electron is predominantly through-space. Simulation of orientation-selective spectra revealed that subtle structural differences in the complex, namely in the phenyl ring conformations, occur as a function of ligand type. Bond lengths and angles between the two interacting spins with respect to the field were calculated from the anisotropic component of the coupling. ^{31}P couplings, conversely, were determined

to have a large isotropic contribution to their interaction, confirming the nature of their coupling as observed in the EPR spectra. Both superhyperfine and quadrupolar interactions were observed in the ^{14}N ENDOR spectra, and the $\boldsymbol{A}$ and $\boldsymbol{Q}$ matrices typical for a weakly coupled nitrogen nucleus.

Q-band EPR and ENDOR characterisation experiments were also carried out. The resolution of g values was increased, but no phosphorus coupling was visible in the EPR or ENDOR spectra. A broad proton coupling was detected in the ^{1}H ENDOR spectra, but lack of resolution meant no further information could be obtained.

Pulsed experiments were also conducted, in order to confirm the data obtained *via* CW-methods and also to test its efficacy for future work on the activated systems. Field-swept echo-detected EPR spectra were recorded for **2b** and **2g**, and the spin Hamiltonian parameters extracted were in excellent agreement with those obtained in the continuous-wave experiments. The ESEEM spectra recorded were however more ambiguous; ^{1}H peaks were clearly present but there was some difficulty in assigning other peaks. The Davies ENDOR (recorded of **2g**) was more straightforward since ^{31}P and ^{1}H couplings were easily determined, and agreed with both CW-EPR and ENDOR assignments. These initial pulsed experiments on the pre-catalyst proved that the technique is valid and viable for further work on the activated system.

The parameters gathered for the series of complexes provides a thorough characterisation of their electronic and structural properties. An analysis of the relevant catalytic data did not show any trends that correlate between the two; however, the nature of the activated catalyst is thought to be significantly different from that of the pre-catalyst and so this is not surprising. These data are invaluable though for comparison with the activated species (see Chapters 5 and 6); the changes that occur to the spectroscopic data will reflect the changes to the systems themselves.

4.5 References

1. J. T. Dixon, M. J. Green, F. M. Hess and D. H. Morgan, *J. Organomet. Chem.*, 2004, **689**, 3641.
2. A. J. Rucklidge, D. S. McGuinness, R. P. Tooze, A. M. Z. Slawin, J. D. A. Pelletier, M. J. Hanton and P. B. Webb, *Organometallics*, 2007, **26**, 2782.
3. *WO 03053891A1, Sasol Technology (Pty) Ltd Pat.*, 2003.
4. D. S. McGuinness, P. Wasserscheid, W. Keim, D. Morgan, J. T. Dixon, A. Bollmann, H. Maumela, F. Hess and U. Englert, *J. Am. Chem. Soc.*, 2003, **125**, 5272.
5. *WO 03053890A1, Sasol Technology (Pty) Ltd Pat.*, 2003.
6. L. E. Bowen, M. F. Haddow, A. G. Orpen and D. F. Wass, *Dalton Trans.*, 2007, 1160.
7. D. A. Cummings, J. McMaster, A. L. Rieger and P. H. Rieger, *Organometallics*, 1997, **16**, 4362.
8. A. L. Rieger and P. H. Rieger, *Organometallics*, 2002, **21**, 5868.
9. R. N. Bagchi, A. M. Bond, G. Brain, R. Colton, T. L. E. Henderson and J. E. Kevekordes, *Organometallics*, 1984, **3**, 4.
10. A. M. Bond, S. W. Carr and R. Colton, *Inorg. Chem.*, 1984, **23**, 2343.
11. M. P. Castellani, N. G. Connelly, R. D. Pike, A. L. Rieger and P. H. Rieger, *Organometallics*, 1997, **16**, 4369.
12. M. J. Overett, K. Blann, A. Bollmann, R. de Villiers, J. T. Dixon, E. Killian, M. C. Maumela, H. Maumela, D. S. McGuinness, D. H. Morgan, A. Rucklidge and A. M. Z. Slawin, *J. Mol. Catal. A: Chem.*, 2008, **283**, 114.
13. A. Carter, S. A. Cohen, N. A. Cooley, A. Murphy, J. Scutt and D. F. Wass, *Chem. Commun.*, 2002, 858.
14. K. Blann, A. Bollmann, J. T. Dixon, F. M. Hess, E. Killian, H. Maumela, D. H. Morgan, A. Neveling, S. Otto and M. J. Overett, *Chem. Commun.*, 2005, 620.
15. M. J. Overett, K. Blann, A. Bollmann, J. T. Dixon, F. Hess, E. Killian, H. Maumela, D. H. Morgan, A. Neveling and S. Otto, *Chem. Commun.*, 2005, 622-624.
16. D. M. Murphy and R. D. Farley, *Chem. Soc. Rev.*, 2006, **35**, 249.
17. P. H. Rieger, *Coord. Chem. Rev.* , 2004, **135-136**, 203.
18. B. R. McGarvey, *Coord. Chem. Rev.*, 1998, **170**, 75.
19. M. Brustolon and E. Giamello, eds., *Electron Paramagnetic Resonance - A Practitioner's Toolkit*, Wiley, 2009.
20. K. Mobius, A. Savitsky, C. Wegener, M. Rato, M. Fuchs, A. Schnegg, A. A. Dubinskii, Y. A. Grishin, I. A. Grigor'ev, M. Kuhn, D. Duche, H. Zimmermann and H. J. Steinhoff, *Magn. Reson. Chem.*, 2005, **43**, S4-S19.
21. J. R. Pilbrow, *Transition Ion Electron Paramagnetic Resonance*, OUP, Oxford, 1990.
22. A. Schweiger and G. Jeschke, *Principles of Pulse Electron Paramagnetic Resonance*, OUP, Oxford, 2001.
23. P. A. Snetsinger, J. B. Cornelius, R. B. Clarkson, M. K. Bowman and R. L. Belford, *J. Phys. Chem.*, 1988, **92**, 3696.
24. T. A. Konovalova, S. A. Dikanov, M. K. Bowman and L. D. Kispert, *J. Phys. Chem. B.*, 2001, **105**, 8361.
25. D. Arieli, D. E. W. Vaughan, K. G. Strohmaier and D. Goldfarb, *J. Am. Chem. Soc.*, 1999, **121**, 6028.
26. B. M. Hoffman, J. Martinsen and R. A. Venters, *J. Mag. Reson.*, 1984, **59**, 110.

27. G. C. Hurst, T. A. Henderson and R. W. Kreilick, *J. Am. Chem. Soc.*, 1985, **107**, 7294.
28. T. A. Henderson, G. C. Hurst and R. W. Kreilick, *J. Am. Chem. Soc.*, 1985, **107**, 7299.
29. M. J. Bennett, F. A. Cotton and M. D. Laprade, *Acta Cryst. B.*, 1971, **B 27**, 1899.
30. W. B. Mims, *Proc. R. Soc. Lond. Ser. A. Math. Phys. Sci.*, 1965, **283**, 279.
31. E. R. Davies, *Phys. Lett. A*, 1974, **47**, 1.
32. K. Blann, A. Bollmann, H. de Bod, J. T. Dixon, E. Killian, P. Nongodlwana, M. C. Maumela, H. Maumela, A. E. C. McConnell, D. H. Morgan, M. J. Overett, M. Pretorius, S. Kuhlmann and P. J. Wasserscheid, *J. Catal.*, 2007, **249**, 244.
33. T. Agapie, S. J. Schofer, J. A. Labinger and J. E. Bercaw, *J. Am. Chem. Soc.*, 2004, **126**, 1304.

Chapter 5

An EPR Investigation into the Intramolecular formation of Cr^{I}(bis-arene) species *via* R_3Al activation of $[Cr(CO)_4PP]^+$ (PP = $Ph_2PN(R)PPh_2$, $Ph_2P(R)PPh_2$)

5.1 Introduction

The vast majority of oligomerisation catalysis is performed at elevated temperatures, under a pressure of ethylene. For the types of system under investigation in this thesis, namely a series of Cr pre-catalyst species containing bis(diphenylphosphine) ligands, various conditions have been used by different groups. However, all employ an autoclave temperature of around 60°C under a pressure of ethylene. The activation step of the reaction, i.e., the addition of the co-catalyst (R_3Al or MAO) to the pre-catalyst, is usually carried out at room temperature.[1-5]

Variable temperature EPR and ENDOR spectroscopy are valuable techniques for the study of such activation and alkene addition processes. Recording and analysing the spectra at varying temperatures allows different physical and chemical properties of the sample to be analysed. This experimental capability allows spectra to be recorded at liquid helium temperatures (4 K) to room temperature (298 K). Most of the EPR spectra in this thesis were recorded between 140 K and room temperature. The advantages of low temperatures include slower relaxation times to achieve saturation for the ENDOR experiment, or to detect fast-relaxing transition metal ions. Valuable structural information on the molecular geometry and corresponding orbital configuration can be gained from the 'powder pattern' of a frozen solution. Conversely, the room temperature spectrum provides information on the isotropic characteristics of the sample, e.g., the contribution of the Fermi contact interaction to the hyperfine coupling, and the fraction of spin present in *s* orbitals. Recording spectra over a range of temperatures can enable molecular dynamics to be investigated. The spectral profile depends on the rate of tumbling compared to the frequency difference between the anisotropic components of the spin Hamiltonian; if the tumbling is faster than the difference between the components, the average of the components is detected.

This rotational correlation time for a solution is dependent on temperature and viscosity of the medium, and can be investigated as a function of temperature. Additionally, different species that may be present in the reaction mixture may produce signals at different temperatures. Each species has its own characteristic relaxation

times T_1 (spin-lattice) and T_2 (spin-spin). The relationship between the relaxation time and the rate of microwave absorption is dependent in part on temperature. Certain species may only be visible at low temperatures due to short relaxation times, and others may be detectable at higher temperatures that were masked by the aforementioned species and / or saturate too easily at low temperatures.

For all these reasons it is instructive to perform variable temperature studies. Recording spectra of activated species at room temperature mimics industrial conditions. Even though we cannot record spectra above this temperature, e.g., at 60°C as the oligomerisation process generally occurs at, any species detected at room temperature are likely to be present at elevated temperatures as well. Preparing samples and recording spectra at low temperatures may enable transient species to be detected, and more structural information obtained.

There is extremely little research as yet into oligomerisation catalysts *via* EPR and ENDOR. Brückner *et al.*,[6] investigated the activation of (and addition of ethylene to) $Cr(acac)_3$/PNP and $[(PNP)CrCl_2(\mu\text{-}Cl)]_2$ (where PNP = $Ph_2PN(i Pr)PPh_2$). Upon addition of MMAO/heptane to $Cr(acac)_3$/PNP, the EPR signal intensity diminished and split into two signals, attributed to methylated Cr(III) species. A simultaneous signal arose, seemingly with components from two different Cr(I) sites, with spin Hamiltonian parameters of (a) $g_{\|} = 2.0127$ and $g_{\perp} = 1.9868$, and (b) $g_1 = 2.0406$, $g_2 = 2.0099$ and $g_3 = 1.9695$. At 313 K, two broad isotropic signals were detected with g values of 2.012 and 1.995. The maximum Cr(I) intensity was reached after 1h at 313 K, but was only 5 % of the original Cr intensity, suggesting an EPR-silent Cr species was formed. This was postulated as either antiferromagnetically coupled Cr(I) dimers, or production of Cr(II) species. Upon pressurising the system with ethylene at 333 K, one Cr(I) isotropic signal broadened reversibly, postulated by the authors to indicate a Cr(I)/Cr(III) redox cycle, the dynamics of which caused the line broadening. No hyperfine structure was visible in any spectra. Upon activation of a solution of $[(PNP)CrCl_2(\mu\text{-}Cl)]_2$ in toluene with MMAO, the Cr(III) EPR signal decreased and a signal characteristic of Cr(I) arose, with $g_{\|} = 2.011$ and $g_{\perp} = 1.989$, similar to the axial parameters observed previously in this paper. However at room temperature, instead of the broad isotropic signal observed previously, an 11-line multiplet characteristic of a $[Cr(\eta^6\text{-}C_6H_5CH_3)]^+$ species was observed ($g_{iso} = 1.988$, $^{1H}a_{iso} = 3.57$ G, $^{53Cr}a_{iso} = 18$ G). This was postulated to arise due to release of the PNP ligand and saturation of the Cr co-ordination sites by two toluene

solvent molecules. Upon addition of ethylene at 323 K the intensity of this species increases.

In this study the focus was on attempting to identify and characterise both potential changes to chromium oxidation state, and potential intermediates, as this has not been done before.

5.2 Experimental Details

Full details of the synthetic procedures used to prepare the Cr(I) pre-catalyst complexes were given in Chapter 3. All manipulations were performed using standard Schlenk techniques or in a glove box under an argon or nitrogen atmosphere. EPR/ENDOR sample preparation of the pre-catalysts was performed as described in Chapter 4.

The complexes were activated by the *in situ* addition of various equivalents of either Et_3Al or Me_3Al in toluene or hexane. All alkylaluminium activation agents were supplied from *Aldrich* and degassed prior to use. Upon addition of the alkylaluminium, the pre-catalyst solutions turned from a deep blue or purple solution to a pale brown solution. Activation was conducted at room temperature, but once the sample had been prepared, the solution was immediately frozen by placing the tube in liquid nitrogen. EPR spectra were recorded as described in Chapters 3 and 4. Nomenclature of complexes is as described in Chapters 3 and 4.

5.3 Results and Discussion

5.3.1 Addition of Et_3Al in toluene

In order to investigate the changes that occur to the pre-catalyst systems after activation, various experiments involving the addition of Et_3Al dissolved in toluene (hereafter referred to as TEA/toluene) to the pre-catalyst complexes were performed. The EPR spectra were recorded over a range of temperatures (from 10 K to 300 K). As will be evidenced later (and in Chapter 6), two distinct types of paramagnetic centres can be identified from the EPR spectra. The first species is visible at relatively high temperatures ($\geq$ 180 K) and therefore this Chapter will focus singularly on this complex. The remaining centres formed in the activated system are only observed at low temperatures (< 180 K) and will therefore be the focus of Chapter 6.

A variable temperature EPR study (140 – 280 K) was conducted on $[Cr(CO)_4\mathbf{b}]^+$ after activation with 60 equivalents of TEA/toluene (Figure 5.1). The unactivated pre-

catalyst spectra (recorded at 140 and 298 K) are shown in the inset for comparison. As discussed in Chapter 4, the spectrum of the pre-catalyst at room temperature simply displays a broad isotropic signal.

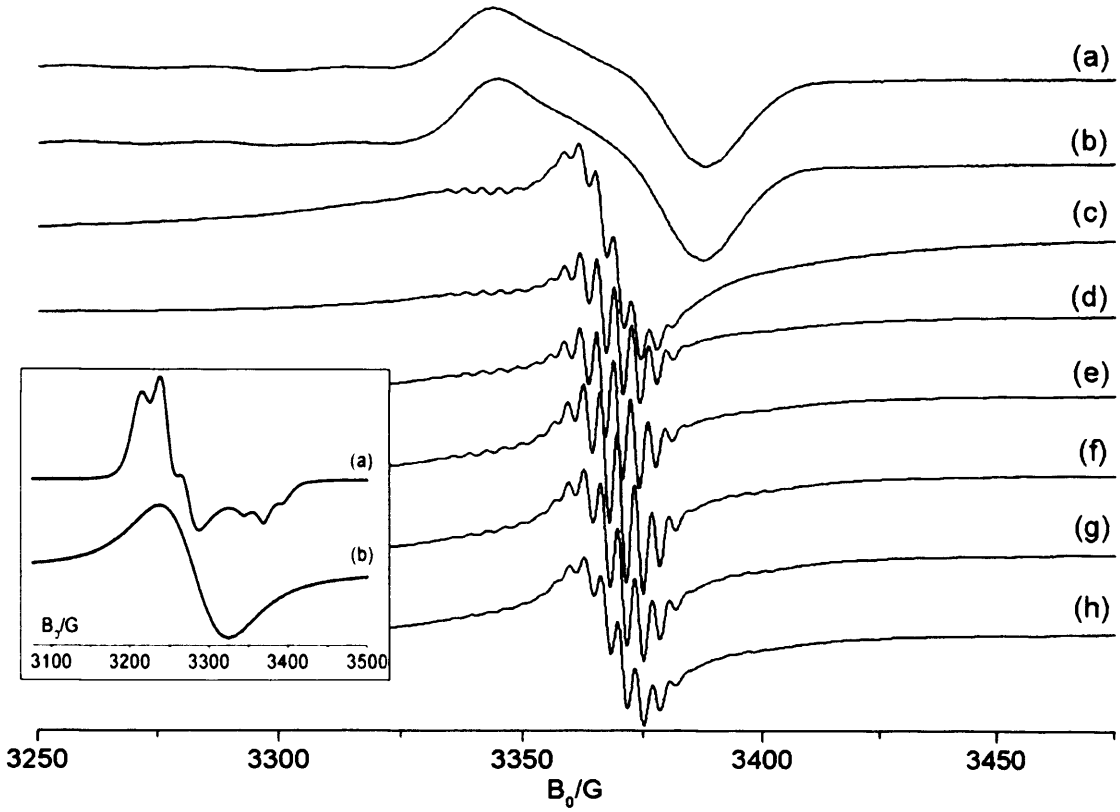

Figure 5.1: Experimental CW-EPR spectra of $[Cr(CO)_4(dppp)]^+$ (**2b**) in dichloromethane/toluene after activation with approximately 60 equivalents of TEA/toluene. The spectra were recorded from 140 K to 280 K in 20 K increments ((a) – (h)). The pre-catalyst spectra ((a) 140 K and (b) 298 K) are shown in the inset.

Upon activation, the EPR signal recorded at 140 K changes dramatically compared to that of the pre-catalyst (Figure 5.1: inset, spectrum (a)), and a new signal appears (Figure 5.1a,b). Addition of TEA must significantly modify the structure, symmetry and electronic properties of $[Cr(CO)_4\mathbf{b}]^+$, producing the new signal which is only observed at temperatures below 180 K (due to rapid spin relaxation). Details of the CW and pulsed EPR/ENDOR investigation of this activated complex at 140 and 10 K will be reported in Chapter 6.

As the temperature is raised, a second EPR signal progressively emerges (Figure 5.1c - h). For clarity, an expanded view of this multiplet signal is shown in Figure 5.2.

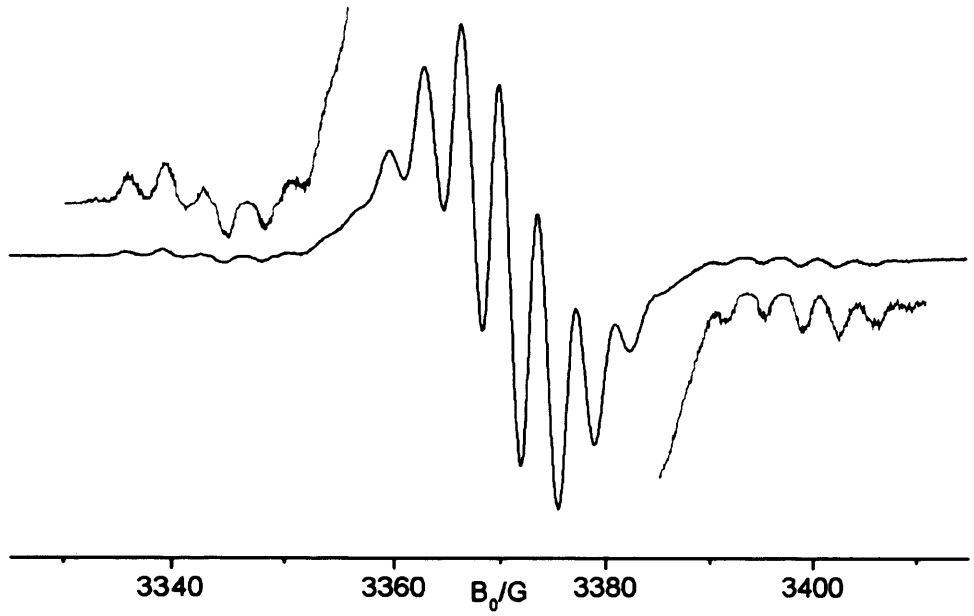

Figure 5.2: Experimental CW-EPR spectrum of $[Cr(CO)_4(dppp)]^+$ (**2b**) in dichloromethane/toluene after activation with approximately 60 equivalents of TEA/toluene. The outer hyperfine couplings are shown with x10 magnification. Recorded at 200 K.

This signal is first observed at 180 K, and it is observable at all higher temperatures up to and including room temperature. The signal appears to consist of an 11-peak central multiplet, along with satellite peaks. To investigate whether the presence of this signal was dependent on the type of complex activated, (i.e., as a function of ligand type), the experiment was repeated by activation of a variety of the pre-catalyst complexes, namely $[Cr(CO)_4\mathbf{d}]^+$, $[Cr(CO)_4\mathbf{e}]^+$ and $[Cr(CO)_4\mathbf{g}]^+$. Exactly the same result was found for each system; namely, an 11-peak multiplet was observed at ≥ 180 K, each with a g_{iso} value determined as 1.988 (spectra not shown for brevity). Therefore the presence of this species is not dependent on ligand type, suggesting it is a feature of all activated $[Cr(CO)_4PP]^+$ complexes. This signal is only present in small amounts, representing *ca.* 10% of the total Cr(I) content.

To determine the dependence of this multiplet signal on the amount of TEA present in the system, various equivalents of TEA were added to the pre-catalyst. The results are shown in Figure 5.3. The multiplet signal first appears at around 2 equivalents of TEA/toluene:Cr(I), and is seen to be superimposed on the pre-catalyst spectrum. At this low level of TEA concentration, only a small fraction of the Cr(I) pre-catalyst has reacted, as evidenced by a very strong pre-catalyst signal. From 10 equivalents and above, the multiplet is the only EPR signal present at this temperature, and appears to be identical at every concentration of TEA. Slight differences may be

observed in the resolution of the spectra, but this is most likely due to concentration effects.

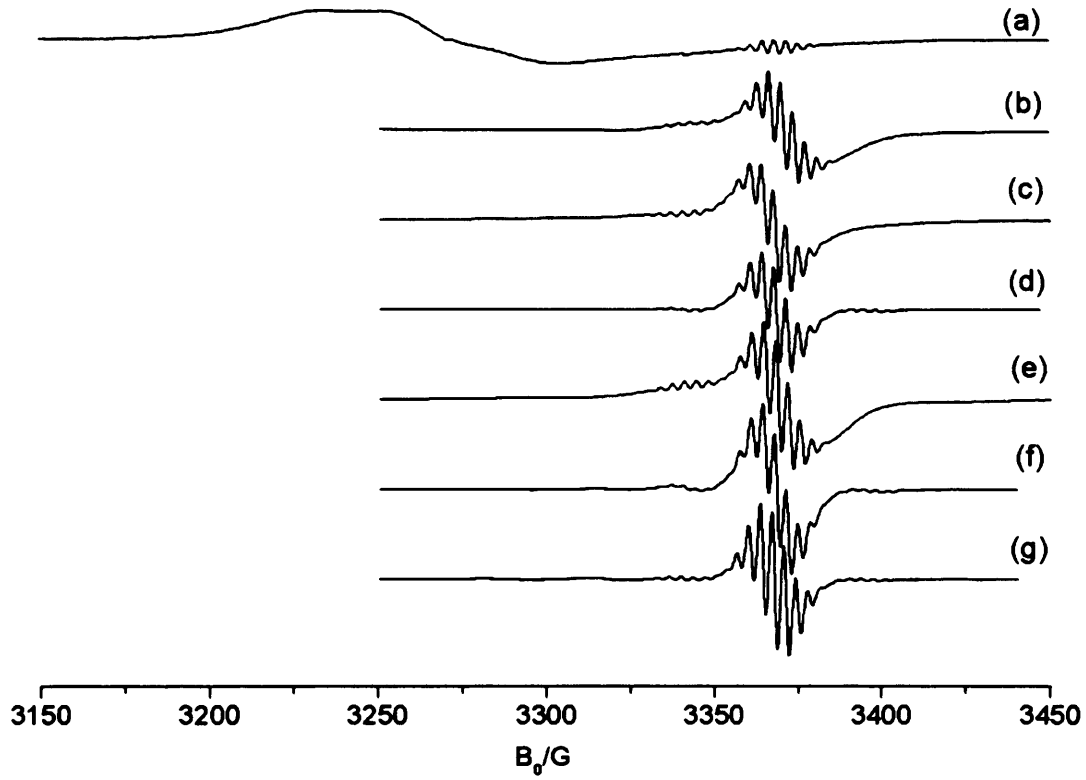

Figure 5.3: Experimental CW-EPR spectra of $[Cr(CO)_4(dppp)]^+$ (**2b**) in dichloromethane/toluene after activation with approximately (a) 2, (b) 10, (c) 20, (d) 60, (e) 100, (f) 300 and (g) 1000 equivalents of TEA/toluene. All spectra recorded at 185 K.

Various interpretations may be advanced to account for the origin of this new multiplet signal. One role of the co-catalyst (usually an alkylaluminium or MAO) is thought to be alkylation of the metal centre.[7] Köhn *et al.*,[8] provided evidence for the formation of a dinuclear chromium-alkyl intermediate species during the activation of Cr-triazacyclohexane systems with MAO. Jabri *et al.*,[9] reacted the catalyst precursor $[CySCH_2CH_2N(H)CH_2CH_2SCy]CrCl_3$ with excess Me_3Al and isolated a dinuclear chromium system with terminal methyl groups. One may consider that the multiplet is possibly due to an anisotropic summation of hyperfine couplings arising from an ethyl fragment co-ordinated to the chromium centre. To test this, the activation experiment was repeated using Me_3Al in toluene (hereafter referred to as TMA/toluene) (see Figure 5.4). The use of both Me_3Al and iBu$_3$Al as co-catalysts has been shown to produce active catalysts for oligomerisation.[4, 10]

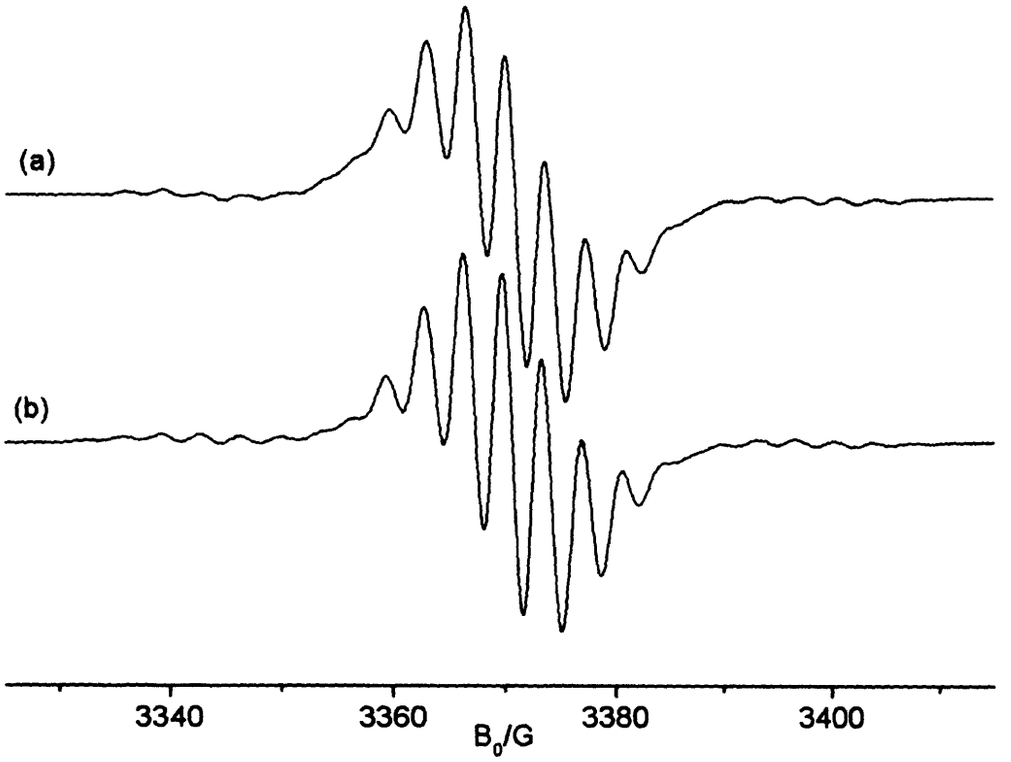

Figure 5.4: Experimental CW-EPR spectra of $[Cr(CO)_4\mathbf{b}]^+$ in dichloromethane/toluene after activation with approximately 60 equivalents of (a) TEA/toluene and (b) TMA/toluene. Recorded at 185 K.

As is evident from Figure 5.4, an identical signal is observed whether TEA or TMA is used in the activation. A slightly different signal, depending on the co-catalyst, would have been expected if co-ordinated alkyl groups were responsible; fewer protons would interact with the metal centre if they originated from TMA rather than TEA. However, the similarity of the two signals shows that the signal must be due to a different species, independent of the co-catalyst. Larger proton couplings would also be expected if co-ordinated alkyl groups were present.

It has been reported, and was discussed in the Introduction (Section 5.1), that one of the paramagnetic species formed upon activation of a $[(PNP)CrCl_2(\mu\text{-}Cl)]_2$ (PNP = $Ph_2PN(i\text{-}Pr)PPh_2$) system, *via* MMAO addition in toluene solvent, is a Cr(I) bis-arene complex, $[Cr(\eta^6\text{-}CH_3C_6H_5)_2]^+$.[6] The isotropic spin Hamiltonian parameters extracted from this complex were g_{iso} = 1.988, $^{1H}a_{iso}$ = 3.57 G (from 10 equivalent protons) and $^{53Cr}a_{iso}$ = 18 G. The same species was reported to be found in $Cr(acac)_3/Et_3Al$ systems in various aromatic solvents;[11] in all cases an isotropic g value of 1.987 was observed. Superhyperfine coupling to arene protons was not always detected, but in toluene solution it was measured as a_{iso} = 3.11 G.

The formation of this sandwich structure was attributed to demetallation of the complex and interaction of the released Cr(I) ions with the aromatic solvent molecules.[6, 11] Similar types of sandwich complexes have been synthesised directly and studied in detail by EPR,[12-15] and all produce a very characteristic isotropic EPR signal based on 10 equivalent protons (for the toluene complex). In all cases, the g value was determined as being 1.988 (± 0.001), the proton superhyperfine coupling as 3.5 (± 0.1) G and where observed, the chromium hyperfine coupling as 18.0 (± 0.1) G.[12-15]

This interpretation could clearly account for the multiplet signal observed in Figures 5.1 – 5.4. The experimental EPR signal (Figure 5.5a) was simulated (Figure 5.5b) with a g_{iso} = 1.988 and based on ten equivalent protons (^{1}H; I = ½, a_{iso} = 3.45 G); the match between the experimental and simulated spectra, including the ^{53}Cr hyperfine pattern (9.5% abundant, I = $^{3}/_{2}$, a_{iso} = 18.0 G) visible in the spectral wings, is excellent. These spin Hamiltonian parameters are identical to those established by the various groups mentioned above. Therefore it is extremely likely that the complex responsible for the new multiplet signal is a chromium sandwich-type complex.

For comparison, simulations were also attempted based on many combinations of couplings that could arise from co-ordinated alkyl groups. The best fitting simulation is shown in Figure 5.5c, and is based on a g_{iso} of 1.988, hyperfine coupling to one ^{53}Cr nucleus (18.3 G), and superhyperfine coupling to two equivalent ^{31}P nuclei (7 G) and to two sets of three equivalent protons (i.e., methyl groups) (3.3 G and 2.8 G). As is evident from the Figure, particularly with respect to the components labelled *, the fit between experimental and simulated data is not as good as that based on ten equivalent protons (5.5b), again making it unlikely that the signal is due to co-ordinated alkyl fragments.

If the signal responsible for this multiplet is indeed attributed to a bis-arene type complex, the question arises as to how it is formed. As mentioned previously, some groups had attributed its formation to demetallation of the complex and interaction of the released Cr(I) ions with the aromatic solvent molecules.[6, 11] This seems entirely possible for the complexes studied here since toluene was used as a solvent both for dissolving the pre-catalyst and in the TEA/toluene co-catalyst mixture.

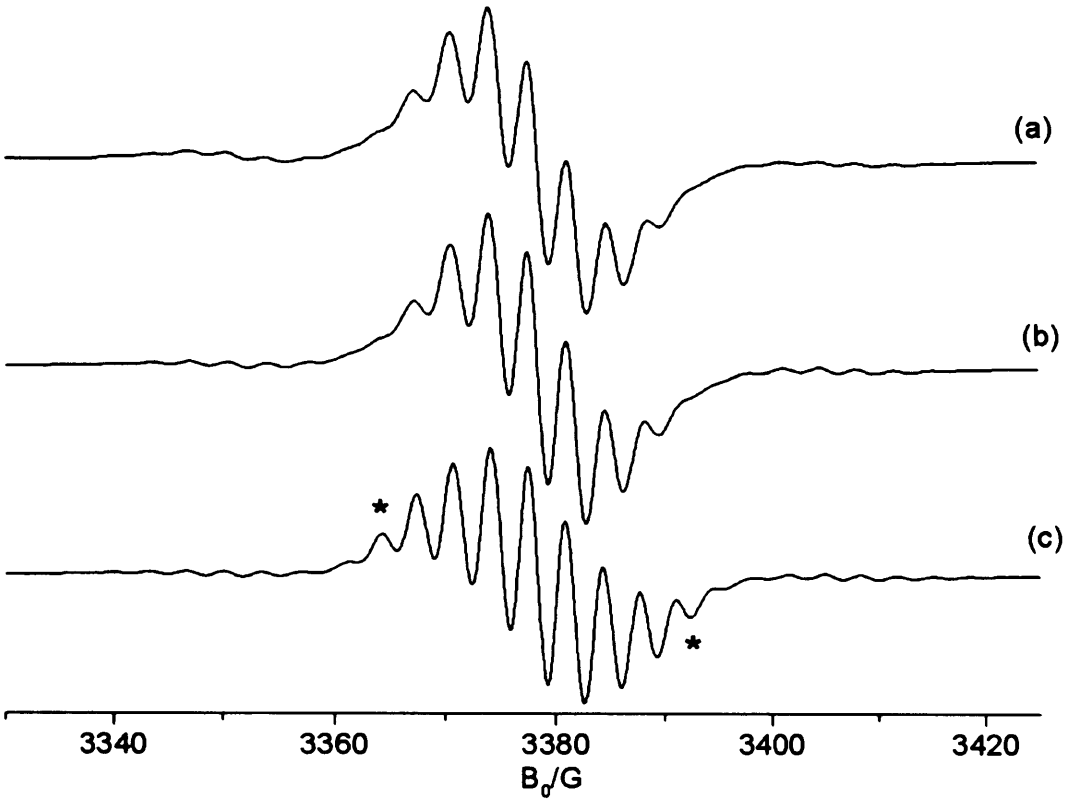

Figure 5.5: Experimental (a) and simulated (b, c) CW-EPR spectra of $[Cr(CO)_4(dppp)]^+$ (**2b**) in DCM/toluene after activation with approximately 60 equivalents of TEA/toluene. * See text for discussion of the parameters used in the simulations. Recorded at 185 K. A linewidth of 2.5 G was used for all CW-EPR simulations (185 K) in this Chapter.

5.3.2 Addition of Et_3Al in hexane

To test this latter hypothesis, the experiment was repeated, but instead of using TEA dissolved in toluene, the pre-catalysts were activated with TEA dissolved in hexane. Firstly it was necessary to check that the pre-catalyst spectra were exactly the same in the absence of any aromatic solvent, so the Cr(I) pre-catalyst was dissolved in dichloromethane only. The spectra of all complexes were identical to those recorded in dichloromethane/toluene (spectra not shown for brevity). Henceforth all samples were prepared in the absence of any aromatic solvent.

$[Cr(CO)_4(dppe)]^+$ (**2b**) dissolved in DCM was activated *via* addition of 60 equivalents of TEA/hexane, and the spectra recorded at 185 K are displayed in Figure 5.6. The spectrum arising from the activation of $[Cr(CO)_4\mathbf{b}]^+$ *via* TEA/hexane addition, in the absence of any aromatic solvent, is identical to that previously observed in toluene. The spin Hamiltonian parameters extracted from the simulation were g_{iso} = 1.988; $^{1H}a_{iso}$ = 3.45 G; $^{53Cr}a_{iso}$ = 18.0 G, (i.e., identical to those using toluene).

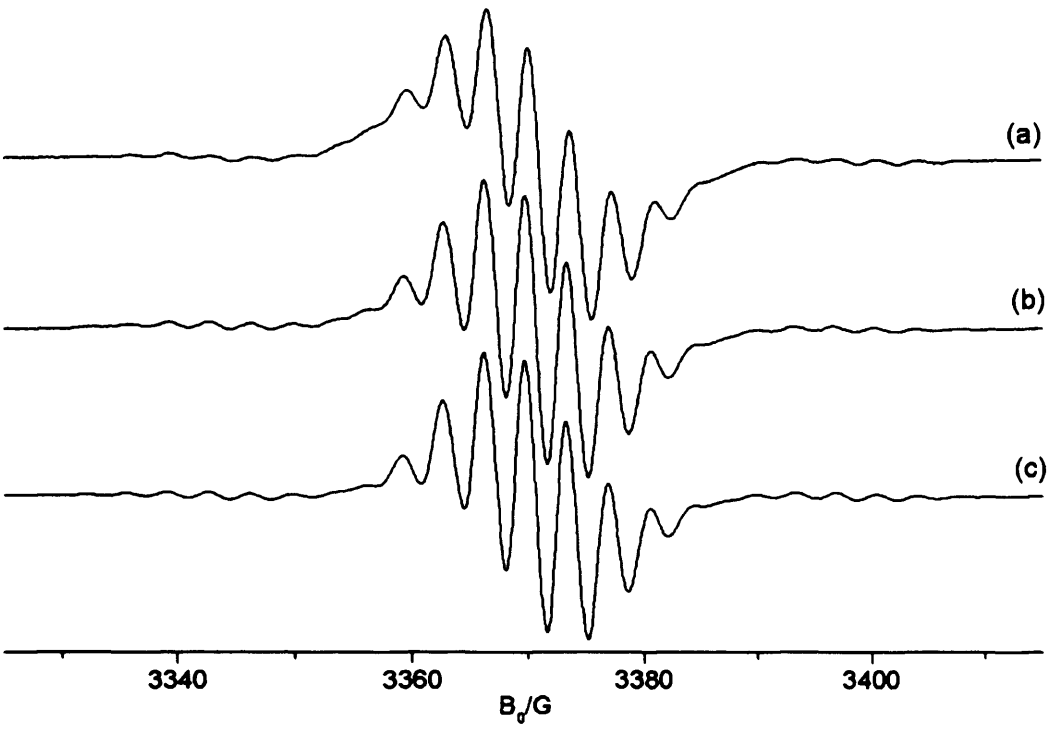

Figure 5.6: Experimental (a, b) and simulated (c) CW-EPR spectrum of [Cr(CO)4(dppp)]+ (**2b**) in dichloromethane after activation with approximately 60 equivalents of (a) TEA/toluene and (b, c) TEA/hexane. Recorded at 185 K.

The observation of this species in the absence of any aromatic solvent is extremely interesting. It was identified previously as a $[Cr(bis\text{-}arene)]^+$ complex, where the arene originated from the aromatic (toluene) based solvent. However, it cannot be solvent-based in this case due to the lack of aromatic solvent molecules. The only remaining explanation for such a distinctive EPR signal, in the absence of aromatic solvent, is the intramolecular co-ordination of two of the phenyl rings from the ligand itself, to the chromium centre. If the bis(diphenylphosphine) ligand is still intact, each phenyl ring posesses 5 ring protons. If two of these rings co-ordinate to the metal centre in an η^6 fashion, this would indeed lead to a situation where 10 quasi-equivalent protons could interact with the electron. This is illustrated in Scheme 5.1:

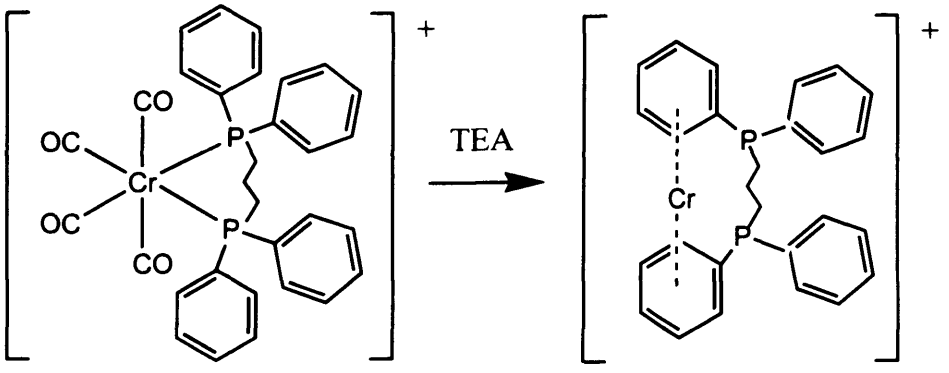

Scheme 5.1: Proposed intramolecular co-ordination of phenyl rings to metal.

Although most Cr(I)(bis-arene) complexes adopt a *trans*-configuration of the aromatic rings, Cr(I) salts with sterically demanding anions have been shown to adopt a *cis*-conformation,[12, 16, 17] lending weight to the scenario described above. Presumably, addition of TEA removes the carbonyl ligands. Decarbonylation of the complex following TEA activation thus destabilises the Cr(I) centres, creating this slipped binding mode with the two ligand phenyl groups rather than the two phosphine centres. In the absence of ^{13}C labelled CO, we cannot determine the number of residual carbonyl groups in $[Cr(L\text{-bis-}\eta^6\text{-arene})(CO)_x]^+$, but it is expected to be zero, hence the nomenclature $[Cr(L\text{-bis-}\eta^6\text{-arene})]^+$. The lack of an EPR-observable phosphorus superhyperfine coupling for this species is not surprising, owing to the displaced location of the Cr, and the absence of *s* ^{31}P in the SOMO of the complex.

There is literature precedent for this type of rearrangement, although it is quite rare. For example, Herwig and Zeiss[18] demonstrated that rearrangement of σ-bonded triphenyl chromium(III) to a bis-arene Cr π-complex occurs upon loss of co-ordinating THF molecules; their stabilising influence was essential to the existence of the σ compound. Similarly, Hsu *et al.*,[19] showed that $Ru_6C(CO)_{16}PPh_3$ converts to $Ru_6C(CO)_{13}((PPh_2(\mu\text{-}\eta^6\text{-}C_6H_5))$ after refluxing in chlorobenzene. One of the phenyl substituents replaces the three carbonyl groups with a change in hapticity of its co-ordination mode. Theopold *et al.*,[20, 21] showed that in solution a dinuclear chromium species containing bridging phenyl groups converted to a mixed-valent species with one benzyl ligand co-ordinating in an η^6 arrangement to one chromium and in an η^3-allyl to the other. Upon heating, this rearranged to yield two Cr(I) bis-arene sandwich complexes linked by an alkyl bridge.[21]

To further confirm this bis-arene proposal, the $[Cr(CO)_4$bis(dicyclohexylphosphino-propane)$]^+$ complex, $[Cr(CO)_4(dcpp)]^+$ (**2h**), was prepared (see Scheme 5.2), in which the ligand phenyl groups are replaced by cyclohexyl groups. The experimental EPR spectrum and corresponding simulation of the newly synthesised $[Cr(CO)_4\mathbf{h}]^+$ complex are shown in Figure 5.7. The spin Hamiltonian parameters extracted are shown in Table 5.1 and as can be observed, are very similar to that of $[Cr(CO)_4\mathbf{b}]^+$ prior to activation.

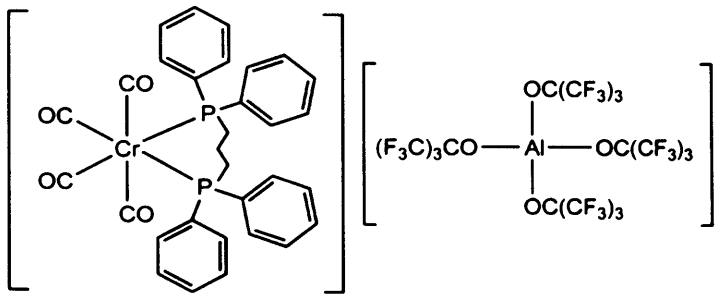

$[Cr(CO)_4\mathbf{b}]^+$

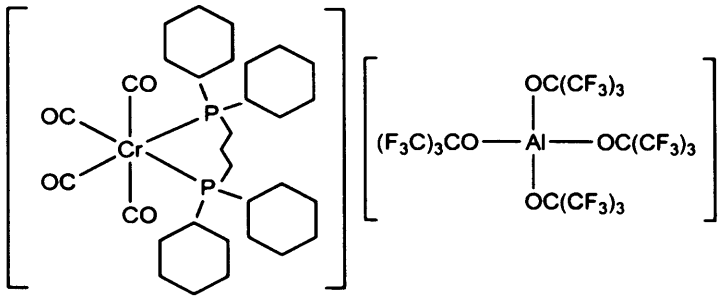

$[Cr(CO)_4\mathbf{h}]^+$

Scheme 5.2: Comparison between Cr^I(bis)diphenylphosphine and Cr^I(bis)dicyclohexylphosphine complexes.

Importantly, this indicates that the structure and electronic properties of the Cr(I) ions are similar in both complexes. This also suggests that they should behave in a similar manner when activated with TEA; any observed differences will then be attributed to the presence of the cyclohexyl rather than the phenyl rings.

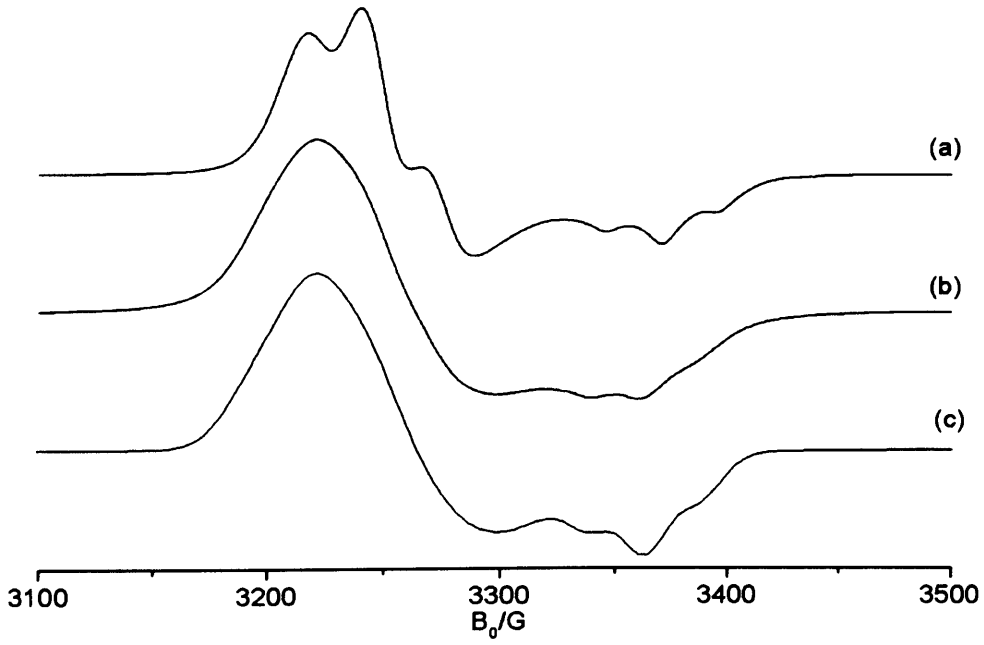

Figure 5.7: Experimental (a, b) and simulated (c) CW-EPR spectra of (a) $[Cr(CO)_4(dppp)]^+$ (**2b**) and (b, c) $[Cr(CO)_4(dcpp)]^+$ (**2h**) in dichloromethane. Recorded at 140 K.

Table 5.1: Spin Hamiltonian parameters extracted from simulation of $[Cr(CO)_4(dppp)]^+$ (**2b**) and $[Cr(CO)_4(dcpp)]^+$ (**2h**)

Complex	g_1	g_2	g_3	$^{31}P\ A_1$ / MHz	$^{31}P\ A_2$ / MHz	$^{31}P\ A_3$ / MHz
$[Cr(CO)_4\mathbf{b})]^+$	2.064	2.064	1.987	71.9	71.9	68.1
$[Cr(CO)_4\mathbf{h}]^+$	2.081	2.051	1.992	67.0	71.8	66.9

These spin Hamiltonian parameters are still consistent with a low-spin d^5 complex where the metal contribution to the SOMO is primarily d_{xy}. There is now however a slight rhombicity to the system: $g_1 \neq g_2 \neq g_3$, and $A_1 \neq A_2 \neq A_3$. The rhombic nature of the system is expected; cyclohexyl groups exhibit either a chair or boat conformation while phenyl groups are planar, so the complex **2h** will not display the distinct axial symmetry of the complexes **2a** – **g**. However, the spectra are still very similar and comparison between them is valid.

The complex $[Cr(CO)_4\mathbf{h}]^+$ was subsequently activated with both TEA/toluene and TEA/hexane. Following activation of $[Cr(CO)_4\mathbf{h}]^+$ with TEA/hexane, no [Cr(bis-arene)]$^+$ species were observed (Figure 5.8a). (* cavity artefact. Note: the sloping baseline in (a) is due to residual $[Cr(CO)_4\mathbf{h}]^+$ producing a weak and broad signal at this temperature). However, when the complex was dissolved in dichloromethane/toluene (1:1) and subsequently activated using TEA/hexane, the formation of [Cr(bis-arene)]$^+$ species could be readily observed (Figure 5.8b); in this case one must specifically form $[Cr(\eta^6\text{-}CH_3C_6H_5)_2]^+$ complexes by reaction of Cr(I) ions with the toluene in solution (see Scheme 5.3).

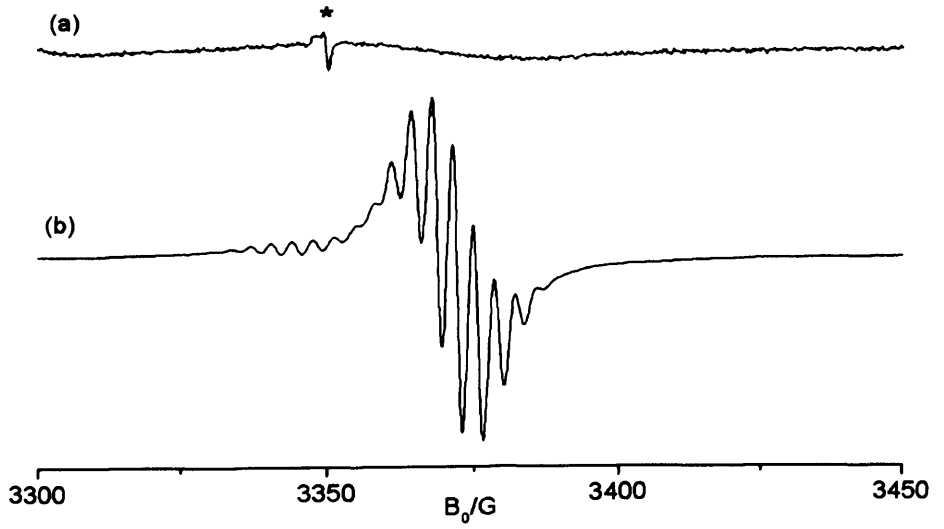

Figure 5.8: Experimental CW-EPR spectra of $[Cr(CO)_4(dcpp)]^+$ (**2h**) in (a) dichloromethane and (b) dichloromethane/toluene after activation with approximately 25 equivalents TEA/hexane. Recorded at 185 K.

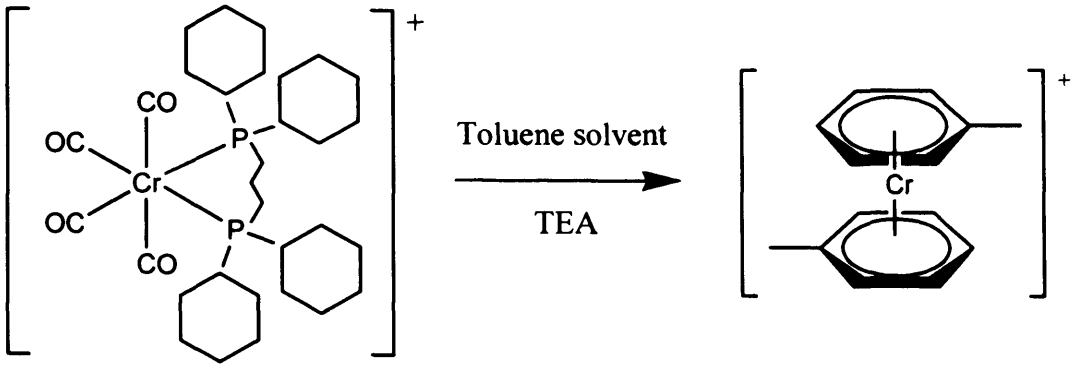

Scheme 5.3: Interaction of pre-catalyst with aromatic solvent.

The lack of the distinctive bis-arene signal when activating a chromium complex without phenyl groups is further confirmation that the signal for **2a-g** in the absence of aromatic solvent must arise due to intramolecular arene co-ordination.

The above EPR findings therefore indicate that two types of $[Cr(bis\text{-}arene)]^+$ complexes (with similar EPR parameters) can form following activation of $[Cr(CO)_4\mathbf{b}]^+$ and $[Cr(CO)_4\mathbf{h}]^+$ with TEA; namely the intramolecular rearranged $[Cr(L\text{-}bis\text{-}\eta^6\text{-}arene)]^+$ complex and the purely solvent (toluene) derived $[Cr(\eta^6\text{-}CH_3C_6H_5)_2]^+$ species. A question arises as to whether solvent (toluene) derived $[Cr(\eta^6\text{-}CH_3C_6H_5)_2]^+$ species can therefore form when the diphenylphosphine complex $[Cr(CO)_4\mathbf{b}]^+$ is dissolved in an aromatic solvent. To investigate this, $[Cr(CO)_4\mathbf{b}]^+$ was dissolved in dichloromethane and activated using TEA/hexane; the resulting EPR spectrum shown in Figure 5.9a is due to $[Cr(L\text{-}bis\text{-}\eta^6\text{-}arene)]^+$. Next $[Cr(CO)_4\mathbf{b}]^+$ was dissolved in dichloromethane/*perdeuterated*-toluene and again activated using TEA/hexane; the resulting spectrum is shown in Figure 5.9b. The spectral resolution, previously found in Figure 5.9a, has disappeared; this is due to the greater number of expected lines and smaller hyperfine coupling for ^2H compared to ^1H. The spectrum was simulated (Figure 5.9) based on the spin Hamiltonian parameters $g_{iso} = 1.987$, $^{2H}a_{iso} = 0.5$ G, $^{53Cr}a_{iso} = 18.0$ G. In other words, this spectrum clearly arises from the $[Cr(\eta^6\text{-}CD_3C_6D_5)_2]^+$ species, which are now preferred compared to the intramolecular $[Cr(L\text{-}bis\text{-}\eta^6\text{-}arene)]^+$ complex (Scheme 5.4).

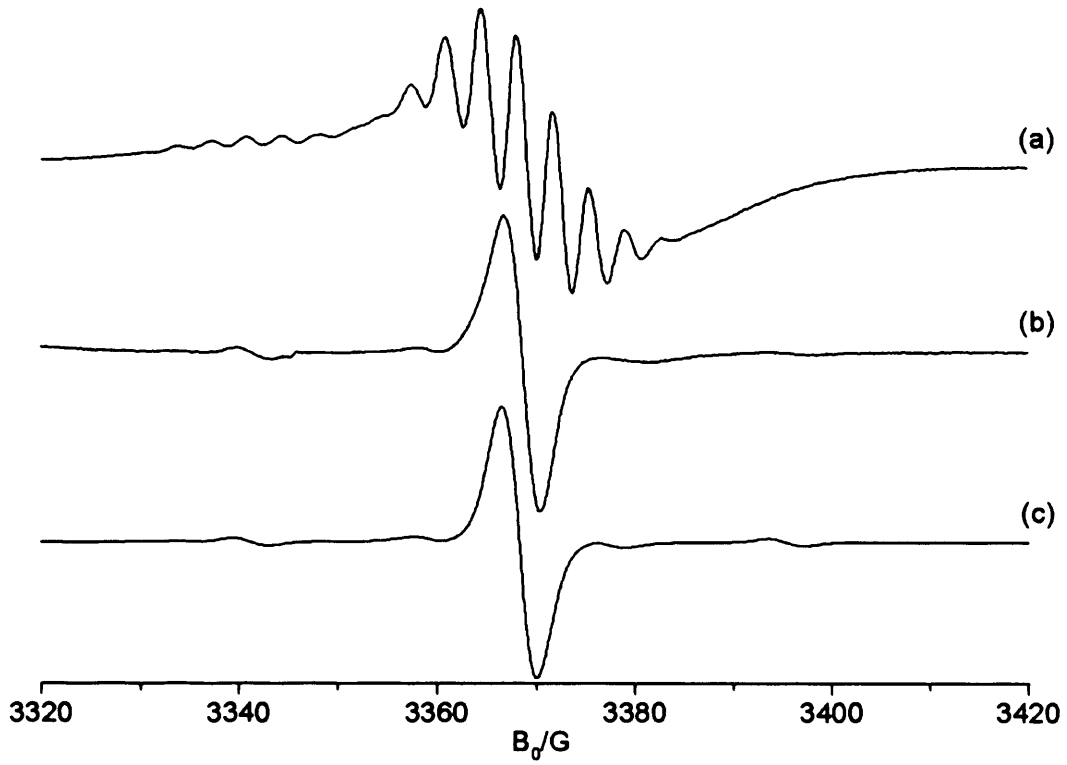

Figure 5.9: Experimental (a, b) and simulated (c) CW-EPR spectra of $[Cr(CO)_4(dppp)]^+$ (**2b**) in (a) dichloromethane and (b, c) dichloromethane/$CD_3C_6D_5$ after activation with approximately 25 equivalents TEA/hexane. Recorded at 185 K.

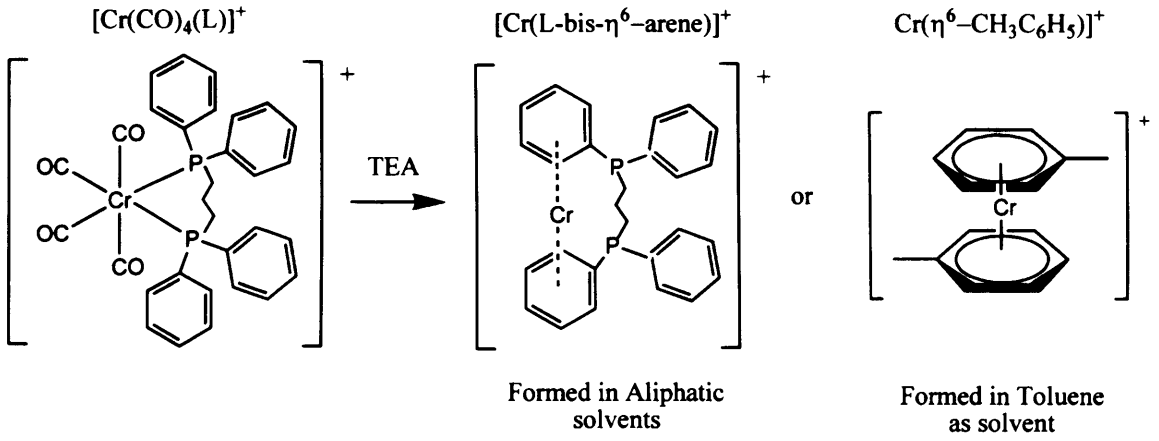

Scheme 5.4: Modes of interaction of metal centre with arene groups.

Importantly, it is known that catalyst systems generated from the combination of Cr/PNP ligands (where the ligands contain aryl substituents), have been shown to be highly sensitive to the choice of ligand used, and both activity and selectivity are affected.[22-24] This would imply that the ligand is not lost during activation; from these studies, such a scenario is possible if intramolecular ligand "slippage" rather than ligand loss occurs. With the ligand now bound in a bis(arene) structure, ligand influences are still possible. Co-ordination of a pendant arene moiety in certain ethylene trimerisation

catalysts is already a well-established phenomenon, and was discussed in Chapter 1. For example, Deckers *et al.*,[25] demonstrated that the selectivity for trimerisation of [η^5-C_5H_3R-(bridge)-Ar]$TiCl_3$ catalysts activated with MAO was dependent on the presence of the pendant arene group on the Cp ligand. Without it, predominantly polyethylene was formed. It was proposed that the arene moiety co-ordinates to the metal during catalysis, stabilising intermediates by η^6 co-ordination, and then dissociating/slipping to make room for incoming substrates. This proposal was supported in work by Blok *et al.*,[26] and de Bruin and co-workers.[27] Similarly, the hemi-labile nature of the pyrrole ligand in the Phillips system was investigated by Rensburg *et al.*,[28] and found to have an important effect on catalysis. Facile ring slippage between η^5- and σ-bonding modes to the metal was postulated to enable formation of both metallacyclic intermediates and alkene products respectively.

The phenomenon of competitive intra- and intermolecular (solvent) arene co-ordination may explain why a significant reduction in catalytic performance for oligomerisation is observed when Cr(I)bis(diphenylphosphine) complexes are used in aromatic solvents compared to aliphatic solvents.[3, 24] Partial inhibition of the catalyst presumably occurs, due to co-ordination of the aromatic solvent to the active Cr centre, reducing the space available for substrate co-ordination.[26] This effect is displayed in the catalytic behaviour of a pre-formed Cr(I) sandwich complex, which is catalytically inactive in aromatic solvents, attributed to the poisoning effect of co-ordination of toluene, but active in methylcyclohexane.[29]

5.4 Conclusions

In conclusion, it has been demonstrated that intramolecular co-ordination (involving change in hapticity) of the Cr(I) centre to the ligand phenyl groups occurs when the $[Cr(CO)_4$bis(diphenylphosphine)$]^+$ complex is activated using TEA or TMA in the absence of aromatic solvents. The resulting bis-arene complex has been labelled [Cr(L-bis-η^6-arene)]$^+$. Formation of this complex following activation probably prevents loss of Cr(I) ions and allows retention of ligand influences. However in aromatic solvents (such as toluene), $[Cr(\eta^6\text{-}CH_3C_6H_5)_2]^+$ solvent based bis(arene) species are preferentially formed. These results may explain why the catalytic performance is significantly reduced when Cr(I)bis(diphenylphosphine) complexes are used in aromatic solvents compared to aliphatic solvents.[3, 24]

Upon activation, only around 10 % of the Cr(I) signal intensity is retained. The loss in intensity may be due to the formation of Cr(I) dimers, as postulated by Brückner *et al.*,[6] or the formation of Cr species with spin-silent oxidation states, which will be discussed further in Chapter 6.

5.5 References

1. *US 5856257, Phillips Petroleum Company Pat.*, 1999.
2. M. J. Overett, K. Blann, A. Bollmann, J. T. Dixon, D. Haasbroek, E. Killian, H. Maumela, D. S. McGuinness and D. H. Morgan, *J. Am. Chem. Soc.*, 2005, **127**, 10723.
3. K. Blann, A. Bollmann, H. de Bod, J. T. Dixon, E. Killian, P. Nongodlwana, M. C. Maumela, H. Maumela, A. E. C. McConnell, D. H. Morgan, M. J. Overett, M. Pretorius, S. Kuhlmann and P. J. Wasserscheid, *J. Catal.*, 2007, **249**, 244.
4. A. J. Rucklidge, D. S. McGuinness, R. P. Tooze, A. M. Z. Slawin, J. D. A. Pelletier, M. J. Hanton and P. B. Webb, *Organometallics*, 2007, **26**, 2782.
5. L. E. Bowen, M. F. Haddow, A. G. Orpen and D. F. Wass, *Dalton Trans.*, 2007, 1160.
6. A. Brückner, J. K. Jabor, A. E. C. McConnell and P. B. Webb, *Organometallics*, 2008, **27**, 3849.
7. J. T. Dixon, M. J. Green, F. M. Hess and D. H. Morgan, *J. Organomet. Chem.*, 2004, **689**, 3641.
8. R. D. Köhn, M. Haufe, S. Mihan and D. Lilge, *Chem. Commun.*, 2000, 1927.
9. A. Jabri, C. Temple, P. Crewdson, S. Gambarotta, I. Korobkev and R. Duchateau, *J. Am. Chem. Soc.*, 2006, **128**, 9238.
10. D. S. McGuinness, M. Overett, R. P. Tooze, K. Blann, J. T. Dixon and A. M. Z. Slawin, *Organometallics*, 2007, **26**, 1108.
11. E. Angelescu, C. Nicolau and Z. Simon, *J. Am. Chem. Soc.*, 1966, **88**, 3910.
12. L. Calucci, U. Englert, E. Grigiotti, F. Laschi, G. Pampaloni, C. Pinzino, M. Volpe and P. Zanello, *J. Organomet. Chem.*, 2006, **691**, 829.
13. T. T. Li, W. Kung, D. L. Ward, B. McCulloch and C. H. Brubaker Jr., *Organometallics*, 1982, **1**, 1229.
14. R. Prins, *J. Chem. Phys.*, 1968, **50**, 4804.
15. R. Prins and F. J. Reinders, *Chem. Phys. Lett.*, 1969, **3**, 45.
16. F. Benetollo, E. Grigiotti, F. Laschi, G. Pampaloni, M. Volpe and P. Zanello, *J. Solid State Electrochem.*, 2005, **9**, 732.
17. R. D. Köhn, D. Smith, M. F. Mahon, M. Prinz, S. Mihan and G. Kociok-Köhn, *J. Organmet. Chem.*, 2003, **683**, 200.
18. W. Herwig and H. Zeiss, *J. Am. Chem. Soc.*, 1959, **81**, 4798.
19. H. F. Hsu, S. R. Wilson and J. R. Shapley, *Organometallics*, 1997, **16**, 4937.
20. W. H. Monillas, G. P. A. Yap and K. H. Theopold, *Angew. Chem. Int. Ed.*, 2007, **46**, 6692.
21. G. Bhandari, A. L. Rheingold and K. H. Theopold, *Chem. Eur. J.*, 1995, **1**, 199.
22. M. J. Overett, K. Blann, A. Bollmann, J. T. Dixon, F. Hess, E. Killian, H. Maumela, D. H. Morgan, A. Neveling and S. Otto, *Chem. Commun.*, 2005, 622.
23. D. S. McGuinness, P. Wasserscheid, W. Keim, C. H. Hu, U. Englert, J. T. Dixon and C. Grove, *Chem. Commun.*, 2003, 334.

24. A. Bollmann, K. Blann, J. T. Dixon, F. M. Hess, E. Killian, H. Maumela, D. S. McGuinness, D. H. Morgan, A. Neveling, S. Otto, M. Overett, A. M. Z. Slawin, P. Wasserscheid and S. Kuhlmann, *J. Am. Chem. Soc.*, 2004, **126**, 14712.
25. P. J. W. Deckers, B. Hessen and J. H. Teuben, *Organometallics*, 2002, **21**, 5122.
26. A. N. J. Blok, P. H. M. Budzelaar and A. W. Gal, *Organometallics*, 2003, **22**, 2564.
27. T. J. M. de Bruin, L. Magna, P. Raybaud and H. Toulhoat, *Organometallics*, 2003, **22**, 3404.
28. W. J. van Rensburg, C. Grove, J. P. Steynberg, K. B. Stark, J. J. Huyser and P. J. Steynberg, *Organometallics*, 2004, **23**, 1207.
29. A. Jabri, C. B. Mason, Y. Sim, S. Gambarotta, T. J. Burchell and R. Duchateau, *Angew. Chem. Int. Ed.*, 2008, **47**, 9717.

Chapter 6

A Low-Temperature EPR and ENDOR Investigation of the Interaction of TEA with the Cr(I) 'pre-catalyst' complexes $[Cr(CO)_4PP]^+$ (PP = $Ph_2PN(R)PPh_2$, $Ph_2P(R)PPh_2$)

6.1 Introduction

The selective production of linear α-olefins, in particular 1-hexene and 1-octene, (as opposed to the original, non-selective oligomerisation method, which produced a statistical distribution of olefin chain lengths),[1, 2] has been demonstrated *via* deuterium labelling to occur *via* a metallacyclic mechanism.[3-5] The active catalyst is generated *in situ* by the addition of a co-catalyst, thought to play the role of alkylating agent,[6] for example an aluminium alkyl or an alkylaluminoxane. The alkylated species then purportedly reacts with ethylene to generate 1-hexene or 1-octene, depending on the reaction conditions.[7] The exact details underpinning this mechanism have however long been inadequately understood. The nature of the active catalyst itself is not fully known; for example, the oxidation state of the chromium during the process is still under debate, although a redox cycle is thought likely. Although several papers have appeared on the correlation between ligand structure and reaction selectivity,[7] a definitive relationship has yet to be discovered, and differences in both activity and selectivity of the catalytic reaction can be tuned depending on which ligand is used.[8, 9]

It is therefore highly desirable to obtain more fundamental information on these systems once they have been activated and after addition of alkene. The characterisation of the pre-catalysts *via* EPR and ENDOR was discussed in Chapter 4, and a high temperature study of the activated complex was subsequently examined in Chapter 5. Here a more detailed characterisation of the activated species at low temperature (≤ 140 K) will be discussed. Comparison of the data will provide an insight into the changes that occur to the systems upon activation, and may provide important information regarding the intermediates in the catalysic reaction. Unlike the well defined paramagnetic systems, and corresponding well resolved EPR spectra obtained for the pre-catalyst complex (Chapter 4) and the resulting Cr(I) bis-arene complex formed in the TEA-activated system (Chapter 5), the remaining EPR spectra (presented in this Chapter) observed for the activated system are very complex and not fully understood. Therefore although the structures of the paramagnetic complexes generated after TEA

addition are not known, this Chapter will nevertheless present the results that were obtained in order to provide an over-view of the changes that occur to the pre-catalyst complex following addition of increasing levels of TEA. Whilst the assignments are speculative for the moment, they nevertheless do demonstrate the complexity of the catalytic system following activation with TEA.

6.2 Experimental Details

Full details of the synthetic procedures used to prepare the Cr(I) pre-catalyst complexes were given in Chapter 3. All manipulations were performed using standard Schlenk techniques or in a glove box under an argon or nitrogen atmosphere. EPR/ENDOR sample preparation of the pre-catalysts was performed as described in Chapters 3 and 4.

The complexes were activated by the *in situ* addition of various equivalents of Et_3Al (hereafter referred to as TEA) in toluene or hexane. All alkylaluminium activation agents were supplied from *Aldrich* and degassed prior to use. 1-hexene was purchased from *Aldrich* and degassed prior to use. Activation and alkene addition were conducted at room temperature, but once the sample had been prepared, the solution was immediately frozen by placing the tube in liquid nitrogen. Upon addition of the alkylaluminium, the pre-catalyst solutions turned from a deep blue or purple solution to a pale brown solution. There was no colour change upon alkene addition. Spectra were recorded as described in Chapters 3 and 4. Nomenclature of complexes is as described in Chapters 3 and 4.

6.3 Results and Discussion

Upon activation, a whole host of paramagnetic species were detected in the low temperature EPR and ENDOR spectra. For ease of discussion and presentation, the following experimental results will be presented for samples activated with low and subsequently higher loadings of TEA.

6.3.1 Addition of low TEA levels (0 – 10 equivalents of TEA)

To examine the changes that occur to the pre-catalyst after activation with TEA, the CW-EPR spectra of $[Cr(CO)_4\mathbf{g}]^+$ were recorded after addition of varying amounts of TEA in toluene. The resulting low temperature spectra are displayed in Figures 6.1 – 6.4. There is negligible change to the pre-catalyst EPR spectrum upon addition of 0.25 – 1.5 equivalents of TEA/toluene (Figure 6.1). Simulation of the spectrum, activated with

1.5 equivalents TEA, enabled the spin Hamiltonian parameters to be extracted. These were identical to those of the pre-catalyst (see Chapter 4, Table 4.1). Addition of 0.25 – 1.5 equivalents of TEA therefore does not measurably alter the electronic or structural characteristics of the complex.

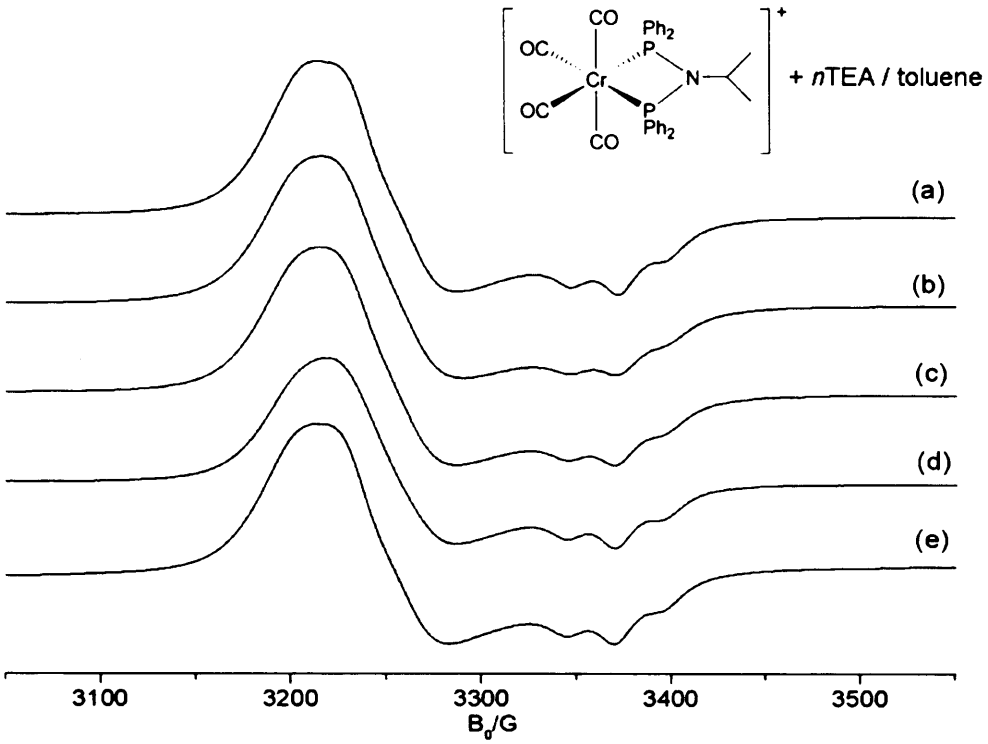

Figure 6.1: Experimental CW-EPR spectra of $[Cr(CO)_4g]^+$ in dichloromethane/toluene, (a) unactivated, and (b-e) after activation with approximately 0.25, 0.5, 1 and 1.5 equivalents of TEA/toluene respectively. Recorded at 140 K.

Addition of 2 – 10 equivalents TEA/toluene was then performed, and the resulting spectra are displayed in Figure 6.2. At a [TEA:Cr] ratio of 2:1, a notable change occurs to the EPR spectrum (Figure 6.2b). The original pre-catalyst spectral profile is still evident but an additional signal now emerges. At approximately 2.5 equivalents [TEA:Cr] only this new signal is visible (Figure 6.2c). The spectrum of [TEA:Cr] 10:1 ratio appears to display a similar signal. Closer inspection reveals the presence of additional minor peaks at ~ 3300 G (labelled * in Figure 6.2c). These peaks are considerably reduced in intensity in Figure 6.2d. As will be discussed later, the origin of these additional peaks are due to ^{31}P interactions.

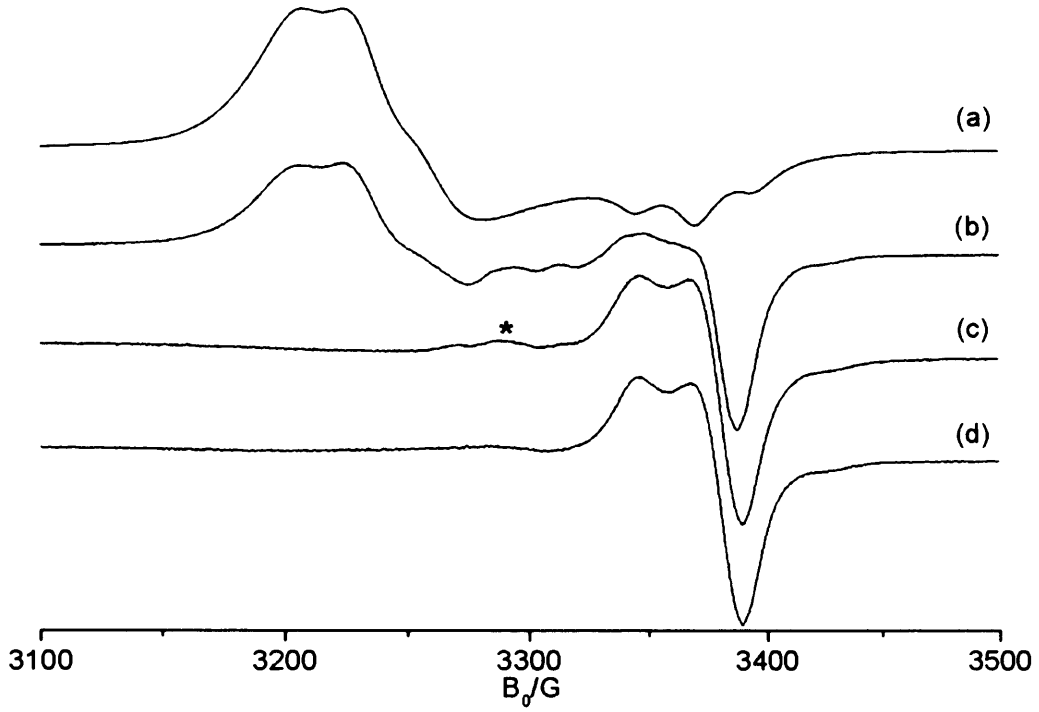

Figure 6.2: Experimental CW-EPR spectra of $[Cr(CO)_4g]^+$ in dichloromethane/toluene, (a) unactivated, and (b-d) after activation with approximately 2, 2.5 and 10 equivalents of TEA/toluene respectively. Recorded at 140 K.

The experiment was repeated to test the reproducibility of the system, and the same results were obtained (shown in Figure A.11 in the Appendix). The experimental and simulated spectra of $[Cr(CO)_4g]^+$, following addition of 2, 2.5 and 10 equivalents of TEA, are shown in Figure 6.3a, b and c respectively. The simulation parameters providing the best fit to Figure 6.3a are based on three separate paramagnetic centres. The first centre is the pre-catalyst species itself, with axial $\boldsymbol{g}$ and $\boldsymbol{A}$ matrices as described previously. This species contributes *ca.* 85% of the total intensity to this spectrum. The second centre (hereafter referred to as Species I) also consists of an axial $\boldsymbol{g}$ matrix, but with reversed g values (i.e., for the pre-catalyst $g_\perp > g_\parallel$ whilst for Species I $g_\parallel > g_\perp$). The spin Hamiltonian parameters extracted from the simulation are given in Table 6.1. Phosphorus superhyperfine couplings are indeed still present in the signal responsible for Species I, but are smaller compared to the pre-catalyst. Species I contributes *ca.* 13% of the spectral intensity at 2 equivalents of [TEA:Cr].

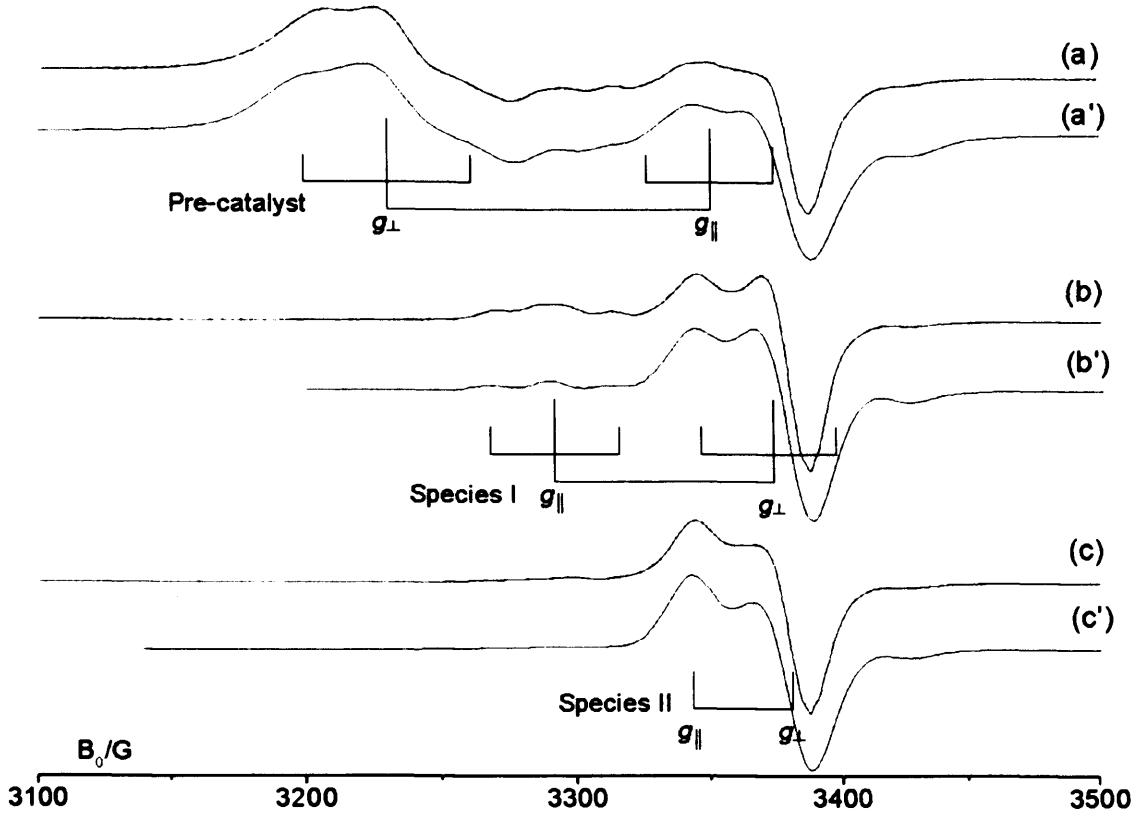

Figure 6.3: Experimental (a, b and c) and simulated (a', b' and c') CW-EPR spectra of $[Cr(CO)_4g]^+$ in dichloromethane/toluene after activation with approximately (a) 2, (b) 2.5 and (c) 10 equivalents of TEA/toluene. Recorded at 140 K. For illustrative purposes, the stick diagrams of the pre-catalyst and Species I and II are shown. Note: each spectrum consists of a combination of all three paramagnetic centres.

The third paramagnetic centre contributing to the spectrum (labelled Species II) also displays an axial ***g*** matrix; a ^{53}Cr hyperfine coupling (natural abundance = 9.5%) is also observable in the perpendicular region of the spectrum (^{53}Cr $A\perp$ = 26G). Presumably the ^{53}Cr coupling in the parallel direction is smaller than the EPR linewdith (~16 G) and hence not visible. The spin Hamiltonian parameters assigned to Species II are summarised in Table 6.1. This centre contributes only ~ 2% to the total spectral intensity.

The spin Hamiltonian parameters of Species I and II were then used to simulate the experimental spectrum corresponding to 2.5 equivalents of TEA (Figure 6.2b). The only difference to the simulation parameters in this case are the relative contributions of each species to the spectrum (see Table 6.1). After taking into consideration the complete absence of the pre-catalyst complex, Species II now contributes a relatively greater amount to the total spectral intensity (22 %) than before. Therefore exactly the same two species are present at this level of TEA activation, but in different relative

quantities. The relative proportion of Species II appears to increase while that of Species I decreases as more TEA is added.

Table 6.1: Spin Hamiltonian parameters obtained by simulation for $[Cr(CO)_4g]^+$ activated with 2, 2.5 and 10 equivalents TEA/toluene.

Figure	TEA:Cr ratio	Species	$g_\perp$	$g_\parallel$	$^{P}A_\perp$*	$^{P}A_\parallel$	$^{Cr}A_\perp$	Abundance (%)
6.3a	2	Pre-catalyst	2.072	1.988	27.0	25.5		**85**
		I	1.968	2.035	24.0	22.0		**13**
		II	1.979	2.0023			26	**2**
6.3b	2.5	Pre-catalyst	2.072	1.988	27.0	25.5		**0**
		I	1.968	2.035	24.0	22.0		**78**
		II	1.979	2.0023			26	**22**
6.3c	10	Precatalyst	2.072	1.988	27.0	25.5		**0**
		I	1.968	2.035	24.0	22.0		**44**
		II	1.979	2.0023			26	**56**

* All A values given in field units of Gauss.

The experimental and simulated spectra corresponding to $[Cr(CO)_4g]^+$ activated with 10 equivalents TEA/toluene are shown in Figure 6.3c. Species I and II were again found to contribute to this spectrum. In this case only the relative intensities of the two species has changed. Now Species II makes up 56% of the total intensity and Species I, 44% (Table 6.1).

A variable power study was conducted on $[Cr(CO)_4g]^+$ activated with approximately 2 equivalents TEA/toluene (Figure A.12 in the Appendix). Variable microwave powers can be used to distinguish between different species contributing to the spectrum. Each species will have its own particular relaxation rate and its spin transition will saturate at a particular microwave power. By comparing the spectrum at various powers, it may be possible to differentiate the components due to a decrease in intensity when saturation is reached. In this case the various components of the spectra all appear to display similar saturation characteristics so it is not possible to distinguish between them. However, this observation has added to the evidence that each species is chromium-based. If Species I or II for example was based on an organic radical, it would have a much longer relaxation time and its intensity would decrease less with increasing power compared to a metal (i.e., Cr) based system.

6.3.1a Identity of Species I

As shown above, addition of approximately 2 equivalents [TEA:Cr] results in a mixed EPR spectrum containing the unactivated pre-catalyst $[Cr(CO)_4\mathbf{g}]^+$ plus two new paramagnetic species, labelled I and II. Both of these latter paramagnetic species are chromium-based, evidenced by the aforementioned saturation studies; the ***g*** matrices exhibit typical characteristics of a transition-metal based system, with a relatively large deviation from the free spin g value. The saturation characteristics are also similar for each species and typical of the Cr(I) pre-catalyst complex.

The first new species (Species I) displays axial ***g*** and ***A*** matrices (Table 6.1). In contrast to the pre-catalyst, these assume the order $g_{\parallel} > g_e > g_{\perp}$. It is known that the ***g*** matrix is dependent on the local magnetic field, which differs as a function of the degree of spin-orbit coupling in the system. In turn, the extent of spin-orbit coupling depends on the molecular orbital coefficients. Hence a change to the ***g*** matrix reflects a change in molecular symmetry. The difference between $g_{\parallel}$ and $g_{\perp}$ (i.e. Δg) has also decreased by comparison to the pre-catalyst, where much larger g anisotropy was observed. Therefore upon addition of TEA, the symmetry of the parent pre-catalyst paramagnetic centre has changed, resulting in the formation of Species I.

Appreciable ^{31}P superhyperfine couplings are visible in the spectrum of Species I, suggesting the presence of two ^{31}P nuclei (see Figure 6.3a). Hence in this species the bis(diphenylphosphine) ligand must still be interacting with the metal centre. The magnitude of the phosphorus interaction has decreased however. As the coupling is still predominantly isotropic, it is likely that the ^{31}P 3*s* character in the SOMO has decreased slightly.

The precise structure of the complex responsible for Species I is not known at this stage. Rieger[10] has presented a detailed review of the EPR parameters for a wide range of low-spin d^5 transition metal complexes, including Cr(I), Mo(I) and W(I). For most reported Cr(I) complexes, the observed order of the ***g*** matrix components is $g_{\perp} > g_e > g_{\parallel}$ (not the reversed values as observed for Species I). In many of these reported systems, the complexes were well-defined (e.g., carbonyl, tris-bipyridyl or nitrosyl complexes). In the current system, it is known that TEA addition results in the loss of carbonyl groups.[11] Partial decarbonylation of $[Cr(CO)_4\mathbf{g}]^+$ would result in a complex with reduced symmetry, i.e., $[Cr(CO)_x\mathbf{g}]^+$, where $x < 4$, and would be likely to exhibit substantially different g values from the parent complex. Without ^{13}CO labelling, one cannot definitively characterise the nature of Species I, but based on the g values alone

one can propose a preliminary structure of a $[Cr(CO)_xg]^+$ type complex, with a d_{xy} or d_{yz} ground state, to account for the reversed ***g*** tensor.[10] Although the precise structure of this $[Cr(CO)_xg]^+$ complex is not know at this stage, one can speculate about its identity based on the available (albeit limited) EPR data. The simulation shown in Figure 6.3b for Species I was based on an axial ***g*** tensor with two equivalent ^{31}P nuclei. However, the resolution of the spectrum, particularly in the perpendicular region, was very poor so the accuracy of the simulation will be compromised. Indeed the parallel components, shown *via* the stick diagram in Figure 6.3b, could equally well be simulated based on two inequivalent ^{31}P couplings (such that the resulting doublet of doublets hyperfine pattern has the appearance of a triplet). It has been reported that piano-stool type complexes can produce axial and rhombic ***g*** tensors with values close to free spin. For example, the symmetric (classic) piano-stool complex (**1**) shown in Scheme 6.1 has reported anisotropic tensors of $g_1 = 1.9969$, $g_2 = 2.0353$ and $g_3 = 2.1339$.[10] However for the more asymmetric complexes, such as (**2**), (**3**) and (**4**) shown in Scheme 6.1, the EPR spectra can possess an axial tensor with g values close to those observed for Species I. For example, (**2**) had reported values of $g_1 = 1.979$, $g_2 = 1.995$ and $g_3 = 2.007$ (i.e., $g_\perp \approx 1.987$ and $g_\parallel = 2.007$)[12] while (**3**) had values of 1.975, 1.997 and 2.010 (i.e., $g_\perp \approx 1.986$ and $g_\parallel = 2.010$) .[13]

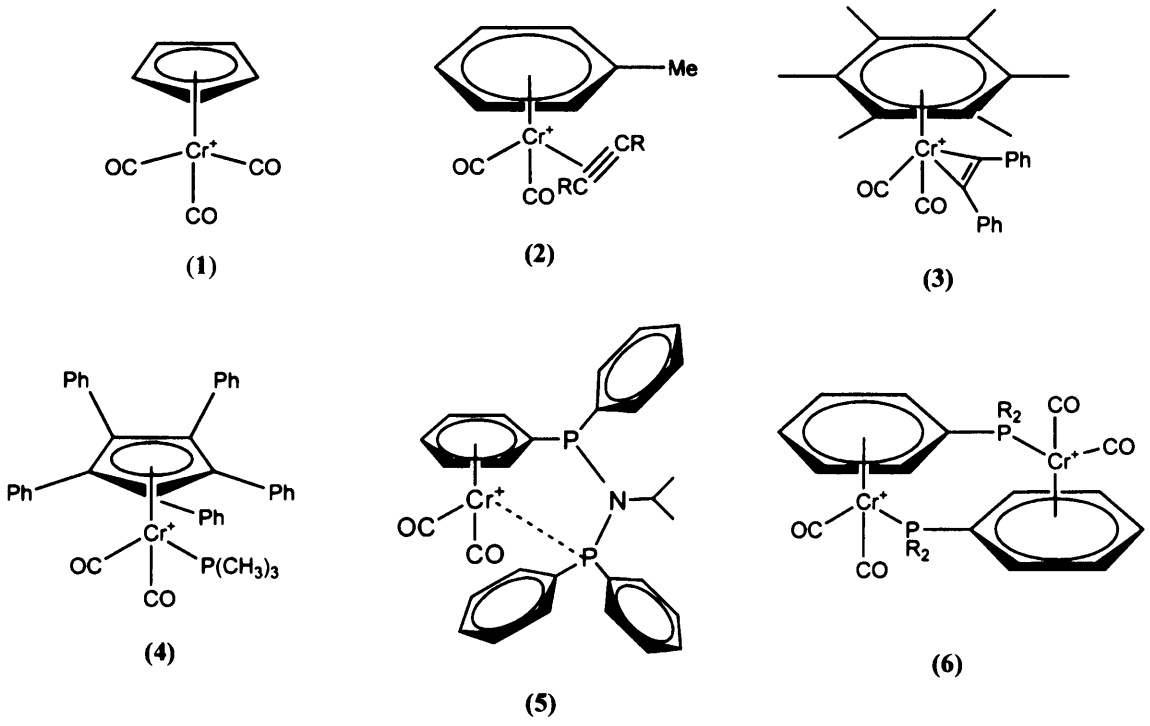

Scheme 6.1: Reported and postulated Cr(I) 'piano-stool' type complexes.

Therefore a very tentative assignment for the structure of Species I is shown in (**5**) in Scheme 1. This complex would be expected to produce g values with $g_{\|} > g_e > g_{\perp}$ (these unusual g values for Cr^+ centres are only observed for piano-stool type complexes). The two ^{31}P nuclei would be inequivalent in this case. It has already been shown in the previous chapter, that addition of TEA leads to the formation of the bis-arene complex *via* decarbonylation of the complex. Complete decarbonylation of the complex clearly leads to bis-arene formation, but partial loss of CO (as in the $[Cr(CO)_x\mathbf{g}]^+$ Species I) could conceivably lead to an intermediate situation, as illustrated in (**5**). Similar types of complexes have been previously reported by Elschenbroich as shown in (**6**),[14] so their existence is not without precedence. This assignment for Species I as (**5**) would of course require further experimentation and theoretical calculations to verify the structure, but the current proposal is a good starting point based on the EPR data.

6.3.1b Identity of Species II

The second Species (II) also displays an axial $\boldsymbol{g}$ matrix with $g_{\|} > g_{\perp}$. However the principal values of the parallel and perpendicular components to the $\boldsymbol{g}$ matrix are different compared to Species I (Table 6.1). Interestingly, the $g_{\|}$ value is equal to that of the free electron spin-only g value. This indicates a high contribution of d_{z^2} to the SOMO. Because the z component of the orbital angular momentum operator l_z does not couple d_{z^2} to any other orbital, the extent of orbital angular momentum in the d_{z^2} orbital is small compared with other d orbitals.[15] Therefore a much smaller deviation of the g factor occurs if the electron is found in this orbital. A ^{53}Cr hyperfine coupling appears to be present in the spectrum of Species II; it is only visible in the perpendicular component however. It is likely that the magnitude of the ^{53}Cr coupling in the parallel direction is smaller than the EPR linewidth and so not visible.

It was already established in Chapter 5 that upon activation, a $[Cr(bis\text{-}arene)]^+$ sandwich complex was formed, and its isotropic spectrum was detected at temperatures of $\geq$ 185 K. As discussed, the complex $[Cr(\eta^6\text{-}CH_3C_6H_5)_2]^+$, or variations thereof, has been extensively studied by various groups *via* EPR spectroscopy. The isotropic spin Hamiltonian parameters of these reported species are identical to those extracted in the current system at higher temperatures (see Chapter 5). Some groups however have also studied the anisotropic, low-temperature spectrum of this $[Cr(bis\text{-}arene)]^+$ complex.[16-19]

Prins and Reinders[16] detected the frozen solution EPR spectrum of $[Cr(\eta^6\text{-}C_6H_6)_2]^+$. An axial signal with $g\perp = 1.9785$ and $g\parallel = 2.0023$ was obtained at 120 K. A proton superhyperfine structure was still visible even at 120 K in certain solvent systems, both in the parallel and perpendicular directions ($^{1H}A\perp = 3.64$ G and $^{1H}A\parallel = 3.1$ G). ^{53}Cr hyperfine coupling was visible only on the perpendicular component ($^{53Cr}A\perp = 26.9$ G). From comparison with the observed isotropic ^{53}Cr coupling value of 18.1 G, the parallel component of the anisotropic coupling was calculated as only 0.5 G, which explains why it is not visible in the spectrum. It is noteworthy that the authors observed no proton hyperfine structure in the frozen solution spectra of $[Cr(\eta^6\text{-}CH_3C_6H_5)_2]^+$; hindered rotation due to the methyl groups was identified as the cause.

Similarly, Li *et al.*,[17] investigated substituent effects in cationic bis(arene) chromium compounds. The spin Hamiltonian parameters obtained were extremely similar to those observed by Prins and Reinders;[16] for $[Cr(\eta^6\text{-}CH_3C_6H_5)_2]^+$ at 133 K Li *et al.*,[17] observed an axial ***g*** tensor with $g\perp = 1.9785$ and $g\parallel = 2.0051$ (where $^{1H}A\perp = 3.7$ G and $^{1H}A\parallel = 3.0$ G); and again, ^{53}Cr coupling was only visible in the perpendicular component with a value of 25.7 G. Calucci *et al.*,[18] observed both frozen solution and solid state spectra of $[Cr(\eta^6\text{-}CH_3C_6H_5)_2][X]$ where X^- = dbcp$^-$ (1,2-dibenzoylcyclopentadienyl) or pcmcp$^-$ (*pentakis*(methoxycarbonyl)cyclopentadienyl). The frozen solutions of these systems exhibited g values of $g\perp = 1.983$ and $g\parallel = 2.004$, and $g\perp = 1.984$ and $g\parallel = 2.007$ respectively; no hyperfine structure was visible. Interestingly, the crystal structure of $[Cr(\eta^6\text{-}CH_3C_6H_5)_2][dbcp]\cdot THF$ displayed an almost *cis*-eclipsed conformation of the toluene rings with respect to the methyl groups. Most $Cr(\eta^6\text{-}CH_3C_6H_5)_2$ complexes adopt a *trans*-conformation. However, although rare, the *cis*- conformation has been observed before.[19]

It is striking that the anisotropic spin Hamiltonian parameters observed by all of these groups[16-19] for related $[Cr(bis\text{-}arene)]^+$ complexes are practically identical to those observed for Species II at 140 K ($g\perp = 1.979$, $g\parallel = 2.0023$ and $^{53Cr}A\perp = 26$ G; see Chapter 5). The average of these g values from the literature is 1.987, which matches the isotropic g value reported here at 180 K. Therefore it is certain that Species II (and the isotropic spectrum of this observed at $\geq$ 180 K) is the $[Cr(bis\text{-}arene)]^+$ complex.

As was discussed in Chapter 5, two types of $[Cr(bis\text{-}arene)]^+$ complexes (with similar EPR parameters) can form following activation of the pre-catalyst with TEA; the intramolecular rearranged $[Cr(L\text{-}bis\text{-}\eta^6\text{-}arene)]^+$ complex and the purely solvent (toluene) derived $[Cr(\eta^6\text{-}CH_3C_6H_5)_2]^+$ species. The solvent derived species was found to

be formed preferentially if both options were possible. The bis-arene signal detected at low temperature in Figures 6.2 and 6.3 was obtained using toluene as solvent. Presumably this is the solvent-derived version of the complex as toluene was used in all experiments. To test if the intramolecular rearranged [Cr(L-bis-η^6-arene)]$^+$ complex could be detected, the pre-catalyst was activated with TEA dissolved in hexane and the frozen solution spectrum recorded. All pre-catalyst spectra were recorded again in DCM only and found to be identical to those recorded in DCM/toluene. The spectrum corresponding to [Cr(CO)$_4$g]$^+$ activated with 10 equivalents TEA/hexane was then simulated and the results are displayed in Figure 6.4.

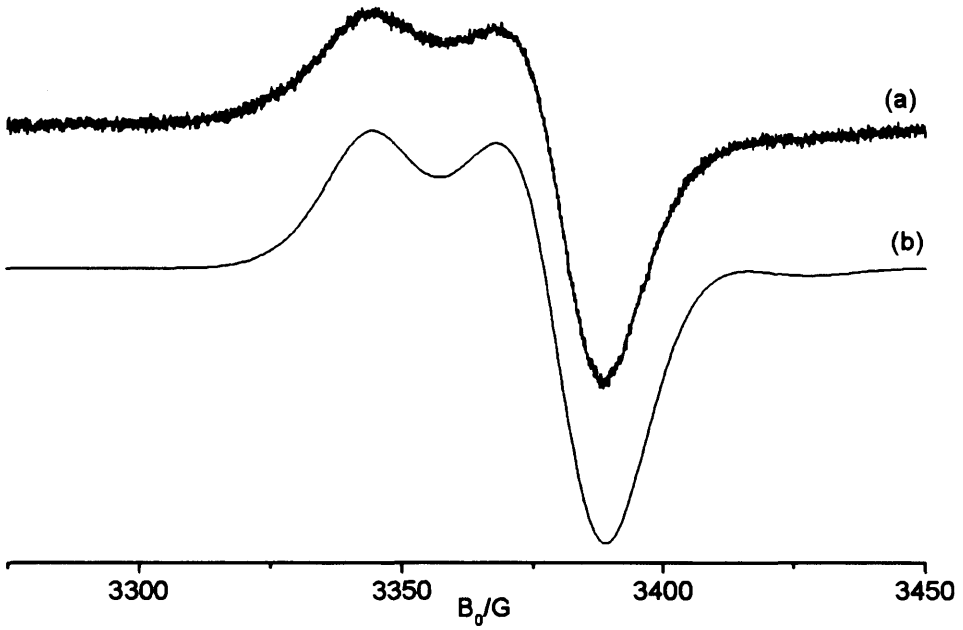

Figure 6.4: Experimental (a) and simulated (b) CW-EPR spectra of [Cr(CO)$_4$g]$^+$ in dichloromethane after activation with approximately 10 equivalents of TEA/hexane. Recorded at 140 K.

As before, the best fit is obtained by introducing two paramagnetic centres into the simulation, namely Species I and Species II. Species I exhibited parameters of $g\perp$ = 1.968, $g_\parallel$ = 2.035 and $^{31P}A\perp$ = 24 G, $^{31P}A_\parallel$ = 22 G, and contributed 50 % to the spectral intensity. It is difficult to determine the accuracy of these parameters as the features are masked by the broad linewidth (~ 20 G in the perpendicular component and ~ 18 G in thr parallel component); however, without these parameters the simulated spectrum did not produce a good fit. Species II exhibited parameters of $g\perp$ = 1.979, $g_\parallel$ = 2.0023 and $^{53Cr}A\perp$ = 26 G, and contributed 50 % to the total intensity. These are identical to the parameters observed above for Species II when the complex had been activated in TEA/toluene.

Therefore, the EPR spectrum shown in Figure 6.4, with spectral features characteristic of a $[Cr(bis\text{-}arene)]^+$ complex, does not arise from co-ordination of Cr(I) by toluene. The same species as was observed at $\geq$ 180 K is being formed; an intramolecular rearrangement of Cr(I) in the activated and decarbonylated $[Cr(CO)_x\mathbf{g}]^+$ complex to produce a bis-arene complex labelled $[Cr(L\text{-}bis\text{-}\eta^6\text{-}arene)]^+$ in which the Cr(I) is now co-ordinated to the ligand phenyl groups.

6.3.2 Addition of high TEA levels (15 – 1000 equivalents)

The EPR spectra of $[Cr(CO)_4\mathbf{g}]^+$ activated with 15 – 1000 equivalents of TEA/toluene are displayed in Figure 6.5. These spectra are dramatically different compared to those shown earlier for the low levels of TEA (see earlier Figures 6.1 - 6.4). Due to the very broad EPR linewidths present in these spectra, an accurate and reliable simulation of the spectra is not possible based only at this frequency. However, owing to the similarity between Figure 6.5a and Figure 6.4a shown earlier, it is clear that the Cr(I) bis-arene complex is still a major component of the system following activation with 15 equiavlent of TEA (Figure 6.5a). As the TEA levels increase, the spectra evolve as another signal emerges, until eventually at 1000 equivalents of TEA this new signal (herafter labelled Species III) dominates the spectrum. Whilst the EPR spectrum of Species III could not be reliably simulated based on the available data, it does appear to possess a low *g* anisotropy with *g* values close to free spin.

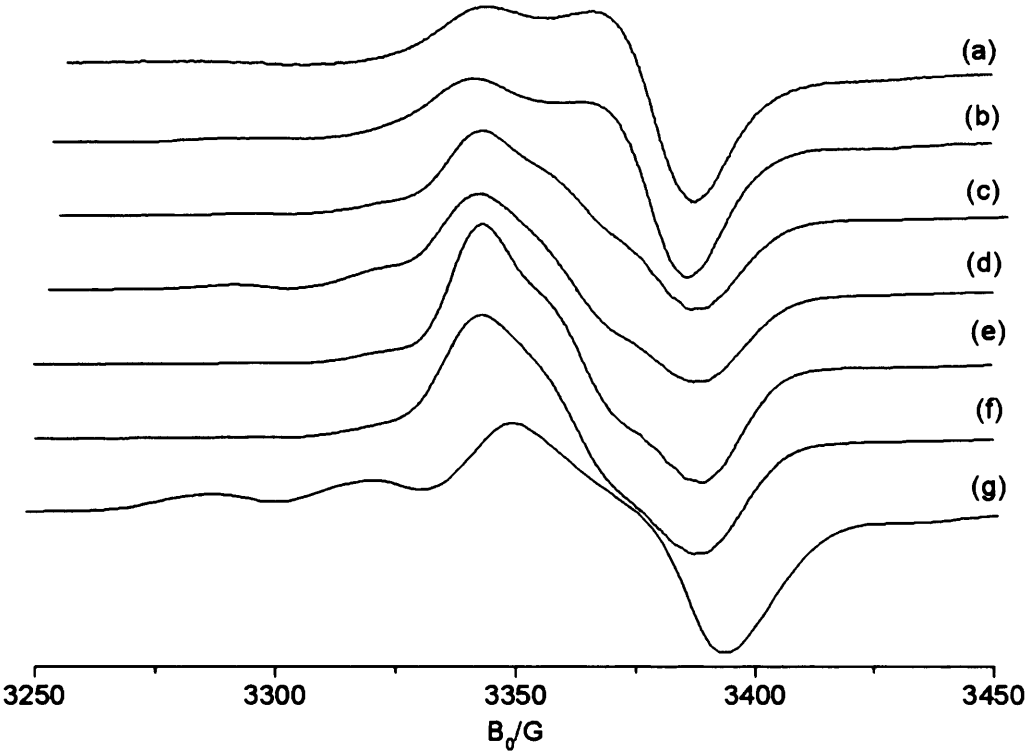

Figure 6.5: Experimental CW-EPR spectra of $[Cr(CO)_4g]^+$ in dichloromethane/toluene after activation with approximately (a) 15 (b) 20 (c) 40 and (d) 60 (e) 100 (f) 300 and (g) 1000 equivalents of TEA/toluene. Recorded at 140 K.

6.3.2a Identity of Species III

It has been proposed that decarbonylation and subsequent alkylation of the metal centre must occur in order to generate an active catalyst for oligomerisation. Indeed, this is thought to be the role of the co-catalyst.[20] It has even been proposed that the addition of the co-catalyst changes the redox state of the chromium. The loss of *x*CO ligands would change the geometry of the chromium complex and consequently be reflected in the EPR spectra (*via* the changes to the ***g/A*** matrix, as observed for Species I and II). Rucklidge *et al.*,[11] conducted an experimental catalytic study into the activity and selectivity of complex $[Cr(CO)_4g]^+$ for oligomerisation as a function of increasing TEA level. The complex was active for oligomerisation only after addition of 50 – 400 equivalents TEA, with an optimum activity at around 200 equivalents. No exploration of TEA levels lower than 50 equivalents was investigated. In other words, the quantity of added TEA is crucial to the catalytic performance of these Cr complexes. For this reason it is important to understand the nature of the paramagnetic centres formed under these high TEA conditions (i.e, the conditions under which Species III is found).

Various plausible interpretations can be advanced on the identity of Species III. First of all, the alternative oxidation states of Cr(II), Cr(IV) and Cr(V) can all be

immediately discounted since they are either EPR silent at these (X-band) frequencies or have characteristic features that are not remisicent of Species III. Secondly, one may consider the possibility that Species III originates from a high spin ($S > ½$) centre. However, high spin Cr(I) (d^5) is unlikely to account for the signal shown in Figure 6.5g as the expected zero field splitting parameters would be very large at X-band. Thirdly, one may consider the possibility of interacting Cr....Cr centres as a plausible explanation. Elschenbroich *et al.*,[21, 22] have reported the EPR spectra of several types of Cr(I) bis-arene complexes, including the EPR spectra for a series of high spin Cr(I)...Cr(I) dications.[21, 22] For example, the monocations of the complexes shown in Scheme 6.2, labelled (**7**) and (**8**), were reported to possess spin Hamiltonian parameters typical of the Cr(I) bis-arene complexes discussed earlier (i.e., an axial ***g*** matrix with $g_{\|} \approx g_e > g_{\perp}$; see Table 6.1, Species II). By comparison, the dications of (**7**) and (**8**) displayed EPR spectra typical for randomly oriented triplet state species ($S = 1$) caused by spin-spin interactions between the two neighbouring Cr(I)...Cr(I) centres.

Table 6.2: Spin Hamiltonian parameters obtained for the monocation and dication complexes (**7**) and (**7**), illustrated in Scheme 6.2.

Monocation	$g_{\|}$	$g_{\perp}$	$A_{\|}$ (^{1}H) / G	$A_{\perp}$ (^{1}H) / G	$A_{\perp}$ (^{53}Cr) / G
(**7**)	2.0025	1.9792	3.2	3.7	26.0
(**8**)	2.0030	1.9792	3.2	3.7	26.0

Dication	g_x	g_y	g_z	$\|D\|$ / cm^{-1}	$\|E\|$ / cm^{-1}
(**7**)	2.001	1.983	1.975	0.0321	0.0079
(**8**)	1.982	1.995	1.988	0.0257	0.0038

These dications produced a distinctive half field peak (typical of triplet state paramagnets). A calculation of the interspin distance between the two chromium centres in (**7**), based on these EPR parameters, was 4.31 Å, which was in good agreement with the 4.36 Å estimated from the molecular model. A reliable interspin distance in (**8**) was not possible because of the range of conformations about the C-C bond linking the two bis-arene units.[22] Elschenbroich also studied the radical dication of (**9**). In this case, the exchange interaction J was much smaller than the hyperfine interactions of a(^{1}H) and a(^{53}Cr). Thus in fluid solution the EPR linewidth for (**9**) was only slightly broader than the linewidth typical for the monocation of (**9**). This behaviour is in good agreement with the presence of two singly occupied, orthogonal Cr($3d_z^2$) orbitals separated by 8.49 Å. However, at low temperature an anisotropic EPR spectrum was obtained with a very

weak half field transition, possessing zero field parameters of $|D|$ = 0.0027 cm^{-1}, $|E|$ = 0.0006 cm^{-1}.[21] Thus even in cases where the Cr(I) bis-arene complexes are separated by large distances, evidence of their interaction can still be obtained by observation of the half field transition.

To explore further the possibility that Species III originates from an interacting dimeric Cr(I)...Cr(I) centre, the half field region of the EPR spectrum was examined. The resulting spectra are shown in Figure 6.6, and a distinctive half field peak was observed.

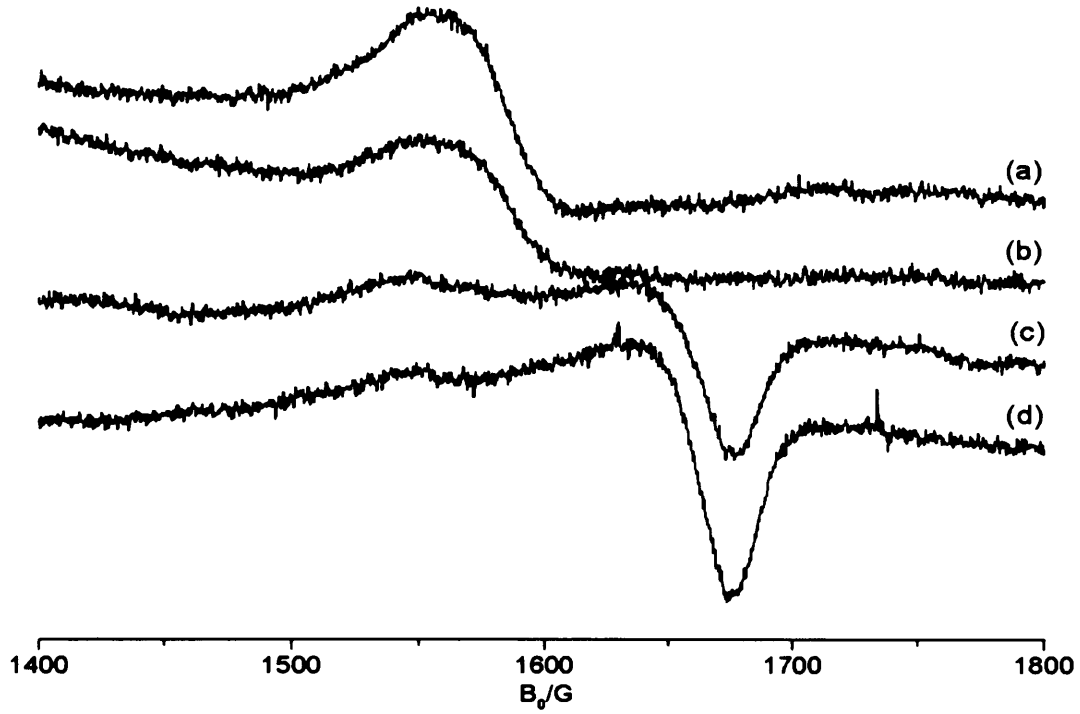

Figure 6.6: Experimental CW-EPR spectra of $[Cr(CO)_4\mathbf{g}]^+$ in dichloromethane/toluene after activation with approximately (a) 10 (b) 20 (c) 60 and (d) 100 equivalents of TEA/toluene. Recorded at 140 K.

Without doubt, this spectrum proves the existence of high spin Cr centres in the TEA activated system (it should be noted that no half field transitions were visible in the pre-catalyst spectrum). The reproducibility in the generation of these half field features was unfortunately poor from experiment to experiment. Nevertheless, the general trend seemed to indicate that the intensity of this half field resonance increased as a function of increasing TEA levels.

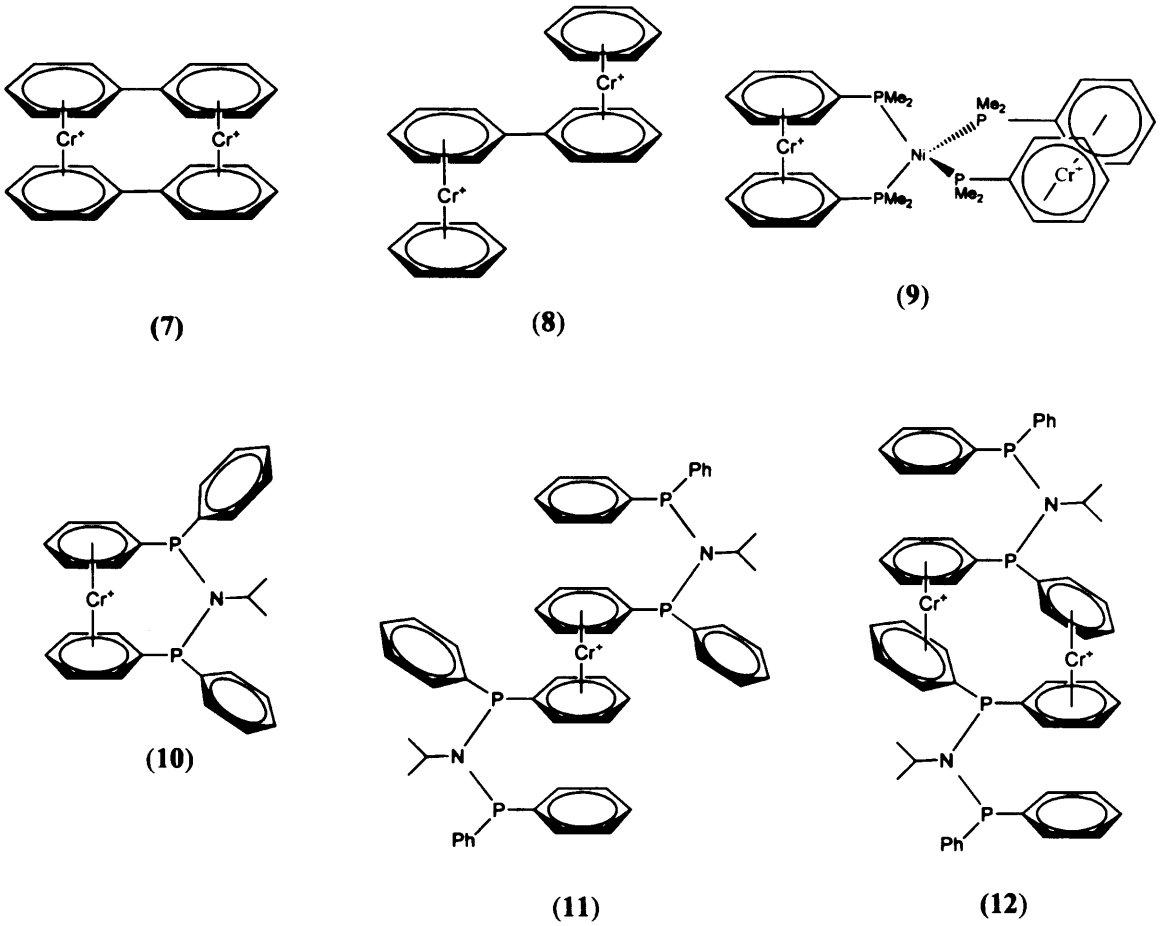

Scheme 6.2: Reported and postulated bis-arene complexes.

It has already been shown that Species II is attributed to the intramolecularly formed bis-arene complex (**10**) (see Scheme 6.2). This centre was formed at lower levels of TEA (the experimental evidence points to the structure illustrated in (**10**), rather than (**11**), as the same signal was observed even under dilute conditions). Extensive decarbonylation of the the entire solution would be required to form the bis-arene complexes of the type shown in (**11**), where most of the complexes have become demetallated. However the half field signal was more pronounced at higher TEA levels, suggesting that Species III could be associated with the highly demetallated case and dimers of the type shown in (**12**) could easily be formed in these circumstances. As the work of Elschenbroich has shown, such dimers can indeed be formed and characterised by relatively small zero field parameters. Elschenbroich *et al.*,[22] confirmed the propensity of a dinuclear bis(arene) complex to exhibit paramagnetism, i.e. a triplet state of the two electrons, rather than spin-pairing. This is compared to a dinuclear ferrocene analogue, where a diamagnetic state is favoured due to the closer proximity of the the metal atoms.

6.3.3 Diamagnetic vs paramagnetic centres in TEA activated system

It has been reported that the addition of a co-catalyst, such as modified methylaluminoxane (MMAO), to the Cr(III)-PNP systems leads to a substantial decrease in the EPR signal intensity.[23] This was attributed to the formation of diamagnetic Cr(II) centres or 'EPR silent' spin paired paramagnetic Cr(I)-Cr(I) centres. To examine this effect, starting from the Cr(I)-PNP pre-catalyst, quantative EPR measurements were therefore performed.

It should be noted that the absorption of microwave energy is directly proportional to the number of spins present. The rate of energy absorption is expressed as:[15]

$$\frac{dE}{dt} = N\frac{(\Delta E)^2}{kT}\frac{P}{1+2PT_1} \qquad (6.1)$$

where N is the total number of spins, P the transition probability, T_1 the spin-lattice relaxation time, ΔE the spin level energy separation and the other symbols have their usual meaning. Therefore whilst the absorption signal is inversely proportional to the relaxation time, which may be different between the pre-catalyst and the activated species, some general trends are still evident in the EPR comparison between the pre-catalyst intensities and the activated intensities (i.e., the EPR spectra before and after TEA addition).

In all cases, an overall decrease in signal intensity was observed following addition of TEA/toluene. At low levels of TEA addition (2 – 10 equivalents), the relative intensity of the EPR signal is extremely low; less than 10 % of the original pre-catalyst signal, so most of the species formed are in fact EPR silent. Interestingly, as the amount of TEA added to the system was increased, the signal intensity also increased slightly. At 300 equivalents [TEA:Cr], the signal intensity was around 35% that of the pre-catalyst. Unfortunately no comparison was made between the pre-catalyst and activated complex above this concentration.

This dramatic decrease in signal intensity upon addition of TEA indicates that the activation of the Cr(I) pre-catalyst results in a mixture of paramagnetic (i.e., Species I, II and III) and 'spin-silent' Cr species. These spin-silent entities could either be diamagnetic complexes, or alternatively species with a total electron spin quantum number that is an integer (as opposed to half-integer), or even a mixture of both species. Half-integer spin species (Kramers ions) always have an allowed $\Delta M_S = \pm 1$ transition within the $M_S = \pm 1/2$ levels, at any frequency. Integer-spin species (non-Kramers ions)

do not have this allowed transition.[24] To observe a resonance, an increase in operating frequency by an order of magnitude is needed for an inter-Kramers ($\Delta M_S = \pm 1$) transition. Hence no resonant absorption is possible in diamagnetic / non-Kramers species, or the spectra are broadened to such an extent they are not visible due to the extremely low intensity. The only way of distinguishing between these two types of spin-silent species is to record the spectra at a higher microwave frequency, which may enable existing spin transitions to be observed. However to observe a non-Kramers transition an operating frequency of around 95 GHz would be necessary (W-band), which was not performed on these highly air sensitive compounds.

It is also possible that some spin-silent species may be anti-ferromagnetically coupled Cr(I) dimers. In this case spin-pairing would lead to a total spin quantum number of $S = 0$ and therefore loss of EPR intensity. This theory has been postulated by Brückner *et al.*,[23] to explain the decrease in signal intensity to only *ca.* 5% of the original, upon activation of a $Cr(acac)_3$/PNP system. It was proposed that dimer (or cluster) formation may have occurred to alleviate unsaturation of a transient species, formed perhaps after alkylation then reductive elimination of ethane. Dimerisation is also proposed for a Cr(III) triazacyclohexane system, which upon activation with MAO purportedly becomes a dinuclear species.[25] In this case however, each chromium atom retains its valence oxidation state.

As discussed in Chapter 1, the addition of 1-hexene as a model alkene can be used in the current Cr(I) system. This alkene is easier to handle and the solution can be quickly frozen, facilitating the immediate or rapid identification of a short-lived species. Furthermore, it has been demonstrated that selective oligomerisation of longer chain alkenes can occur, appearing to operate *via* the same metallacycle mechanism as the oligomerisation of ethylene.[25]

Therefore 1-hexene was systematically added to a range of different complexes (**2b**, **d**, **e**, **g**) at different concentrations. In general, **no** change in the signal profile was observed. For example, the variable temperature EPR spectra of TEA-activated $[Cr(CO)_4\mathbf{g}]^+$ following addition of 100 equivalents of 1-hexene are shown in Figure 6.7. The spectra are virtually identical to those previously shown for this activated complex; both Species I and II are visible, and the presence of 1-hexene does not appear to have altered the signals. However, even though there was no change in the shape and profile of the spectra, the signal intensity increased in all cases (to a maximum of 2.4 times).

No obvious correlation could be detected in the amount of alkene added versus the increase in signal intensity.

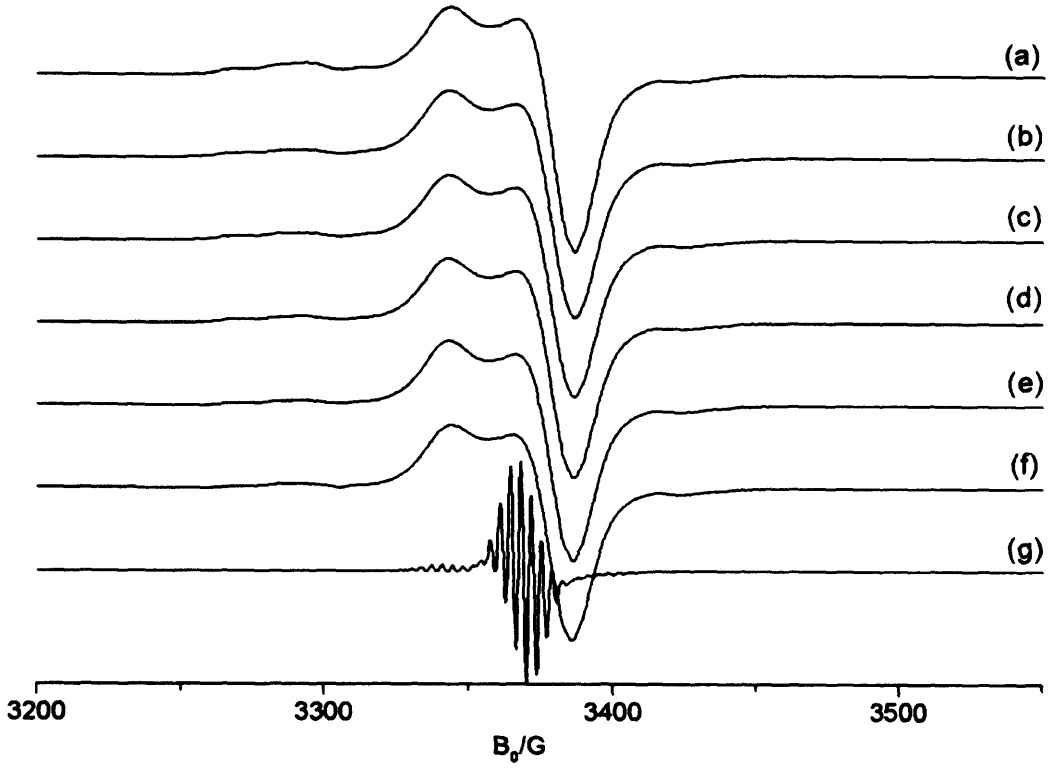

Figure 6.7: Experimental CW-EPR spectra of $[Cr(CO)_4g]^+$ in dichloromethane, activated with approximately (a) 10 equivalents TEA/toluene and (b – g) 10 equivalents TEA/toluene and 100 equivalents 1-hexene. Recorded at (a, b) 140, (c) 150, (d) 160, (e) 170, (f) 180 and (g) 185 K.

6.3.4 Analysis of activated system using advanced EPR techniques

In order to obtain further information on the structures of the activated Cr(I) centres, a series of advanced EPR methodologies were applied, including CW and pulsed ENDOR and ESEEM. For this analysis the $[Cr(CO)_4g]^+$ complex was activated with approximately 60 equivalents TEA/toluene; the resulting EPR spectrum and associated field positions used in the field selective ENDOR analysis are shown in the inset to Figure 6.8. Simulation of this EPR spectrum indicated that Species II and III are the dominant centres present.

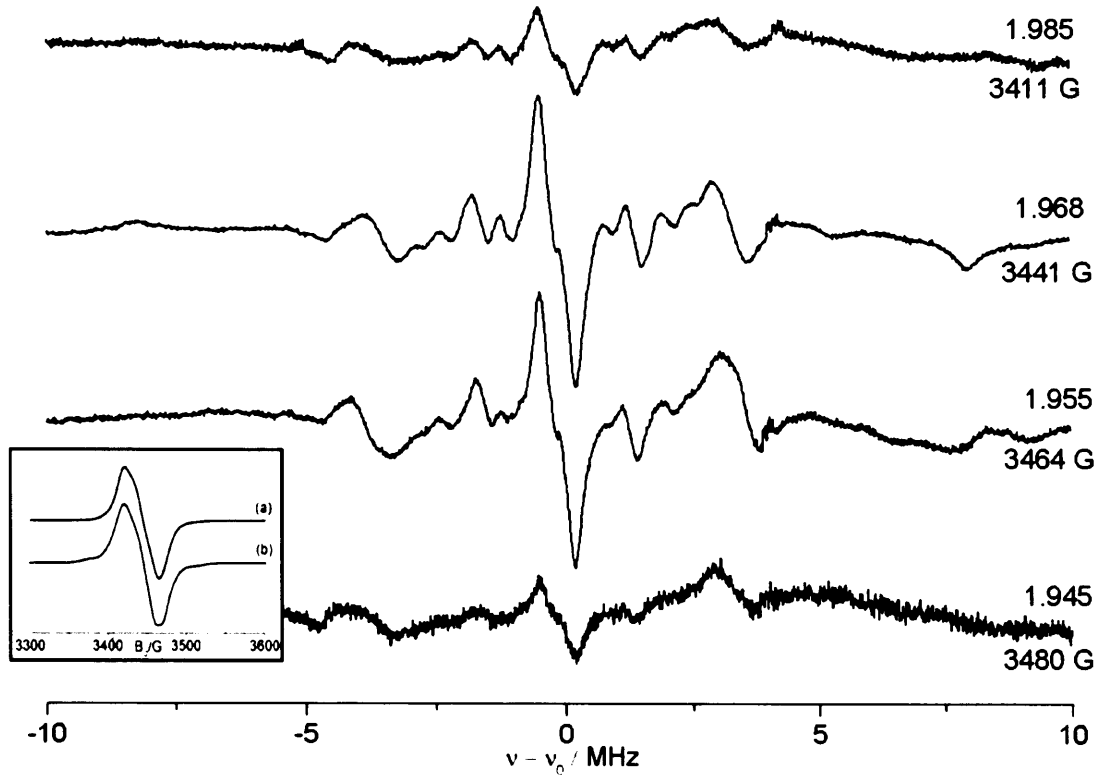

Figure 6.8: Experimental CW-ENDOR spectra of $[Cr(CO)_4\mathbf{g}]^+$ in dichloromethane / toluene after activation with approximately 60 equivalents TEA/toluene. Recorded at the various field positions and corresponding *g* values shown in the Figure. The experimental (a) and simulated (b) CW-EPR spectra are shown in the inset. Recorded at 10 K

The resulting ^1H CW ENDOR spectra are shown in Figure 6.8. One of the crucial features of these ENDOR spectra is the extremely large proton couplings; one observed coupling is approximately 16 MHz (in the spectrum recorded at 3441 G). This can be compared to the proton ENDOR spectra, reported earlier in Chapter 4, for the unactivated pre-catalyst. In that case, the couplings were very small; the largest value was only 5.4 MHz. Clearly these strong couplings observed in the activated catalyst reveal a significant change in the proton environment around the Cr centre.

It is already known from the EPR spectra, that this sample contains a considerable amount of $[Cr(bis\text{-}arene)]^+$ complex. As mentioned previously, Prins and Reinders[16] reported a proton superhyperfine structure of $^{1H}A\perp = 3.64$ G (10.1 MHz) and $^{1H}A_{\|} = 3.1$ G (8.7 MHz) in the frozen solution spectrum of $[Cr(\eta^6\text{-}C_6H_6)_2]^+$ whilst Li *et al.*,[17] reported a proton coupling in $[Cr(\eta^6\text{-}CH_3C_6H_5)_2]^+$ as $^{1H}A\perp = 3.7$ G (10.2 MHz) and $^{1H}A_{\|} = 3.0$ G (8.4 MHz). Regardless of the derivatisation or functionalisation of the aromatic ring, the proton hyperfine couplings in these bis-arene complexes do not change significantly. Therefore the largest coupling expected in the ENDOR spectrum for a pure bis-arene complex is only 10.2 MHz. Even the suggested $S = 1$ triplet

structure (**12**) described earlier, should still have a maximum coupling of 10 MHz. How then can the large 16 MHz coupling be explained?

Without further experimentation this question cannot be definitively answered at this stage. However, it is possible to speculate on two possible and intriguing interpretation, which is that the large couplings arise from co-ordinated alkyl fragments on the chromium centre (after decarbonylation of *x*CO ligands), or alternatively a strongly interacting phenyl group with large isotropic and anisotropic couplings). The large magnitude of the coupling suggests that the protons must be in close proximity to the chromium ion, as expected for an alkyl fragment.

Next, in an attempt to investigate the possibility that relaxation effects of the various activated complexes (I,II,III) were different, pulsed EPR and ENDOR spectra were performed. In this series of experiments, the complex $[Cr(CO)_4\mathbf{d}]^+$ was activated with approximately 20 equivalents TEA/toluene; the resulting field-swept echo detected spectrum (FSED) is shown in Figure 6.9. The spin Hamiltonian parameters extracted *via* simulation of the spectrum are typical for those described earlier for Species II and III. Therefore the spectrum confirms the earlier CW-EPR observations revealing the presence of centres II and III.

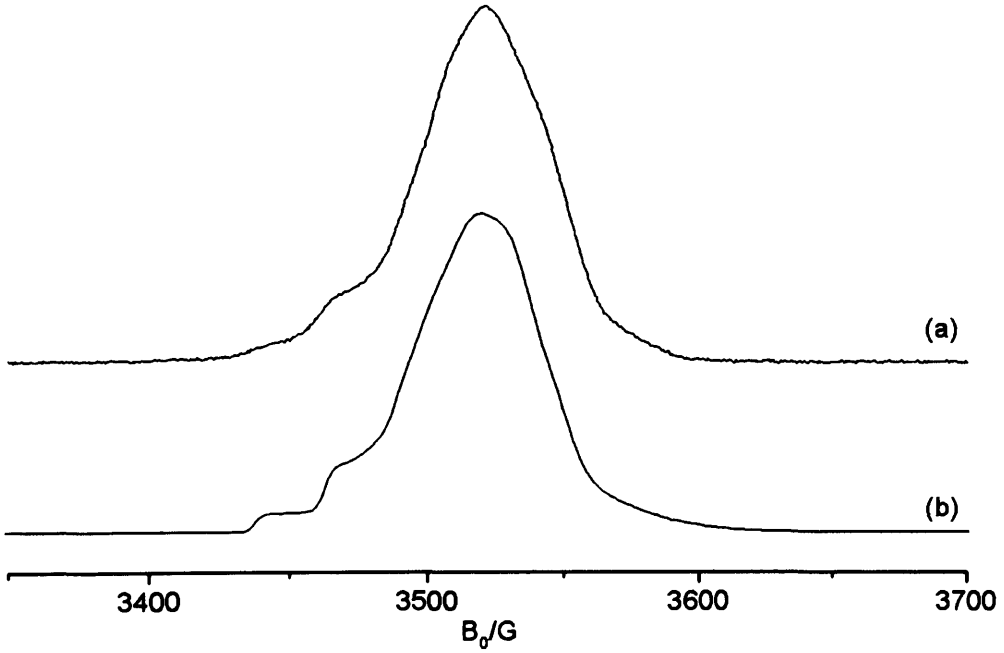

Figure 6.9: Experimental (a) and simulated (b) FSED-EPR spectra of $[Cr(CO)_4\mathbf{d}]^+$ in dichloromethane after activation with approximately 20 equivalents of TEA/toluene. Recorded at 10 K.

As discussed earlier, difficulties were encountered in saturating the EPR transition in order to perform the CW-ENDOR experiment, attributed to the short relaxation time. Pulsed ENDOR techniques do not suffer from this drawback however,

and proton Mims ENDOR data was collected for the system. The spectra obtained at various field positions, correponding to $[Cr(CO)_4\mathbf{d}]^+$ activated with 20 equivalents TEA/toluene, are displayed in Figure 6.10.

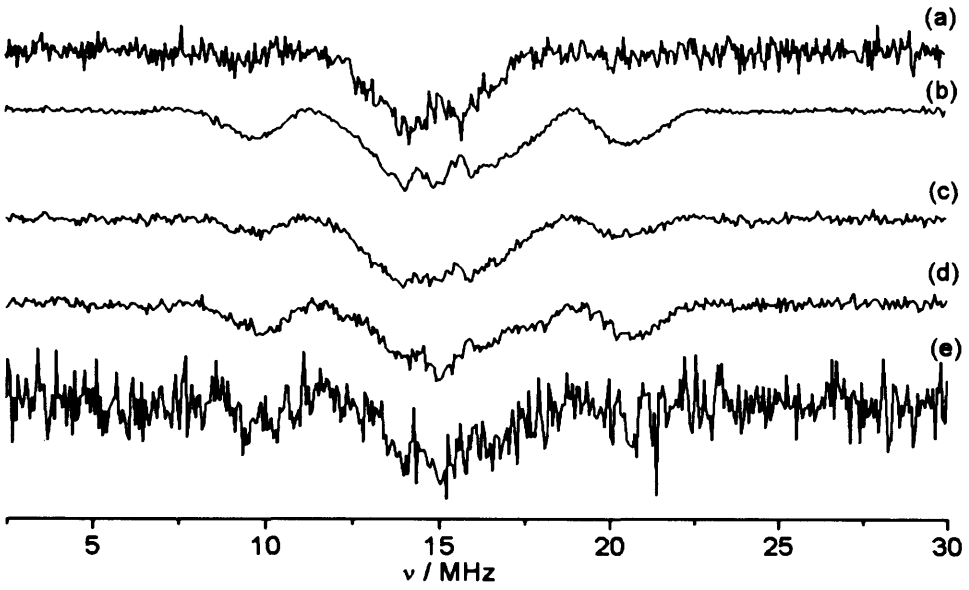

Figure 6.10: Experimental Mims ENDOR spectra of $[Cr(CO)_4\mathbf{d}]^+$ in dichloromethane after activation with approximately 20 equivalents of TEA/toluene. Recorded at (a) 3456, (b) 3495, (c) 3520, (d) 3550 and (e) 3580 G. Recorded at 10 K.

What is immediately clear is the relatively large proton coupling at all field positions of approximately 12 MHz, centred around the nuclear Larmor frequency of the proton (around 15 MHz). Similarly to that detected in the CW-ENDOR data, this coupling is much larger than that of the pre-catalyst, indicating the presence of protons much closer to the chromium centre. The magnitude of the coupling is not quite as large as that observed in the CW-ENDOR spectra for activated $[Cr(CO)_4\mathbf{g}]^+$. Mims ENDOR is more accurate for smaller couplings, and larger couplings may not be observed due to 'blind spots' in the spectrum, which is what may have occurred in this case. Further experimentation, including Davies ENDOR (which is accurate for larger couplings) would be needed to confirm this.

6.3.5 Intermediate Activated Species

For all experiments thus far described, a concentration of 6 mg Cr(I) complex was placed in the EPR tube and various equivalents of alkylaluminium added. However, it was found that for the pulsed measurements described above, an extremely weak echo was obtained using these relatively dilute solutions. Hence, a higher concentration of Cr(I) pre-catalyst was used in the EPR tube (12 mg), in order to produce a stronger spin

echo. The CW-EPR spectrum of this more concentrated solution of pre-catalyst was identical to that using 6 mg, described in Chapter 4. This more concentrated solution of complex (12 mg) was subsequently activated with *ca.* 10 equivalents of TEA/toluene, and the CW-EPR spectrum was recorded. The resulting spectra are shown in Figure 6.11.

Interestingly, and surprisingly, a new EPR signal was observed under these conditions. It consists of axial ***g*** and ***A*** matrices, and similarly to the pre-catalyst spectra, the principal components of the ***g*** matrix assume the order $g\perp > g\parallel$. However computer simulation reveals that the principal values obtained by simulation are different compared to the pre-catalyst with parameters of $g\perp = 2.014$, $g\parallel = 1.9705$, $^{31P}A\perp$ = 31 G and $^{31P}A\parallel$ = 35 G . These g values ($g\perp > g_c > g\parallel$) indicate that the molecular orbital arrangement in this species is similar to that of the pre-catalyst; i.e. a SOMO where the metal contribution is primarily d_{xy}. Similarly to the pre-catalyst, it is proposed that π-back donation to CO helps to stabilize the d_{xz} and d_{yz} relative to the d_{xy} based HOMO.

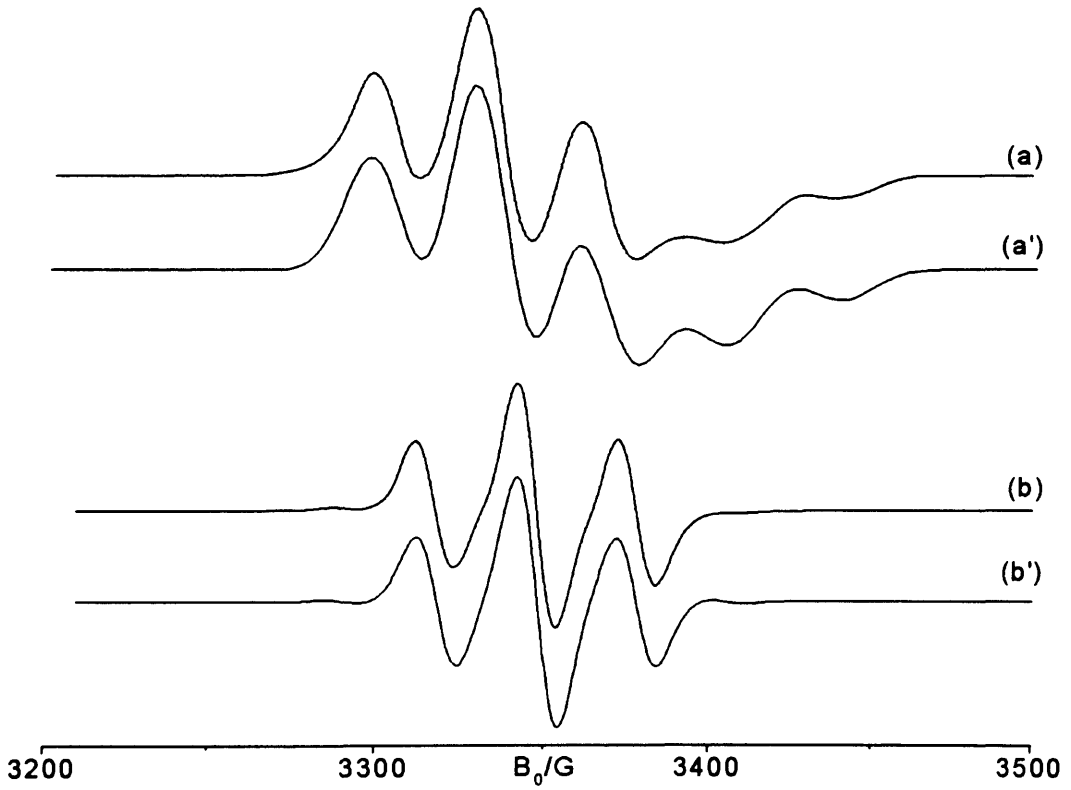

Figure 6.11 Experimental (a, b) and simulated (a', b') CW-EPR spectra of a doubly concentrated solution of $[Cr(CO)_4g]^+$ in dichloromethane after activation with approximately 10 equivalents TEA/toluene. Recorded at (a) 140 K and (b) 270 K. A linewidth of 15 G was used for both simulations.

The g values in this activated system are closer to each other (i.e., the magnitude of Δg is less). This anisotropy in g arises due to the interaction between spin- and orbital-angular momenta, causing residual orbital angular momentum (l) to appear in the ground state. The degree to which this occurs depends on, among other factors, the energy difference between the excited state orbital contributing to this and the ground state. Therefore the differences in g between the pre-catalyst and this intermediate species must be related to the extent of tetragonal distortion from octahedral symmetry. The decrease in Δg for this activated species indicates that there is less distortion compared to the pre-catalyst. Interestingly, the ^{31}P superhyperfine coupling values have actually increased in magnitude. This indicates that the nuclei are closer to the metal centre or that they simply possess a higher spin density.

It appears that the activation of a more concentrated solution of the pre-catalyst complex results in a modification of the structure of the pre-catalyst. It seems likely that this species (hereafter referred to as Species IV) is an intermediate stage between the pre-catalyst and the 'activated' Species I, II and III. The evidence for this is the indication that a high symmetry structure must still exist, to account for the axial g matrix ($g_\perp > g_\parallel$) and the presence of relatively large ^{31}P coupling. This could still occur if, for example, one or two of the CO groups were lost (eg., $[Cr(CO)_2\mathbf{g}]^+$). This situation is illustrated in Scheme 6.3.

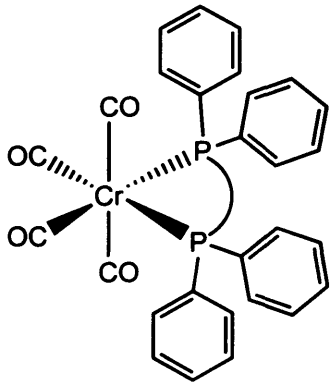

Pre-catalyst

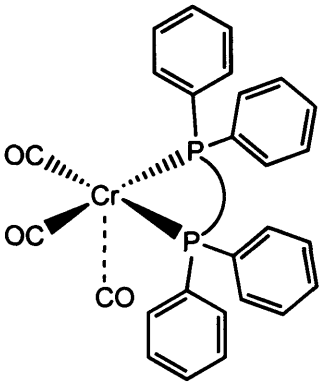

Species IV

Scheme 6.3: Comparison between Cr(I) pre-catalyst and proposed Species IV.

A variable temperature study of this activated complex was then performed. The resulting spectra are shown below in Figure 6.12 As the temperature is increased, a decrease in g/A anisotropy is observed until eventually (at 270K) an isotropic signal is detected.

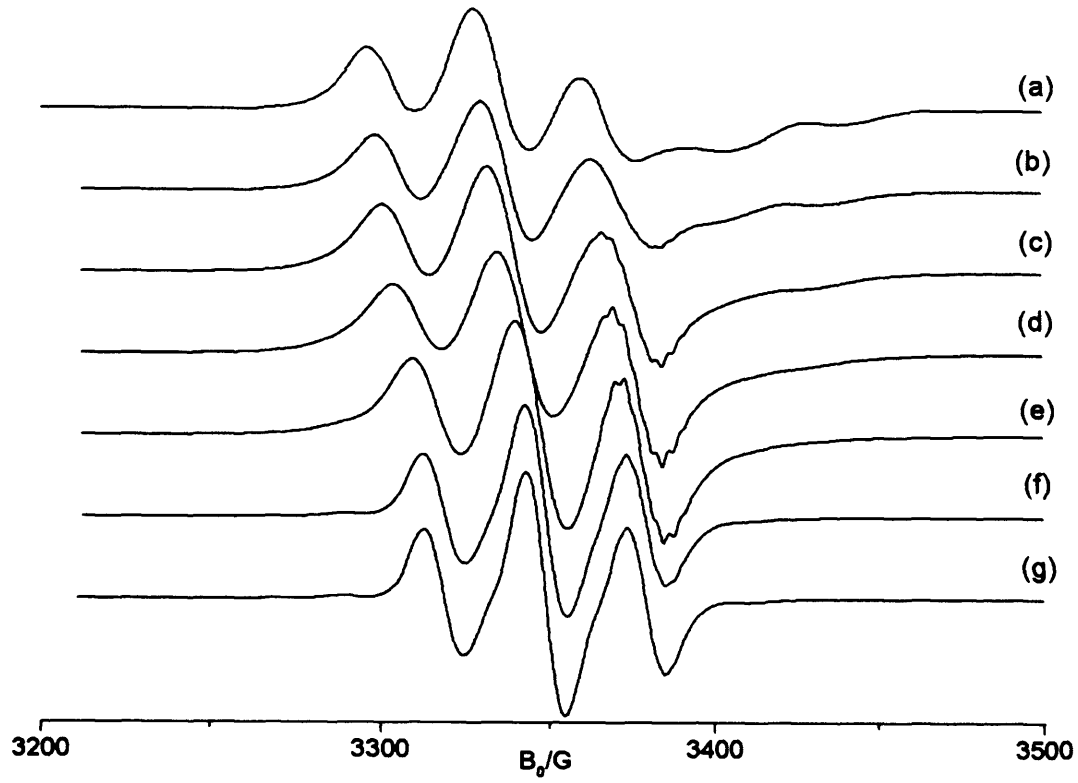

Figure 6.12 Experimental CW-EPR spectra of a doubly concentrated solution of $[Cr(CO)_4g]^+$ in dichloromethane after activation with approximately 10 equivalents TEA/toluene. Recorded at (a) 140, (b) 185, (c) 195, (d) 205, (e) 220, (f) 250 and (g) 270 K.

At temperatures of 185 K and above, superhyperfine coupling at around 3380 G (g = 1.988) is observed. This resembles that previously observed at higher temperatures, which was attributed to a $[Cr(bis\text{-}arene)]^+$ species. Therefore as well as the intermediate Species IV, the bis-arene Species II is also present in this system. Computer simulation revealed that only 5% of the signal arises from Species II. The remaining 95% of the spectrum originates from Species IV which was simulated using the isotropic parameters g_{iso} = 2.00, $^{31P}a_{iso}$ = 32 G, $^{53Cr}a_{iso}$ = 18 G. As expected, the g and ^{31}P a_{iso} values are the average of those extracted at 140 K. ^{53}Cr coupling also becomes visible. Interestingly, the magnitude of this Cr coupling is identical to that observed for Species II.

A series of pulsed EPR measurements were also carried out on this sample. The FSED EPR spectrum was recorded and the spin Hamiltonian parameters extracted from simulation were $g_\perp$ = 2.014 , $g_\parallel$ = 1.971, $^{31P}A_\perp$ = 30 G and $^{31P}A_\parallel$ = 35 G. As expected they are extremely similar to those recorded in continuous-wave mode. For brevity, the experimental and simulated FSED spectra are therefore given in Figure A.14 in the Appendix. Relaxation measurements were also performed on the sample to determine

both T_1 and T_2. The resulting time traces and resulting 3-pulse ESEEM spectra are shown in Figure 6.13 below.

The spin-lattice (T_1) relaxation time was calculated *via* a bi-exponential decay function and was determined as $\tau_1 = 2.11 \times 10^7$ ns and $\tau_2 = 1.18 \times 10^6$ ns. The total spin-lattice relaxation is composed of more than one contribution, as observed by the two distinct times determined in the experiment. Interestingly, these relaxation times are longer than those determined for the corresponding pre-catalyst complex at a similar field position (τ_1 = 714141 ns, τ_2 = 146435 ns). The spin-spin relaxation times T_2 (the time taken for the transverse component of the macroscopic magnetization to decay) were extracted from the raw data *via* a stretched exponential decay fitting, and calculated as 632 ns (3450 G), 798 ns (3514 G) and 823 ns (3555 G). These relaxation times are shorter than those of the corresponding pre-catalyst (1781 ns at 3373 G and 5570 ns at 3491 G). This is expected; if there is a high-spin species present (for example, Species III) in the reaction mixture as was postulated (even if only present in a small proportion), the interaction between the electrons decreases the spin-spin relaxation time.

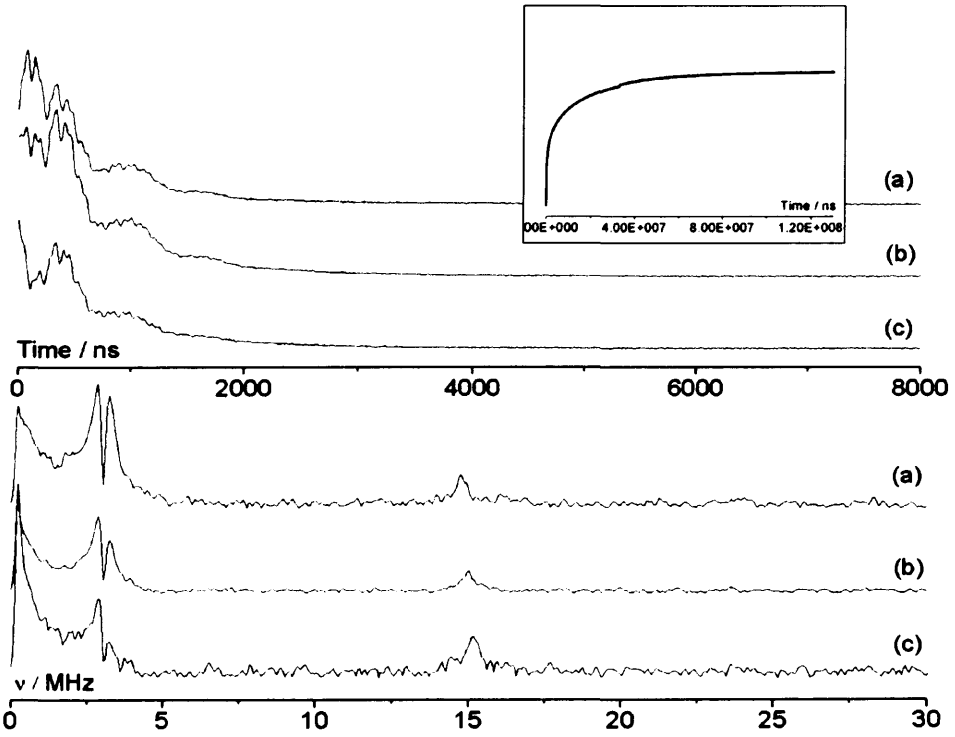

Figure 6.13 Inset: Experimental T_1 measurement of a doubly concentrated solution of $[Cr(CO)_4g]^+$ in dichloromethane after activation with approximately 10 equivalents TEA/toluene. Recorded at 3514 G. Top: Experimental T_2 measurements of $[Cr(CO)_4g]^+$ in dichloromethane after activation with approximately 10 equivalents TEA/toluene. Recorded at (a) 3450, (b) 3514 and (c) 3555 G. Bottom: 3-pulse ESEEM spectra of $[Cr(CO)_4g]^+$ in dichloromethane after activation with approximately 10 equivalents TEA/toluene. Recorded at (a) 3450, (b) 3514 and (c) 3555 G. Recorded at 10 K.

The data were Fourier transformed from the time domain to the frequency domain to obtain the nuclear frequencies present, and these spectra are shown in the bottom plot of Figure 6.13. It is important to note, that proton resonances are clearly present; a peak is observed at approximately 15 MHz. Additionally, there are two peaks visible at lower frequency. At 3450 G these occur at approximately 2.8 and 3.2 MHz. These could correspond to ^{27}Al; however, the nuclear Larmor frequency of this nucleus at the field position should occur at 3.83 MHz.

The orientation-selective Davies ENDOR spectra of this activated $[Cr(CO)_4\mathbf{g}]^+$ complex are shown in Figure 6.14. Similarly to the Mims ENDOR spectra of the activated system $[Cr(CO)_4\mathbf{d}]^+$, the Davies ENDOR of activated $[Cr(CO)_4\mathbf{g}]^+$ show much larger proton couplings compared to the pre-catalyst alone. The spectrum shown in Figure 6.14c in particular demonstrates this. Two large interactions of approximately 12.5 and 8.2 MHz are clearly observed. Again, these must be due to protons much closer to the Cr centre than were present in the pre-catalyst. ^{31}P superhyperfine couplings are also clearly observed; two peaks are centred on $A/2$ and split by $2\nu_N$, at each field position. These components of the spectra were simulated and the resulting experimental and simulated spectra are shown in Figure 6.15. The superhyperfine coupling constants for the ^{31}P nuclei extracted from the simulation are $A\perp$ = 80 MHz (28.3 G) and $A_\parallel$ = 92 MHz (33.3 G). These agree very well with the parameters extracted from the FSED EPR spectrum, i.e., $A\perp$ = 30 G, $A_\parallel$ = 32.5 G.

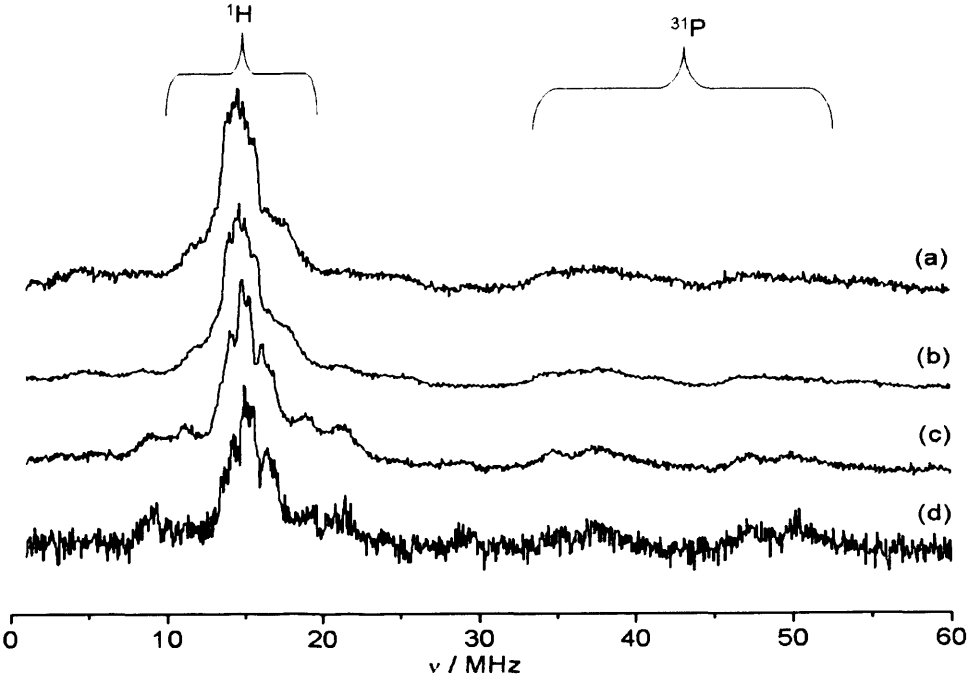

Figure 6.14: Experimental Davies ENDOR spectra of $[Cr(CO)_4\mathbf{g}]^+$ in dichloromethane, activated with approximately 10 equivalents TEA/toluene. Recorded at (a) 3445, (b) 3476, (c) 3533 and (d) 3572 G. Recorded at 10 K.

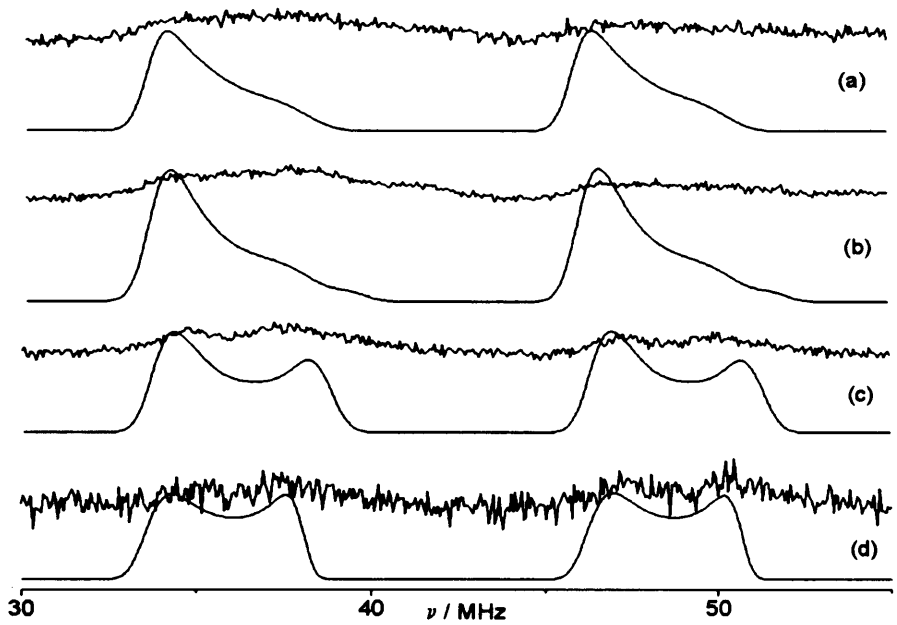

Figure 6.15: Experimental (top) and simulated (bottom) Davies ENDOR spectra of $[Cr(CO)_4g]^+$ in dichloromethane, activated with approximately 10 equivalents TEA/toluene. Recorded at (a) 3445, (b) 3476, (c) 3533 and (d) 3572 G. Recorded at 10 K. A linewidth of 10 MHz was used in the simulations.

6.4 Conclusions

The activation of $[Cr(CO)_4g]^+$ was studied at low temperatures following the addition of a co-catalyst (i.e., triethylaluminium). The EPR spectrum of the parent complex changed dramatically following addition of TEA, but the nature of the resulting signals were found to depend on the levels of added co-catalyst.

No changes to the EPR spectra of the pre-catalyst $[Cr(CO)_4g]^+$ were detected until approximately 2 equivalents of TEA/toluene were added. At these low levels of TEA, two paramagnetic species were identified, labelled Species I and II. Species I possessed an apparent axial ***g*** tensor, with $g_{\|} > g_e > g_{\perp}$, and superhyperfine coupling to two ^{31}P nuclei. The 'reversal' of the g values compared to the pre-catalyst showed that a modification to the geometry of this chromium species had occurred upon activation. The presence of ^{31}P coupling proved that the ligand is still co-ordinated to the chromium centre in this species, albeit with reduced magnitude. Species II also displayed an axial ***g*** matrix, with $g_{\|} \approx g_e > g_{\perp}$, and hyperfine coupling to ^{53}Cr visible. The spin Hamiltonian parameters were consistent with a $[Cr(bis\text{-}arene)]^+$ complex, as discussed in Chapter 5. Both species were present up until approximately 10 equivalents TEA, with the abundance of I decreasing relative to II as the TEA levels increased.

At higher levels of TEA (15 equivalents onwards), Species II still persists in solutions of the activated Cr system with the additional presence of a third species labelled III. The resolution of this species is poor, owing partly to the overlapping features from Species II. A possible explanation for the origin of this signal, and also to account for the presence of a half field transition, is the possibility of Cr...Cr dimers. These could likely be formed from neighbouring Cr bis-arene complexes.

In all cases, activation of the pre-catalyst resulted in a dramatic decrease in signal intensity. This is either due to the formation of formally diamagnetic centres, or also due to formation of 'EPR silent' centres. It is possible that spin-paired chromium dimers make up some part of the reaction mixture.

CW and pulsed ENDOR measurements were also performed on the activated system. The most notable observation from this analysis was the appearance of exceptionally large proton couplings. These couplings are too large to be explained only on the basis of a bis-arene complex for which the maximum coupling expected should be approximately 11 MHz. Instead the large 16 MHz couplings may arise from co-ordinated alkyl groups, but further work is required to confirm this.

Finally in a rather curious observation, activation of a more 'concentrated' solution of the Cr(I) pre-catalyst resulted in the formation of a fourth paramagnetic centre labelled Species IV (classed as an intermediate species). The observation is curious in the sense that the species was not observed using low levels of TEA in the non-concentrated conditions. This Species IV was extremely well resolved (and unlike all other cases which produced mixed/overlapping signals) and present as a single species. It possessed a $\boldsymbol{g}$ matrix with $g_{\perp} > g_e > g_{\parallel}$, and superhyperfine ^{31}P coupling of an increased magnitude compared to the pre-catalyst. The nature of this complex is not known (without recourse to ^{13}C-labelled CO), but based on the well defined $\boldsymbol{g}$ tensor, appears to be a complex possessing high symmetry.

6.5 References

1. G. V. Schulz, *Z. Phys. Chem. B.*, 1935, **30**, 379.
2. P. J. Flory, *J. Am. Chem. Soc.*, 1940, **62**, 1561.
3. R. M. Manyik, W. E. Walker and T. P. Wilson, *J. Catal.*, 1977, **47**, 197.
4. M. J. Overett, K. Blann, A. Bollmann, J. T. Dixon, D. Haasbroek, E. Killian, H. Maumela, D. S. McGuinness and D. H. Morgan, *J. Am. Chem. Soc.*, 2005, **127**, 10723.
5. R. Walsh, D. H. Morgan, A. Bollmann and J. T. Dixon, *Appl. Catal. A.*, 2006, **306**, 184.
6. Z. Yu and K. N. Houk, *Angew. Chem. Int. Ed.*, 2003, **42**, 808.

7. A. Bollmann, K. Blann, J. T. Dixon, F. M. Hess, E. Killian, H. Maumela, D. S. McGuinness, D. H. Morgan, A. Neveling, S. Otto, M. Overett, A. M. Z. Slawin, P. Wasserscheid and S. Kuhlmann, *J. Am. Chem. Soc.*, 2004, **126**, 14712.
8. M. J. Overett, K. Blann, A. Bollmann, J. T. Dixon, F. Hess, E. Killian, H. Maumela, D. H. Morgan, A. Neveling and S. Otto, *Chem. Commun.*, 2005, 622-624.
9. D. S. McGuinness, P. Wasserscheid, W. Keim, C. H. Hu, U. Englert, J. T. Dixon and C. Grove, *Chem. Commun.*, 2003, 334-335.
10. P. H. Rieger, *Coord. Chem. Rev.*, 1994, **135-136**, 203.
11. A. J. Rucklidge, D. S. McGuinness, R. P. Tooze, A. M. Z. Slawin, J. D. A. Pelletier, M. J. Hanton and P. B. Webb, *Organometallics*, 2007, **26**, 2782.
12. N. G. Connelly, A. G. Orpen, A. L. Rieger, P. H. Rieger, C. J. Scott and G. M. Rosair, *J. Chem. Soc., Chem. Commun.*, 1992, 1293.
13. C. J. Adams, I. M. Bartlett, N. G. Connelly, D. J. Harding, O. D. Hayward, A. J. Martin, A. G. Orpen, M. J. Quayle and P. H. Rieger, *J. Chem. Soc., Dalton Trans.*, 2002, 4281.
14. C. Elschenbroich and F. Stohler, *Angew. Chem. Int. Ed.*, 1975, **14**, 174.
15. M. Brustolon and E. Giamello, eds., *Electron Paramagnetic Resonance - A Practitioner's Toolkit*, Wiley, 2009.
16. R. Prins and F. J. Reinders, *Chem. Phys. Lett.*, 1969, **3**, 45.
17. T. T. Li, W. Kung, D. L. Ward, B. McCulloch and C. H. Brubaker Jr., *Organometallics*, 1982, **1**, 1229.
18. L. Calucci, U. Englert, E. Grigiotti, F. Laschi, G. Pampaloni, C. Pinzino, M. Volpe and P. Zanello, *J. Organomet. Chem.*, 2006, **691**, 829.
19. F. Benetollo, E. Grigiotti, F. Laschi, G. Pampaloni, M. Volpe and P. Zanello, *J. Solid State Electrochem.*, 2005, **9**, 732.
20. J. T. Dixon, M. J. Green, F. M. Hess and D. H. Morgan, *J. Organomet. Chem.*, 2004, **689**, 3641.
21. C. Elschenbroich, G. Heikenfeld, M. Wunsch, W. Massa and G. Baum, *Angew. Chem. Int. Ed.*, 1988, **27**, 414.
22. C. Elschenbroich and J. Heck, *J. Am. Chem. Soc.*, 1979, **101**, 6773.
23. A. Brückner, J. K. Jabor, A. E. C. McConnell and P. B. Webb, *Organometallics*, 2008, **27**, 3849.
24. J. Krzystek, A. Ozarowski and J. Telser, *Coord. Chem. Rev.*, 2006, **250**, 2308.
25. R. D. Köhn, M. Haufe, G. Kociok-Köhn, S. Grimm, P. Wasserscheid and W. Keim, *Angew. Chem. Int. Ed.*, 2000, **39**, 4337.

Chapter 7

EPR spectroscopic analysis of N-heterocyclic carbene complexes of Cr(I), Cr(III) and Ti(III)

7.1 Introduction

Along with the bis(diphenylphosphine) ligands discussed previously in the thesis, N-heterocyclic carbenes (NHC) are frequently-used ligands in transition metal chemistry. The first NHC-metal complexes were reported by Wanzlick[1] and Öfele[2] in 1968. These type of complexes are particularly utilised in homogeneous catalysis; C-C cross-coupling reactions[3] and olefin metathesis[4] both utilise NHC complexes as catalysts. Donor functionalised expanded NHC complexes, recently reported by Cavell and co-workers,[5] demonstrate excellent catalytic activity in hydrogenation reactions. Cr-based NHC complexes have been shown to be active ethylene oligomerisation catalysts;[6-8] in some cases, NHCs even exceed phosphines in catalytic activity and scope,[9, 10] exhibiting properties such as higher thermal and oxidative stability; they also have lower toxicity. The synthesis of various transition-metal NHC complexes was concurrently being investigated by the Cavell group of Cardiff University at the time of this study; therefore, it was thought timely and relevant to this work to investigate the structural and electronic characteristics of such carbene complexes *via* CW-EPR spectroscopy.

Free carbenes ($:CR_2$) are formally described as neutral divalent compounds containing two non-bonding electrons. The electrons can either occupy the same orbital, resulting in a singlet ground state, or different orbitals, resulting in a triplet ground state. The geometry of the triplet state carbene can be linear, if the carbon is *sp*-hybridised and the electrons exist in two degenerate *p* orbitals. Alternatively, a bent geometry is found if the carbon is sp^2-hybridised and one electron now resides in an sp^2 (referred to as σ) orbital. Singlet carbenes also display a bent geometry, but now both electrons occupy the σ orbital (Scheme 7.1).

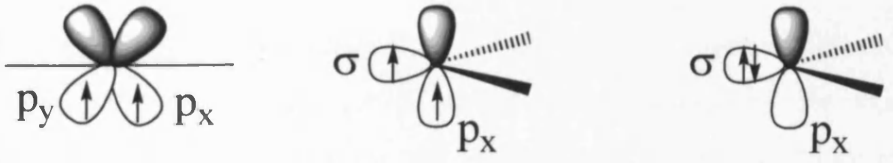

Triplet Linear | Triplet Bent | Singlet Bent

Scheme 7.1: Possible geometries of free carbenes.

The ground state multiplicity is determined by the relative energies of the σ and p_x orbitals, in turn determined by the electronic and steric effects of the substituents on the carbon atom.[11] The singlet state is stabilised by σ-electron withdrawing substituents, which lower the relative energy of the σ-orbital.[12, 13] Mesomeric effects also play a role; if the substituents are also π-donating (for example nitrogen atoms), the interaction with the p_x orbital raises its relative energy resulting in further stabilisation of the bent singlet ground state.[11] This is visualised in Scheme 7.2.

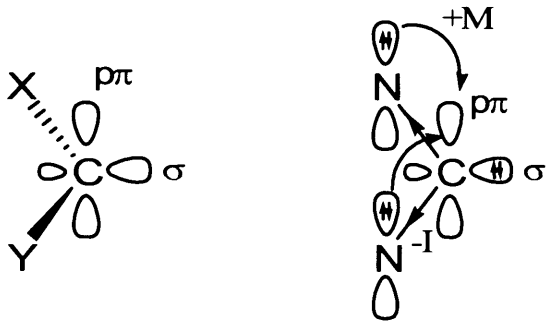

Scheme 7.2: Stabilisation of the bent singlet ground state.

This situation occurs with N-heterocyclic carbenes, or NHCs, which contain exclusively singlet carbene centres.[11] The first free NHC was isolated by Arduengo *et al.*,[14] and was a 5-membered imidazole-2-ylidene. Here, the interaction of π-electrons of the nitrogen atoms with the p_π-orbital on the carbene carbon results in a delocalised system in which the N-C bonds have partial double bond character (Scheme 7.3). This type of NHC will remain the focus of this work.

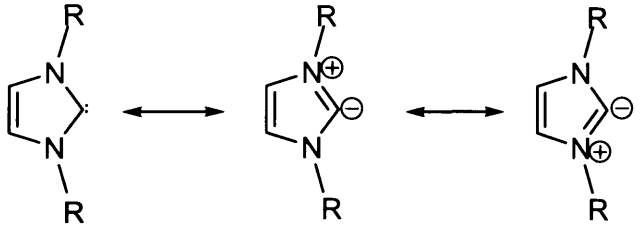

Scheme 7.3: Resonance structures of five-membered N-heterocyclic carbenes.

NHCs are similar to phosphine ligands in that they are neutral 2-electron donors whose steric and electronic properties can be easily modified, for example by substitution on the nitrogen atoms or the ring. However, they are more basic than phosphines and exhibit stronger σ-donor properties. NHC-Cr bonds are consequently much stronger than phosphine-Cr bonds in Cr(0) complexes,[15] which suggests that Cr(I)

(and Cr(III))-NHC complexes should be stabilised to a greater extent than the phosphine-containing complexes. It is not necessary for π-back bonding from the metal to the carbene to occur to generate a stable complex, unlike the general case with phosphines.

As discussed in Chapter 1, chromium is the most widely used metal in ethylene oligomerisation catalysis, and both Cr(I) and Cr(III) oxidation states are thought to be implicated in the reaction.[16-19] Cr(I)-NHC complexes are rare, but possible due to the strong donating abilities of the NHC ligand, which is able to stabilise the oxidised chromium centre. The first reported examples of NHC-containing Cr(I) complexes were described by Lappert and co-workers in 1980.[20] Hirao *et al.*,[21] characterised an oxidated benzanulated NHC-Cr(0) complex *via* EPR spectroscopy. In this case the unpaired electron was situated within the benzimidazolylidene ring, as evidenced by the *g* value close to free spin ($g = 2.005$), the absence of a hyperfine coupling to chromium, and an interaction with nitrogen and ring protons. It was proposed that the conjugation of the π-system stabilised the electron in the ring.

Cr(I) NHC systems have not as yet been tested for oligomerisation activity, probably due to the relatively unstable nature of the system compared to a Cr(III) complex; but due to the fact that Cr(I) precursors in general have been shown to produce active oligomerisation catalysts,[22] a fundamental understanding of these systems is of importance.

Cr(III) represents one of the more stable oxidation states, and a number of Cr(III) systems have been evaluated for catalytic potential. Rüther and co-workers[6] reported a series of Cr(III) complexes bearing imidazole-based chelate ligands, which were found to be active catalysts upon activation with modified MAO. Gibson *et al.*,[7] investigated a series of Cr(III) complexes bearing tridentate CNC 'pincer' carbene ligands. Upon activation with MAO, they produced exceptionally active ethylene oligomerisation catalysts. McGuinness *et al.*,[23] studied the catalytic behaviour of early and middle transition metal-bis(carbene) pyridine complexes, and the Cr(III) complexes were again very active for oligomerisation. A metallacycle mechanism, similar to that for the more conventional Cr bis(phosphine) catalyst systems, was established to be at work.[8] Theopold reported a bidentate bis(carbene) complex; this however displayed only low ethylene polymerisation activity.[24]

Titanium-based phosphine systems are also utilised frequently in ethylene oligomerisation catalysis, as discussed in Chapter 1.[25-27] Therefore there is interest in

exploring and developing analogous systems bearing NHC ligands. Some highly active polymerisation catalysts based on Ti(III) carbene complexes have also been reported (producing polyethylene of a high molecular weight)[23, 28] but none active for ethylene oligomerisation has yet been identified. EPR data have been reported on two Ti(III) NHC complexes; Arnold *et al.*,[29] recorded the room temperature spectrum of a titanium complex bearing three bidentate alkoxy-NHC ligands. Isotropic parameters of g_{iso} = 1.970 and $^{Ti}a_{iso}$ = 12.48 G were obtained. Lorber *et al.*,[30] studied the complex $TiCl_2(NMe)_2(IMes)_2$, where IMes is the monodentate NHC ligand 1,3-dimesitylimidazol-2-ylidene. The EPR spectrum at room temperature displayed an isotropic *g* value of 1.943.

NHC ligands clearly have the potential to produce catalysts with excellent oligomerisation capabilities, but the variation in activities and selectivities means further study in this area of chemistry is required to investigate the exact influence of the NHC ligand. Given the increased use of these ligands in complexes as catalysts for alkene oligomerisation and polymerisation, it was of interest to develop the fundamental understanding of these compounds by preparing a series of Cr(I), Cr(III) and Ti(III)-NHC complexes for EPR analysis. As discussed above, there is extremely little EPR data on these types of complexes; therefore the information obtained will be novel and may shed new light on these catalytic systems.

7.2 Experimental Details

Full details of the synthetic procedures used to prepare the chromium and titanium complexes were given in Chapter 3. The NHC ligands used in the synthesis of the complexes are shown in Scheme 7.4. The general forms of the Cr(I) bidentate and monodentate complexes studied are shown in Scheme 7.5. The general forms of the Cr(III) and Ti(III) complexes studied are shown in Schemes 7.6 and 7.7 respectively.

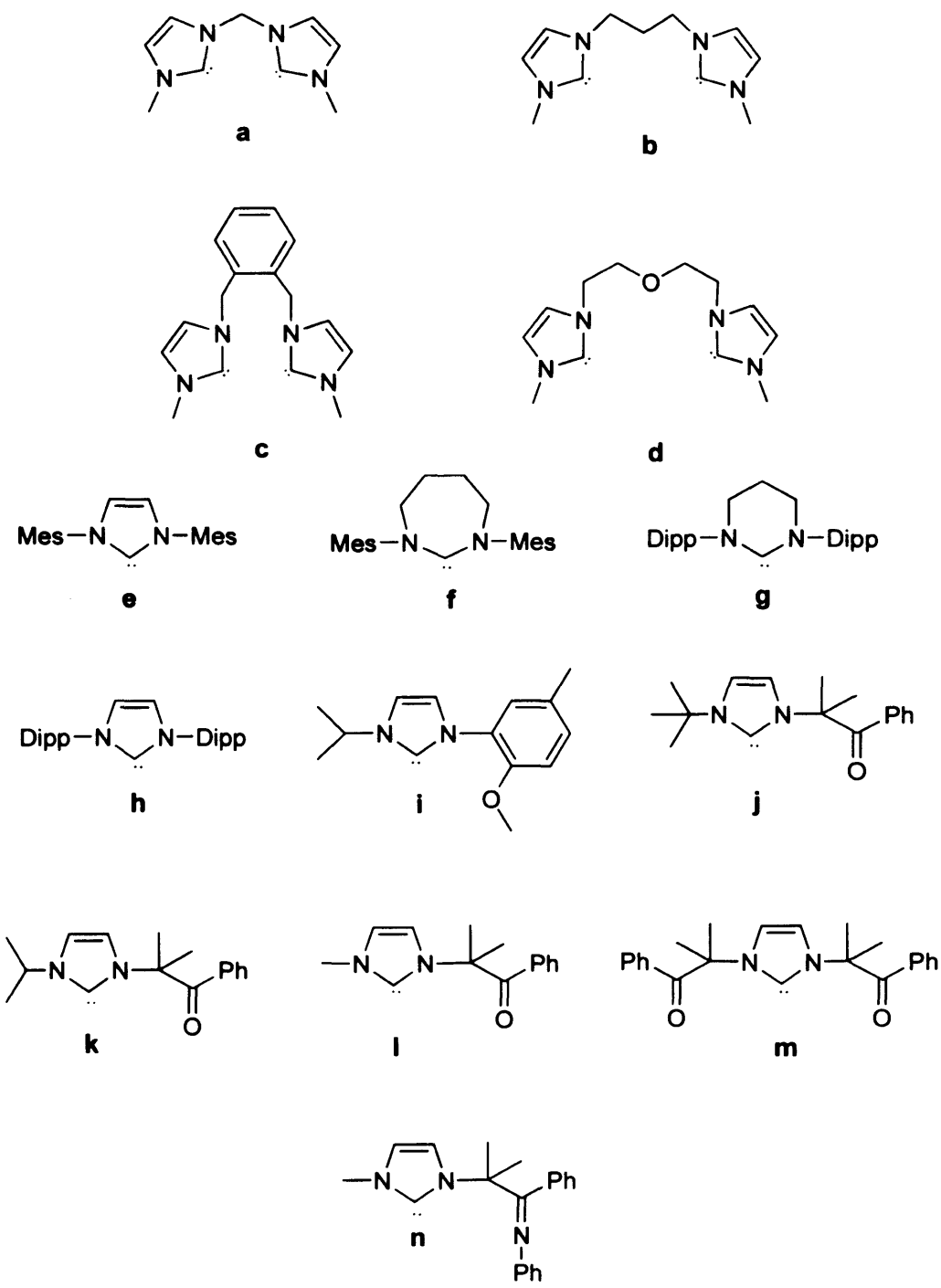

Scheme 7.4: Bidentate (**a** – **d**) and monodentate (**e** – **n**) NHC ligands.

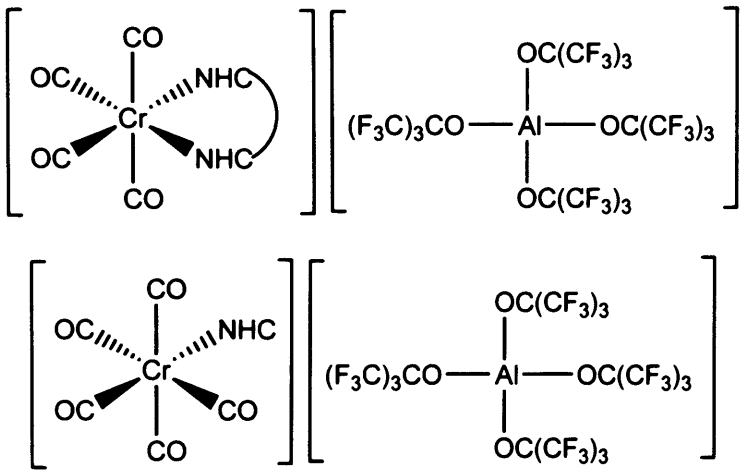

Scheme 7.5: Top: Cr(I) bidentate NHC complexes **4a – c.**
Bottom: Cr(I) monodentate NHC complexes **4e, g** and **h.**

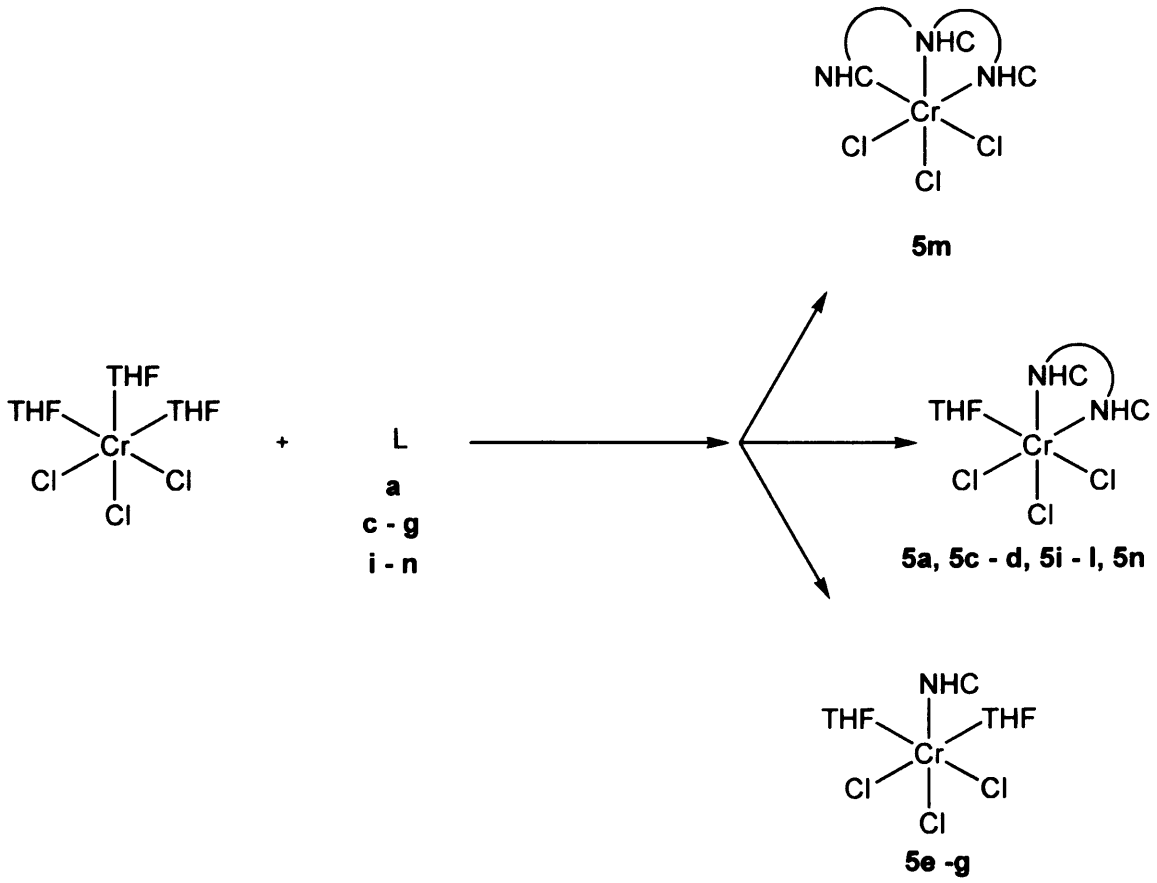

Scheme 7.6: Cr(III) complexes; L = NHC ligand.

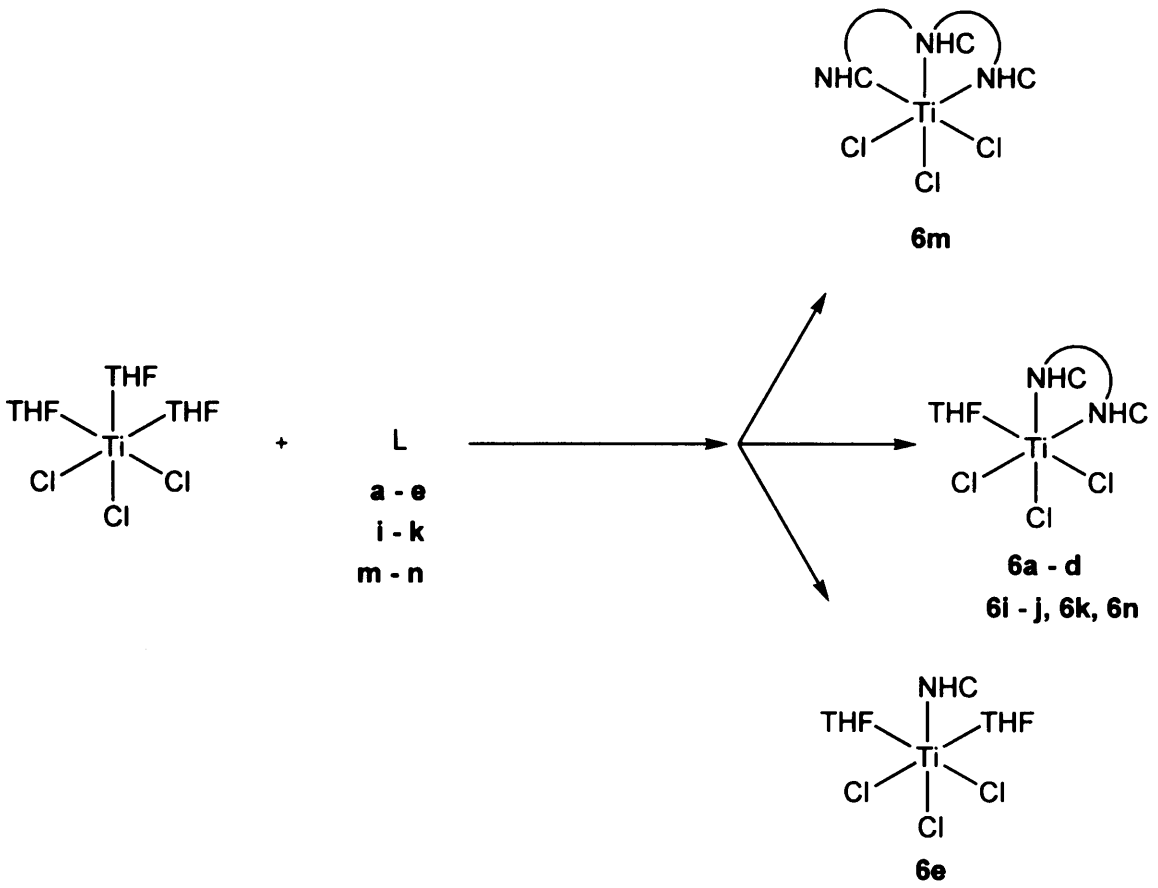

Scheme 7.7: Ti(III) complexes; L = NHC ligand.

Syntheses of chromium and titanium complexes of these ligands followed published procedures and are described in the experimental section. All sample preparations were carried out under an inert atmosphere, either in a glove box or on the Schlenk line.

For X-band CW-EPR sample preparation, each complex (6 mg) was placed in the Schlenk-adapted EPR tube and dissolved in 200 µl dry dichloromethane / toluene. A frozen solution was produced by immediately placing the tube in liquid nitrogen once the sample was prepared. Spectra were recorded at 140 K. The methodology for recording CW spectra was provided in Chapter 3.

7.3 Results and Discussion

7.3.1 Cr(I) complexes

The X-band CW-EPR spectra were recorded for the bidentate complexes **4a** - **c**, and the resulting experimental and simulated spectra are shown in Figure 7.1.

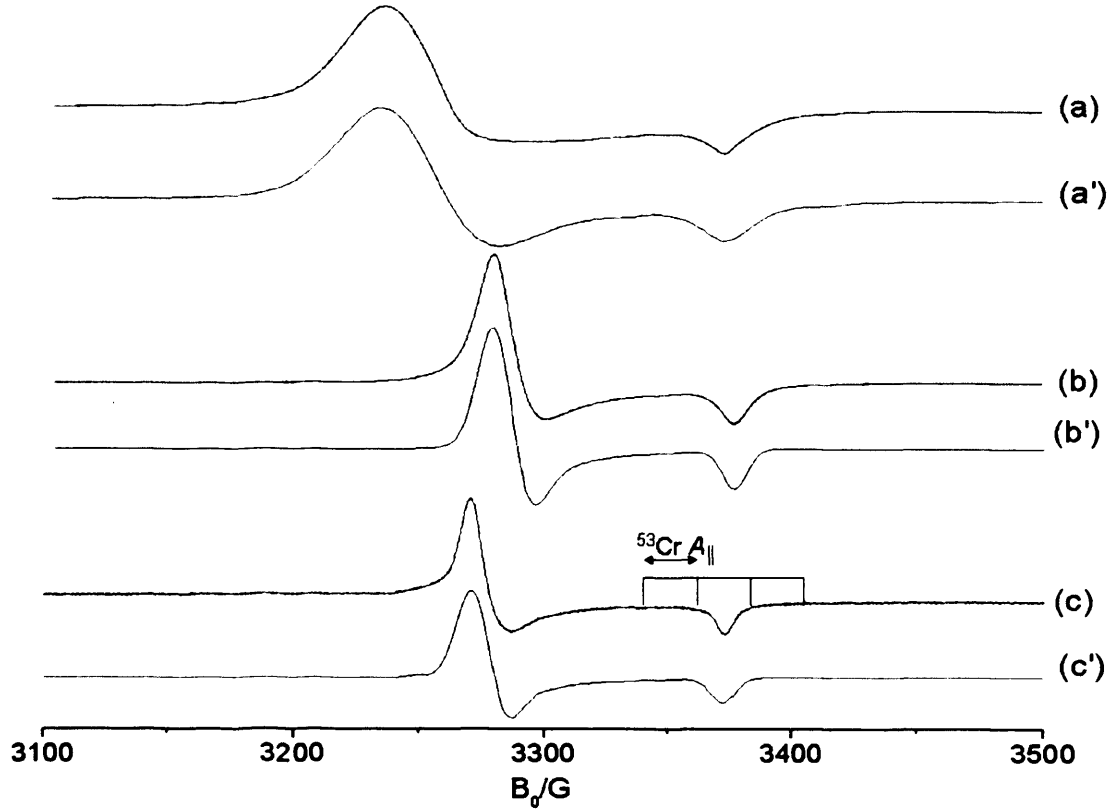

Figure 7.1: Experimental (a, b, c) and simulated (a', b', c') CW-EPR spectra (140K) of (a) **4a**, (b) **4b** and (c) **4c**, recorded in dichloromethane/toluene. Recorded at 140 K. For simulation parameters refer to Table 7.1.

Table 7.1: Spin Hamiltonian parameters obtained by simulation for the compounds **4a** - **c**.

Complex	$g_{\perp}$	$g_{\|}$	g_{iso}	$^{53Cr}A_{\perp}$ / G	$^{53Cr}A_{\|}$ / G	$^{53Cr}a_{iso}$ / G
4a	2.065	1.987	2.039	17	27	20.3
4b	2.045	1.988	2.026	15	23	17.7
4c	2.048	1.987	2.028	12	22	15.3

The spectra corresponding to complexes **4a** - **c** can be described as possessing axial ***g*** and ***A*** matrices, with resolved ^{53}Cr hyperfine coupling particularly in the parallel component. By comparison to the $[Cr(CO)_4PP]^+$ complexes discussed in Chapter 4, the carbene complexes **4a** - **c** are hexaco-ordinate, tetracarbonyl Cr(I) species with a chelating bis(NHC) ligand. As a result their EPR spectra are expected to be qualitatively

similar to those of the bis(phosphine) complexes. This indeed is the case; a pronounced axial symmetry is observed for each carbene complex **4a - c**, with $g\perp > g_e > g\parallel$. As with the bis(phosphine) complexes, the strong ligand fields have caused a large splitting between the t_{2g} orbitals and the e_g orbitals resulting in a low spin (LS) d^5 state ($S = ½$). π-back donation to CO is proposed to stabilize the d_{xz} and d_{yz} relative to the d_{xy} based HOMO. The components of the ***g*** matrix are thus given by the equations discussed in Chapter 4,[31-34] which predict that d_{xz} and d_{yz} will lie just below the SOMO, while $d_{x^2-y^2}$ will be empty and much higher in energy; therefore the g_{xx} and g_{yy} values should be significantly higher than g_e while g_{zz} should be slightly less than g_e. These trends are indeed observed experimentally for the Cr(I) bidentate carbene complexes under consideration.

The values of $g\parallel$ for **4a - c** are, within the margin of error, identical. However, the value of $g\perp$ is much higher for **4a** (2.065) than it is for **4b** (2.045) and **4c** (2.048). The extent of deviation from free spin (i.e., anisotropy in g), is a function of which excited-state orbital contributes to the ground state and also the energy difference between them, as discussed in Chapters 2 and 4. The larger deviation from free spin for complex **4a** must relate to the energy difference between the xy- and z-based orbitals, i.e., the extent of tetragonal distortion from octahedral symmetry. The N-heterocyclic carbene ligand **a** must impart a larger degree of tetragonal distortion, *via* the molecular orbital coefficients, to the Cr(I) ion.

^{53}Cr hyperfine couplings were visible in all spectra; the low intensity of the peaks is due to the only 9.5 % natural abundance of this isotope. The absence of the broad superhyperfine pattern of the ^{31}P nuclei present in the bis(phosphine) complexes means that the metal – electron hyperfine interaction can be observed. The ^{53}Cr hyperfine coupling is largest for complex **4a**, indicating a higher degree of spin density on the metal in this complex, with less delocalisation onto the ligands.

A similar Cr(I) carbene complex to the ones studied in this work has been investigated *via* EPR spectroscopy, by Lappert *et al.*,[20] The complex *cis*-$[Cr(CO)_4(L)_2]^+$ (where L is the monodentate N-heterocyclic carbene ligand $CN(Et)CH_2CH_2N(Et)$), displayed a broad singlet with an isotropic g value of 2.018. This value is slightly lower than the isotropic g values determines for the bidentate carbene complexes **4a - c**; the presence of chelation in the complexes in this work presumably affects the molecular orbital coefficients differently. The authors also characterised other Cr(I) monodentate carbene complexes, which also contained phosphine ligands $[Cr(CO)_3(L)(PP)]^+$. The

presence of ^{31}P superhyperfine coupling dominated the spectra; however, in some cases ^{53}Cr isotropic couplings of *ca.* 13 G were observed. This is slightly lower magnitude than that observed in this work (see Table 7.1); it seems likely that there is more delocalisation of electron density away from the metal, on to the phosphine ligands, presumably *via* backbonding, resulting in a smaller hyperfine coupling in the systems studied by Lappert and co-workers.[20]

The X-band CW-EPR spectra were recorded for the monodentate complexes **4e**, **4h** and **4g**, and the resulting experimental and simulated spectra are shown in Figure 7.2.

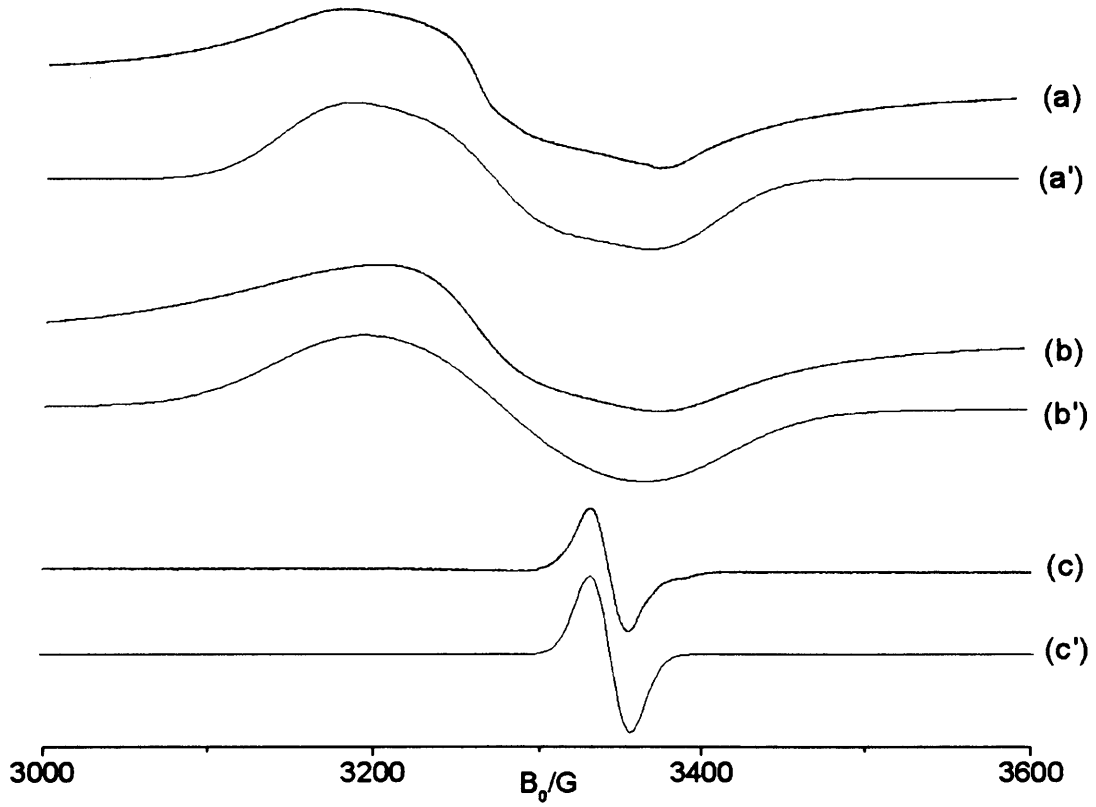

Figure 7.2: Experimental (a, b, c) and simulated (a', b', c') CW-EPR spectra (140K) of (a) **4e**, (b) **4h** and (c) **4g**, recorded in dichloromethane/toluene. Recorded at 140 K. For simulation parameters refer to Table 7.2.

Table 7.2: Spin Hamiltonian parameters for the compounds **4e, 4h** and **4g**.

Complex	g_1	g_2	g_3
4e	2.11	2.045	1.979
4h	2.10	2.045	1.982
4g	2.004	-	-

The monodentate complexes **4e** and **4h** display EPR profiles with rhombic symmetry. The *g* values extracted *via* simulation were approximately 2.1, 2.05 and 1.98 for both complexes (Table 7.2). Monosubstitution or disubstitution is equivalent to a tetragonal distortion from octahedral symmetry. In the case of MA_5B (C_{4v} symmetry), *trans*-MA_4B_2 (D_{4h} symmetry) or *cis*-MA_4B_2 (C_{2v} symmetry) complexes, the t_{2g} orbitals split into b_2 or $b_{2g}(d_{xy})$ and e or $e_g(d_{xz}, d_{yz})$ (Scheme 7.8). As was described in Chapter 4, and above for complexes **4a - c**, the ***g*** tensor for all complexes was consistent with a SOMO based primarily on a d_{xy} ground state. The z-axis of the 'disubstituted' (bidentate) complex (defined as the CO-Cr-CO direction) was unique, and the *xy* axes (defined as CO-Cr-L) were equivalent.

The EPR spectra for complexes **4e** and **4h** indicate that further distortion is occurring to the tetragonal symmetry, *via* the lifting of the degeneracy of the t_{2g} set. Two situations can account for this, as illustrated in Scheme 7.8. On the left hand side is seen the common $(d_{xy})^2(d_{xz},d_{yz})^3$ electronic ground state, whereas the right hand side corresponds to the less common $(d_{xz},d_{yz})^4(d_{xy})^1$ ground state. The unique x-axis in the monodentate complex removes the degeneracy of the d_{xz}, d_{yz} orbitals, so the resulting EPR spectrum would be expected to possess a rhombic profile. Two components of the ***g*** tensor (g_{xx} and g_{yy}) should be greater than g_e, whereas g_{zz} should be lower than g_e. This is indeed observed experimentally ($2.1, 2.05 > g_e > 1.979$), which suggests that the Cr(I) monodentate carbene complexes **4e** and **4h** possess the d_{xy} ground state.

Unexpectedly, complex **4g** appears to produce an isotropic signal, with g_{iso} = 2.004. It would be expected that this complex should produce a similar EPR signal to those of **4e** and **4h**, as its molecular geometry is purportedly very similar. It is possible that, as in the situation described by Hirao *et al.*,[21] the electron is found within the conjugated ring system. The *g* value found for **4g** is very close to free spin, consistent with a radical cation of the NHC ring. The dipp ligands may be stabilising this arrangement *via* the conjugated system. However, no coupling to nitrogens or protons is visible, and additionally the similar complexes **4e** and **4h** do not give rise to this situation, so we assume this result is anomalous, and further experiments would be required to better understand the EPR features of this complex.

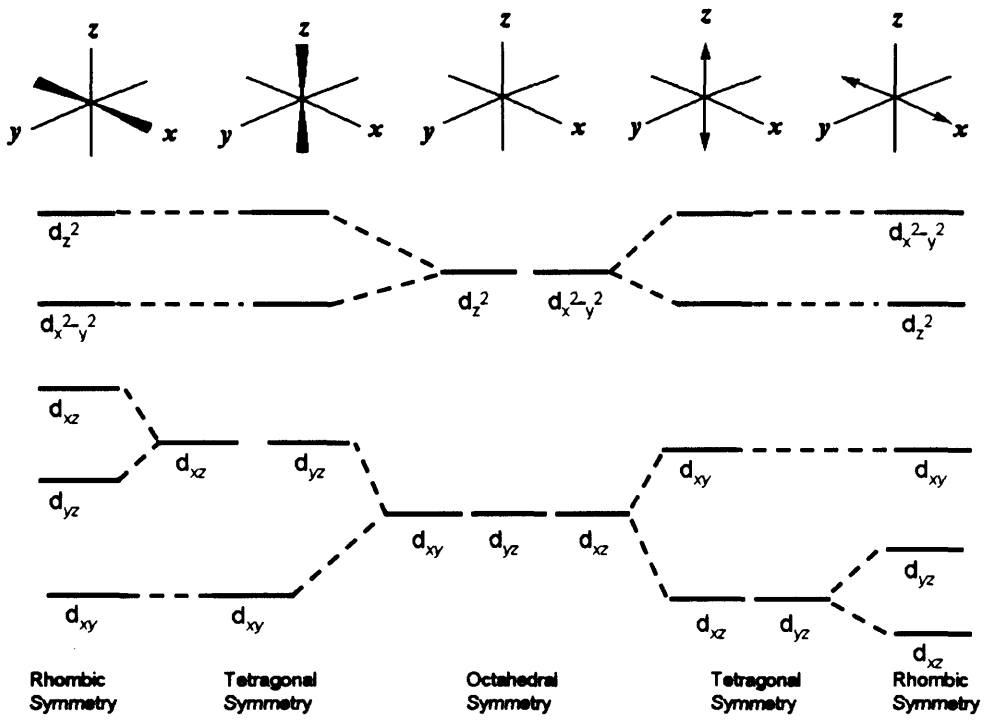

Scheme 7.8: The effects of symmetry on electronic structure.

7.3.2 Cr(III) complexes

The X-band CW-EPR spectra were recorded for the Cr(III)-NHC complexes **5a, 5c – g** and **5i - m**, and the resulting spectra are shown in Figures 7.3 and 7.4.

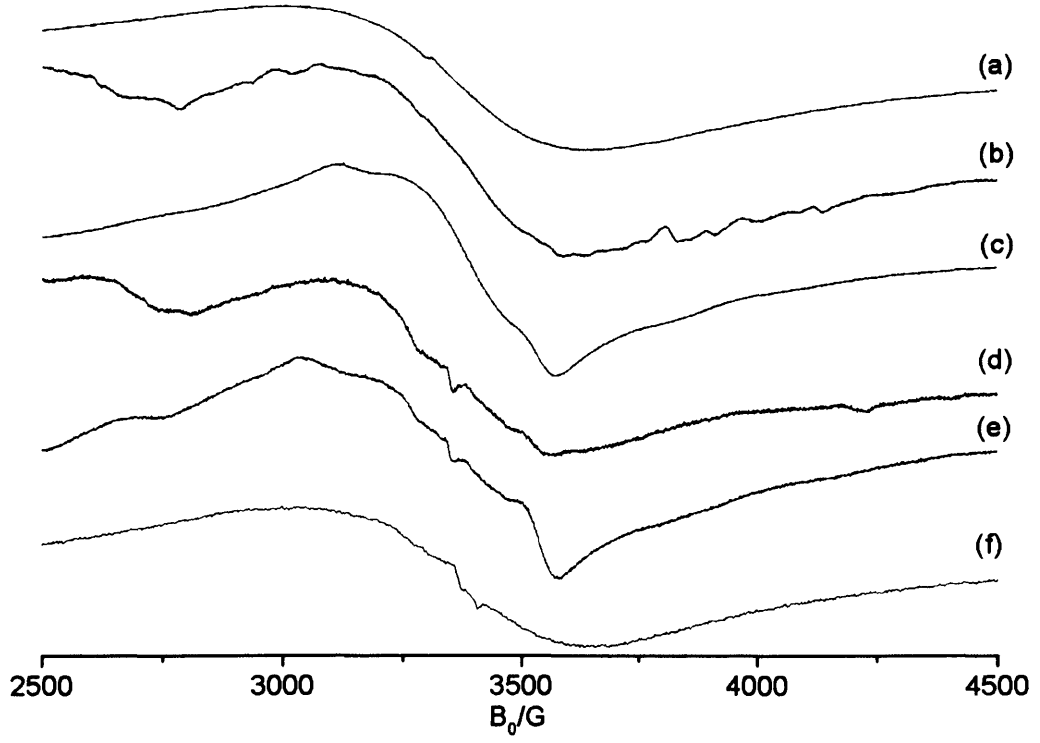

Figure 7.3: Experimental CW-EPR spectra of (a) **5a,** (b) **5l,** (c) **5n,** (d) **5k,** (e) **5m** and (f) **5d.** Recorded in dichloromethane/toluene. Recorded at 140 K.

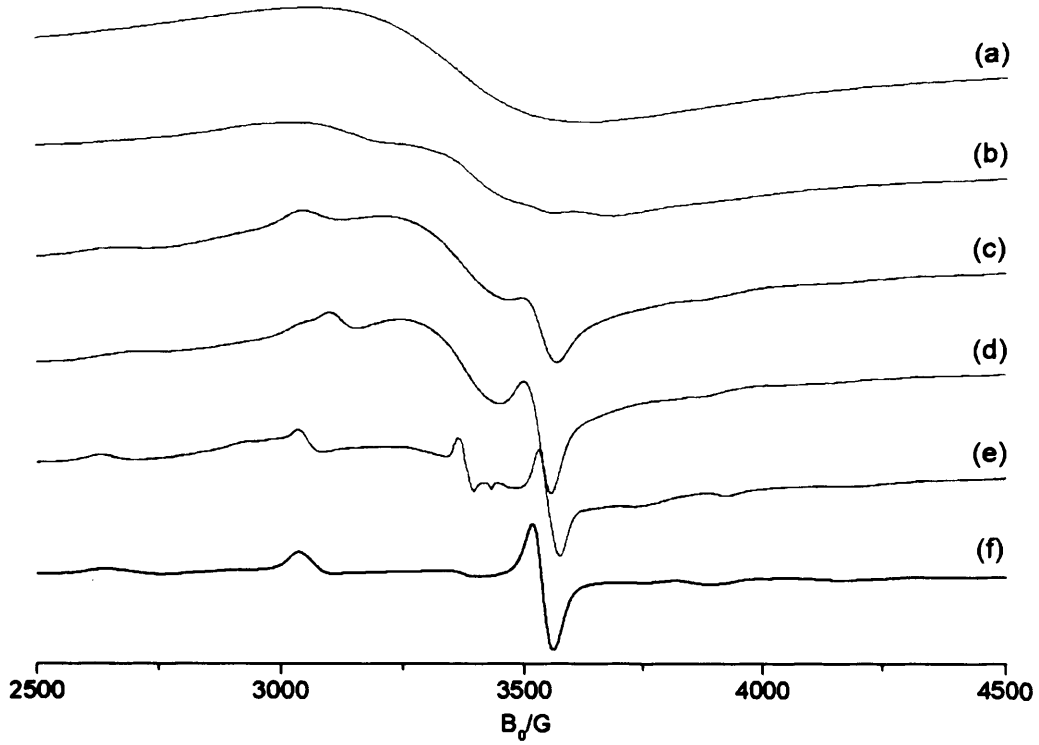

Figure 7.4: Experimental CW-EPR spectra of (a) **5c,** (b) **5i,** (c) **5j,** (d) **5g,** (e) **5e** and (f) **5f.** Recorded in dichloromethane/toluene. Recorded at 140 K.

All the complexes display broad EPR spectra, consistent with a system of total spin $S > {}^1/_2$. This is expected for Cr(III) complexes, which usually have an electronic ground state of $3d^3$ ($^4F_{3/2}$), i.e. total spin of $S = {}^3/_2$. In addition to the electronic Zeeman interaction (and nuclear interactions), the zero field splitting (discussed in Chapter 2) contributes to the spectrum, and in fact dominates it in the case of high-spin transition metal ions, where it can reach values of up to hundreds of gigahertz.[35] Consequently the spectra become much broader than those for $S = ½$ species. As discussed in Chapter 6 and in the Appendix, integer-spin systems are unlikely to be detected at X-band, as they do not have an allowed transition from $M_S = - ½$ to $M_S = ½$ at this frequency. Half-integer spin species, such as Cr(III), do however have this transition detectable at any operating frequency, at around $g = 2$. This is visible in all the spectra above. Additional peaks are visible, arising from the transitions between the Kramer's doublets $|{}^3/_2, \pm {}^1/_2>$ and $|{}^3/_2, \pm {}^3/_2>$, separated by $|2D|$.

Interpretation of the spectra is not straightforward, due to the multitude of possible transitions and complicated by zero-field splitting. Recording the spectra at multiple frequencies would help to de-convolute the spectra. However, it was not possible to access the frequencies needed, e.g. W-band. The spectra do however confirm

the high spin nature of the Cr(III) systems and confirm that the co-ordination mode is a distorted octahedral system.

7.3.3 Ti(III) complexes

The X-band CW-EPR spectra were recorded for the Ti(III)-bidentate NHC complexes **6a - d**, and the resulting spectra and corresponding simulations are shown in Figures 7.5 and 7.6. The spectrum of **6d** displays an axial symmetry. The spin Hamiltonian parameters obtained *via* simulation were: $g_{\|}$= 1.965 and $g_{\perp}$ = 1.895. The remaining Ti(III)-bidentate NHC complexes also appear to display axial symmetry, although the spectra are not as well-resolved as that of **6d**, probably due to a bad glass forming. Unfortunately the limited amount of sample available meant that a good glass for this system could not be established.

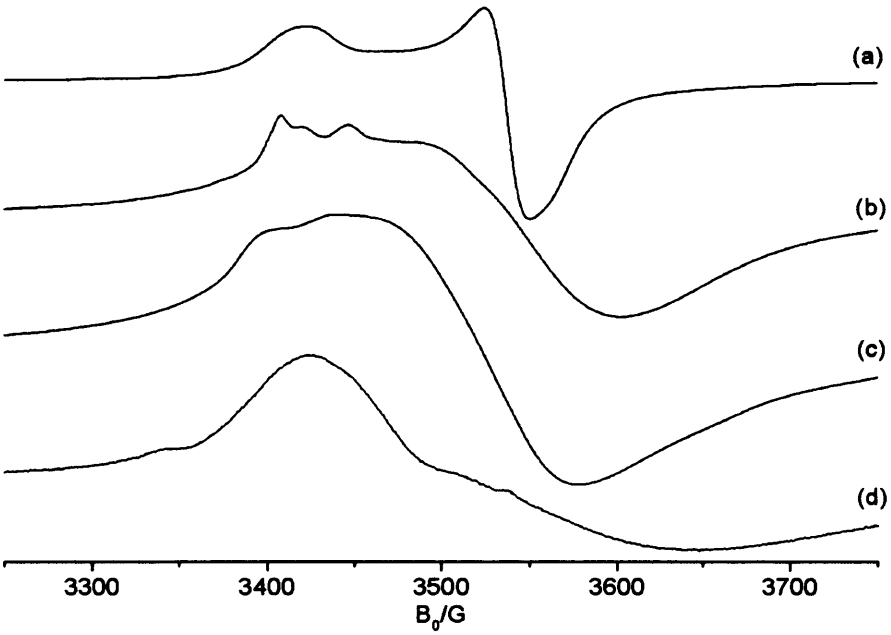

Figure 7.5: Experimental CW-EPR spectra of (a) **6d,** (b) **6b,** (c) **6a** and (d) **6c,** recorded in dichloromethane/toluene. Recorded at 140 K.

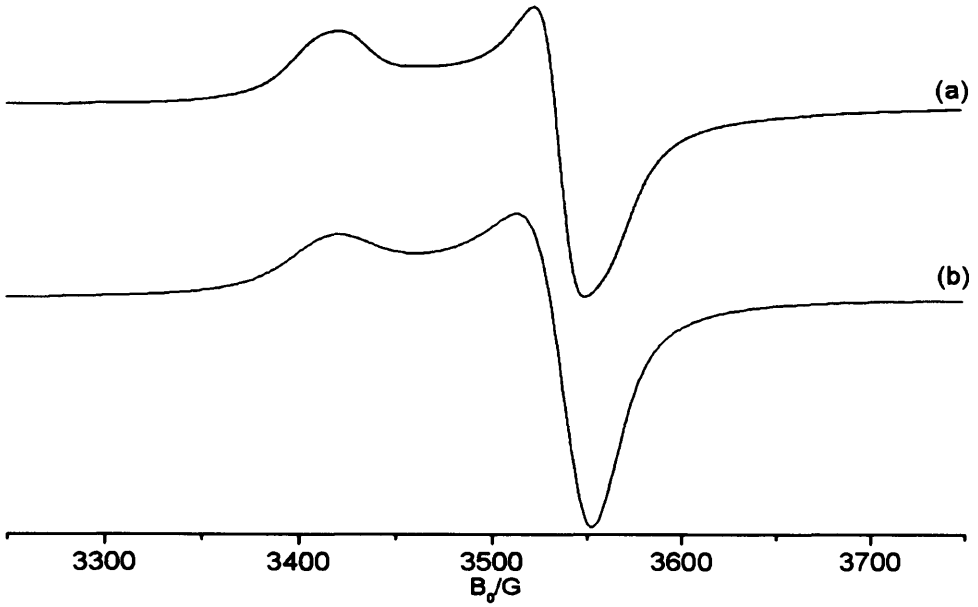

Figure 7.6: Experimental (a) and simulated (b) CW-EPR spectra of **6d,** recorded in dichloromethane/toluene. Recorded at 140 K.

The X-band CW-EPR spectra were recorded for the Ti(III)-monodentate NHC complexes **6e, 6i – k** and **6m – n,** and the resulting spectra and corresponding simulations are shown in Figures 7.7 and 7.8.

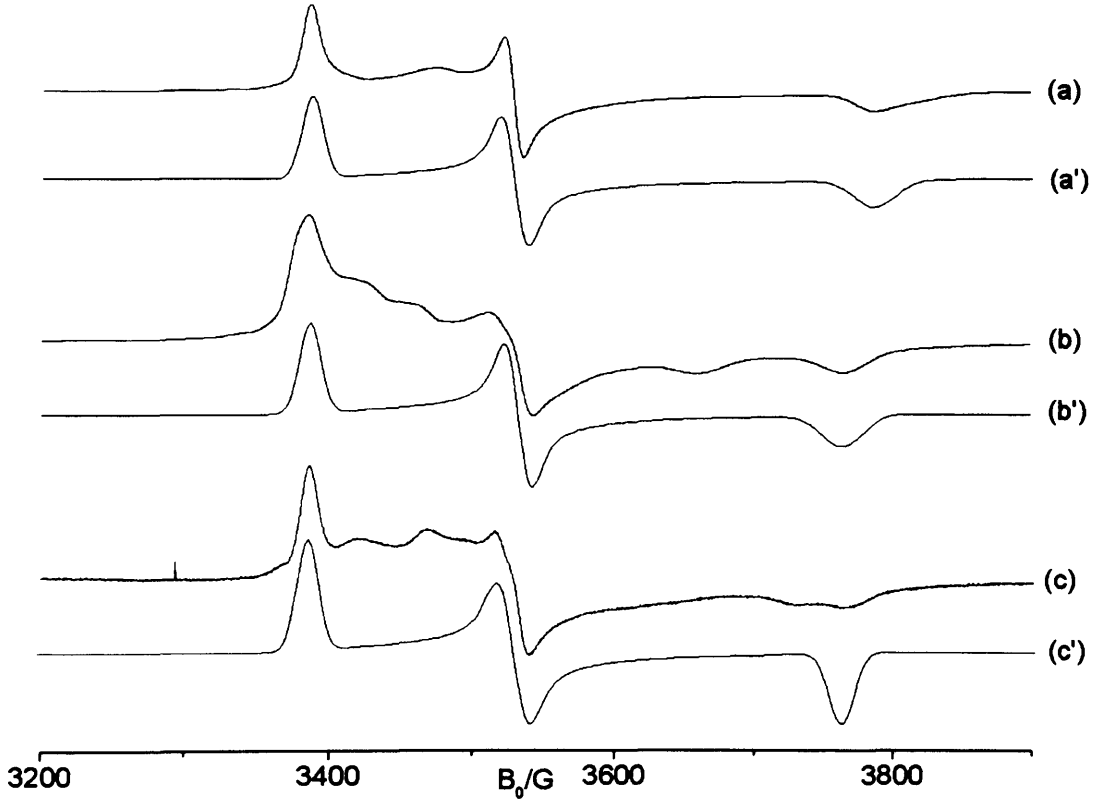

Figure 7.7: Experimental (a, b, c) and simulated (a', b', c') CW-EPR spectra (140K) of (a) **6e,** (b) **6i** and (c) **6j**, recorded in dichloromethane/toluene. Recorded at 140 K. For simulation parameters refer to Table 7.3.

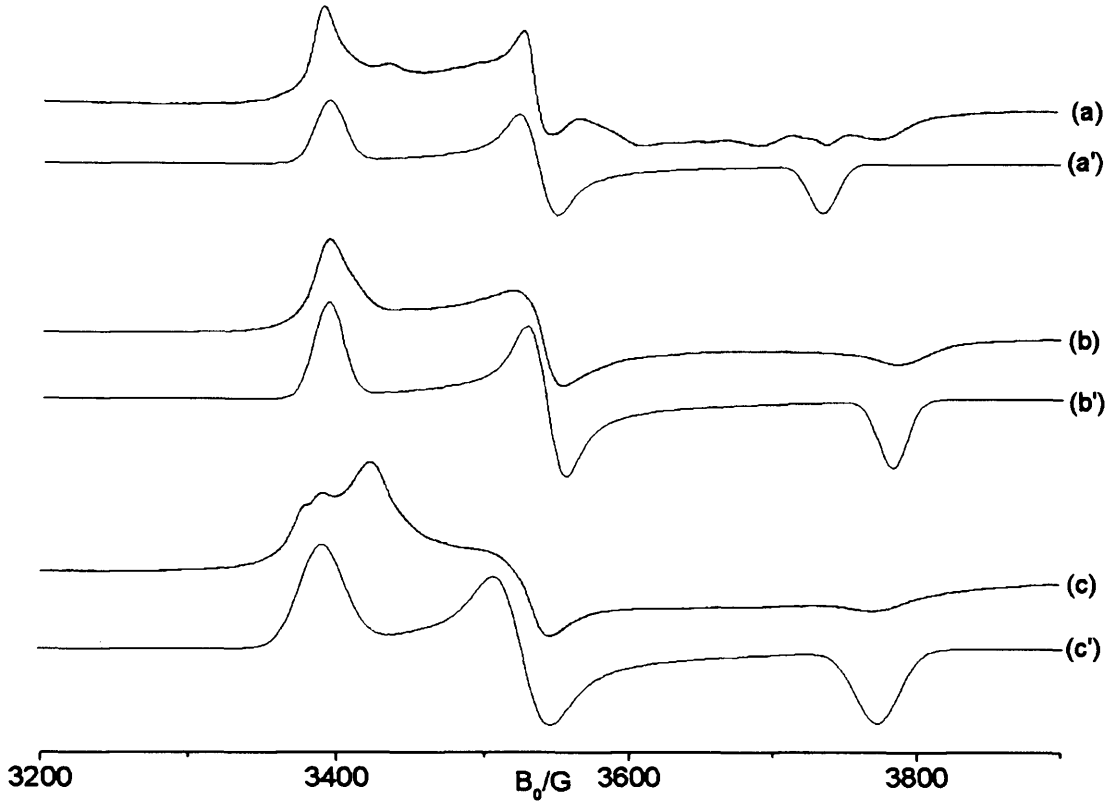

Figure 7.8: Experimental (a, b, c) and simulated (a', b', c') CW-EPR spectra (140K) of (a) **6e**, (b) **6m** and (c) **6n**, recorded in dichloromethane/toluene. Recorded at 140 K. For simulation parameters refer to Table 7.3.

The Ti(III) monodentate NHC complexes all possess a pronounced rhombic EPR symmetry. Some of the spectra contain additional features, which are likely to be a result of semi-orientation of crystallites caused by the solvent system used. Limited amounts of paramagnetic complexes were available for analysis, so a study of which solvent system produced the best glass could not be carried out. However, the principal components of the ***g*** tensor for each system could still be obtained *via* simulation.

Table 7.3: Spin Hamiltonian parameters obtained by simulation for the compounds **6e, 6i - k** and **6m - n**.

Complex	g_1	g_2	g_3
6e	1.976	1.897	1.768
6i	1.978	1.897	1.780
6j	1.978	1.898	1.780
6k	1.975	1.895	1.795
6m	1.978	1.895	1.775
6n	1.976	1.898	1.776

The g values extracted are all less than free spin, as expected for a d^1 transition metal ion. For transition metal complexes of the type $[MA_5B]$ possessing C_{4v} symmetry, $g_x = g_y \neq g_z$. For $[MA_4B_2]$, the *trans* complex possesses D_{4h} symmetry with $g_x = g_y \neq g_z$, whilst the *cis* complex of C_{2v} symmetry produces $g_x \neq g_y \neq g_z$ (in theory, although in practice it often appears as axial since $g_x \approx g_y$). Hence a simple analysis of the EPR data was possible for the $[Cr(CO)_4$-bis(phosphine)] complexes discussed in Chapters 4 - 6 and the $[Cr(CO)_4$-(NHC-NHC)] and $[Cr(CO)_5(NHC)]$ complexes discussed earlier in this Chapter. However, the monodentate $[Ti(III)(Cl)_3(NHC)(THF)_n]$ and the bidentate $[Ti(III)(Cl)_3$(NHC-NHC)$(THF)_n]$ complexes are less straightforward to analyse simply.

The orbital splitting pattern for an octahedral complex with tetragonal distortion (either elongation or compression) was shown in Scheme 7.8. Elongation of the M-L bonds along the z-axis produces the expected terms $^2A_{1g}$ and $^2B_{1g}$ (in the upper ^2E_g state) and ^2E_g and $^2B_{2g}$ (in the lower $^2T_{2g}$ state). Such a splitting pattern produces a paramagnetic state for a low spin d^5 system (such as Cr(I)) but would lead to an EPR silent ground state for a d^1 system in the absence of additional rhombic distortion. In other words, the single unpaired electron in the degenerate d_{xz} and d_{yz} orbitals would be EPR silent. If this degeneracy was lifted by rhombic distortion (eg., d_{xz} lowest level as shown in Scheme 7.8) then an EPR spectrum would be seen. Alternatively, with compression of the M-L bonds along the z-axis, the single d_{xy} orbital now has lowest energy and this will lead to an EPR signal both in a tetragonal distortion and subsequent rhombic distortion. The observation of the EPR spectra from the mono- and bidentate carbene complexes suggests that this situation must be occurring. The axial g values for complex **6d** ($g_{\|} = 1.965$, $g_{\perp} = 1.895$) and the rhombic g values for complexes **6e, i, j, k, m and n** ($g_1 \approx 1.987$, $g_2 \approx 1.877$, and $g_3 \approx 1.779$) are both consistent with this view and the predicted structures given in Figure 7.7.

In comparison to the EPR data reported by Arnold *et al.*,[29] on $[Ti\{OCMe_2CH_2(1\text{-}C[NCHCHN^iPr])\}_3]$ ($g_{iso} = 1.970$) and Lorber *et al.*,[30] on $TiCl_2(NMe_2)(IMes)_2$ (IMes = 1,3-dimesitylimidazol-2-ylidene) ($g_{iso} = 1.943$), the isotropic g values determined for the monodentate complexes in this work are all slightly lower (approximately 1.88 for the monodentate complexes, and 1.92 for the bidentate (axial) complex). Presumably the greater deviation from free spin value in the complexes under investigation here is caused by a larger degree of spin-orbit coupling.

7.4 Conclusions

A series of Cr(I), Cr(III) and Ti(III) complexes bearing N-heterocyclic ligands were prepared and analysed *via* continuous-wave EPR spectroscopy. Cr(III) complexes of this type have been shown to be active in ethylene oligomerisation catalysis,[6, 8, 23] so knowledge of their fundamental nature, both in electronic and geometric terms, is needed. Cr(I) and Ti(III) are also well known as active metals for oligomerisation, so study of such complexes bearing NHC ligands as potential catalysts is also desired.

The Cr(I) bidentate NHC complexes exhibited analogous EPR spectra to the corresponding Cr(I) bis(phosphine) complexes, possessing very similar electronic properties; an axial ***g*** matrix was observed with a SOMO based on a metal contribution of d_{xy}. The monodentate complexes appeared to possess rhombic symmetry, indicating a lifting of the degeneracy of the t_{2g} set, but still possessing a SOMO based on a d_{xy} ground state. The spectra of the Cr(III) complexes were very broad due to the high-spin nature of the system, and correspondingly more difficult to interpret. They did however confirm the high spin nature, and that the co-ordination mode is a distorted octahedral system. They also demonstrated that these particular NHC ligands can indeed stabilise a Cr(III) centre.

The Ti(III) complexes all exhibited g factors of less than g_e, confirming a d^1 ground state. Those bearing bidentate NHC complexes appeared to possess axial symmetry, while those bearing monodentate NHC ligands displayed pronounced rhombic symmetry. Observation of both axial and rhombic spectra indicates that the orbital arrangement is that with a single d_{xy} orbital with the lowest energy, leading to an EPR signal both in a tetragonal distortion and subsequent rhombic distortion.

7.5 References

1. H.-W. Wanzlick and H.-J. Schönherr, *Angew. Chem. Int. Ed.*, 1968, **7**, 141.
2. K. Öfele, *J. Organmet. Chem.*, 1968, **12**, 42.
3. A. C. Hillier, G. A. Grasa, M. S. Viciu, H. M. Lee, C. Yang and S. P. Nolan, *J. Organmet. Chem.*, 2002, **653**, 69.
4. A. Fürstner, *Angew. Chem. Int. Ed.*, 2000, **39**, 3012.
5. A. Binobaid, M. Iglesias, D. J. Beetstra, B. Kariuki, A. Dervisi, I. Fallis and K. J. Cavell, *Dalton Trans.*, 2009, 7099.
6. T. Rüther, N. Braussaud and K. J. Cavell, *Organometallics*, 2000, **20**, 1247.
7. D. S. McGuinness, V. C. Gibson, D. F. Wass and J. W. Steed, *J. Am. Chem. Soc.*, 2003, **125**, 12716.
8. D. S. McGuinness, J. A. Suttil, M. G. Gardiner and N. W. Davies, *Organometallics*, 2008, **27**, 4238.

9. W. A. Herrmann, *Angew. Chem. Int. Ed.*, 2002, **41**, 1290.
10. C. M. Crudden and D. P. Allen, *Coord. Chem. Rev.*, 2004, **248**, 2247.
11. F. E. Hahn and M. C. Jahnke, *Angew. Chem. Int. Ed.*, 2008, **47**, 3122.
12. J. F. Harrison, *J. Am. Chem. Soc.*, 1971, **93**, 4112.
13. C. W. Bauschlicher Jr., H. F. Schaefer III and P. S. Bagus, *J. Am. Chem. Soc.*, 1977, **99**, 7106.
14. A. J. Arduengo III, R. L. Harlow and M. Kline, *J. Am. Chem. Soc.*, 1991, **113**, 361.
15. M.-T. Lee and C.-H. Hu, *Organometallics*, 2004, **23**, 976.
16. K. Albahily, D. Al-Baldawi, S. Gambarotta, E. Koç and R. Duchateau, *Organometallics*, 2008, **27**, 5943.
17. R. D. Köhn, M. Haufe, S. Mihan and D. Lilge, *Chem. Commun.*, 2000, 1927.
18. T. Agapie, S. J. Schofer, J. A. Labinger and J. E. Bercaw, *J. Am. Chem. Soc.*, 2004, **126**, 1304.
19. A. Brückner, J. K. Jabor, A. E. C. McConnell and P. B. Webb, *Organometallics*, 2008, **27**, 3849.
20. M. F. Lappert, R. W. McCabe, J. J. MacQuitty, P. L. Pye and P. I. Riley, *J. Chem. Soc., Dalton Trans.*, 1980, 90.
21. H. Sakurai, K. Sugitana, T. Moriuchi and T. Hirao, *J. Organmet. Chem.*, 2005, **690**, 1750.
22. A. J. Rucklidge, D. S. McGuinness, R. P. Tooze, A. M. Z. Slawin, J. D. A. Pelletier, M. J. Hanton and P. B. Webb, *Organometallics*, 2007, **26**, 2782.
23. D. S. McGuinness, V. C. Gibson and J. W. Steed, *Organometallics*, 2004, **23**, 6288.
24. K. A. Kreisel, G. P. A. Yap and K. H. Theopold, *Organometallics*, 2006, **25**, 4670.
25. P. J. W. Deckers, B. Hessen and J. H. Teuben, *Organometallics*, 2002, **21**, 5122.
26. T. J. M. de Bruin, L. Magna, P. Raybaud and H. Toulhoat, *Organometallics*, 2003, **22**, 3404.
27. A. N. J. Blok, P. H. M. Budzelaar and A. W. Gal, *Organometallics*, 2003, **22**, 2564.
28. H. Aihara, T. Matsuo and H. Kawaguchi, *Chem. Commun.*, 2003, 2204.
29. N. A. Jones, S. T. Liddle, C. Wilson and P. L. Arnold, *Organometallics*, 2007, **26**, 755.
30. C. Lorber and L. Vendier, *Dalton Trans.*, 2009, 6972.
31. A. L. Rieger and P. H. Rieger, *Organometallics*, 2002, **21**, 5868.
32. P. H. Rieger, *Coord. Chem. Rev.* , 2004, **135-136**, 203.
33. D. A. Cummings, J. McMaster, A. L. Rieger and P. H. Rieger, *Organometallics*, 1997, **16**, 4362.
34. B. R. McGarvey, *Coord. Chem. Rev.*, 1998, **170**, 75.
35. M. Brustolon and E. Giamello, eds., *Electron Paramagnetic Resonance - A Practitioner's Toolkit*, Wiley, 2009.

Chapter 8
Conclusion

The study of the mechanistic details underpinning selective oligomerisation catalysis is of timely importance, due to the relatively scarce amount of knowledge of their mode of operation. Chromium-based catalysts dominate the literature, and the variety of paramagnetic states which could in principle be involved in the catalytic cycle render EPR spectroscopy an ideal method for investigation of these compounds. The sensitivity of the technique and the ability to conduct variable temperature analyses also add to its suitability.

Firstly, full characterisation of a set of 'pre-catalyst' complexes was undertaken, as discussed in Chapter 4. CW-EPR revealed each complex to possess an axial $\boldsymbol{g}$ matrix ($g_\perp > g_c > g_\parallel$), with superhyperfine coupling to two equivalent ^{31}P nuclei, consistent with a low-spin d^5 species of approximate C_{2v} symmetry, where the metal contribution to the SOMO is primarily d_{xy}. The magnitude of Δg, reflecting the extent of tetragonal distortion to the system, differed from complex to complex; however, no correlation was found between this trend and ligand type. The isotropic component to the ^{31}P coupling also varied as a function of the complex studied; it was of a larger magnitude in those Cr(I) complexes bearing PNP ligands than those bearing PCP, indicating that the phosphorus 3*s* character in the SOMO was higher for the former. CW-ENDOR provided information on the ^{1}H (phenyl ring), ^{31}P and ^{14}N nuclear hyperfine couplings of the pre-catalysts. Subtle structural differences in the complexes, namely in the phenyl ring conformations, were found to occur as a function of ligand type. It was found that ^{31}P couplings possessed a large isotropic contribution to their interaction. Both superhyperfine and quadrupolar interactions were observed in the ^{14}N ENDOR spectra, and the $\boldsymbol{A}$ and $\boldsymbol{Q}$ matrices were typical for a weakly coupled nitrogen nucleus. Pulsed experiments were also conducted, in order to confirm the data obtained *via* CW-methods; the spin Hamiltonian parameters extracted from FSED EPR spectra were in excellent agreement with those obtained in the continuous-wave experiment. The ESEEM spectra recorded were more difficult to assign. The Davies ENDOR provided ^{31}P and ^{1}H couplings in accordance with those obtained by CW methods. These initial pulsed experiments on the pre-catalyst proved that the technique is valid and viable for further work on the activated system.

Analysis of the system after activation with various alkylaluminium activators was then performed, and EPR spectra recorded between 10 K and 300 K. Upon activation, the EPR spectrum changed dramatically from that of the pre-catalyst. A distinctive multiplet signal was observed at temperatures ≥ 180 K for all complexes, and was discussed in Chapter 5. The isotropic spin Hamiltonian parameters extracted *via* simulation, of g_{iso} = 1.988, ten equivalent ^{1}H interactions (I = ½, a_{iso} = 3.45 G) and one ^{53}Cr nucleus (9.5% abundant, I = $^{3}/_{2}$, a_{iso} = 18.0 G), established the existence of a Cr(I) bis-arene complex, $[Cr(\eta^6\text{-}CH_3C_6H_5)_2]^+$. To test whether the co-ordinating arene rings originated from the solvent, TEA in hexane was used as an activator. Exactly the same EPR signal was observed, proving that in this case it cannot arise from an aromatic solvent effect. Intramolecular co-ordination of two of the phenyl rings from the ligand itself, to the chromium centre, was proposed as the explanation. To confirm this proposal, a $[Cr(CO)_4$bis(dicyclohexylphosphino-propane)$]^+$ complex, in which the ligand phenyl groups were replaced by cyclohexyl groups, was prepared and activated in the absence and presence of aromatic solvent respectively. Following activation with TEA/hexane, no $[Cr(\text{bis-arene})]^+$ species were observed. However, when the complex was dissolved in dichloromethane/toluene and subsequently activated using TEA/hexane, the formation of $[Cr(\text{bis-arene})]^+$ species could be readily observed; $[Cr(\eta^6\text{-}CH_3C_6H_5)_2]^+$ complexes must be formed by reaction of Cr(I) ions with the toluene in solution. Repetition of the above experiments using perdeuterated toluene solvent proved that intermolecular arene co-ordination is favoured over intramolecular.

Analysis of the spectra recorded at temperatures below 180 K was then performed, and discussed in Chapter 6. At low levels of TEA activation, two paramagnetic species were identified (Species I and II). Species I possessed an apparent axial $\boldsymbol{g}$ tensor, with $g_{\|} > g_e > g_{\perp}$, and superhyperfine coupling to two ^{31}P nuclei. The 'reversal' of the g values compared to the pre-catalyst showed that a modification to the geometry of this chromium species had occurred upon activation. Species II also displayed an axial $\boldsymbol{g}$ matrix, with $g_{\|} \approx g_e > g_{\perp}$, and hyperfine coupling to ^{53}Cr. The spin Hamiltonian parameters were consistent with a $[Cr(\text{bis-arene})]^+$ complex, and Species II was thus identified as that detected ≥ 180 K. At higher levels of TEA activation, an additional Species (III) is present, with a preliminary assignment of a rhombic $\boldsymbol{g/A}$ tensor. A likely explanation for the origins of this signal, which also accounts for the presence of a half field transition, is the possibility of Cr...Cr dimers formed from neighbouring Cr bis-arene complexes. In all cases, activation of the pre-catalyst resulted

in a dramatic decrease in signal intensity, due either to the formation of diamagnetic centres, or due to the formation of 'EPR silent' centres. CW and pulsed ENDOR measurements were performed on the activated system. Notably, exceptionally large proton couplings were detected, which were too large to be explained only on the basis of a bis-arene complex, but which may instead arise from co-ordinated alkyl groups. Finally, activation of a more 'concentrated' solution of the Cr(I) pre-catalyst resulted in the formation of a fourth paramagnetic centre (Species IV). It possessed a ***g*** matrix with $g_{\perp} > g_e > g_{\parallel}$, and superhyperfine ^{31}P coupling of an increased magnitude compared to the pre-catalyst. The nature of this complex is not known but based on the well defined ***g*** tensor appears to possess high symmetry.

Chapter 7 was concerned with the study of a series of Cr(I), Cr(III) and Ti(III) complexes bearing N-heterocyclic carbene ligands. Complexes of this type are active in ethylene oligomerisation catalysis, so knowledge of their fundamental nature is of interest, and complementary to that of the complexes studied in Chapters 4 to 6. The Cr(I) bidentate NHC complexes exhibited analogous EPR spectra to the corresponding Cr(I) bis(phosphine) complexes, i.e. an axial ***g*** matrix with a SOMO based on a metal contribution of d_{xy}. The monodentate complexes appeared to possess rhombic symmetry, indicating a lifting of the degeneracy of the t_{2g} set. The spectra of the Cr(III) complexes were very broad but did confirm the high spin nature of the system. The Ti(III) complexes all exhibited g factors of less than g_e, confirming a d^1 ground state. Those bearing bidentate NHC complexes appeared to possess axial symmetry, while those bearing monodentate NHC ligands displayed pronounced rhombic symmetry. Observation of both axial and rhombic spectra indicates that the orbital arrangement is that with a single d_{xy} orbital with the lowest energy.

Above all, the experimental results presented in this Thesis have demonstrated that the family of EPR techniques, including CW and pulsed methodologies, can be successfully applied in the study of Cr-based oligomerisation catalysts. The handling of these air sensitive compounds presents only a minor obstacle to their characterisation by EPR, including the pulsed techniques. In that latter case, owing to the design of the pulsed resonator, a modified version of the EPR handling approach had to be devised in order to study the complexes at 10K. However, this was (in the end) easily overcome.

Perhaps the greatest challenge in the project was the difficulty encountered in attempting to achieve precise reproducibility in all the activation studies. In these experiments, particularly upon addition of low levels of triethylaluminium (TEA), very

small quantities of TEA were required (*ca.* 5 μL). As a result, it was always difficult to deliver exactly the same amount of TEA each time. Furthermore, at the higher levels of TEA, a complicated mixture of paramagnetic centres were identified (labelled Species I – IV). It is quite possible that an equilibrium exists between some or all of these centres; one may transform into another, or one may represent a side-product of the other. Therefore, despite delivering the 'same nominal amount' of TEA in each experiment, small variations existed within the EPR spectra, making the analysis and interpretations slow and laborious. Scaling up the amount of TEA used would circumvent this problem, but so doing would require substantially more complex, creating its own problems.

One highlight of this Thesis was undoubtedly the thorough characterisation of the pre-catalyst Cr(I) complexes prior to activation.[1] The scarcity of EPR data in the literature on low valent chromium(I) complexes was striking, let alone such complexes of catalytic relevance, and nothing was available on the analysis of these systems using advanced hyperfine techniques such as ENDOR or ESEEM. Building from these analyses of the pre-catalyst complexes requires a more complete picture of the paramagnetic complexes formed in the activated system. At least one of these complexes formed upon TEA activation was identified as the intramolecularly formed Cr-bis-arene complex.[2]

Among the multitude of other paramagnetic centres formed in the activated system (Species I, III and IV), their precise identification remains elusive. Part of the difficulty in identifying their structure was the presence of overlapping EPR signals observed in all cases. Only for Species IV was a 'clean' EPR signal observed; in all other cases, mixtures of Species I-III complicated not just the EPR, but particularly the ENDOR and pulsed EPR data, which are difficult to interpretet even under ideal conditions. The use of ^{13}C-labelled CO will certainly assist in the characterisation of these remaining unidentified complexes, as it is vital to know if the activated complexes are classed as mono-, di- or tri-carbonylated entities. *In situ* EPR-electrochemistry studies would also offer invaluable insights, as another great unknown in the system is the nature of the redox states formed after activation.

Furthermore, since the Cr(I) bis-arene complex is so stable, and indeed ever present in the activated system, one can speculate whether other related types of complex also exist in this system, such as piano-stool type complexes. Indeed a number of EPR studies have been reported for low valent tricarbonyl Cr(I) centres coordinated to an arene or cyclopentadienyl system. Any further investigation and analysis of the

EPR/ ENDOR data of the activated system should certainly focus on these types of complexes in the first instance, as they may provide a possible structure for Species I.

A further complexity to the problem, and one only touched upon in this Thesis (which focussed on the qualitative description of the paramagnetic centres present), concerns the quantitative aspects of the activation process. After initial activation, almost 90% of the initial Cr(I) signal was lost (at higher levels of TEA this was reduced to 60%). Where and how can this loss of paramagnetism be accounted for? It is an important point because following addition of an alkene (1-hexene) the EPR signal intensity recovered slightly, indicating some interaction of the alkene with EPR silent centres. This clearly needs to be better understood in further work.

Finally it should also be mentioned, that the actual catalysis is performed under high pressures (not the ambient pressures adopted in this study). It is not clear, and one may argue unlikely, that the paramagnetic activated species generated in this study are present under high pressure conditions. It has long being speculated that an equilibrium exists between different activated catalyst states during the reaction, as one converts into another. Pressure would then play a crucial role in any potential loss of the carbonyl groups in a closed system. As the formation of the bis-arene complex has shown, loss of carbonyl destabilises the Cr(I) centres which may lead to an inactive catalyst. Investigations into the loss of CO at higher pressure, or the reversibility of this process which would thereby extend the lifetime of the catalyst, could be monitored by EPR.

To conclude, there are many more EPR-based experiments that can be performed. However, the results presented in this Thesis have provided the first stepping stone along the path to unravel the mystery and complexity of this elusive and challenging catalytic system.

References

1. L. E. McDyre, T. Hamilton, D. M. Murphy, K. J. Cavell, W. F. Gabrielli, M. J. Hanton and D. M. Smith, *Dalton Trans.*, 2010, **39**, 7792.
2. L. E. McDyre, E. Carter, K. J. Cavell, D. M. Murphy, K. Sampford, W. F. Gabrielli, M. J. Hanton and D. M. Smith, *in prep.*, 2011.

APPENDIX

EPR THEORY

A.1 Theory of Systems with $S > ½$

The theory described in Chapter 2 was relevant for systems where the total electron spin quantum number is ½, i.e., systems containing only one unpaired electron. Some systems however contain two or more unpaired electrons; for example highly symmetrical molecules with degenerate orbitals, excited states of organic molecules or transition metal complexes. In Chapter 6, Species III was proposed to arise from a Cr(I)...Cr(I) dimer; hence a brief outline of the theory for high spin systems will be presented below.

For a system with two unpaired electrons, the total spin quantum number can take the value of S = 1or S = 0, depending on whether the spins are parallel or antiparallel. As discussed in Section 2.1.2, the z component of each state can take the values S, $S - 1$, ... , $-S$. The values of the component M_S for the S = 1 state can take the values 1, 0 and -1; it is therefore known as a triplet state. For the $S = 0$ state only $M_S = 0$ is possible, and is hence known as a singlet state. Similarly, for a system with a total electron spin quantum number of $S = {}^3/_2$, the values of M_S are ${}^3/_2$, ½, -½ and $-{}^3/_2$. Transitions $\Delta M_S = 1$ are allowed, as with a single electron.

There is a dipolar interaction between the magnetic moments of the two (or more) spins, analogous to that between electron and nuclear magnetic moments (the hyperfine interaction). High-spin entities also demonstrate a phenomenon known as zero-field splitting (ZFS), where the admixture of excited states to the ground state (spin-orbit coupling) causes the M_S sub-levels to become non-degenerate in the absence of an external magnetic field. ZFS can also be caused by the dipole-dipole interaction. The ZFS can reach values of up to hundreds of gigahertz, especially for transition metal systems, causing line broadening of spectra, sometimes beyond recognition. The additional electron spin transitions and the presence of zero-field splitting for high-spin species add much more complexity to the EPR spectrum than for a single electron.

A.2 Theory of Multifrequency EPR

As discussed in Chapter 2, the energy of the EPR transition is directly proportional to the static field magnitude B_0 :

$$\Delta E = g\mu_B B_0 \qquad \text{(A.1)}$$

For an anisotropic system, the transitions corresponding to the orientations θ, φ of the g matrix principal axes with respect to the field vector occur at field magnitudes of:

$$B_r = \left[\frac{h\nu - M_I A(\theta,\phi)}{\mu_B g(\theta,\phi)}\right] \qquad \text{(A.2)}$$

The field (B_r) is directly proportional to the irradiation frequency ν. This means that the field value that g occurs at will increase linearly with the irradiation frequency. This can be extremely useful for two main purposes: firstly, if the principal components of the g matrix occur at field positions close together, it can be difficult to distinguish them. Increasing the operating frequency means the components will be more widely spaced apart in the field-swept spectrum. For example, at an irradiation frequency of 34.1 GHz ('Q-band') the same value of g will occur at a field approximately 3.6 times greater than that at 9.5 GHz (X-band) (see Figure A.1).

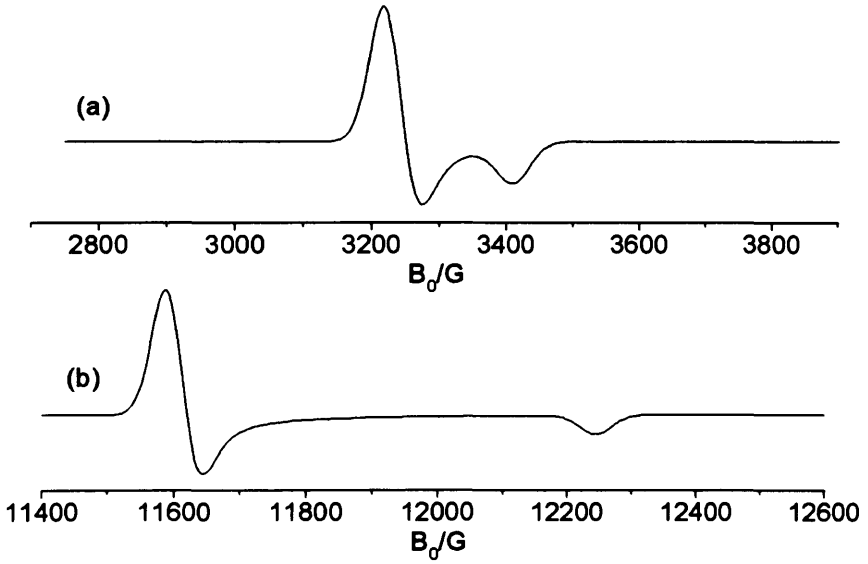

Figure A.1.Simulated axial CW-EPR spectra (S = ½, I = 0) with $g_\perp$ = 2.1, $g_\parallel$ = 1.99 at (a) 9.5 GHz and (b) 34.1 GHz.

Secondly, high-frequency EPR can be essential for interpreting spectra from high-spin (S > ½) species, discussed above. These species can be separated in to two classes; half-integer spin complexes (S = $^3/_2$, $^5/_2$ etc. or Kramers ions) and integer spin

(S = 1, 2 etc. or non-Kramers ions). For an integer spin species there is no intra-Kramers $\Delta M_S = \pm 1$ transition and to observe the inter-Kramers transition a large increase in operating frequency would be needed.[7] Therefore these ions are often EPR-silent under normal conditions. For half-integer spin species there is an allowed transtition at any frequency but it is uninformative with regard to the zero-field splitting parameters; to gain information on this it is preferable to observe the inter-Kramers transition.

Therefore an increase in operating frequency can be beneficial in certain circumstances. However, as mentioned previously the high cost of this equipment makes its use unrealistic in most instances, and most important information can be gained from X- or Q-band work.

A.3 Molecular Description of Low-Spin d^5 Systems

The molecular orbital description of bonding in co-ordination complexes involves combinations of atomic orbitals from separate components to produce new molecular orbitals (MOs), different in energy from the parent orbitals. Some of these new orbitals will be more stable than the parents ('bonding orbitals') and some less stable ('anti-bonding orbitals'). The total number of orbitals however remains the same. A stable bond is formed when there is an excess of electrons in the bonding MOs.

The easiest way to visualise this is *via* an example. In octahedral coordination complexes ML_6 (where M is the central metal and L the coordinating ligands) and considering σ-bonding only, there are 9 valence metal orbitals available; 5 *d* orbitals, 3 *p* and 1 *s*. Six ligands are present and so only 6 ligand orbitals are available. Therefore the total number of molecular orbitals created from combination of ligand orbitals and metal orbitals is 12. The remaining three metal orbitals remain as 'nonbonding' orbitals. The rules governing which atomic orbitals can combine lie in group theory. They are based on symmetry considerations and will not be discussed here in detail. The molecular orbital diagram for ML_6 is shown below. The 6 highest-energy orbitals are anti-bonding orbitals, the middle are nonbonding and the lowest three are bonding. The number of electrons present and the energy of the orbitals contribute to the stability and reactivity of the complex.

The three t_{2g} metal valence orbitals (non-bonding in the scenario below) are frequently of the correct symmetry to interact with filled π (t_{2g}) orbitals on the ligand.

In this case 6 molecular orbitals result. The net result of this is to vary the energy of the t_{2g} molecular orbitals whilst the e_g levels remain the same.

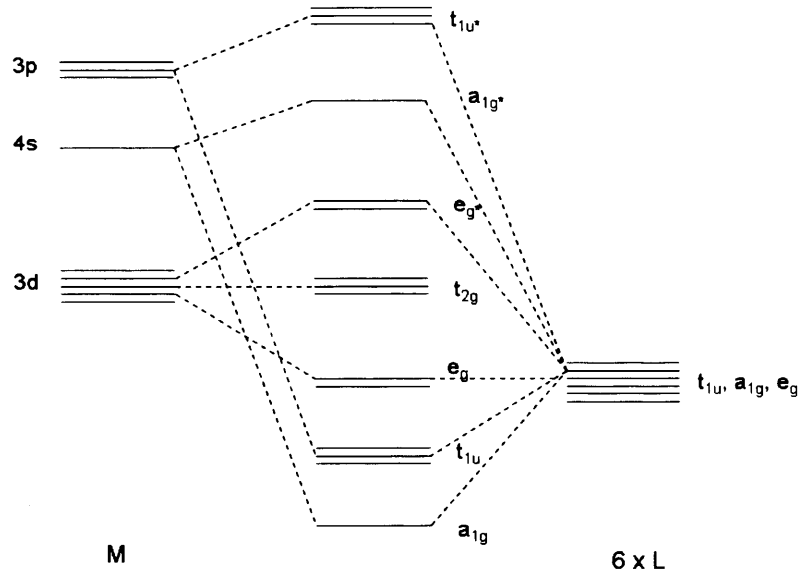

Scheme A.1: Molecular orbital diagram for an octahedral ML_6 complex

If the ligand t_{2g} orbitals are lower in energy than the metal t_{2g} and filled, the ligand acts as a π-base and donates electron density to the metal (see Scheme A.2). The metal t_{2g} are empty, and electron density can be transferred from the metal towards the ligand (shown in Scheme A.3).

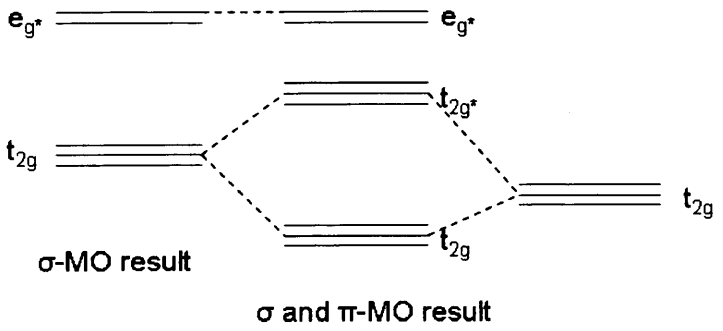

Scheme A.2: Molecular orbital diagram showing the effect of a ligand π-base.
The opposite situation can also occur if the ligand t_{2g} is higher in energy than

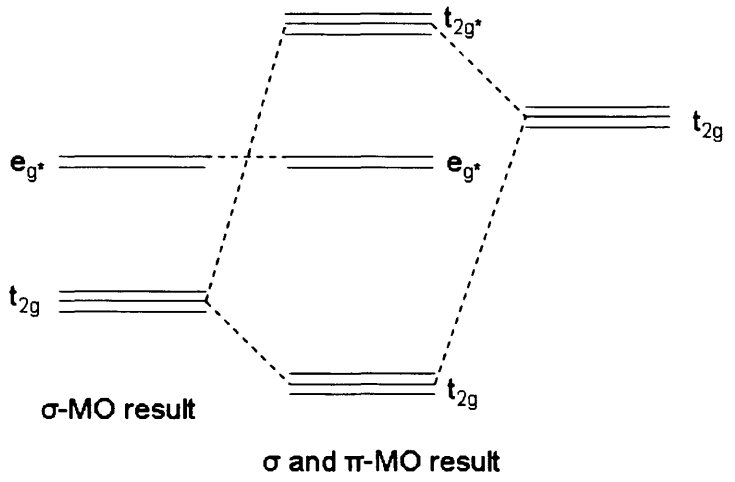

Scheme A.3: Molecular orbital diagram showing the effect of a ligand π-acid.

The situation that occurs depends strongly on the ligand(s) present. CO is a strong π-acceptor ligand and as such can stabilise metals in low oxidation states. Bis(diphenyl) phosphines are also good π-acceptors. This property is very important for the Cr(I) metal centres under consideration in this project, which are stabilised by these ligands. In complexes of lower than octahedral symmetry, e.g. MA_4B_2 which is C_{2v}, a tetragonal distortion from the octahedron has occurred. The degeneracy of the t_{2g} orbitals is now completely lifted. The exact orbital arrangement and the identity of the SOMO depends on the nature of the ligands.

In an idealised situation, as when the SOMO can be described by a single *d* orbital, the magnetic moment results purely from electron spin. The Zeeman levels would in this case by characterised by a *g* value of 2.0023. However, the mechanism of spin-orbit coupling restores some orbital angular momentum to the system and hence the effective *g* value will differ from g_e. The components of the ***g*** matrix therefore provide information on the ligand field splittings of *d* orbitals.

A.4 Fundamentals of Pulsed EPR and ENDOR

A relatively recent development in EPR and ENDOR technology has been that of pulsed techniques. The fundamental difference between these and the continuous-wave methodology is that the measurement of the response in the former is performed in the absence of applied radiation. When an electron spin is placed in a magnetic field, its magnetic moment precesses about the field vector due to the torque on it. The angular frequency of this precession is proportional to the field magnitude:

$$\omega_L = -\gamma B_0 \qquad \text{(A.3)}$$

They are linked by the gyromagnetic ratio γ of the electron. The angular frequency is linked to the EPR transition frequency ν:

$$\omega_L = \frac{\nu}{2\pi} \qquad \text{(A.4)}$$

The magnetically dilute EPR sample consists of many identical, non-interacting spins. Although the behaviour of single spins must be described *via* quantum mechanics, the behaviour of the spin packet (ensemble of identical spins) can be described by a sum average which behaves as a classical vector. This is the magnetisation vector M_0 with components M_x, M_y and M_z (the z direction corresponding to the field vector $B_0 = B_z$). At thermal equilibrium, and in the absence of applied microwaves, there is an excess of spins in the state parallel to the field; M_z is a function of the population difference between the spin levels, and hence on the energy difference between them and the sample temperature (i.e., a Boltzmann distribution). M_z relaxes towards thermal equilibrium with the time constant T_1 (spin-lattice or longitudinal relaxation time). The x and y components of the spin packet are also precessing around B_0 at the frequency γB_0. They decay towards zero with a time constant T_2 (spin-spin or transverse relaxation time). The large number of spins in the xy plane means their varying orientations cancel each other out and the net magnetization vector M_0 is aligned along z.

A.4.1 One microwave pulse

When a pulse is applied, if a co-ordinate system rotating at the frequency of the microwaves applied along B_0 (ω_0) is used, and assuming resonant conditions ($\omega_0 = \omega_L$), the microwave magnetic field B_1 has a constant direction along x during the pulse. Additionally, the field B_0 disappears in the rotating frame. Now the only field is B_1 and so the magnetization precesses about B_1 at a frequency:

$$\omega_1 = -\gamma B_1 \qquad \text{(A.5)}$$

If B_1 is assumed to be parallel to the x axis, the magnetization precesses about x during the pulse. The actual angle by which M_0 is rotated is known as the tip angle:

$$\alpha = -\gamma |B_1| t_p \qquad \text{(A.6)}$$

where t_p is the pulse length. The most common tip angles are $\pi/2$ and π, i.e. 90 and 180°. The effect of a $\pi/2$ pulse along x is to create a stationary magnetisation along –y, as shown in Figure A.2:

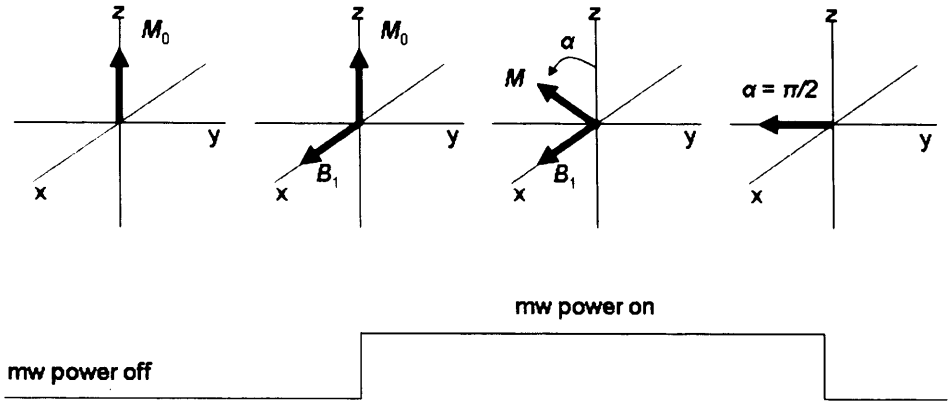

Figure A.2: The effect of a $\pi/2$ pulse on the magnetisation vector M_0.

When viewed from the stationary (laboratory) frame, and once the pulse has finished ($B_1 = 0$), the static magnetisation along –y is rotating in the xy plane, generating a microwave signal in the resonator. The above theory is valid if all spins are exactly at resonance with the applied radiation, i.e., $\omega_0 = \omega_L$. However in a real sample, there is an envelope of many different frequencies ('inhomogeneous broadening'). Immediately after a $\pi/2$ pulse the magnetization will be along –y as discussed above. However because now $\omega_0 \neq \omega_L$, the magnetization will appear to rotate in the xy plane; each frequency component of the EPR spectrum will rotate at a different rate ($\Delta\omega$). Therefore measurement of the transverse magnetization and extraction of the individual frequency components enables the envelope of EPR absorption to be reconstructed, i.e., the EPR spectrum. As time passes the transverse magnetisation will decay; the frequencies of the individual spin packets will gradually cancel each other out. The characteristic time constant for this type of decay as known as T_2*. Additonally, there will be decay due to spin interactions, resulting in mutual and random spin flip-flops ('homogeneous broadening'). The decay of the transverse magnetisation from this mechanism is characterised by T_2. The sum of the various relaxation processes adds up to the free induction decay (FID). The overall decay can be characterised by the phase memory time T_M. Both the frequency and spin-spin relaxation time are measured in the experiment.

If the spectrum is broad ($\Delta\omega > \omega_1$), not all the magnetisation can be tipped into the xy plane to create the FID. It is important to maximise ω_1 or minimize $\pi/2$, so more of the spectrum can be detected.

A.4.2 Two microwave pulses

The spin-spin relaxation time T_2 could be measured directly from the FID after one pulse; measurement of the spin-lattice relaxation time requires two pulses. The 'inversion recovery' experiment involves a π pulse being applied to the system. The net magnetization M_0 is rotated by 180° so it is anti-parallel to the z axis. After a time τ, during which $-M_0$ starts to decay to thermal equilibrium *via* spin-lattice relaxation, a $\pi/2$ pulse is applied which flips the remaining magnetisation into the xy plane (the amount of decay is proportional to the length of τ). The FID is then measured. By repeating the experiment many times and varying the value of τ, the amplitude of the FID as a function of τ can be established, which provides a direct measurement of T_1.

A.4.3 The spin echo

The concept of the spin echo is an extremely important one in pulsed EPR. It was first discovered by Hahn during NMR studies.[11, 12] The decay of the FID was previously discussed. This transverse relaxation occurs *via* two processes: homogeneous and inhomogeneous broadening. Inhomogenous broadening occurs because each of the spins experiences a slightly different field. As mentioned previously, after a $\pi/2$ pulse there is a distribution of $\Delta\omega$ in the rotating frame. The magnetisation will therefore 'fan out' in the xy plane causing the net transverse magnetisation to decay:

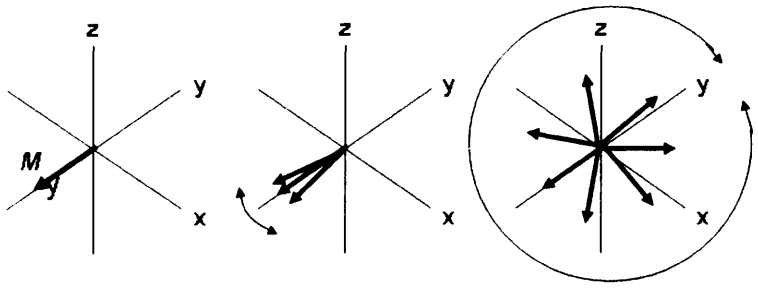

Figure A.3: Fanning out of the transverse magnetisation.

After a time τ, if a π pulse is applied to the system, the magnetisation will be flipped about the x axis. The magnetisation of each spin packet will still be rotating in

the same direction and speed, but with opposite phase. After another τ, the magnetisation will refocus, and this constructive interference at 2τ results in a signal. This signal is an echo of the magnetisation generated immediately after the first pulse.

The spin echo experiment is extremely useful because in lots of cases, the FID cannot be measured accurately from just one pulse; there is a 'dead time' of the spectrometer (approximately 80 ns) where no measurements can be taken until a certain time has elapsed. Therefore vital information may be lost if only observing one pulse. Additionally, at 2τ the echo amplitude is independent of the inhomogeneous broadening of the spin packets. However, the echo amplitude still decays as a function of 2τ. The decrease in echo height occurs because of decay due to homogeneous broadening; as discussed before, with spectral diffusion being a large contributor (interactions between spins, molecular motion and molecular rotation causing this). Not all of the magnetisation refocuses due to this and so the echo height decreases the longer τ is. The overall decay constant for the echo decrease, which takes T_2 in to account, is the phase memory time T_M.

A.4.4 FSED EPR

A common use of the spin echo is to obtain an EPR spectrum. This is known as field-swept echo-detected (FSED) EPR. The echo amplitude is recorded as the magnetic field is swept. As discussed previously, the echo height decays as a function of the homogeneous broadening with a time constant T_M. This phase memory time is dependent on orientation for slowly tumbling radicals and where relaxation is caused by small-angle libration.[13] Anisotropy of the *g* factor, and hence the net magnetisation and corresponding spin echo intensity, is reflected in the spectral profile.

A.4.5 ESEEM

Electron spin echo envelope modulation (ESEEM) is a phenomenon that occurs due to the coupling between the unpaired electron and any spin-active nuclei present in the system. The echo intensity is modulated due to these weak hyperfine or quadrupolar interactions. The modulations arise due to simultaneous excitation of allowed and forbidden transitions. The variation in intensity of the echo as a function of the time between the pulses is measured.

ESEEM can either be detected via a two-pulse method as described previously, or a three-pulse stimulated echo method, also discovered by Hahn.[11] This

is usually a $\pi/2 - \tau - \pi/2 - T - \pi/2 - \tau -$ echo. The echo amplitude is measured as a function of time T at constant τ. ESEEM occurs when the normal EPR selection rules break down and forbidden nuclear spin transitions can occur. The forbidden transition consists of a nuclear spin-flip along with that of the electron spin. This results in a precessing nuclear magnetisation at the ENDOR frequency of that nucleus. As τ is varied the probability of forbidden transitions varies. Hence the echo intensity as a function of T is modulated at the ENDOR frequencies and the amplitude of the modulation depends on τ. In this way direct identification of spin-active nuclei present is achieved, as their nuclear Larmor frequencies are encoded in the modulation.

A.4.6 Pulsed ENDOR

The theory of CW-ENDOR was discussed previously and as mentioned, relies heavily on the relative relaxation times of the electrons and nuclei. This can be problematic if, for example, the electronic relaxation time is too short to permit saturation. However in the pulsed method, the relaxation times are not so critical as the pulses of radiation are so short and intense that T_1 and T_2 are negligible during the pulse.

The two main ways of performing pulsed ENDOR are the Mims method based on the stimulated echo and the Davies experiment based on inversion recovery. Mims was the first to discover pulsed ENDOR.[14] The stimulated echo sequence described earlier is used, but an RF pulse is inserted during the delay T; the pulse sequence is shown in Figure A.4. The RF pulse will flip the nuclear spin; the electron spin then changes its resonant frequency by the hyperfine coupling A. When the stimulated echo is observed, the phase of the spin will be different by $A\tau$ than without the RF pulse. The ENDOR signal is observed as a decrease in the intensity of the echo.

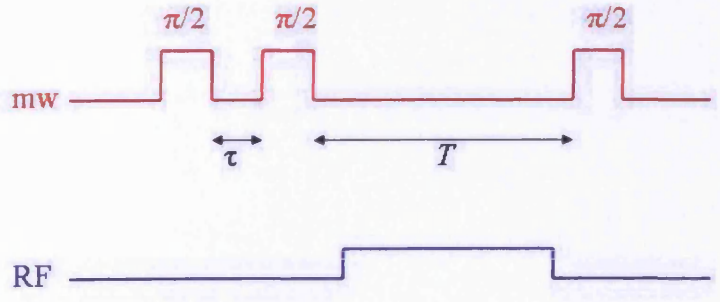

Figure A.4: Mims ENDOR pulse sequence.

The Davies method[15] consists of a selective π pulse which inverts the magnetisation of only one allowed EPR transition. During a delay *T* an RF pulse is applied; the pulse sequence is shown in Figure 2.16. This inverts the magnetisation of the NMR transition and consequently the magnetisation of the EPR transition disappers. There is then either a single pulse and the FID that follows is measured, or a pair of pulses and the primary echo is detected, all as a function of the RF frequency.

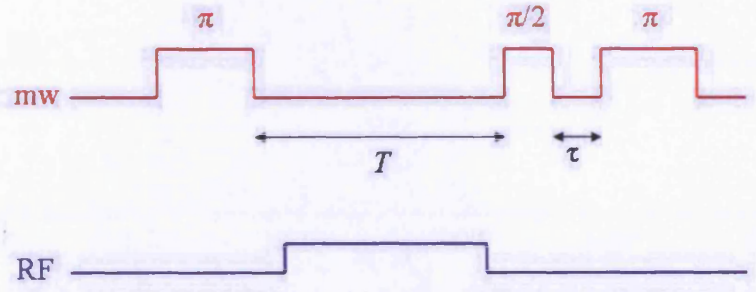

Figure A.5: Davies ENDOR pulse sequence.

A.5 Appendix to Chapter 4 (Supporting & Additional EPR spectra)

A.5.1 CW-EPR

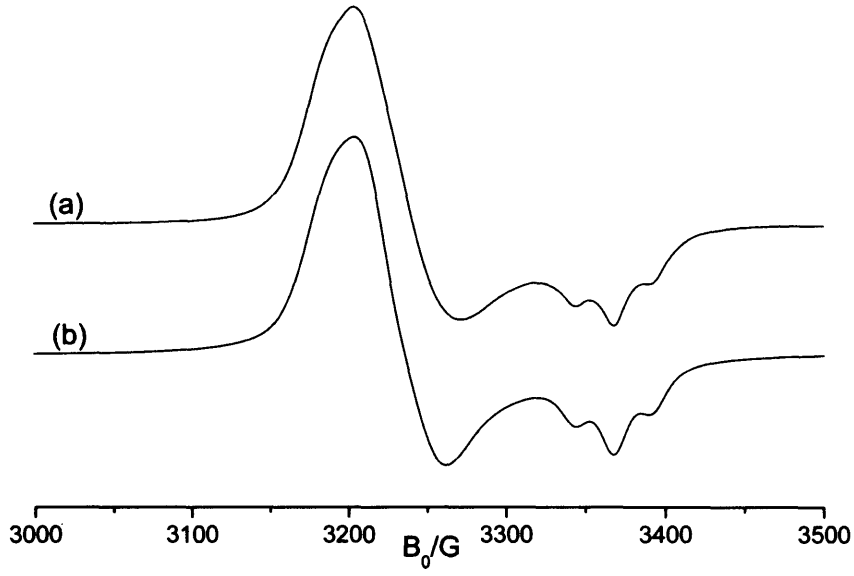

Figure A.6a: Experimental (a) and simulated (b) cw-EPR spectra (140K) of $[Cr(CO)_4(dppe)]^+$ (**2a**) recorded in dichloromethane/toluene at a microwave frequency of 9.381 GHz. For simulation parameters refer to Table 4.1 (Chapter 4).

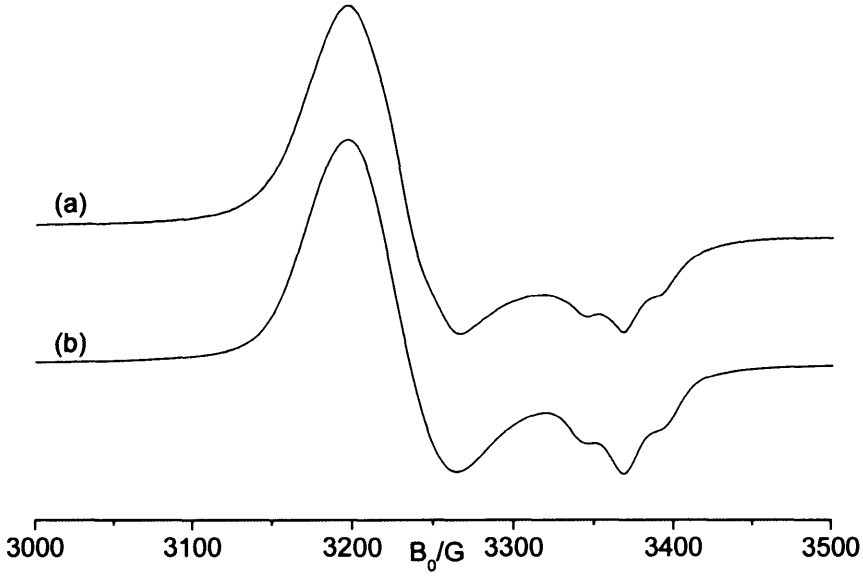

Figure A.6b: Experimental (a) and simulated (b) cw-EPR spectra (140K) of $[Cr(CO)_4(Ph_2PBzPPh_2)]^+$ (**2c**) recorded in dichloromethane/toluene at a microwave frequency of 9.375 GHz. For simulation parameters refer to Table 4.1.

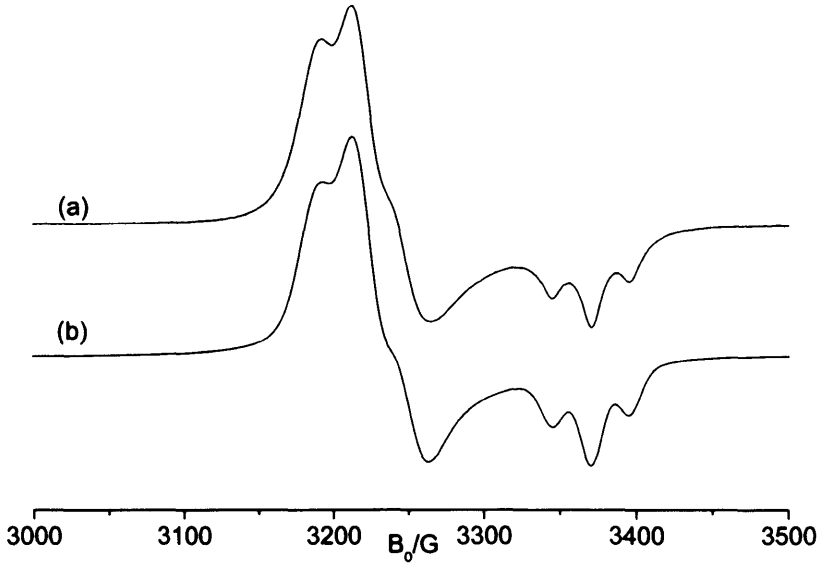

Figure A.6c: Experimental (a) and simulated (b) cw-EPR spectra (140K) of $[Cr(CO)_4(Ph_2PN(Et)PPh_2)]^+$ (**2d**) recorded in dichloromethane/toluene at a microwave frequency of 9.363 GHz. For simulation parameters refer to Table 4.1.

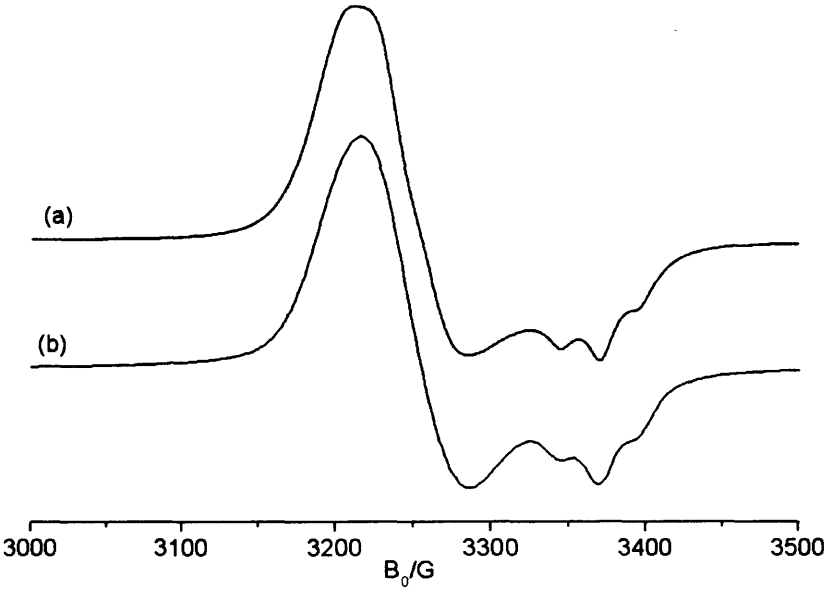

Figure A.6d: Experimental (a) and simulated (b) cw-EPR spectra (140K) of $[Cr(CO)_4((Ph_2PN(iPr)PPh_2)]^+$ (**2g**) recorded in dichloromethane/toluene at a microwave frequency of 9.376 GHz. For simulation parameters refer to Table 4.1.

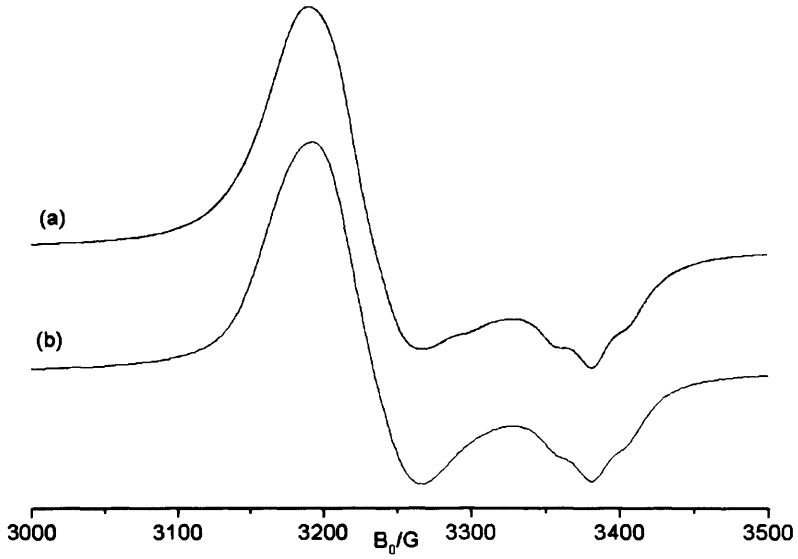

Figure A.6e: Experimental (a) and simulated (b) cw-EPR spectra (140K) of $[Cr(CO)_4(Ar_2PN(Me)PAr_2)]^+$ Ar = 2-C_6H_4(Et) (**2e**) recorded in dichloromethane/toluene at a microwave frequency of 9.386 GHz. For simulation parameters refer to Table 4.1.

Complex	**CW EPR simulation linewidth (parallel component) / G**	**CW EPR simulation linewidth (perpendicular component) / G**
2a	14.5	30
2b	16.5	21.5
2c	18.5	40.0
2d	14.5	23.8
2e	19.0	40.0
2f	10.5	23.5
2g	14.5	22.5

A.5.2 CW- ^{1}*H ENDOR*

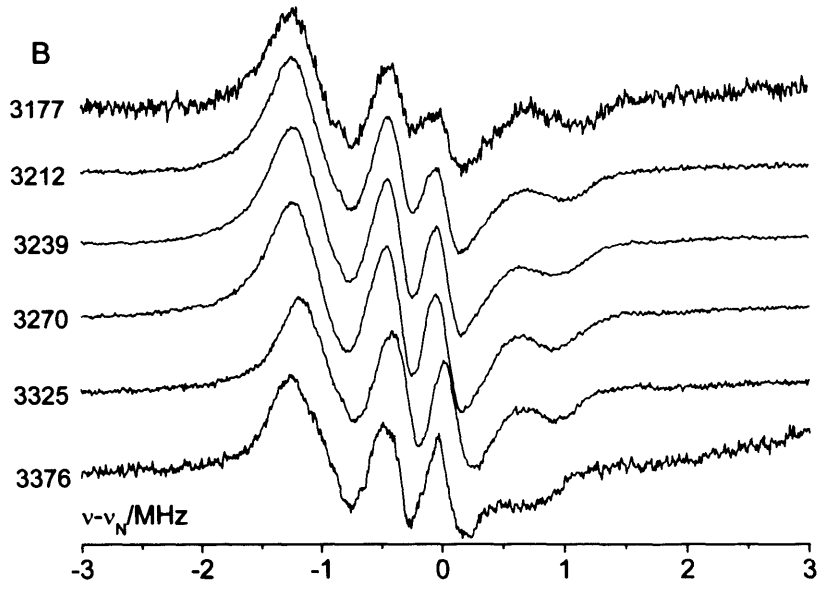

Figure A.7a: Experimental CW-^{1}H ENDOR spectra (10K) of $[Cr(CO)_4(dppe)]^+$ **(2a)** recorded in deuterated dichloromethane/toluene at a microwave frequency of 9.493 GHz and a modulation depth of 79 kHz. The angular selective spectra were obtained at the magnetic field positions (*B* in Gauss) shown in the Figure.

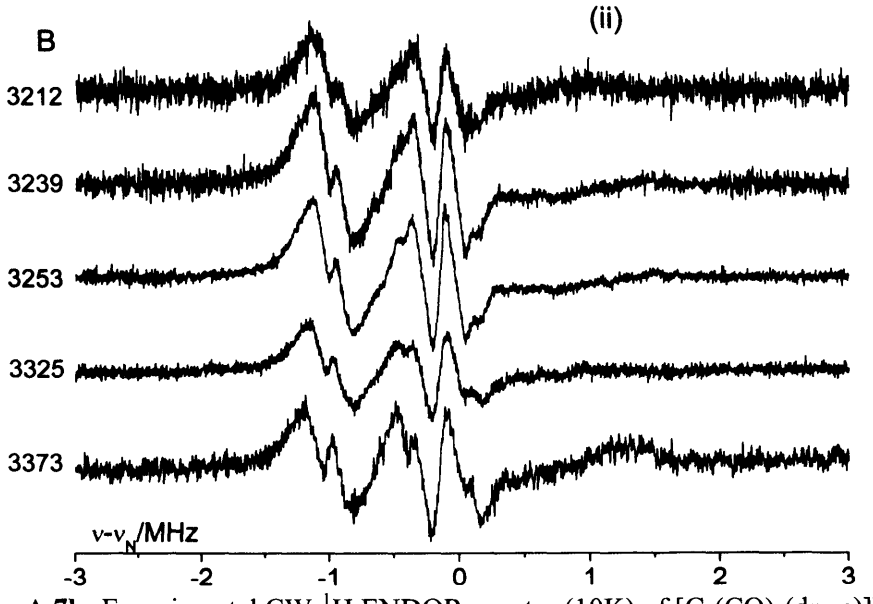

Figure A.7b: Experimental CW-^{1}H ENDOR spectra (10K) of $[Cr(CO)_4(dppp)]^+$ **(2b)** recorded in deuterated dichloromethane/toluene at a microwave frequency of 9.493 GHz and a modulation depth of 79 kHz. The angular selective spectra were obtained at the magnetic field positions (*B* in Gauss) shown in the Figure.

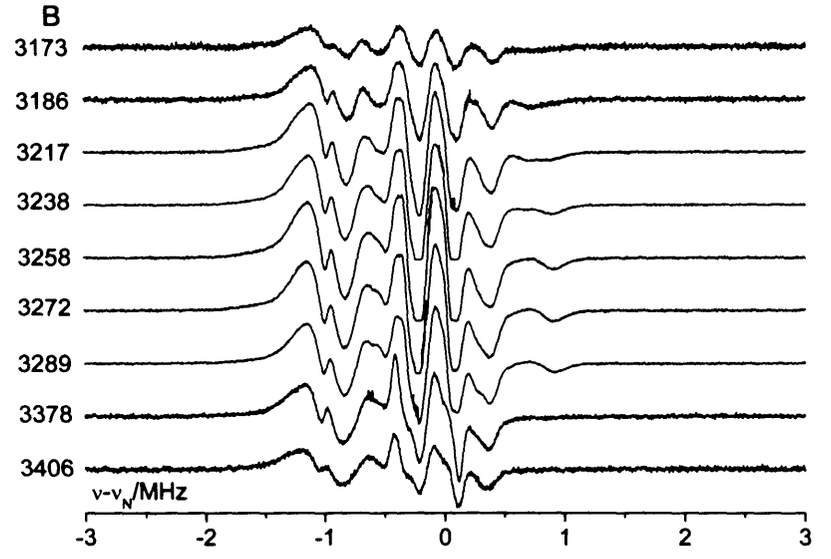

Figure A.7c: Experimental CW-^{1}H ENDOR spectra (10K) of $[Cr(CO)_4(Ph_2PN(Et)PPh_2)]^+$ (**2d**) recorded in deuterated dichloromethane/toluene at a microwave frequency of 9.486 GHz and a modulation depth of 79 kHz. The angular selective spectra were obtained at the magnetic field positions (*B* in Gauss) shown in the Figure.

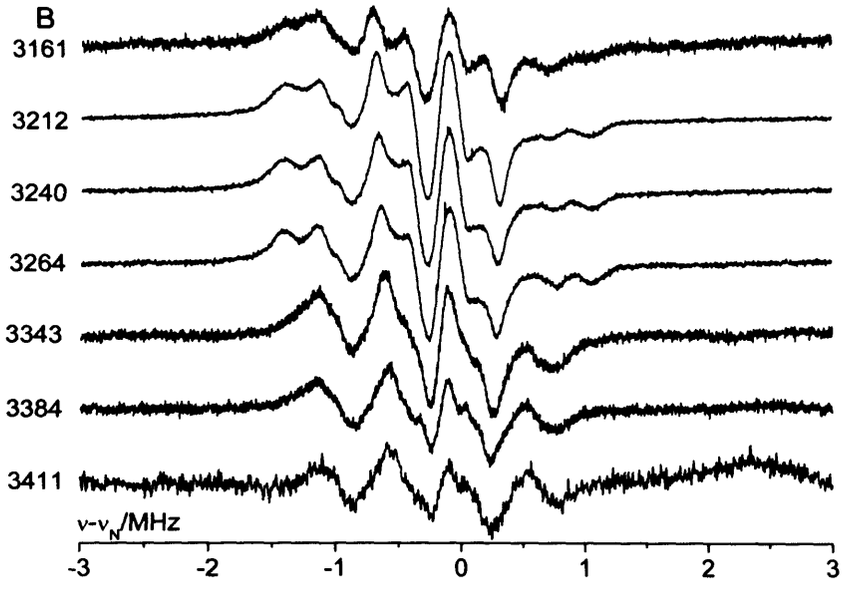

Figure A.7d: Experimental CW-^{1}H ENDOR spectra (10K) of $[Cr(CO)_4(Ar_2PN(Me)PAr_2)]^+$ (Ar = 2-C_6H_4(Et)) (**2e**) recorded in deuterated dichloromethane/toluene at a microwave frequency of 9.475 GHz and a modulation depth of 79 kHz. The angular selective spectra were obtained at the magnetic field positions (*B* in Gauss) shown in the Figure.

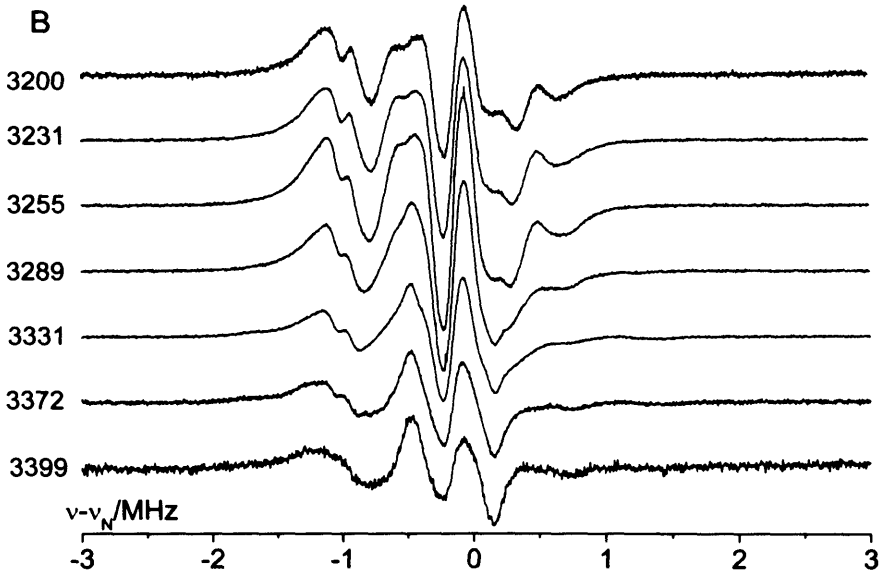

Figure A.7e: Experimental CW-^{1}H ENDOR spectra (10K) of $[Cr(CO)_4(Ph_2PN(iBu)PPh_2)]^+$ (**2f**) recorded in deuterated dichloromethane/toluene at a microwave frequency of 9.476 GHz and a modulation depth of 79 kHz. The angular selective spectra were obtained at the magnetic field positions (*B* in Gauss) shown in the Figure.

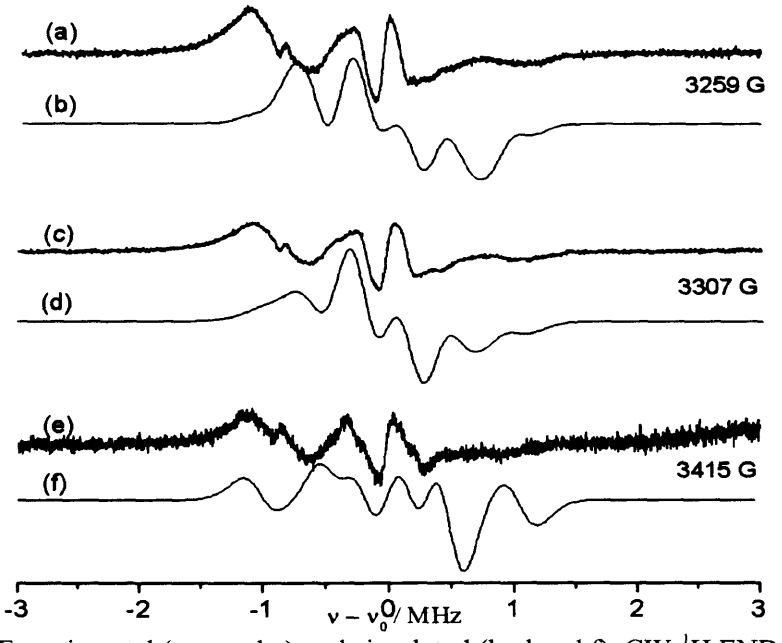

Figure A.7f: Experimental (a, c and e) and simulated (b, d and f) CW-^{1}H ENDOR spectra (10K) of $[Cr(CO)_4\mathbf{a}]^+$ recorded in deuterated dichloromethane/toluene. The angular selective spectra were obtained at the magnetic field positions (*B* in Gauss) shown in the Figure.

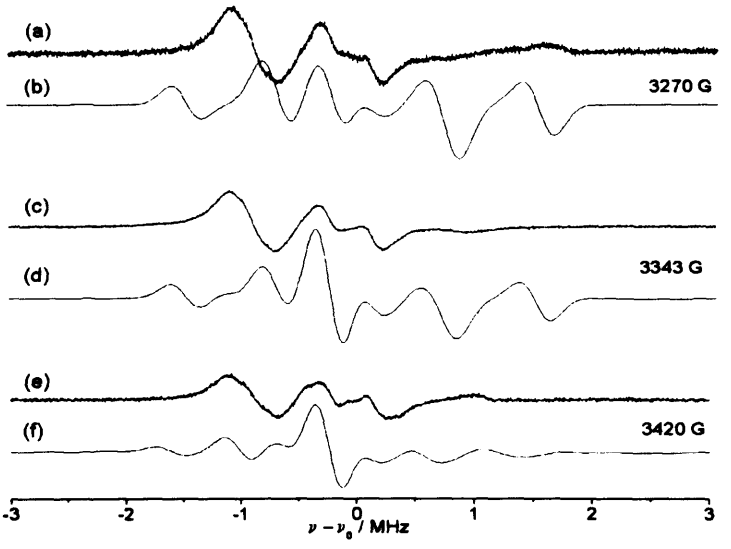

Figure A.7g: Experimental (a, c and e) and simulated (b, d and f) CW-^{1}H ENDOR spectra (10K) of $[Cr(CO)_4\mathbf{b}]^+$ recorded in deuterated dichloromethane/toluene. The angular selective spectra were obtained at the magnetic field positions *(B* in Gauss) shown in the Figure.

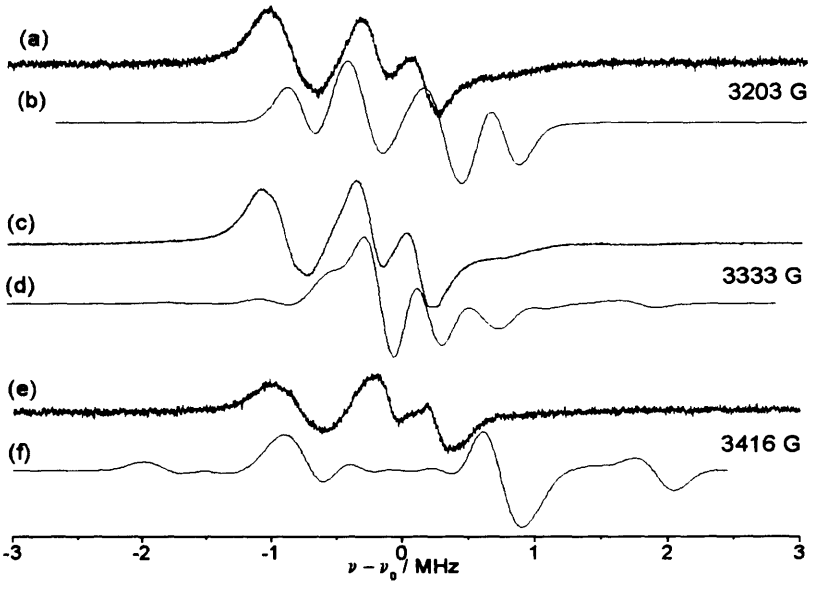

Figure A.7h: Experimental (a, c and e) and simulated (b, d and f) CW-^{1}H ENDOR spectra (10K) of $[Cr(CO)_4\mathbf{c}]^+$ recorded in deuterated dichloromethane/toluene. The angular selective spectra were obtained at the magnetic field positions (*B* in Gauss) shown in the Figure.

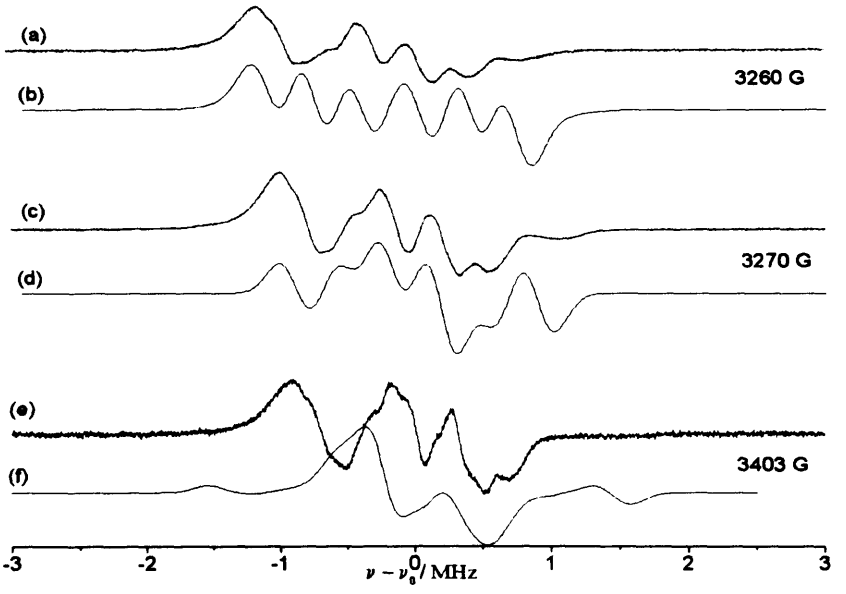

Figure A.7i: Experimental (a, c and e) and simulated (b, d and f) CW-^{1}H ENDOR spectra (10K) of $[Cr(CO)_4\mathbf{d}]^+$ recorded in deuterated dichloromethane/toluene. The angular selective spectra were obtained at the magnetic field positions (*B* in Gauss) shown in the Figure.

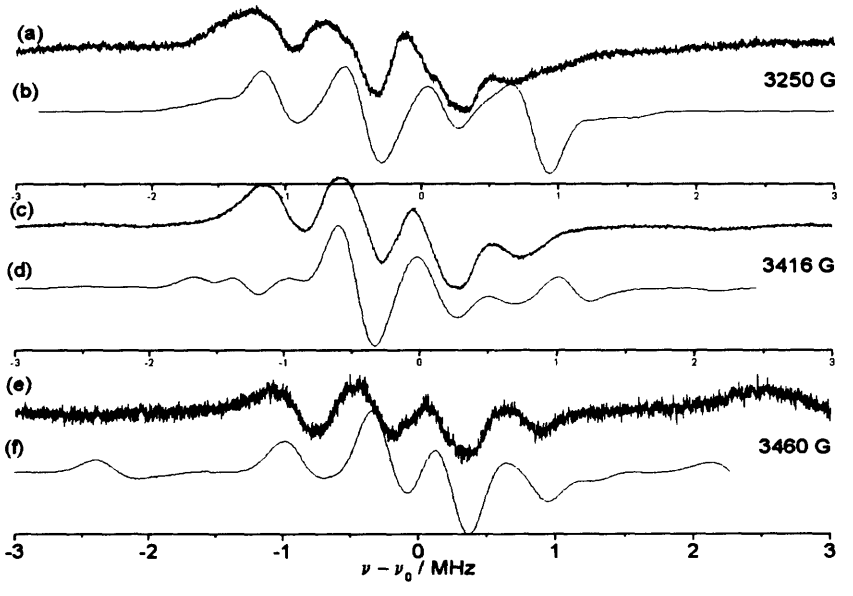

Figure A.7j: Experimental (a, c and e) and simulated (b, d and f) CW-^{1}H ENDOR spectra (10K) of $[Cr(CO)_4\mathbf{e}]^+$ recorded in deuterated dichloromethane/toluene. The angular selective spectra were obtained at the magnetic field positions (*B* in Gauss) shown in the Figure.

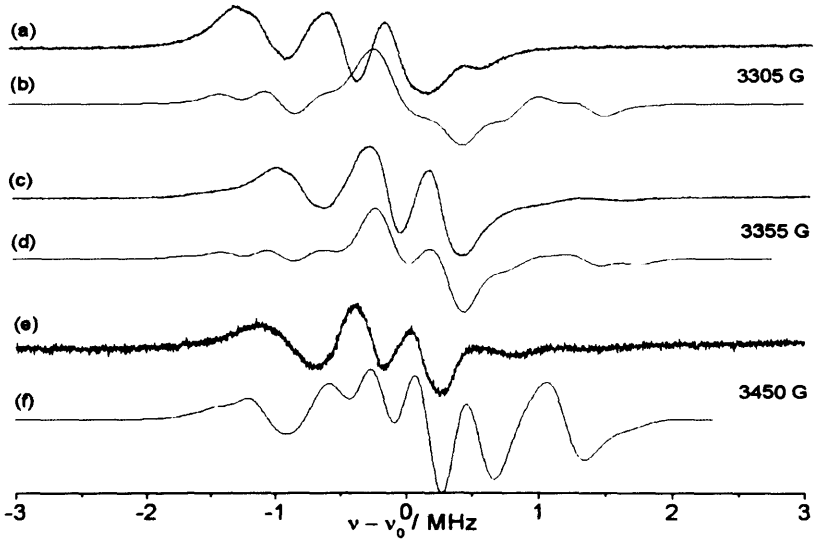

Figure A.7k: Experimental (a, c and e) and simulated (b, d and f) cw ^{1}H ENDOR spectra (10K) of $[Cr(CO)_4\mathbf{f}]^+$ recorded in deuterated dichloromethane/toluene. The angular selective spectra were obtained at the magnetic field positions (*B* in Gauss) shown in the Figure.

Orientation-selective ENDOR measurements at Q-band (34.1 GHz) were carried out on $[Cr(CO)_4\mathbf{g}]^+$. Weakly coupled ^{1}H nuclei were visible in the spectra, with the couplings centred on the nuclear Larmor frequency ν_N (~ 50 MHz at 12000 G) and the peaks split by the hyperfine coupling *A*.

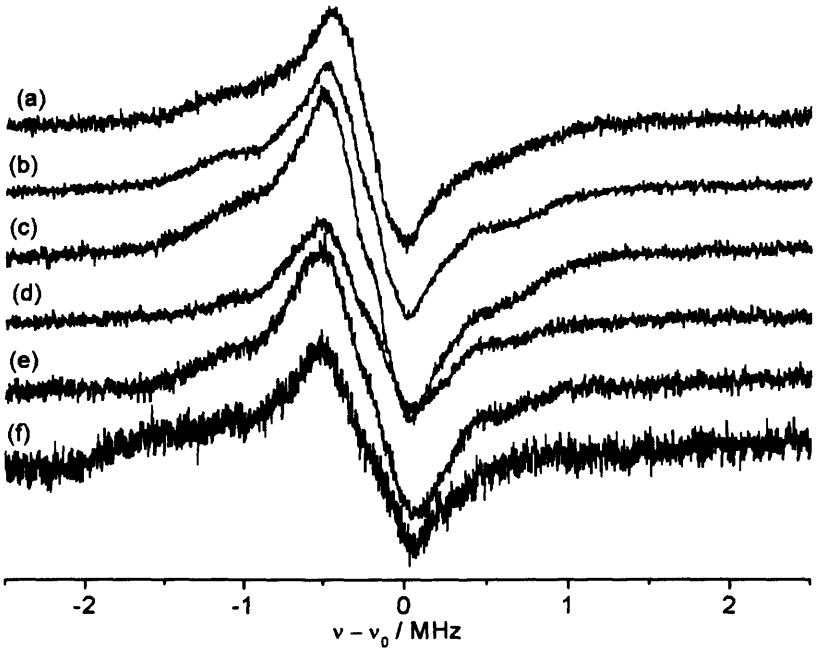

Figure A.8: Experimental CW-^{1}H ENDOR spectra (10K) of $[Cr(CO)_4\mathbf{g}]^+$ recorded in deuterated dichloromethane/toluene. The angular selective spectra were obtained at: (a) 11780 G, (b) 11857 G, (c) 11926 G, (d) 12080 G, (e) 12208 G and (f) 12328 G.

The spectra are not as well-resolved as those recorded at X-band, and only one broad pair of peaks can be seen in each spectrum. The lack of resolution of the angular dependency of the ^{1}H couplings means that simulation of the data would not be as informative as that already performed on the X-band spectra. No peaks attributable to ^{31}P nuclei were observed in any of the spectra.

A.5.3 CW- ^{31}P ENDOR

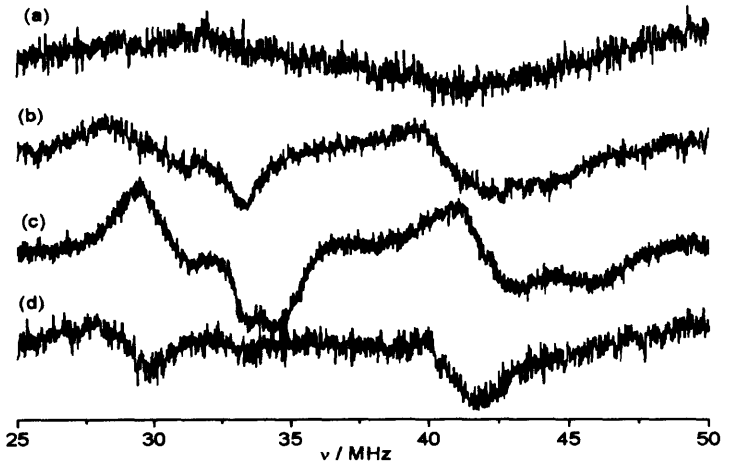

Figure A.9a: Experimental CW-^{31}P ENDOR spectra (10K) of $[Cr(CO)_4\mathbf{d}]^+$ recorded at: (a) 3229 G, (b) 3287 G, (c) 3362 G and (d) 3441 G. The spectra were recorded in deuterated dichloromethane/toluene.

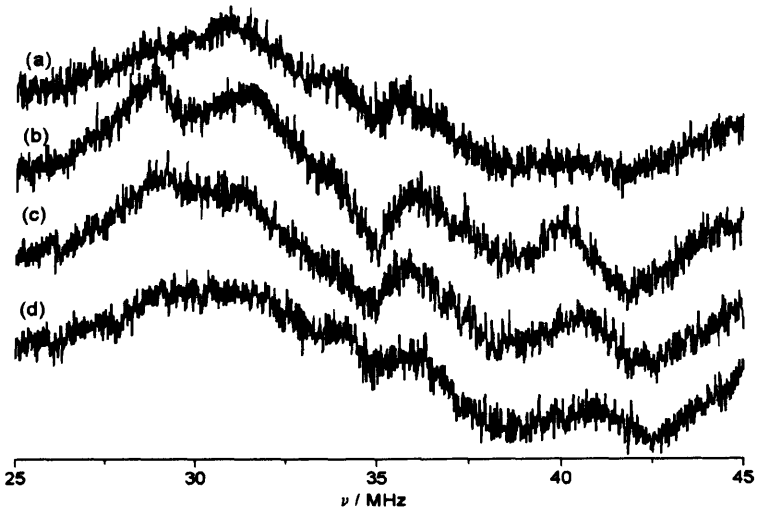

Figure A.9b: Experimental CW-^{31}P ENDOR spectra (10K) of $[Cr(CO)_4\mathbf{e}]^+$ recorded at: (a) 3234 G, (b) 3285 G, (c) 3337 G and (d) 3457 G. The spectra were recorded in deuterated dichloromethane/toluene.

A.5.4 CW- ^{14}N ENDOR

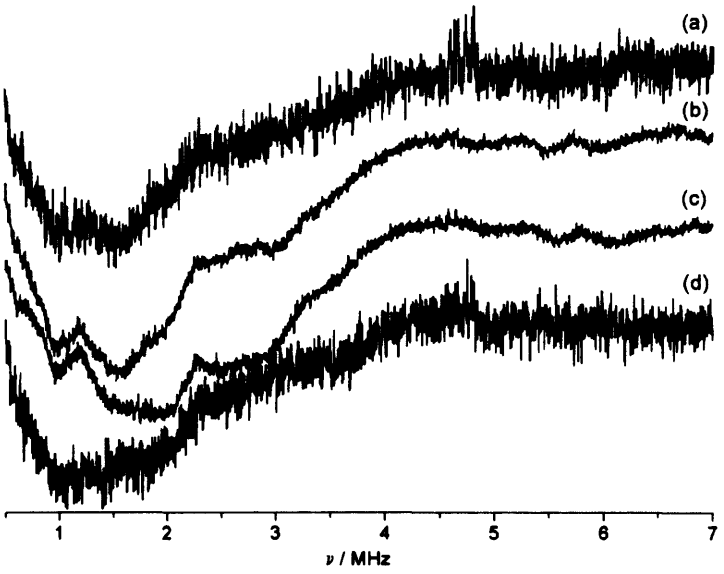

Figure A.10a: Experimental CW-^{14}N ENDOR spectra (10K) of $[Cr(CO)_4e]^+$ recorded in deuterated dichloromethane/toluene. The angular selective spectra were obtained at: (a) 3234 G, (b) 3285 G, (c) 3337 G and (d) 3457 G.

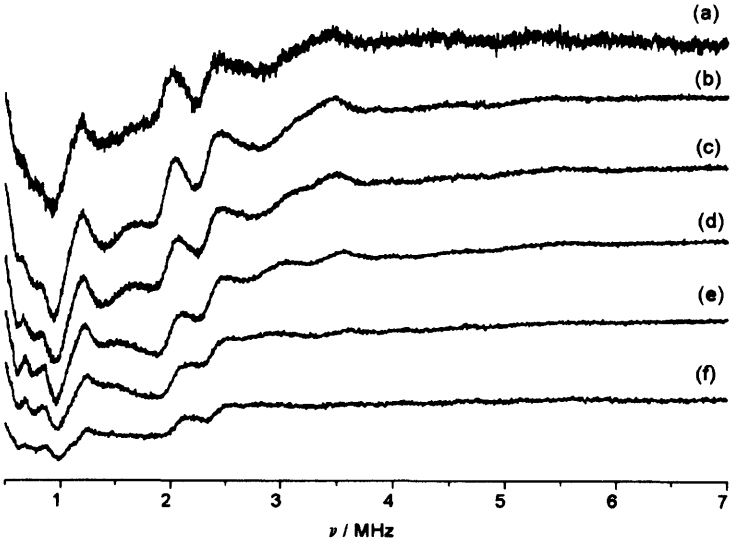

Figure A.10b: Experimental CW-^{14}N ENDOR spectra (10K) of $[Cr(CO)_4g]^+$ recorded in deuterated dichloromethane/toluene. The angular selective spectra were obtained at: (a) 3273 G, (b) 3304 G, (c) 3328 G, (d) 3362 G, (e) 3404 G and (f) 3445 G.

A.6 Appendix to Chapter 6 (Supporting & additional EPR spectra)

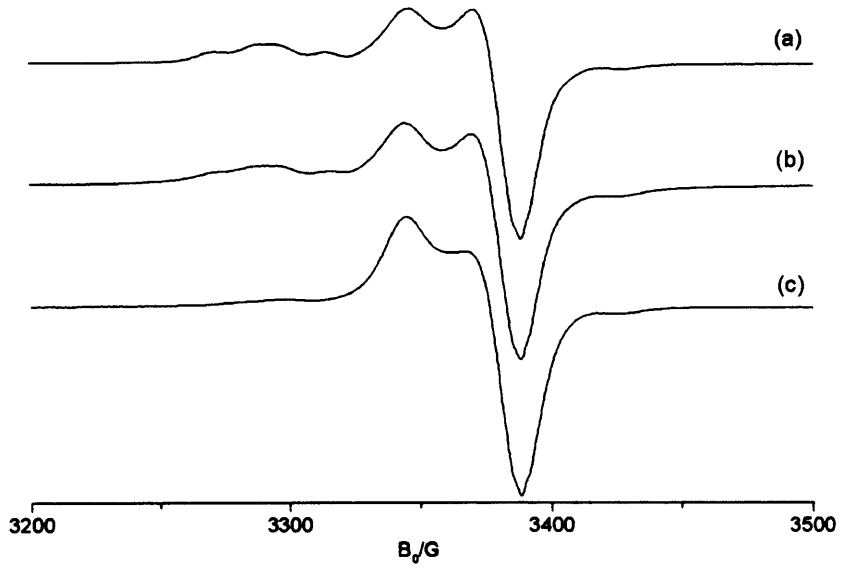

Figure A.11: Experimental CW-EPR spectra of $[Cr(CO)_4\mathbf{g}]^+$ in dichloromethane/toluene after activation with approximately (a) 2.5, (b) 5 and (c) 10 equivalents of TEA/toluene. Recorded at 140 K.

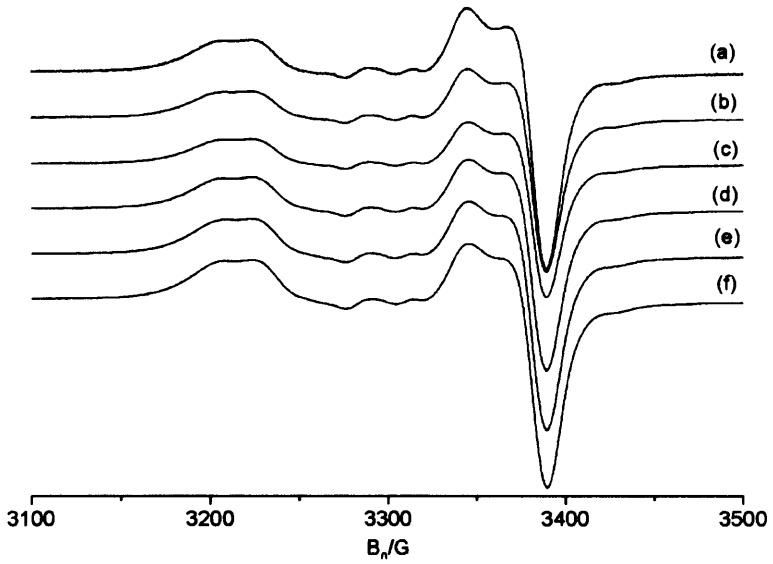

Figure A.12: Experimental CW-EPR spectra of $[Cr(CO)_4\mathbf{g}]^+$ in dichloromethane/toluene after activation with approximately 10 equivalents of TEA/toluene. Recorded at (a) 1, (b) 5, (c) 10, (d) 15, (e) 20 and (f) 25 mW. All recorded at 140 K.

A.6.1 Ligand studies

The addition of TEA/toluene was repeated using different complexes to probe the effect of ligand type on activation results. Therefore $[Cr(CO)_4\mathbf{b}]^+$ and $[Cr(CO)_4\mathbf{d}]^+$ were activated with various equivalents of TEA/toluene and the results shown in Figures A.13a and A.13b respectively.

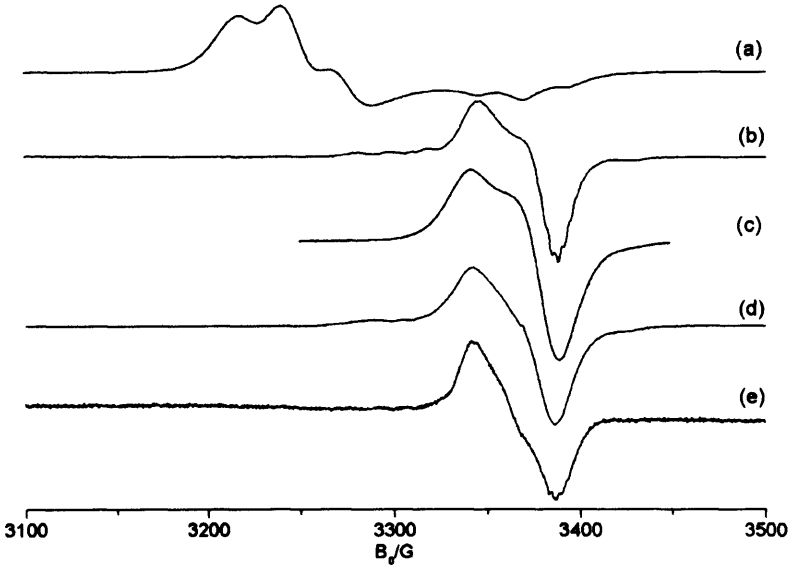

Figure A.13a: Experimental CW-EPR spectra of $[Cr(CO)_4(dppp)]^+$ (**2b**) in dichloromethane (a) unactivated, and after activation with approximately (b) 2, (c) 10, (d) 20 and (e) 60 equivalents of TEA/toluene.

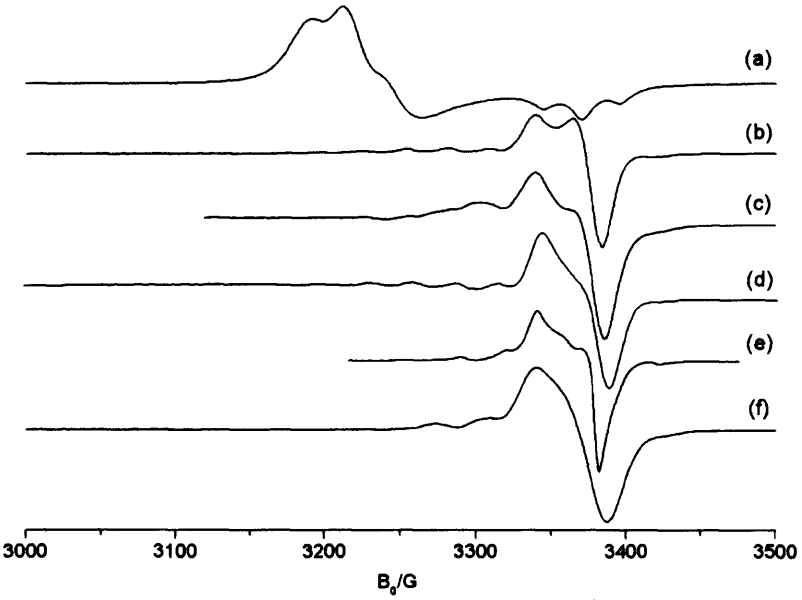

Figure A.13b: Experimental CW-EPR spectra of $[Cr(CO)_4\mathbf{d}]^+$ in dichloromethane/toluene after activation with approximately (b) 2, (c) 10, (d) 60, (e) 100 and (f) 500 equivalents of TEA/toluene.

A.6.2 FSED-EPR Spectrum of Species IV

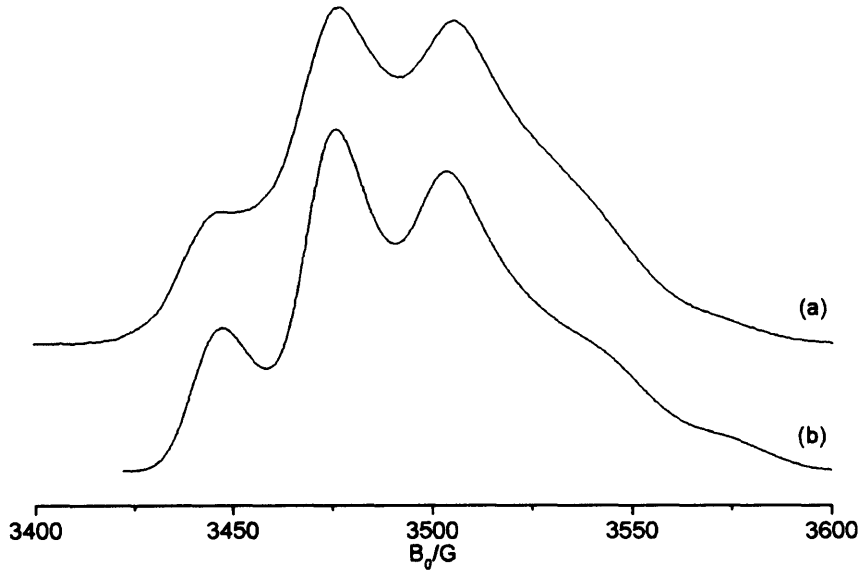

Figure A.14: Experimental (a) and simulated (b) FSED-EPR spectra of $[Cr(CO)_4g]^+$ in dichloromethane after activation with approximately 10 equivalents TEA/toluene. Recorded at 10 K.